TOWARDS AN UNDERSTANDING OF THE SELF-ASSEMBLY AND APPLICATIONS OF PHOSPHOLIPID-CONTAINING NANOPARTICLES

STEPHEN CHRISTOPHER LEWIS HALL

A thesis submitted to the University of Birmingham
for the degree of DOCTOR OF PHILOSOPHY

School of Biosciences
College of Life and Environmental Sciences
University of Birmingham
September 2018

ABSTRACT

Polymer-stabilized phospholipid nanodiscs are nanoscale, discoidal assemblies containing a central core of lipid bilayer stabilized in aqueous solution by an amphipathic copolymer belt. Recently, nanodiscs have been applied to the extraction of membrane proteins directly from cellular membranes. However, the rapid adoption of nanodisc technology for biomolecular studies has outpaced the communities understanding of the fundamental properties of nanodisc-forming polymers which influence nanodisc self-assembly, as well as the inherent properties of the nanodiscs themselves.

In this study, the thermodynamics of nanodisc self-assembly have been probed in order to gain insights into the structural properties of existing and novel polymers which affect the self-assembly process. Subsequently, their application to solubilisation of biological membranes has been investigated, overcoming limitations of the current technology. Following these studies, investigations into the interaction of nanodiscs with pre-existing membranes at interfaces were performed, revealing how lipid exchange kinetics vary between nanodisc types. Furthermore, polymer-stabilised nanodiscs were observed to adsorb to lipid bilayers, enabling future surface-based studies of nanodisc-encapsulated membrane proteins. Finally, polymer-stabilized nanodiscs were shown to provide a soluble membrane surface for investigation of protein-lipid interactions. This has revealed a membrane-induced fibrilization of the bacterial lipoprotein YraP, providing clues as to its currently unknown function.

This thesis is dedicated to my parents.

For endless encouragement, love and support, I am forever grateful.

ACKNOWLEDGEMENTS

Over the course of my 4 years at Birmingham and Diamond, I have received the help and support from countless people, without which I would have floundered in the scientific abyss. First and foremost, I'd like to thank my two supervisors: Tim Dafforn and Tom Arnold. Both of you have provided me with much appreciated support, advice and most crucially, understood that I'm human and told me to take a break/ go to sleep when I was at my most dishevelled after a week of beam time. It's been a pleasure to work with both of you.

I need to give special thanks to Tim Knowles. Firstly, thanks for letting me muscle in on your projects after a slightly inebriated conversation at a Christmas party. But more importantly, you have given up so much of your time (and so many gels/ detergents) helping me tackle a whole host of conundrums. More than anyone, you reignited my passion for science after a particularly thrilling period of collecting seemingly endless isotherms. Thanks for everything mate!

My time at Birmingham was made infinitely more enjoyable as a result of the great bunch of people I got to know and work with. So thanks to members of the Dafforn Lab, past and present: Rich Logan, Aysha Ali, Charles Moore-Kelly, Matt Tridgett, Zoe Stroud, Julia Kraemer, Sarah Lee, Naomi Pollock, Haydn Little and of course Rosemary Parslow! Additionally, I'd like to thank all the other members of the 7th floor with whom I've had the pleasure of working alongside, so thanks to Mark Wheatley, Andy Lovering, Pooja Sridhar, Gareth Hughes, Pete Wotherspoon, Rich Meek, Ian Cadby, Jack Charlton, Sian Bailey, Penny La-Borde, Chris Harding, Scott White, Eva Hyde, Klaus Futterer and the rest of the inhabitants of the 7th floor, past and present. From the Diamond camp, I'd like to thank fellow 'Tom's Angels', Toby Robson and Joe Thompson. It was great working with both of you, and I wish you both the best of success.

From Bath, I'd like to thank Karen Edler for assuming the role of my unofficial tertiary supervisor. Thank you for all of your help and for tolerating the token biologist! Also, thanks to Cecilia Tognoloni, you have been a great friend and colleague, experiments with you were always great fun. So long and thanks for all the polymer!

I've received so much support from instrument scientists and facilities staff, well over and above the call of duty! So an enormous thank you to Najet Mahmoudi, James Doutch, Richard Campbell, Gemma Harris, Iain Walmsley and Asha Dopplapudi. I can't not make a special mention of Luke Clifton. I can't thank you enough for the amount of time and effort you put into helping me, in training, data analysis and applying for *very* last minute rapid-access beam time, not to mention the odd free beam time snuck in for good measure! I'll leave you with my legacy of the broken QCM-D cell!

On a personal note, I'd like to thank my family. Mum, Dad, and Kieran, I know you didn't really get why I was staying up all night using a "really big thing to look at really little things", but whenever I visited home, overly excited because I got another squiggly line, you always pretended to be happy for me, which meant the world. I'd never have got this far without your endless encouragement and unwavering support in everything I've done. Not to mention free food, that helped too!

The biggest thanks of all goes to Éilís. Thank you for putting up with me. I know I've been *slightly* stressed at times, but through it all you've had belief in me, been more than understanding about my constant state of chaos and perpetual tardiness because I 'just need one more measurement', you've picked me up when I'm down and constantly given me confidence in myself. You have been awesome.

Finally, I wish to express my gratitude to the EPSRC and Diamond Light Source for PhD studentship funding, and the ISIS pulsed neutron source, the Institut Laue Langevin, Synchrotron Soleil and Diamond Light Source for beamtime allocations.

Apologies if I've missed anyone, I am running out of adjectives anyway, but needless to say, I couldn't have done it without any of you.

TABLE OF CONTENTS

LIST OF FIGURES

LIST OF TABLES

LIST OF ABBREVIATIONS

$A_{2A}R$	Adenosine A_{2A} receptor
ABC	ATP binding cassette
ACMW	Air contrast-matched water
ATR	Attenuated total reflectance
AVP	Vasopressin
BLM	Black lipid membrane
C phase	Condensed phase
CD	Circular dichroism
CHAPSO	3-([3-cholamidopropyl]dimethylammonio)-2-hydroxy-1-propanesulfonate
CL	Cardiolipin
CMC	Critical micelle concentration
CSTR	Continually stirring tank reactor
D_2O	^2H_2O
DDM	n-dodecyl β-D-maltoside
dDMPC	1,2-dimyristoyl-$^2H_{54}$-*sn*-glycero-3-phosphocholine
D_h	Hydrodynamic diameter
DHPC	1,2-dihexanoyl-*sn*-glycero-3-phosphocholine
DIBMA	poly(diisobutylene-*alt*-maleic acid)
DMPC	1,2-dimyristoyl-*sn*-glycero-3-phosphocholine
dn/dc	Refractive index increment
E. coli	*Escherichia coli*
EDTA	Ethylenediaminetetraacetic acid
FTIR	Fourier--transform infrared
G phase	Gaseous phase
GPCR	G-protein-coupled receptor
HEK	Human embryonic kidney

IMAC	Immobilized metal affinity chromatography
LC phase	Liquid-condensed phase
LCP	Lipidic cubic phase
LE phase	Liquid-expanded phase
L_O	Liquid-ordered phase
LPS	Lipopolysaccharide
LUV	Large unilamellar vesivle
L_α	Fluid phase
L_β	Gel phase
MALS	Multi-angle light scattering
M_n	Number averaged molar mass
MSP	Membrane scaffold protein
M_w	Mass averaged molar masd
MWCO	Molecular weight cut-off
NMR	Nuclear magnetic resonance
NOESY	Nuclear Overhauser effect spectroscopy
NR	Neutron reflectometry
NTA	Nitrilotriacetic acid
OD	Optical density
OM	Outer membrane
OMP	Outer membrane protein
PAGE	poly(acrylamide) gel electrophoresis
PBS	Phosphate buffered saline
PC	Phosphatidylcholine
PDI	Polydispersity index
PE	Phosphatidylethanolamine
PG	Phosphatidylglycerol
PI	Phosphatidylinositol
PMA	Poly(methacrylate)
PMF	Proton motive force
POPC	1-palmitoyl-2-oleoyl-*sn*-glycero-3-phosphocholine
PS	Phosphatidyl-L-serine
PSD	Particle size distribution

$P_{\beta'}$	Ripple phase
QELS	Quasielastic light scattering
RAFT	Reversible addition-fragmentation chain transfer polymerization
RAFT-SMA	RAFT-synthesized poly(styrene-*co*-maleic acid)
R_g	Radius of gyration
R_h	Hydrodynamic radius
s.e.m.	Standard error of the mean
SANS	Small-angle neutron scattering
SAT	Saturation boundary
SAXS	Small-angle X-ray scattering
SDS	Sodium dodecyl sulfate
SEC	Size exclusion chromatography
SiMW	Silicon-contrast-matched water
SLB	Supported lipid bilayer
SLD	Scattering length density
SMA	Poly(styrene-*co*-maleic acid)
SMAd-A	Poly(styrene-*co*-maleic acid)-primary amine
SMA-ED	Poly(styrene-*co*-maleic acid)-ethylenediamine
SMALP	Poly(styrene-*co*-maleic acid) lipid particle
SMAnh	Poly(styrene-*co*-maleic anhydride)
SMA-QA	Poly(styrene-*co*-maleic acid)-quaternary amine
SMA-SH	Poly(styrene-*co*-maleic acid)-sulfhydryl
SMI	Poly(styrene-*co*-maleimide)
SMILP	Poly(styrene-*co*-maleimide) lipid particle
SOL	Solubilization boundary
SPR	Surface plasmon resonance
SRCD	Synchrotron radiation circular dichroism
TEM	Transmission electron microscopy
THF	Tetrahydrofuran
ThT	Thioflavin T
T_m	Gel-to-liquid phase transition temperature
TM	Transmembrane
TOF	Time-of-flight

T_P	Pre-transition temperature
UV	Ultraviolet
$V_{1a}R$	Vasopressin 1_a receptor
B-OG	Octyl β-D-glucopyranoside
ΔG	Gibbs energy change

CHAPTER 1

INTRODUCTION

1.1 THE IMPORTANCE OF BIOLOGICAL MEMBRANES

Within biology, membranes represent arguably the most fundamental and important interface, fulfilling both structural and functional roles in the cell. They are responsible for defining the boundary of the cell, as well as compartmentalization of cellular processes within organelles.[1] In addition, membranes represent the interface through which signals must be mediated to elicit a response,[2] whilst themselves being directly involved in cellular signaling.[3] Membranes are directly involved in microbial infection,[4,5] and antimicrobial resistance.[6,7] Viruses must cross membranes in order to initially infect the host cell, while daughter virions must once again cross the membrane to propagate. [8–11] Drugs and therapies which target intracellular components must enter the cell through the membrane – either by hijacking an existing mechanism, or being encapsulated in a membrane-permeable delivery system.[12–14] Drugs that do not require entry to the cell for function will frequently interact with the extracellular face of the membrane to interact with signaling cascades to alter metabolism.[15,16] Given the highly diverse roles that the membrane can assume, it is unsurprising that biological membrane research is a heavily studied field of paramount importance.

1.2 COMPOSITION, STRUCTURE AND PROPERTIES OF BIOLOGICAL MEMBRANES

Biological membranes have diverse structures and architectures throughout nature, with variations between different organisms and cell types. However, all membranes share a common property in that they contain amphiphilic molecules, which have both hydrophobic ‘tail’ groups and hydrophilic ‘head’ groups. In the simplest case, a surfactant monolayer will self-assemble at the air-liquid interface. Here,

hydrophilic head groups will interact with the aqueous solvent, while the hydrophobic head groups protrude from solution. In biological systems, membranes take the form of a bilayer whereby hydrophobic tail groups are excluded from solution by flanking layers of hydrophilic head groups. In the following section, an overview of common classes of surfactants found in biological membranes will be introduced, before briefly discussing the variety of biological membrane architectures. Finally, the factors affecting the physical-chemical properties of membranes will be discussed.

1.2.1 Chemical constituents of biological membranes

Amongst the most common surfactants found in biological membranes are phospholipids. Phospholipids contain a core structure of a phosphodiacylglycerol (Figure 1.1a). The fatty acid tail groups which are esterified to the core glycerol consist of an aliphatic hydrocarbon chain with lengths between C_{12} and C_{24}. The two fatty acid chains of the tail groups can be identical although are frequently asymmetric with differing degrees of unsaturation. The hydrophilic headgroup comprises the phosphate group which is covalently bound to a range of groups (Figure 1.1b). The most abundant eukaryotic phospholipid head group is the zwitterionic phosphatidylcholine (PC), which can be responsible for more than 50% of phospholipids found in the membrane. Other headgroups include the zwitterionic phosphatidylethanolamine (PE) and anionic phosphatidyl-L-serine (PS) and phosphatidylglycerol (PG). In addition to these common lipid headgroups, monosaccharide phosphatidylinositol (PI) lipids are frequently employed in eukaryotic membranes where phosphorylation of the inositol ring at different positions elicits specific cellular signaling responses. Cardiolipin (CL) is a phospholipid unique to bacterial and mitochondrial membranes. CL contains two phosphodiacylglycerol groups which are covalently linked by ether bonds to an additional glycerol. When exposed to osmotic stress, bacteria will increase the proportion of CL in their membranes in order to bolster membrane rigidity.[17]

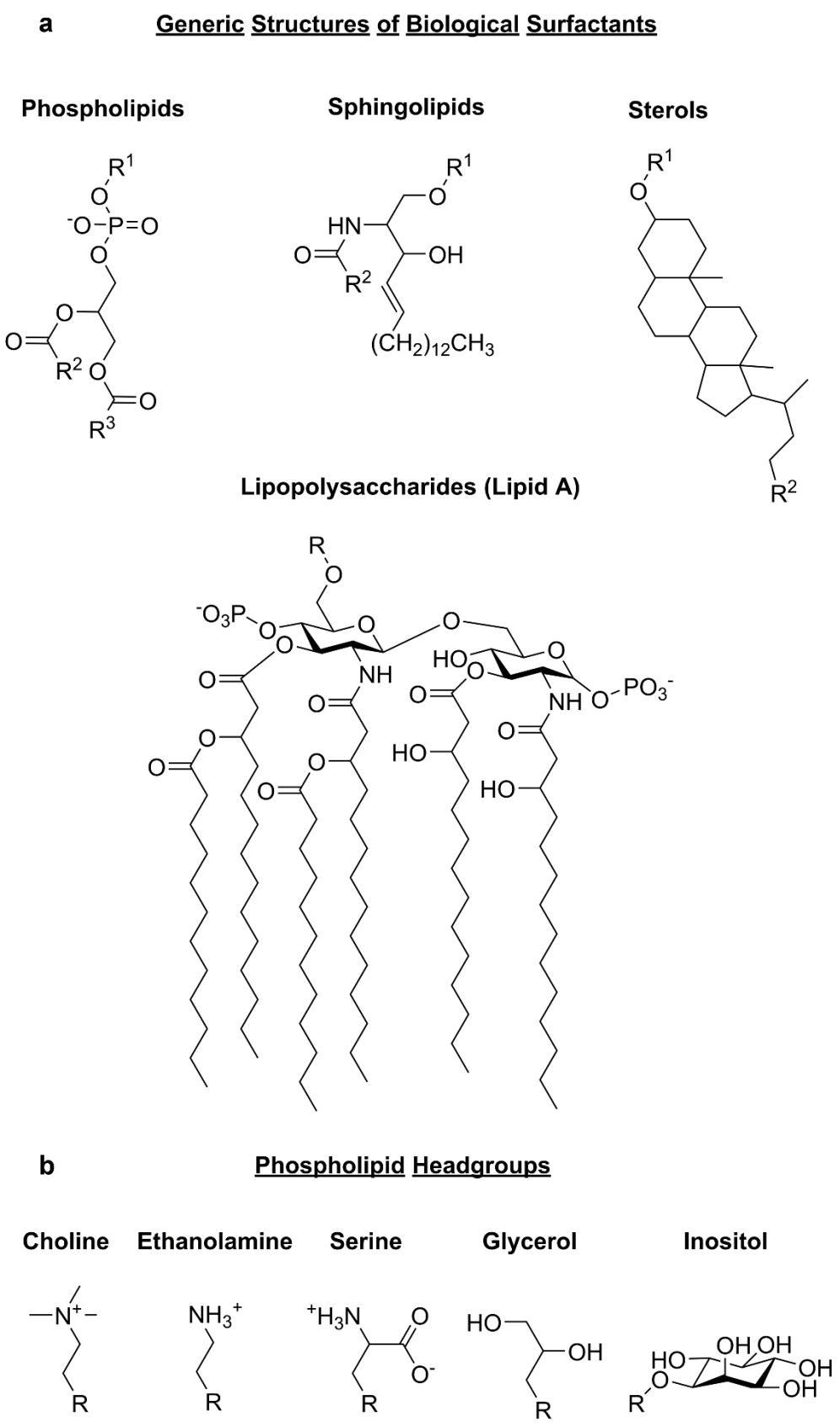

Figure 1.1. **a.** Chemical structures of backbones of common biological surfactants. **b**. Chemical structures of phospholipid headgroups found within biological membranes.

In addition to phospholipids, eukaryotic membranes also contain sphingolipids. Sphingolipids are characterized by their sphingosine backbone (Figure 1.1a), which can be acylated via an amide bond to a fatty acid chain to produce ceramides. Similarly to phospholipids, sphingolipids can have O-linked PC and PE headgroups, collectively known as sphingomyelins. Both phospholipids and sphingolipids can have one or more sugar residues bound to the lipid headgroups via the glycerol or sphingosine backbone to forming glycoglycerolipids and glycosphingolipids, respectively. To add further complexity to the composition of eukaryotic membranes, as much as 50 % of the membrane is composed of sterols.[18] Sterols are defined by a common aliphatic, poly-cyclic structure (Figure 1.1a). Like phospholipids and sphingolipids, sterols also have polar headgroup modifications and 'tail' modifications, although these are typically shorter than the fatty acid esters found on phospholipids and sphingolipids. Furthermore, the sterol backbone can exhibit different degrees of unsaturation. While proteobacteria contain no sphingolipids or sterols, they contain a unique class of lipid, lipopolysaccharide (LPS, Figure 1.1a). LPS is defined by a common 'lipid A' structure, where a disaccharide contains N- and O-linked, branched fatty acid chains.[19] The structure of lipid A varies amongst species with respect to chain length and the number of fatty acid chains and frequently has long, repeating oligosaccharide chains conjugated to the lipid A headgroup.[19]

1.2.2 Structures of biological membranes

Given the diversity of chemical species present in membranes across different phylum, species and even cell type, it is unsurprising that the structural architecture of membranes follows a similar pattern of diversity. As the diversity across all membranes throughout the multitude of phylogenetic branches is beyond the scope of this thesis, here the discussion will be limited to standard eukaryotic and bacterial membranes.

1.2.2.1 The eukaryotic plasma membrane

Eukaryotes, by definition, contain subcellular organelles compartmentalized by membranes, although here the discussion will be limited to the plasma membrane, that which encapsulates the cell. Figure 1.2a shows a schematic of the eukaryotic plasma membrane. The precise composition varies

amongst cell type and species, although common features can be identified. The plasma membrane has a bilayer structure and is composed of phospholipids, sphingolipids, sterols and glycolipids.[20] The plasma membrane displays a high degree of lipid asymmetry. For example, the inner, cytoplasmic leaflet is composed predominantly of PE, PS and PI lipids, while the outer leaflet is rich in PC and sphingomyelins.[21] Additionally, glycolipids are exclusively present in the outer leaflet [22] where they provide recognition sites for immunological signalling.[23] Abolishment of lipid asymmetry, either aberrant or deliberate, is associated with a range of disease states and cellular signaling events.[21]

1.2.2.2 Bacterial membranes

Compared to the eukaryotic plasma membrane, bacterial membranes display markedly different architectures and lipid composition. Gram-positive bacteria have an asymmetric single bilayer, with PI and PE present in the inner leaflet, PG lipids in the outer leaflet[24] and cardiolipin in both leaflets.[25] A unique outer-leaflet lipid to gram-positive bacteria is lipoteichoic acid, a diacylglycerol glycolipid with extended poly(phosphoglycerol) chains extending through a 40 – 80 nm thick peptidoglycan cell wall (Figure 1.3b).[25,26] In contrast, Gram-negative bacteria contain two membranes separated by the periplasm which contains a thin peptidoglycan layer (Figure 1.3c). The inner membrane is predominantly composed of PG, PE and CL phospholipids distributed across both leaflets, although some species have recently been found to contain PI and PC lipids.[27] The outer membrane, however, is highly asymmetric containing an inner leaflet of phospholipids and an outer leaflet of LPS,[28,29] coating the outside of the bacterium with oligosaccharide chains crosslinked by divalent cations to serve as a protective barrier against osmotic stresses and antimicrobial agents.[30]

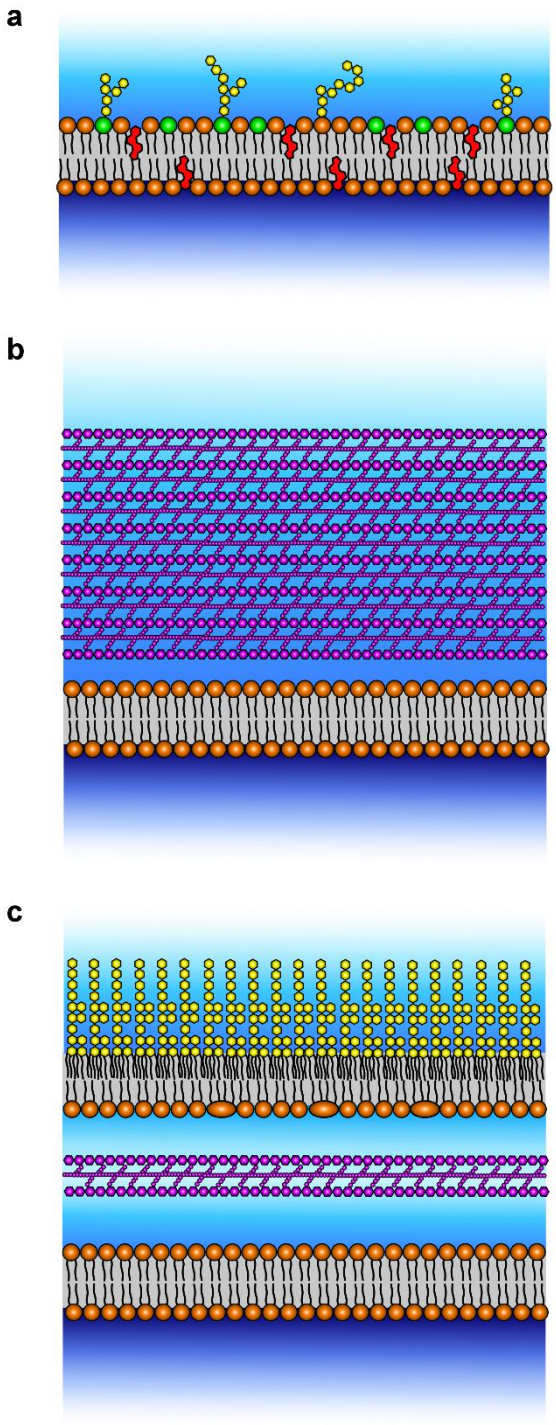

Figure 1.2. Schematics of biological membranes. **a.** A typical eukaryotic membrane. Phospholipids are depicted as orange, sterols as red, sphingolipids as green and glycosyl modifications to lipids are shown in yellow. **b.** A schematic of a Gram-positive membrane. The cell membrane is composed predominantly of phospholipids, shown in orange, with a thick cell wall formed of peptidoglycan, shown in purple. **c.** A schematic of the Gram-negative cell envelope. The inner membrane is composed of phospholipids, shown in orange, where a thin peptidoglycan layer resides in the periplasm, shown in purple. The outer membrane contains an inner leaflet composed of phospholipids, orange, and an outer leaflet of LPS, shown in yellow.

1.2.3 Physicochemical properties of membranes

The complexity of membrane composition and architectures serves to control the physicochemical properties of the membrane. In discussing the influence of membrane composition on the membrane properties, we will start with the simplest model; that of a phospholipid monolayer at the air-water interface.

1.2.3.1 Isothermal phase behaviour of Langmuir monolayers

A lipid monolayer, or Langmuir monolayer, will spontaneously self-assemble when lipids are spread on the surface of an aqueous subphase. This is entropically driven by the hydrophobic effect such that the surface tension of the aqueous subphase is minimized, as described by the Gibbs adsorption isotherm,[31]

$$\Gamma = -\frac{1}{RT} \cdot \frac{d\gamma}{d(\ln(C))}$$

Where Γ represents the surface excess (the difference in the interfacial concentration compared that to a cross section through bulk solution, with units of μmol m^{-2}), γ represents the surface tension, C represents the total concentration of surfactant, and R and T are the universal gas constant and temperature, respectively.

If a known quantity of lipids at the air-liquid interface are contained within a defined area by impermeable barriers using a Langmuir trough, the surface pressure can be monitored as a function of area by means of the Wilhelmy plate where surface pressure, π, is defined as the difference between the surface tension of the subphase without surfactant, $\gamma_{solvent}$, and that with surfactant present, $\gamma_{solution}$, as given by,[31]

$$\pi = \gamma_{solvent} - \gamma_{solution}$$

Therefore, surface pressure-area (π-A) isotherms are a direct measure of interactions between surfactant molecules at the interface. Through these measurements, distinct regions can be identified which correspond to discreet lipid phases (Figure 1.3). Where the area per molecule is large enough so that

lipids are effectively non-interacting, they behave as an ideal gas exhibiting 2D diffusion, where there are no changes in surface tension of the subphase upon compression. [32,33] This is known as the gaseous (G) phase. Compression of the monolayer leads to Van der Waals and electrostatic interactions between interfacial lipids as they behave as a liquid, and they pass through a transition to the liquid-expanded phase (LE). Here, interactions are still weak and so the tails still display a high degree of disorder. Further compression leads to a phase transition where a plateau is observed in the π-A isotherm as phase separation occurs between LE and liquid-condensed (LC) phases in coexistence at equilibrium with each other.[32,33] This can be seen as a quasi-crystalline ordering through X-ray diffraction measurements as lipids become packed together and tails become aligned with a uniform tilt.[34] As the monolayer is compressed further still, it passes through a phase transition from the coexistence region to the LC phase and then to the condensed phase (C), where the interactions between lipids resembles that of a solid material. Here, lipids are packed together so tightly that the tails are perpendicular to the interface[34] and the most force is required to compress the monolayer.[32,33] Compression beyond C-phase leads to collapse, where the monolayer buckles, folds into sections of bilayer protruding into the subphase and can bud into vesicular bilayers.[35] While challenging to measure directly, it has been estimated that the lateral pressure acting on biological bilayers is approximately 30 mN m^{-2},[36] placing them within the LC phase for most mixed Langmuir monolayers studied.

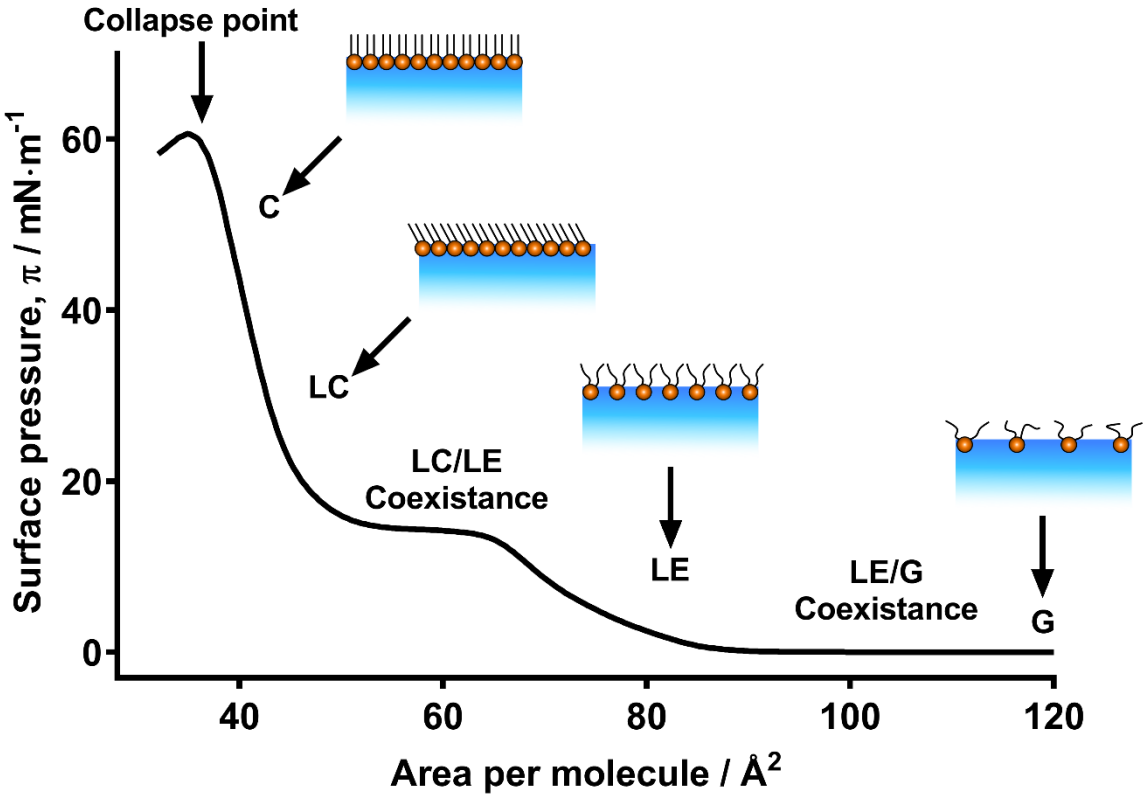

Figure 1.3. A typical surface pressure-area isotherm for a Langmuir monolayer of phospholipids at the air-water interface. Regions of the isotherm corresponding to each phase are labelled along with schematic representations of lipid phases.

1.2.3.2 Thermotropic phase behaviour of lipid bilayers

Most of the understanding of the phase behaviour of lipid bilayers comes from thermotropic phase transitions (Figure 1.4). At low temperatures, membranes exist in a gel phase. In this phase, the lipids are closely packed together exhibiting ordered packing of the tails perpendicular to the plane of the bilayer, limiting their lateral diffusion through the membrane.[37] Depending on the ratio of the headgroup and tail volumes, this can either be the $L_{ß}$ or the $L_{ß'}$ phase, distinguished by the tilt of the tails. For example, PE lipids have a small headgroup, therefore will pack as a hexagonal array of cylinders with the tails perpendicular to the plane of the membrane ($L_{ß}$ phase) . PC lipids, however, have a larger headgroup and will therefore exhibit a tilted orientation ($L_{ß'}$ phase) for optimal packing.[38] As temperature increases, membranes in the $L_{ß'}$ phase pass through a pre-transition, T_P, to the ripple phase, $P_{ß'}$. This is characterized by an observable out of plane, static oscillation with alternating regions tending more towards either gel or fluid phase. Increasing temperature further, the membrane will cross the gel-to-liquid phase transition temperature, T_m, and the membrane will enter the fluid phase, L_{α}.[37] For membranes in the $L_{ß}$ phase, this transition proceeds directly to L_{α} without passing through $P_{ß'}$.[39] When in the liquid phase, the lateral diffusion of lipid molecules is greatly increased and tails show the least amount of ordering. This can increase the permeability of the membrane to hydrophilic solutes,[40] increases membrane fusion events,[41] and also accelerates the rate of lipids transitioning between bilayer leaflets in a process known as 'flip-flop'.[42]

The plasticity of cells requires membranes to be in this fluid phase and as such the cell will alter the lipid composition of the membranes to maintain an optimum fluidity [43–45]. Bilayers containing a higher proportion of long-chain, unsaturated lipids will have a higher T_m than those containing greater quantities of short chain, unsaturated lipids due to the increased Van der Waals contacts possible between lipids in the bilayer requiring more thermal energy to overcome. The incorporation of sterols in the membrane also has a pronounced influence of the bilayer phase. Intercalation of sterols amongst lipid tails leads to the formation of the liquid-ordered (L_O) phase which can be reached from either the gel or fluid phase to form a coexistence of L_O with either L_{α} or $L_{ß}$/ $L_{ß'}$.[46] Within this phase, the bilayer has properties

between that of the L_α and $L_ß$ phases, displaying more order than in L_α but retaining a high lateral mobility.[47,48] This property means sterols are often employed as a fluidity 'buffer' to ensure the membrane maintains at optimum fluidity.[49] However, the complex lipid composition of biological membranes can lead to phase separation, with high T_m lipids and cholesterol-rich L_O phase regions clustering in gel-like 'islands' amongst a fluid 'ocean'. These regions are known as lipid rafts.[50] The biological significance of lipid rafts remains controversial, although recent evidence points toward important roles in signaling and viral infection[51] with evidence from molecular dynamics simulations suggesting roles in membrane permeability.[52]

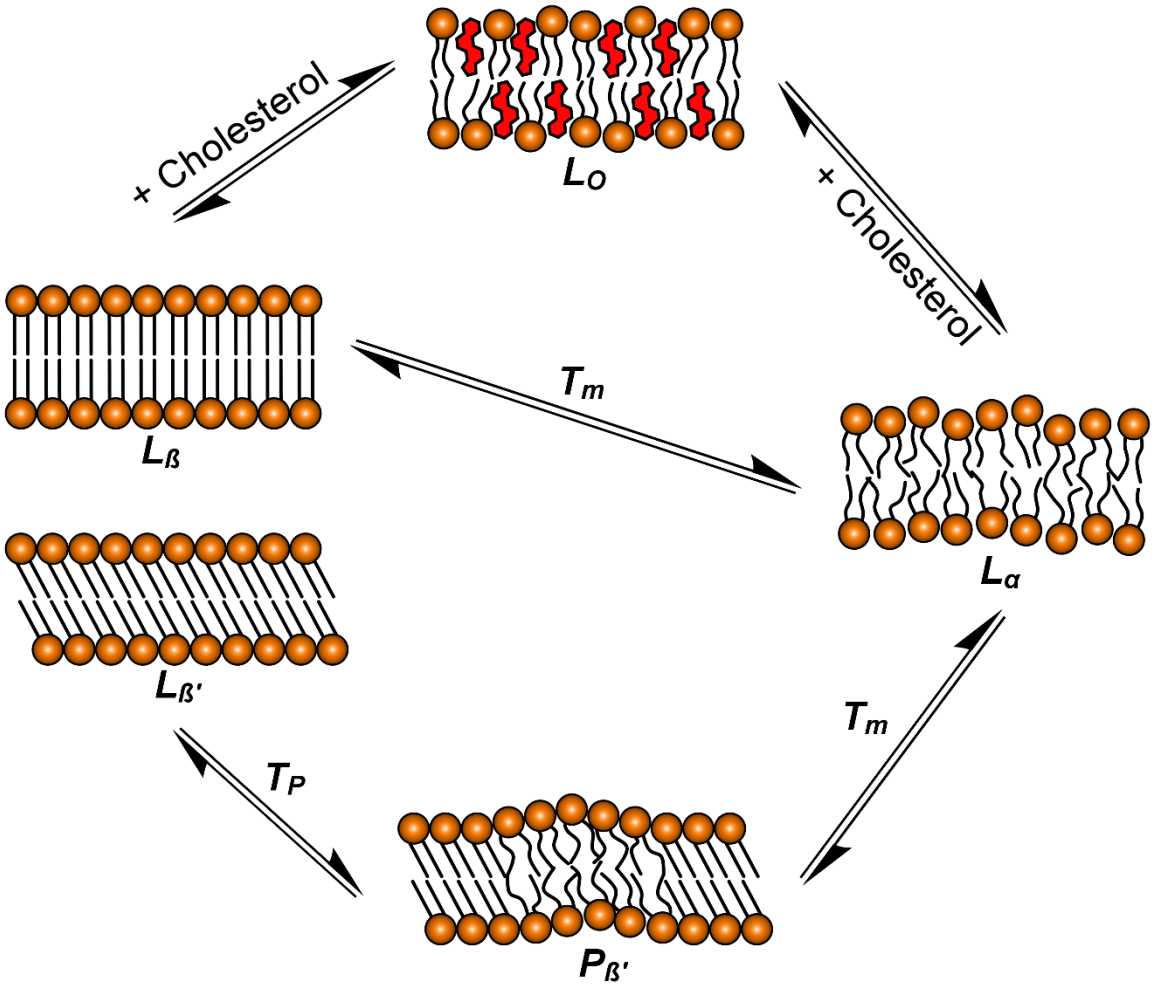

Figure 1.4. Schematic of thermotropic phases and phase transitions experienced by phospholipid bilayers.

1.2.3.3 Membrane polymorphism and curvature

As alluded to above, the relative volumes of the lipid head and tail groups influence the membrane properties, not only in terms of thermotropic phase behaviour, but also by defining membrane curvature and polymorphism (Figure 1.5). Curvature of an aqueous suspension of an individual lipid moiety can be estimated by the critical packing parameter, σ, given by

$$\sigma = \frac{v_m}{a_h \cdot l_c}$$

Where the packing is dependent on the ratio of the molecular volume, v_m, to the product of the headgroup area, a_h, and the tail length given fully extended acyl chains, l_c.[53] Where $\sigma < 1/3$, assemblies will be formed exhibiting positive curvature, *ie*, curving away from the aqueous phase. Where $\sigma \approx 1$, planar lamellar assemblies are formed and where $\sigma > 1$, the membranes will exhibit negative curvature. Both the headgroup and tail properties therefore influence membrane curvature. Saturated PC and PS lipids can be approximated as cylindrical molecules so can pack within a planar lamellar assembly. Similarly, PE and phosphatidic acids are relatively small headgroups and can be approximated as 'wedge' shape, therefore membranes will display negative curvature and larger headgroups such as PI, approximated as a conical shape, enforce positive curvature.[54] As the packing parameter depends on the overall molecular volume, unsaturated acyl chains will increase the molecular volume compared to an otherwise equivalent saturated variant. Therefore, unsaturated lipids can also encourage greater curvature and have been shown to facilitate membrane deformation.[55] Cellular mechanisms can exploit the inherent curvature induced by enrichment in specific lipids where membrane curvature is required. For example, plant cells can form highly curved cylindrical protrusions of the plasma membrane which fuse with adjacent cells.[56] These tubular protrusions are highly enriched in sterols and long-chain saturated sphingolipids which are proposed to stabilize the high degree of membrane curvature. However, as discussed above, biological membranes contain a complex lipid content. For a heterogeneous membrane to exhibit curvature then an asymmetry between bilayer leaflets is required, *ie*, lipids favouring positive curvature on one leaflet and lipids favouring negative curvature in the other. However, the fluidity

requirement of biological membranes results in flip-flop of lipids between leaflets, abolishing asymmetry such that the membrane would exhibit no net curvature.[57] It is for this reason that cells must actively maintain lipid asymmetry to favour curvature, in addition to direct mechanical action on the membrane mediated by the final universal constituent of biomembranes: membrane proteins.[57]

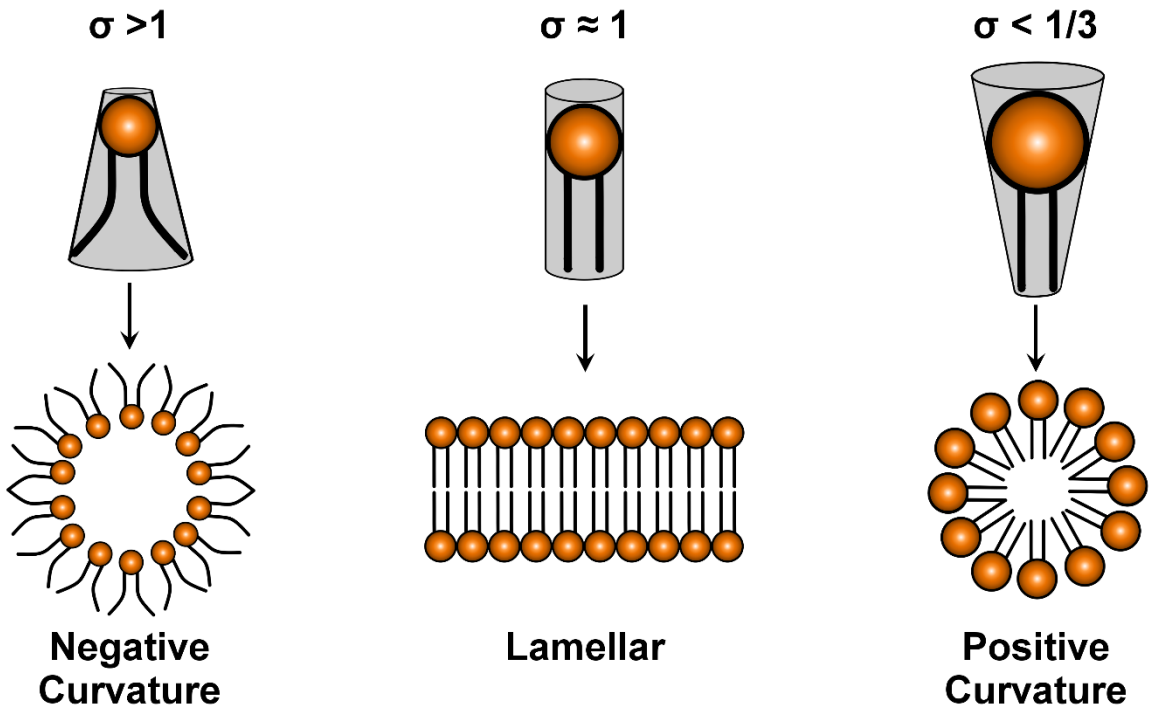

Figure 1.5. Schematic representation of lipid shapes as defined by the critical packing parameter, and the membrane curvature induced by the molecular shape of lipids within the membrane.

1.3 MEMBRANE PROTEINS

Thus far, we have limited the discussion of biological membranes to the lipid content. However, membranes also contain membrane proteins responsible for a host of structural, signaling and catalytic functions. In the following section membrane proteins will be introduced, categorized by their interaction with the membrane and structural properties, with examples given in each case. Following this, the challenges involved in membrane protein solubilization and isolation will be discussed whilst highlighting the poor nature of classical 'head and tail' detergents in mimicking the role of lipids within the membrane.

1.3.1 Structural and functional diversity of membrane proteins

Membrane proteins can be grouped into two broad categories based on their interaction with the membrane: transmembrane proteins that cross both leaflets of the bilayer (bitopic), peripheral membrane proteins that interact with a single leaflet (monotopic) or only with the membrane surface. While first proposed along with the 'fluid-mosaic' model of cellular membranes in 1972 by Singer and Nicholson,[45] this broad classification has largely held true to date.

1.3.1.1 α-helical transmembrane proteins

The transmembrane (TM) spanning component of integral membrane proteins is most frequently composed of a short, hydrophobic α-helix which is approximately 25 residues in length. α-helical membrane proteins can either contain a single TM helix, or can contain several TM helices connected by alternating cytoplasmic and extracellular hydrophilic loops in order to form a TM α-helical bundle. G-protein coupled receptors (GPCRs) are a common example which have a characteristic 7 TM helical bundle structure (Figure 1.6).[58] In proteins containing a TM bundle, hydrophobic side chains are present along one face of the helix solubilizing the protein within hydrophobic core of the bilayer. Hydrophilic side chains tend to be found within the core of the TM bundle, stabilizing the interior of the TM region by partitioning of hydrophilic groups by the hydrophobic effect. In the case of GPCRs mentioned above, ionic locks are formed between adjacent helices within the bundle.[59] This ionic interaction stabilizes

particular conformations of the bundle during receptor activation to enable G-protein coupling and initiation of intracellular signaling cascades. This is in contrast to globular soluble proteins where the tertiary structure is also stabilized by the hydrophobic effect, although by formation a hydrophobic core, with polar, peripheral side chains interacting with the aqueous solvent.[60]

The structures and functions of α-helical membrane proteins are diverse. As well as cellular signaling receptors as mentioned above, selective ion channels, such as the KcsA potassium channel, frequently contain a tetrameric TM bundle, where each KcsA monomer contains 2 TM helices connected by a short monotopic helix, which arrange to form a gated aqueous pore through the membrane (Figure 1.6).[61] Similarly, voltage-gated sodium ion channels form a transmembrane tetrameric helical bundle through the membrane, although each monomer contains 6 TM helices (Figure 1.6).[62] In both cases, ion specificity is provided by loops within the core of the bundle, and conductance is achieved by a voltage or pH induced re-arrangement of the TM bundle to provide an aqueous channel into the cytoplasm.[61–63]

α-helical TM proteins can also use pH gradients across membranes to function in an enzymatic fashion. The F_1/F_0 ATP synthase (Figure 1.6) couples the energy released upon proton diffusion down a concentration gradient, the proton motive force (PMF), to ATP synthesis. The membrane spanning F_0 domain is a large multi-component complex containing the 'a' subunit, forming a transmembrane protein channel from 5 TM helices and a single amphipathic helix, the 'b' homodimer forming an extended helical coiled-coil and a ring of 8 – 15 'c' subunits,[64] each containing 2 TM helices.[65] Flow of protons through F_0 leads to a rotation of the c-ring which is coupled via a coiled-coil stalk (the γ subunit) to the soluble F_1 ATPase domain, resulting in ATP syntheses. Crucially, the F_1/F_0 complex can function in reverse as an ATPase, with ATP hydrolysis causing rotation of the c-ring and generation of a proton motive force by the active pumping of protons against the pH gradient.

As a final example, α-helical TM proteins can function as pumps for small molecules and proteins. The resistance-nodulation-cell division (RND) family of Gram-negative bacterial efflux pumps are responsible for PMF-dependent export of a host of antimicrobial agents and are a continued mechanism of antimicrobial resistance, presenting a global threat to human health.[66,67] Of these multidrug efflux

pumps, the tripartite AcrAB-TolC system is among the best characterized (Figure 1.6).[68–71] AcrB forms a homotrimer within the inner membrane of Gram-negative bacteria, where each monomer contains 12 TM helices. The periplasmic domain of AcrB contains a large central pore where drugs to be exported are proposed to enter via solvent accessible channels from the periplasm or via binding sites within the TM bundle.[68,69] The transient docking of AcrB to TolC mediated by the AcrA adapter protein[70] allows a channel to form to the outside of the cell. Upon PMF-dependent conformational rearrangements of AcrB, drugs within the central cavity are actively pumped out of the bacterial cell.[71]

1.3.1.2 β-barrel transmembrane proteins

While the archetypal transmembrane protein was considered to be α-helical in structure, Gram-negative bacteria, mitochondria and chloroplasts have been found to contain a high proportion of 'ß-barrel' transmembrane proteins situated within the outer membrane (OM).[72] In contrast to α-helices, ß-strands require fewer residues to cross the membrane thanks to the extended backbone conformation, although the precise number varies depending on the tilt of the strand relative to the perpendicular vector through the membrane. The ß-barrel structure is formed as the backbone carbonyl and amide groups of each ß-strand will hydrogen bond with a neighbouring antiparallel strand to form a ß-sheet, and then wrap around to form a cylindrical arrangement so the maximum number of hydrogen bonds are formed between backbone residues. The extensive hydrogen bonding in ß-barrels confers a high level of stability.[73,74] This stability is important given the subcellular location of ß-barrels. Being situated within the Gram-negative outer membrane means the bacterium can only control conditions on one face of the bilayer, so embedded proteins require high tolerance to a broad range of solution conditions.[75] The stereochemistries of the side chains along each ß-strand means that each strand can be amphipathic, with one face containing hydrophobic residues, and the other face containing hydrophilic moieties.[76] As with α-helical bundles, the final barrel structure is further stabilized by the hydrophobic effect with exclusion of hydrophilic residues to the interior of the barrel, allowing hydrophobic residues to maintain solubility within the nonpolar bilayer core.

The hydrophilic interior of ß-barrels is utilized in their frequent roles as pores. OmpF is one of the most highly expressed outer membrane proteins (OMPs) in Gram-negative bacteria, containing a 16-strand ß-barrel which self-associate into a functional trimer (Figure 1.6).[77–80] The core of each barrel forms an aqueous channel through the OM, allowing bidirectional diffusion of small hydrophilic molecules in and out of the periplasm, including antibiotics such as ß-lactams and colicins.[81] The TolC component of the AcrAB-TolC system discussed above contains an outer membrane ß-barrel, although here the barrel is formed from a homotrimer of TolC (Figure 1.6).[70,71] Each monomer commits 4 adjacent antiparallel ß-strands to the barrel, where a large helical domain is formed within the periplasmic loops. Upon assembly of the TolC trimer and docking with AcrAB, a continuous pore of ~ 30 Å diameter is formed through the periplasm and the outer membrane allowing efflux of a broad range of antimicrobial drugs. [70,71]

Due to the segregation of the outer membrane from the sites of protein synthesis in the periplasm, Gram-negative bacteria contain an elegant OM biogenesis pathway enabling folding and insertion of nascent OMPs. Newly synthesized proteins destined for the OM are first secreted into the periplasm where unfolded OMPs are bound to periplasmic chaperones. Chaperone-bound OMPs are then delivered to the ß-barrel assembly machinery (Bam) complex at the OM.[82] The Bam complex itself contains the 16-strand ß-barrel protein BamA, where additional domains are present within periplasmic loops.[83,84] BamA is associated with 4 lipoproteins, BamB-E (Figure 1.6). While the mechanism of Bam-mediated OMP insertion remains unclear, studies of a related mitochondrial ß-barrel protein, the sorting and assembly machinery (Sam), have suggested that the nascent OMP is delivered into the core of the BamA barrel where folding occurs.[85] As ß-strands form, they complex within the ß-barrel of BamA, expanding the total diameter of the barrel.[83] The folded OMP then dissociates from the Bam complex whereby lateral diffusion through the OM is permitted.[85]

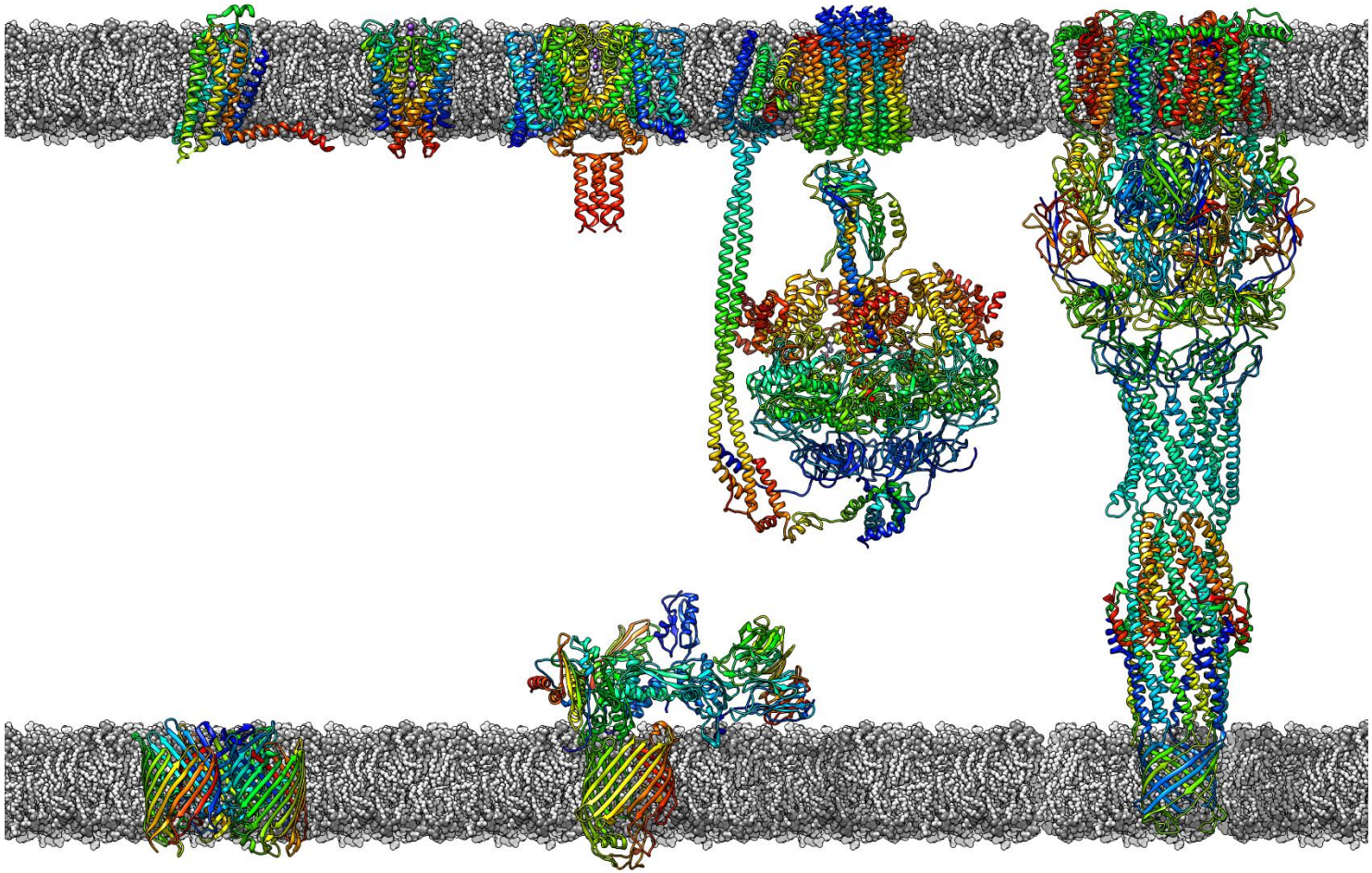

Figure 1.6. Examples of high-resolution membrane protein structures and their orientation within membranes. From left to right, the upper membrane shows examples of TM helix proteins: the adenosine A_{2a} GPCR (PDB ID: 2YDO), the KcsA potassium channel (PDB ID: 1K4C), the voltage-gated sodium ion channel, NavMs (PDB ID: 5HVX), the F_1F_0 ATPase (PDB ID: 5T4O) and the AcrAB/TolC multidrug efflux pump (PDB ID: 5V5S), where the TM helical AcrB sits within the upper membrane and the TolC ß barrell sits within the lower membrane. From left to right, the lower membrane shows examples of ß-barrell proteins: the OmpF porin trimer (PDB ID: 3K19), the ß-barrel assembly machinery BamABCDE complex (PDB ID: 5LJO) and the TolC ß barrel. In all cases each protein chain is colored from blue to red, corresponding to the N- and C-termini, respectively

1.3.1.3 Peripheral membrane proteins

The final category of membrane proteins are peripheral membrane proteins. These proteins will only interact with a single leaflet of the bilayer, though this is achieved by a variety of mechanisms. Monotopic α-helical proteins contain a short α-helix which embeds into the bilayer. A monotopic α-helix can be hydrophobic, where it will embed into an individual leaflet perpendicular to the bilayer, or can be amphipathic in nature, embedding into the bilayer parallel to the bilayer surface at the interface between the hydrophilic lipid head groups and the hydrophobic lipid acyl chains. Cytochrome P450 3A4 (CYP3A4) is a membrane-anchored haem-containing enzyme that contains both hydrophobic and amphipathic monotopic helices. Membrane insertion of CYP3A4 has been proposed to lead to conformational rearrangement to change substrate access routes to the catalytic haem-containing site.[86] This suggests that monotopic helices may play roles extending beyond simply providing localization to the membrane.

Another mechanism by which peripheral membrane proteins can become anchored in the membrane is by means of an acylation site. Here, post translational modification of sulfhydryl groups in cysteine residues with hydrophobic alkyl modifications such as palmitoyl and isoprenyl groups,[87,88] N-terminal modification by the addition of myristoyl groups,[89] or the C-terminal addition of glycosylphosphatidylinositol (GPI)[90] function to target proteins to the membrane. A well characterized example of lipid-modified proteins are members of the Ras GTP-ase family. Ras proteins function in transferring signals between the plasma membrane and the Golgi membrane. While, permanently isoprenylated with a farnesyl group, this group is insufficiently hydrophobic to provide a stable membrane anchor for an otherwise globular, soluble protein. Membrane localization is achieved by means of palmitoylation upon transient interaction with the plasma membrane. In order to dissociate from the plasma membrane, Ras becomes depalmitoylated, allowing trafficking to the Golgi, where it again becomes palmitoylated, leading to a stable interaction with the Golgi membrane.[91]

Many peripheral membranes can transiently interact with the membrane by means of charged residues forming binding sites for specific lipid head groups. The phospholipase A_2 superfamily are a

category of peripheral membrane-activated enzymes responsible for cleavage of lipid acyl chains with roles in inflammation signaling. These enzymes show a transient membrane interaction where they bind membrane associated lipid substrates. Hydrophobic residues penetrate into the core of the bilayer interacting non-specifically with a portion of the lipid acyl chain. The headgroup specificity varies between PLA_2 enzymes, but is mediated by either basic residues in enzymes binding anionic lipids, or aromatic residues in PLA_2s binding zwitterionic lipids.[92]

Finally, as mentioned above, peripheral membrane proteins play an important role in inducting membrane curvature. One such example are proteins containing the BAR (Bin/Amphimysin/Rvs) domain. The BAR domain is present in several proteins involved in sensing or inducing membrane curvature during the early stages of clathrin-mediated endocytosis, forming a functional dimer with a curved structure.[93] The concave face of the BAR dimer contains a high density of basic, positively charged residues which enable binding to negatively charged lipids.[94] Additionally, each BAR domain within the dimer contains an amphipathic helix which is proposed to lead to membrane binding.[95] The incorporation of an amphipathic helix into the membrane itself will lead to a kink in the membrane plane at the point of insertion. Furthermore, the curved domain structure induces a highly curved membrane architecture, where BAR domains have been shown to form membrane tubules of ~ 30 nm radius.[96]

1.3.2 Challenges in membrane protein research and detergent-mediated solubilization

Given the diverse cellular functions of membrane proteins, they are frequently targeted for structural and functional characterization. However, studies of membrane proteins are not without challenges. A metric by which to judge the difficulty in studying membrane proteins is the number of membrane protein depositions within the protein data bank (PDB). At the time of writing, the total number of protein coordinate entries within the PDB is 143840,[97] of which only 2619 are membrane proteins, ie, 1.8 % of the total number of protein entries.[98] To make matters worse, when looking at the number of unique membrane protein depositions the total number of entries decreases to 817.

The classical approach to studying proteins usually relies on isolation of the protein of interest. For membrane proteins, this poses a particular challenge. Membrane proteins are highly amphiphilic molecules, whereby the regions outside of the membrane are hydrophilic so as to be able to hydrogen bond with water molecules, and the membrane interacting region is hydrophobic to maintain stability within the hydrophobic core of the bilayer. To further complicate matters, there are often residues that form specific interactions with lipids or membrane components. It is becoming increasingly apparent that lipids play a key role in membrane protein stability and function.[99–102]

In order to study membrane proteins in isolation, they need to be extracted from the membrane. This has predominantly been achieved with detergents: amphiphilic surfactants which, like lipids, contain polar and hydrophobic regions.[103–105] However, rather than lipids which self-assemble into bilayers in biomembranes, detergents generally self-assemble into micelles when present in solution above a 'critical micelle concentration' (CMC), defined as the surfactant concentration beyond which there is no further decrease in surface tension. It is this property which has led to their use in membrane protein extraction. The hydrophobic detergent tails replace that of the lipid annulus around the protein, the polar headgroups satisfy the hydrogen bonding requirements for solubility in aqueous solution, all whilst being maintained in a colloidal micellar structure.

As ideal as this sounds in principle, in practice, detergents encompass problems of their own. Despite being amphipathic, the 'harsh' nature of detergents will often not maintain membrane proteins in a native conformation leading to precipitation, aggregation or stabilization of a non-physiological structure. As alluded to above, membrane proteins will require specific interactions with lipid molecules to maintain stability. The micellar nature of the protein-detergent micelle can prevent this interaction. Detergent tails can approach the hydrophobic region of the protein parallel to the plane of the membrane in contrast to lipid tails which will largely sit perpendicular. This reduces the contact area between protein and amphiphile, and can also allow detergents to bury into the protein, disrupting secondary and tertiary structure. In addition, the lipid composition of the membrane is important for membrane protein stability and function.[106,107] For example, eukaryotic membranes containing cholesterol can allow pi-pi stacking interactions between the protein and the cholesterol, and headgroups can form stabilizing non-covalent interactions with residues at the membrane periphery.[108] Cholesterol and sphingolipid-rich lipid rafts act to modify the membrane fluidity and thickness within discreet microdomains which can favour incorporation of longer TM regions or post translational acyl groups, effectively targeting proteins to discrete regions of the membrane.[109] Indeed, in the relatively few atomic resolution structures that have been determined of membrane proteins, many contain tightly bound lipids which have not been stripped by detergent.[110–112] Molecular dynamics simulations have shown that even on the short time-scale of the simulation, detergents can render the protein near unrecognizable in structure.[113] This highlights the poor nature of detergents as lipid replacements whilst emphasizing the intrinsic requirement that membrane proteins have for lipids.

1.4 ALTERNATIVE SOLUTIONS TO CLASSICAL SURFACTANTS

1.4.1 Artificial bilayers

The poor nature of detergents as lipid replacements has provided the motivation for the development of non-classical detergents and methods which aim to solubilize membrane proteins whilst providing a more native-like environment, or at least causing less structural or functional perturbations as a result of removal from the native bilayer. Arguably the simplest of these 'membrane mimetic' systems is the

artificial bilayer. Synthetic or naturally extracted phospholipids can be used to form bilayers, into which membrane proteins can be reconstituted upon removal of detergent. There are several permutations of the artificial bilayer. Proteoliposomes are a common solution, often used for measuring transport of a substrate across a membrane, such as with ATP-binding cassette (ABC) transporters.[114] The advantage here is that the protein retains a near-native lipid environment whilst only having one side accessible to the bulk solvent, allowing different conditions within the interior of the liposome. Examples of the application of proteoliposomes include using the compartmentalization of the interior of the vesicle to create a PMF across the membrane. This strategy has been successfully used to study secretion by the bacterial holo-translocon.[115] Similarly to proteoliposomes, membrane proteins can be reconstituted into black lipid membranes (BLMs). These are planar membranes which self-assemble across a small pore. Typical applications of BLMs have been to study ion channel activity by electrochemical assays whereby the movement of ions from one side of the BLM to the other by the channel of interest results in a measurable current.[116]

A more recent use of artificial bilayers has been to create planar supported bilayers on a surface [117,118]. Like proteoliposomes and BLM's, supported bilayers allow the membrane protein of interest to exist in a native-like environment. Supported lipid bilayers (SLBs) are commonly used for binding assays using surface-sensitive techniques such as surface plasmon resonance (SPR) for drug discovery applications.[119–121] SLBs have also been used to measure ion channel activity.[122] Thus far, the applications of artificial planar bilayers have been primarily limited to functional studies, with high resolution structural information proving difficult to obtain due to the intrinsic polydispersity of these systems. However, there have been recent advances made using supported bilayers to obtain structural information on embedded membrane proteins using neutron reflectometry.[123] One such example is the measurement of domain shifts in the Tam complex, involved in outer membrane protein folding upon self-assembly of the complex in a lipid bilayer.[124] Further supported membrane mimetic systems have been developed and structurally characterized. Using a combination of magnetic and isotopic contrast spin polarized neutron reflectometry, a model of the gram-negative bacterial inner and outer membrane has been reconstructed at the solid-liquid interface.[125] Not only does this allow structural information to

be gained on the large-scale organization of the bacterial membrane, but has allowed the investigation of antibiotic interactions with model gram-negative envelopes to determine the influence of membrane phase on antibiotic efficacy.[126] An exciting potential application could be to use these accurate mimetic systems to reconstitute membrane proteins and obtain large scale structural and functional data of purified components in a realistic asymmetric membrane environment.

1.4.2 Bicelles

While artificial bilayers provide a more native-like phospholipid environment for the protein being studied compared to detergent micelles, their large size, transient stability and inherent polydispersity makes them practically challenging. To address some of the issues with membrane protein reconstitution in proteoliposomes whilst maintaining membrane proteins within a phospholipid environment, short chain detergents have been developed to reconstitute the membrane protein within a 'bicelle'.[127] Bicelles are self-assembled discoidal structures containing a central core of planar lipid bilayer, where the hydrophobic core of the bilayer is stabilized by a radial detergent micelle (Figure 1.7a). The choice of detergent is critical for bicelle self-assembly. The detergent forming the micellar rim of the bicelle should have a conical molecular shape with a packing parameter ensuring positive curvature of micelles.[128] Most commonly, 1,2-dihexanoyl-*sn*-phosphatidylcholinie (DHPC) or CHAPSO detergents have been used in combination with 1,2-dimyristoyl-*sn*-phosphatidylcholine (DMPC) phospholipids for bicelle self-assembly (Figure 1.7b).[129]

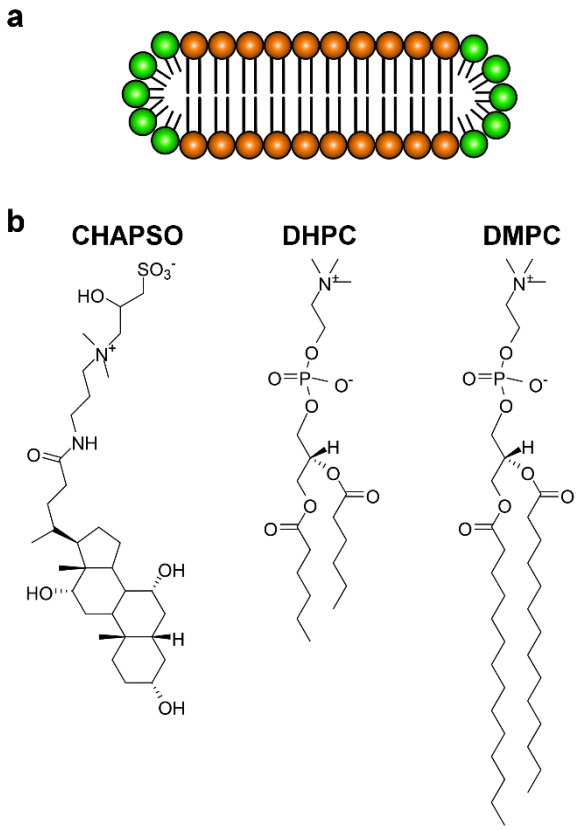

Figure 1.7. a. A schematic representation of a bicelle formed from a planar phospholipid bilayer, shown in orange, which is stabilised by a radial short-chain detergent micelle, shown in green. **b.** Chemical structures of detergents (CHAPSO, DHPC) and phospholipids (DMPC) frequently used for the self-assembly of bicelles.

Bicelles have been shown to substantially enhance the stability of membrane proteins compared to detergent micelles, likely due to the increased similarity to native membranes than provided in a pure detergent micelle. This has resulted in bicelles being applied in crystallographic studies of membrane proteins, where stability is an important factor. Bacteriorhodopsin, a 7TM archaeal proton pump, was the first membrane protein crystallized using bicelles, allowing the structure to be solved to 2.0 Å resolution.[130] Since then, there has been a steady increase in the number of crystallographic membrane protein structures determined from bicelles.[129,131] Notable examples include the human ß-adrenergic receptor, the first structure of a human GPCR,[132] structural characterization of a voltage gated sodium ion channel allowing identification of sequential conformational states during a complete conductance cycle to be obtained,[133,134] and the first structure of the transmembrane BamA subunit of the Bam complex.[135] A recent proof-of-principal experiment has demonstrated the applicability of bicelles to microcrystal generation, where the *de novo* structure of bacteriorhodopsin was solved to 2.1 Å resolution using serial femtosecond crystallography (SFX).[136]

The structure of the bicelle assemblies is heavily dependent on two parameters: the ratio of short-chain detergent to phospholipid, and temperature. Discoidal bicelles are only formed below the T_m of the phospholipid, and within a narrow ratio of detergent:phospholipid.[129] With increasing detergent concentration for a given quantity of phospholipids, or decreasing temperature, bicelles pass through various morphological phases, from vesicles with detergent-lined perforations, planar lamellar bilayers, elongated, tubular mixed micelles, and finally discoidal bicelles.[137,138] The complex phase behaviour of bicelles can be utilized, with elongated and lamellar phases displaying magnetic alignment properties for structural studies by solid-state NMR spectroscopy, while small, fast tumbling discoidal bicelles have been used to elucidate structural details of TM helices within a bicelle by solution state NMR.

Investigations into the structural properties of phospholipids within bicelles shows that the tail ordering rapidly decreases with increasing detergent concentration.[139] In addition, a decrease in the apparent DMPC T_m was observed as DHPC concentration was increased beyond equimolar concentrations with DMPC.[140] These results suggest that the bicelle experiences mixing between the

micellar rim and the bilayer core at high detergent concentrations, despite retaining a molar ratio consistent with a discoidal morphology. The effect of this mixing is an alteration to the physicochemical properties of the phospholipid bilayer within the bicelle. Therefore, whilst bicelles provide an improved membrane mimetic over pure detergent micelles, the short chain detergents used may still induce perturbations in membrane protein structure and function, either through direct protein-detergent interactions or by modifying the physicochemical properties of the phospholipid bilayer.

1.4.3 Amphipols

In a similar strategy to bicelles, amphipathic co-polymers have been developed, termed amphipols, which are able to stabilize the hydrophobic TM region of membrane proteins, whilst maintaining interactions with the aqueous solvent in a manner similar to classical detergents (Figure 1.8a).[141] The archetypal amphipol, A8-35 is synthesized from poly(acrylic acid) where ~25 % of the acid groups are modified with N-octyl chains, ~40 % with N-isopropyl chains and the remainder remain as acid groups (Figure 1.8b). These modifications are statistically distributed along the length of the polymer chain.[142] Due to the amphipathic nature imparted on amphipols from their chemical modifications, their behaviour in solution shares similarities to classical detergents. For example, A8-35 has been shown to form micellar-like assemblies when above a critical assembly concentration in solution, similar to the CMC discussed for 'head-and-tail' detergents above.[143] However, the polymeric nature of amphipols means that the cumulative interactions of hydrophobic acyl chains with hydrophobic TM regions of membrane proteins results in a thermodynamic equilibrium with much slower dissociation rates and higher binding affinities than would be obtained with classical detergents.[142] This has the practical benefit that once the membrane protein-amphipol complex has assembled, the amphipol concentration in solution does not need to be maintained above a 'CMC' to prevent dissociation of the amphiphile from the membrane protein.[144,145] However, inclusion of a small excess of amphipol in solution can prevent formation of soluble aggregates by disrupting protein-protein interactions between amphipol-solubilized membrane proteins.[144–146] While the amphipol-protein interaction is stable, it can be disrupted in the presence of

competing surfactants.[147] The practical significance of this is that membrane proteins can be easily transferred between amphipols and detergent micelles, or reconstituted into lipid bilayers.[147,148]

The stabilization of membrane proteins by amphipols in aqueous solution by wrapping of the amphipol chain around the hydrophobic TM region of the membrane protein results in a similar lateral pressure as provided by the membrane fluidity in the native membrane environment.[149] This has been shown to lead to stabilization of the membrane protein structure by minimizing conformational perturbations and fluctuations.[150,151] However, the conformational restraint imparted on the protein has been seen to inhibit function. This was observed with the Ca^{2+} ATPase from the sarcoplasmic reticulum, where a stabilization, but decreased dissociation of calcium ions occurred due to the restricted conformational changes possible within the amphipols.[152] While high resolution structures have been obtained of membrane proteins solubilized in detergents by both cryo-transmission electron microscopy and macromolecular crystallography, the increased stability and decreased conformational fluctuations observed with amphipols make them ideal. Examples include a 3.4 Å resolution structure obtained by cryo-TEM of A8-35 stabilized TRPV1,[153] and a 4.5 Å resolution structure of the human γ secretase.[154] In addition, bacteriorhodopsin has been crystallized by reconstitution into a monoolein lipidic cubic phase (LCP) from amphipols, demonstrating the applicability of amphipols for crystallographic studies.[155] Furthermore, perdeuterated amphipols have been synthesized to improve compatibility with NMR and small-angle neutron scattering (SANS) studies, allowing proton correlations between the amphipol and membrane protein, or scattering from the amphipol to be masked, respectively.[156] Aside from structural studies, amphipols are compatible with a wide range of applications, such as biophysical characterization using UV spectroscopy and analytical ultracentrifugation,[157] surface adsorption for ligand binding studies,[158,159] and amphipol-assisted membrane protein refolding.[160]

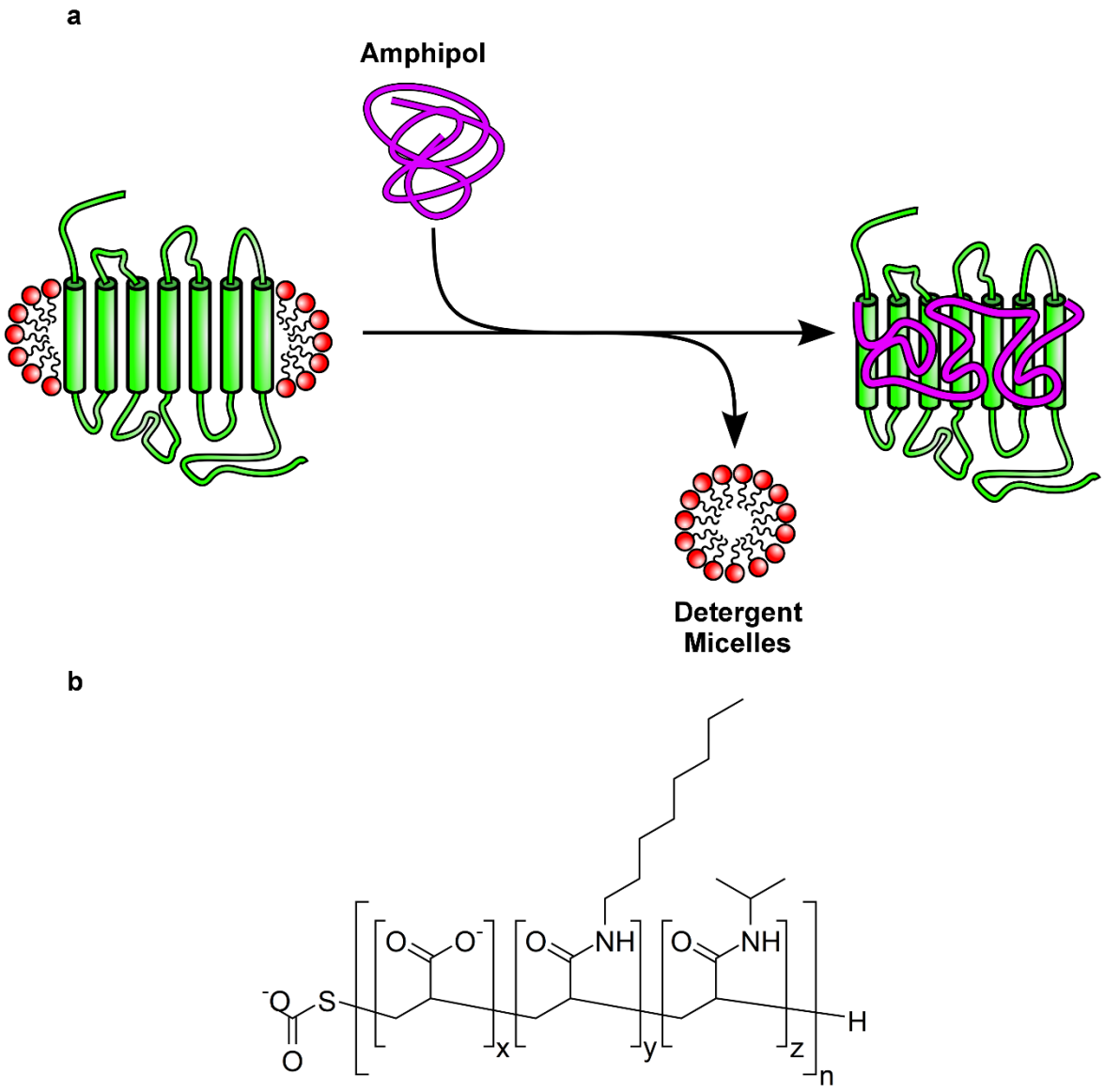

Figure 1.8. a. Schematic representation of membrane protein reconstitution into amphipols upon removal of detergent micelles. **b.** The chemical structure of amphipol A8-35.

However, despite the success of amphipols in stabilizing membrane proteins in aqueous solution, they are not without their limitations. Aside from the conformational restrictions imparted on stabilized membrane proteins discussed above, the chemical environment experienced by an amphipol stabilized membrane protein is more akin to that in detergent micelles rather than a lipid bilayer. The octylamine chains responsible for interaction with the hydrophobic TM region of the MP is substantially shorter than most acyl chains in biological lipids. Furthermore, the requirement of many membrane proteins for specific headgroups for activity or stability is not satisfied by amphipols, although lipids have been identified in complex with amphipol-membrane protein particles which could mitigate this limitation to a certain extent.[161]

1.4.4 Membrane scaffold protein nanodiscs

A similar strategy developed in parallel to amphipols has been the use of nanodiscs. Nanodiscs use the amphipathic 'membrane scaffold protein' (MSP) to form a belt around a discoidal segment of lipid bilayer.[162] The first MSPs to be designed to form nanodiscs were derived from an amphipathic helical segment of the human ApoA1 lipoprotein.[163] The amphipathic helical nature of ApoA1 allows nanodisc self-assembly upon incubation with phospholipids where the hydrophobic residues on one face of the helix interact with phospholipid tails, and hydrophilic residues on the opposite face interact with the aqueous solvent (Figure 1.9a). The nanodisc structure has been confirmed by NMR spectroscopy, electron microscopy, small-angle neutron and X-ray scattering and molecular dynamics simulations, finding bilayer thicknesses consistent with that expected for vesicular membranes.[164–167] By modifying the amino acid sequence of ApoA1 by helical truncations, duplications or deletions to produce a range of MSPs,[164] it has been shown that the size of the resultant nanodisc can be predicted according to the following relationship:

$$M = \frac{2(\pi r + \sqrt{\pi NS})}{L}$$

where M is the number of residues within the MSP belt, r is the mean radius of the helices within the MSP, N is the number of lipids per nanodisc, S is the mean surface area per lipid and L is the helical

pitch per MSP residue.[168] Therefore, modified MSPs have been shown to form highly monodisperse nanodiscs between 8 to 16 nm diameter, consistent with this relationship.[164,169] Once nanodiscs have been formed, no excess MSPs are required in solution to maintain intact particles, and in contrast to amphipols, without the formation of soluble aggregates.[168]

Reconstitution of a detergent solubilized membrane protein within an MSP-nanodisc (Figure 1.9b) will both maintain solubility of the membrane protein upon subsequent removal of detergent, whilst keeping the protein within in a phospholipid bilayer [162,170]. In addition, the T_m of MSP-stabilized bilayers was similar to that expected for vesicles, though broadened and slightly shifted due to decreased cooperativity and interaction with the MSP belt [171]. This suggests a native-like membrane environment is experienced by a protein encapsulated within a nanodisc. This is in contrast to amphipols where the membrane protein is stabilized predominantly by amphipol-protein interactions. Additionally, no short-chain detergents are present, as is the case with bicelles. As with all the membrane mimetics discussed so far, MSP-nanodiscs have been shown to impart a greater degree of stability to the encapsulated membrane protein compared to detergent alternatives [172].

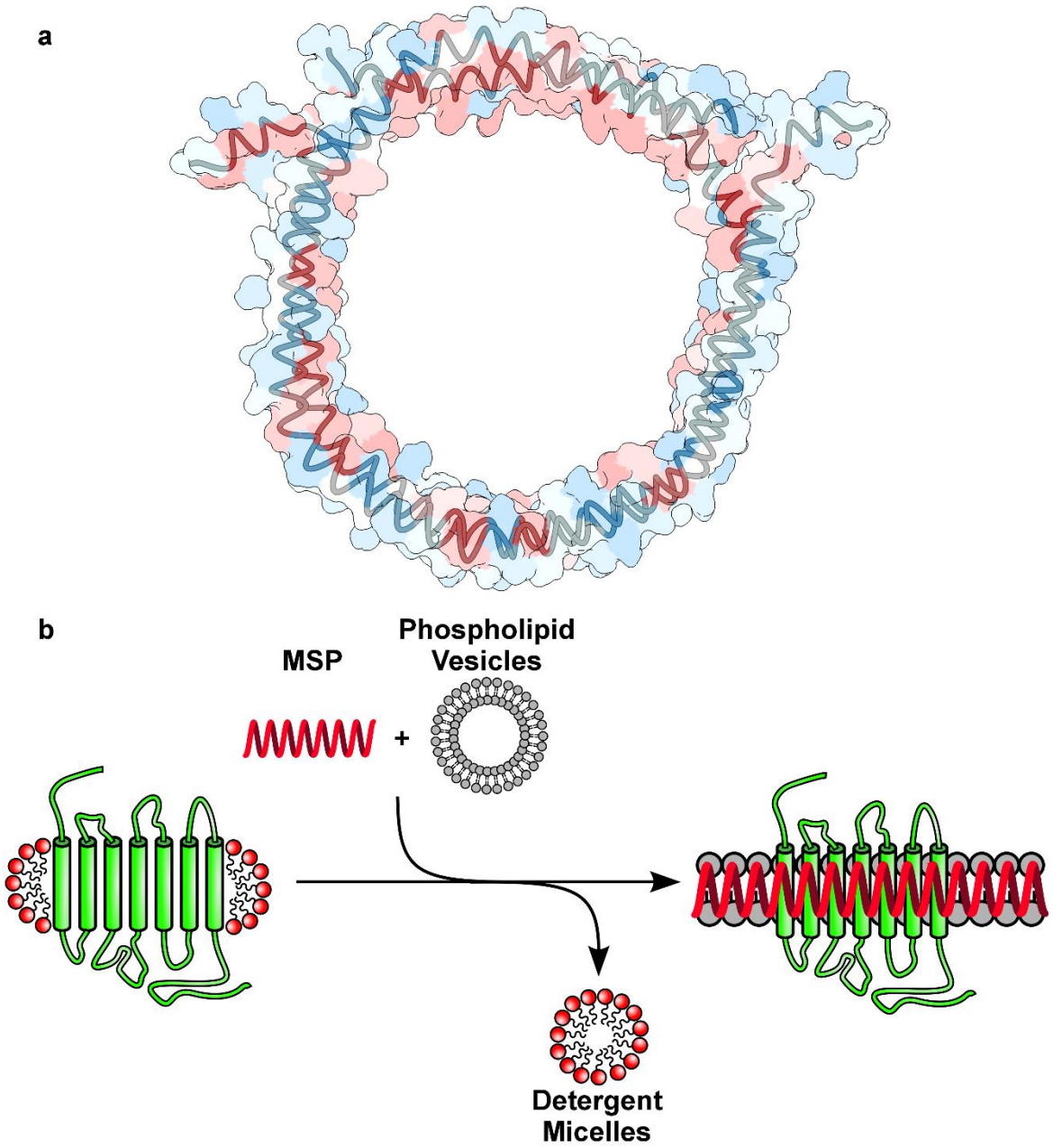

Figure 1.9. a. The structure of MSP1D1-ΔH5 in the absence of phospholipid[166] depicted as a grey ribbon. The semi-transparent molecular surface is coloured according to hydrophobicity, where red represents the most hydrophobic residues and blue the least hydrophobic, in terms of partitioning into lipid bilayers.[173] **b**. Schematic of membrane protein reconstitution into MSP-nanodiscs. Incubation of detergent-solubilized membrane proteins with MSP and phospholipid vesicles and subsequent removal of detergent micelles leads to spontaneous assembly of MSP-nanodiscs containing the membrane protein within a phospholipid bilayer.

There have been a range of tags grafted to the MSP protein to allow for adsorption of MSP-nanodiscs to solid-phase substrates for application in antibody generation and binding studies using surface-sensitive techniques. Biotinylated MSPs have been generated allowing membrane proteins encapsulated in MSP-nanodiscs to specifically adsorb to streptavidin resin. This has been applied to selecting conformationally specific synthetic antibody fragments from a phage-display library,[174] which can in turn be used as 'crystallization chaperones' allowing stabilization of a specific conformational state whilst also providing an increased solvent accessible surface area for crystal contact formation.[175] N-terminal poly(histidine) tags can also be used to capture nanodiscs to immobilized metals on SPR chips allowing identification of binding affinities and specificities in a semi-high-throughput fashion. [176,177] In addition to specific binding to interfaces *via* affinity tags, MSP-nanodiscs have been shown to spontaneously align beneath a phospholipid monolayer at the air-water interface,[178] and to silicon substrates at the solid-liquid interface.[179] In both cases, a high coverage of nanodiscs were achieved at the surface where the nanodiscs were adsorbed such that the plane of the bilayer was parallel with the interface. This has allowed for structural investigation of the large scale conformational changes occurring in cytochrome P450 reductase encapsulated in MSP-nanodiscs upon introduction of NADPH.[180]

As with bicelles and amphipols, membrane proteins solubilized within MSP-stabilized nanodiscs have been successfully applied to structural studies. There has been a large body of work utilizing NMR for structural elucidation of MSP nanodisc encapsulated membrane proteins,[181] using both magic angle spinning solid state NMR[182] and solution state NMR[183] allowing, for example, the determination of the structure of OmpX to atomic resolution.[184] Several membrane protein structures within MSP-nanodiscs have now been determined to near-atomic resolution using cryoTEM.[185–188] Importantly, the presence of the bilayer and MSP belt did not skew alignment of the particles for 2D class averaging in any of these studies. The density of the bilayer can clearly be resolved in the electron density maps, even allowing identification of PI lipids within the ligand binding site of the non-selective cation channel TRPV1.[186] In addition, MSP nanodisc encapsulated bacteriorhodopsin has successfully been transferred to monoolein LCP for *in meso* crystallogenesis. This procedure was able produce diffracting crystals,

allowing structure determination to 1.9 Å, which is the highest resolution achieved to date using nanodiscs.[189]

In addition to their application to TM proteins, MSP nanodiscs provide an ideal platform for investigating lipid-protein interactions of peripheral membrane proteins by providing a soluble membrane surface of controlled chemical composition and well defined size.[190] Examples include determination of the effects of membrane charge as a regulating factor for integrin activation by the talin adapter protein,[191] determination of membrane properties and binding modes which modulate the fibrilization of α-synuclein on MSP-nanodisc encapsulated membrane surfaces by NMR spectroscopy,[192] and determining effects of oncogenic mutations on the orientation of KRAS4b on the membrane using NMR spectroscopy and bilayer interferometry.[193]

However, as with the solutions discussed thus far, MSP-nanodiscs also have certain drawbacks. The most limiting factor of MSP-nanodiscs is the proteinaceous nature of the MSP belt. For spectroscopic applications such as far-UV circular dichroism, intrinsic fluorescence or Fourier transform infra-red (FTIR) spectroscopy, a significant contribution of the measured absorbance/fluorescence will be due to the MSP belt. While theoretically it is possible to subtract spectra obtained for MSP-nanodiscs containing only lipids, the uncertainty in determining precise concentrations makes this challenging if quantitative results are to be obtained. Additionally, the formation a discoidal structure relies heavily on the precise ratio of MSP:lipid. Under- or over-lipidation can lead to the formation of non-planar MSP-lipid assemblies.[194] The volume of the bilayer occupied by the encapsulated membrane protein will also need to be considered.[168] While possible to experimentally determine optimal self-assembly conditions, initial estimates can be challenging for targets with no known structural information.

1.5 POLY(STYRENE-*CO*-MALEIC ACID) LIPID PARTICLES: SMALPS

Despite great strides being made in the developing alternative methods to classical detergents that maintain stability of the reconstituted, or solubilized, membrane protein in a more native-like environment, all the methods discussed so far suffer from a common limitation: the membrane protein in question must first be solubilized from the native membrane using classical detergents. While the solutions discussed thus far provide superior activity and stability once reconstituted, detergent extraction still presents a bottleneck due to potentially irreversible detergent-induced structural and functional perturbations. To address these issues, the past 9 years have seen the development of amphipathic poly(styrene-*co*-maleic acid) (SMA) copolymers (Figure 1.10a). When the maleic acid groups are deprotonated, above a pH of ~ 6.5, SMA is water-soluble and is able to assemble with phospholipid vesicles into nanodiscs: nanoscale, discoidal segments of phospholipid bilayer wrapped by an SMA polymer belt, presenting a hybrid approach between amphipols and MSP-nanodiscs. These SMA-stabilized nanodiscs have been termed SMA lipid particles (SMALPs).

While it has been demonstrated that membrane proteins can be reconstituted into SMALPs from detergent micelles, similarly to amphipol and MSP-nanodiscs,[195] they have the advantage that SMA is able to solubilize membrane proteins directly from native membranes.[196] Once formed SMALPs, unlike detergents, do not require an excess of SMA in solution after solubilization to maintain the nanodisc structure [197–200]. As SMA is able to extract membrane proteins directly from the native bilayer, they will keep the native lipid annulus intact throughout the solubilization and subsequent purification process [201]. This has enabled analysis of the local lipid environment of the Sec translocon to determine the necessity for anionic lipids for function of the complex [202]. Furthermore, SMALPs have been shown to maintain the stability and activity of membrane proteins better than detergent alternatives [201,203].

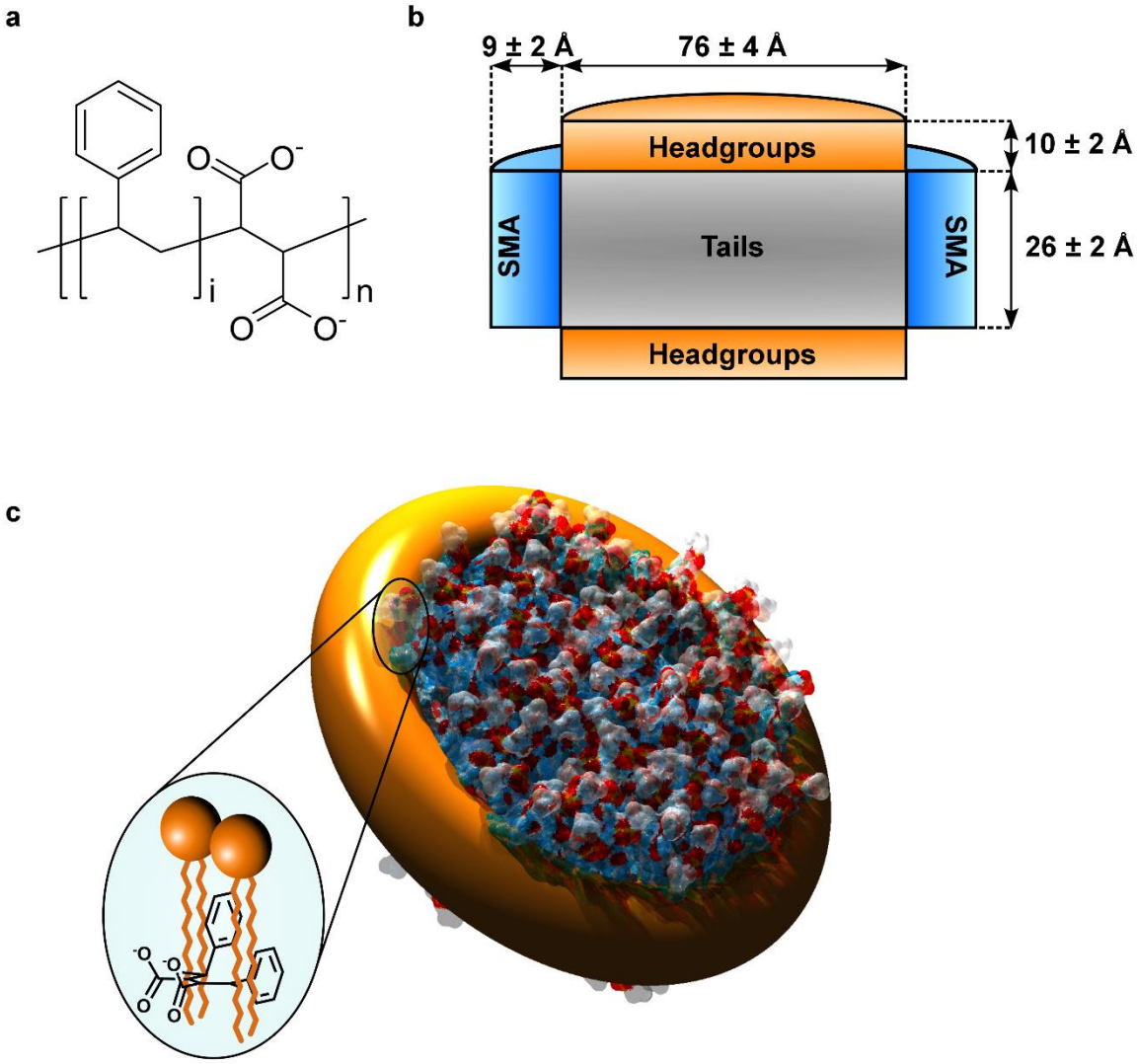

Figure 1.10. a. The chemical structure of the SMA copolymer. **b.** Schematic representation of a cross section through a DMPC-SMALP nanodisc. Dimensions are labelled as determined by SANS. **c.** A rendered model of a DMPC-SMALP. The zoomed region shows a schematic representation of the intercalation of styrene moieties within the phospholipid tails.

In addition to functional studies, SMALPs have been successfully employed in structural studies of membrane proteins. Examples include structural characterization using circular dichroism spectroscopy and analytical ultracentrifugation[196] and high-resolution structural determination of the AcrB trimer and the alternative complex III by cryo-EM.[204,205] High resolution solid state NMR spectra have been obtained for SMALP-CzcD, a bacterial cation diffusion facilitator allowing assignment of 2D and 3D spectra.[206] This demonstrates the potential for SMALP solubilized proteins to be used for high resolution structural determination by solid state NMR. Furthermore, SMALP-solubilized bacteriorhodopsin has been successfully crystallized *in meso* by reconstitution into a LCP allowing structural determination to 2.0 Å resolution.[207] This structure shows no differences to a crystal structure obtained from a detergent solubilized preparation, but could be solved to a slightly higher resolution.

1.5.1 Structural properties of SMALP nanodiscs

The initial report of SMA-mediated solubilization of phospholipid vesicles demonstrated the formation of what appeared to be discoidal assemblies by negative-stain TEM. Despite the artefacts that can be introduced to lipidic samples, the nanodisc structure has since been validated. SANS measurements of SMALP nanodiscs containing DMPC confirmed the presence of discoidal assemblies.[208] The model used to fit the data assumed a central cylindrical core comprised of anhydrous phospholipid tails, with a radial rim of hydrated SMA, and additional cylinders on either face of the core representing hydrated PC headgroups (Figure 1.10b). Dimensions of the central bilayer core are in close agreement with the thickness of DMPC bilayers obtained by X-ray diffraction. The overall diameter of SMALPs was found to be 9.4 nm with a 7.4 nm diameter phospholipid core.[208] However, both SANS and TEM measurements suggest SMALP nanodiscs exhibit increased polydispersity compared to MSP-nanodiscs.[208] Given the apparent diameter of the phospholipid core, and taking the area per molecule for DMPC in a fluid phase bilayer as 60 $Å^2$,[209] would allow for a maximum of 71 DMPC molecules per bilayer leaflet encapsulated by the polymer. However, when taking into account optimal lipid packing, this is likely to be an overestimation.

The phospholipid bilayer within SMALPs is stabilized by embedding of the hydrophobic phenyl group of the styrene moiety into the hydrophobic acyl chains of the lipid bilayer, while the charged acid groups allow solubility to be maintained in aqueous solution. Polarized attenuated total reflectance (ATR) FTIR spectroscopy has suggested that the phenyl rings intercalate between the phospholipid tails, with the plane of the aromatic ring perpendicular to the plane of the bilayer (Figure 1.10c), possibly introducing structural distortions to the lipids in direct contact with the styrene moieties.[208] SANS data suggests that the SMA belt does not penetrate into the bilayer core, likely due to the statistical arrangement of styrene and maleic acid moieties along the chain preventing extended hydrophobic poly(styrene) stretches embedding into the bilayer. [208] In the same study, it was shown that the maleic acid groups of SMA show an absorbance shift in polarised ATR-FTIR spectra.[208] Furthermore, by using ^{1}H-^{1}H Nuclear Overhauser Effect Spectroscopy (NOESY), interactions were observed between SMA and PC headgroups.[208] These data suggest that styrene intercalates along the entire length of the lipid acyl chains and maleic acid groups interact both with the aqueous solvent and the hydrophilic headgroups.

While it has not been possible to directly observe the conformation of SMA when interacting with lipids encapsulated within a nanodisc, the available data does allow speculation. When taking the number averaged molecular weight (M_n) of the SMA copolymer used in this study, as 7500 g/mol we can calculate a median degree of polymerization as 73 monomer units (taking into account the 2:1 ratio of styrene to maleic anhydride monomers). For a carbon-carbon bond length of 1.54 Å, this would mean the maximum extended length the polymer would be 226 Å. The circumference of the lipid core from SANS data can be calculated as 232 Å. This would potentially allow for an individual SMA polymer to wrap once around the lipid core, analogous to a polymeric ‘belt’. The statistical distribution of monomer units along the polymer chain, however, would lead to hydrophobic patches, which for a ‘belt’ polymer conformation would lead to solvent exposed non-polar regions of the polymer belt, leading to nanodisc aggregation. Furthermore, the high polydispersity of SMA would mean a large proportion of chains would be too short to adequately encapsulate a lipid core. A more likely polymer conformation would be to adopt a snake-like conformation to fully shield the hydrophobic lipid acyl chains and phenyl rings

from styrene moieties in the hydrophobic core, whilst positioning acid groups to interact with the aqueous solvent. This would require several polymer chains to interact with each nanodisc. This is supported by the apparent thickness of the SMA polymer rim, as determined by SANS, which is thicker than would be observed for an extended belt conformation. Additionally, as seen with polarized ATR-FTIR and ^{1}H-^{1}H NOESY data, SMA interacts with the lipids across the entire length of the acyl chain whilst also interacting with the headgroups.[208] This further supports a snake-like conformation over an extended belt conformation, where steric hinderance of multiple polymers, each wrapped as an extended belt around the lipid circumference would likely prevent interactions along the entire length of the lipid acyl chain.

1.5.2 Mechanism of SMALP self-assembly

With the adoption of SMALPs as a powerful membrane and membrane-protein solubilization strategy comes a requirement to understand the nanodisc self-assembly process. Initial studies demonstrated that SMA is able to solubilize phospholipids with greatest kinetic efficiency when above the lipid T_m, irrespective of lipid chain length or the presence of different lipid headgroups or tails, providing the distribution of lipid moieties are homogenous throughout the membrane.[210,211] Furthermore, by injecting SMA beneath a phospholipid monolayer, an increase in surface pressure was observed, suggesting adsorption of SMA to the air-water interface, either directly from the surface-activity of SMA, or through interaction with the interfacial lipids.[210] A greater increase in surface pressure was observed with lower initial surface pressures of the monolayer. These data suggest that a low lipid packing density and membrane fluidity within the L_α phase is required for solubilization by SMA.

These observations lead to the proposal of a three-step model describing the solubilization of vesicular membranes by SMA (Figure 1.11).[210] Initially, SMA will adsorb to the surface of the bilayer, driven by the thermodynamically favourable burying of styrene moieties within the acyl core, which is sufficient to overcome electrostatic repulsion between anionic lipid headgroups and maleic acid moieties. Notably, SMA adsorption to lipid monolayers was observed to be disrupted upon decreased

ionic strength, preventing counterions masking lipid/polymer charges, leading to increased electrostatic repulsion and therefore a weaker net thermodynamic driving force for membrane insertion provided by the hydrophobic effect.[210] Once adsorbed, SMA inserts into the core of the bilayer, hence the requirement for a low lipid packing density and high fluidity for efficient solubilization. Finally, disruption of the bilayer by SMA insertion is proposed to lead to nanodisc formation. Recent coarse-grained molecular dynamics simulations have provided evidence in support of this model, where a rapid binding of SMA to the headgroup-tail interface was observed followed by a slower insertion of the remainder of the polymer.[212] Membrane disruption was shown to occur due to increased internal pressure in the bilayer from polymer insertion and the presence of charged, hydrophilic acid groups within the otherwise hydrophobic core. This resulted in out-of-plane buckling of the bilayer and subsequent pore formation, leading to nanodisc self-assembly.

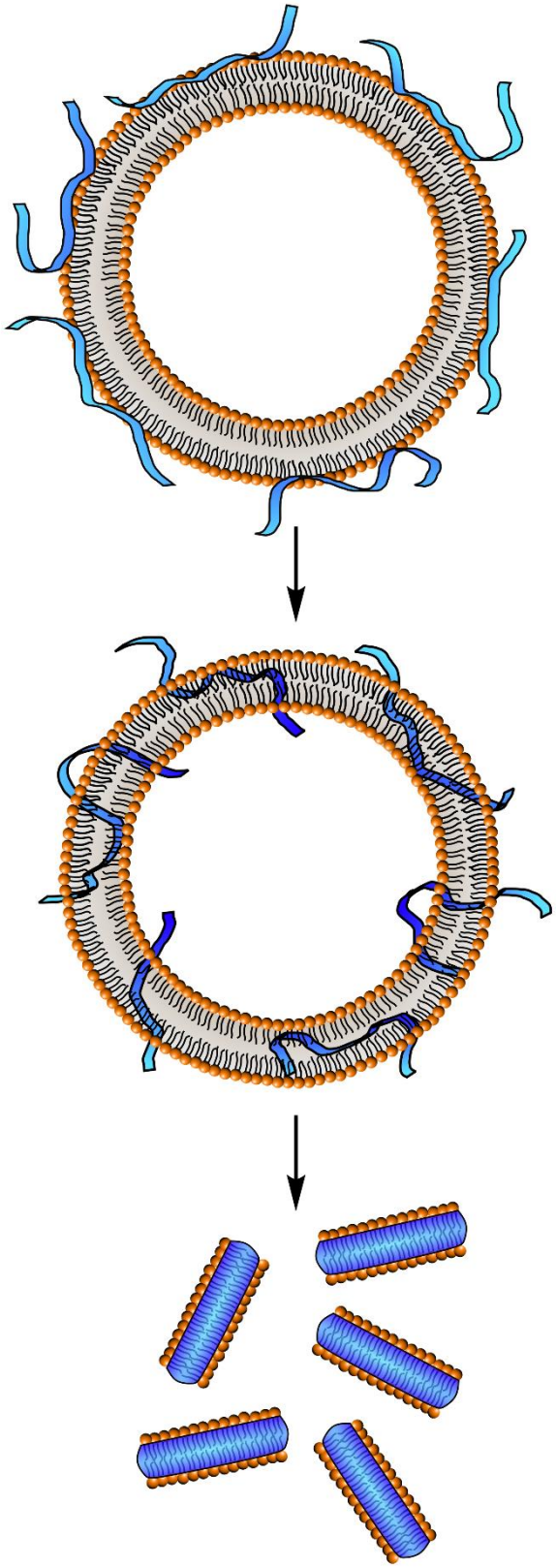

Figure 1.11. Schematic representation of the mechanism of SMALP self-assembly. Initially SMA polymers adsorb to the surface of the bilayer before embedding into the phospholipid tail core of the bilayer. This leads to structural perturbations to the bilayer structure which leads to the formation of SMALP nanodiscs.

1.5.3 Thermodynamics of SMALP self-assembly

Given the evidence supporting the three-step self-assembly model, it is interesting to consider the underlying thermodynamics driving nanodisc self-assembly. Despite not containing the classic 'head-and-tail' detergent structure, SMA can still be considered detergent-like, due to the alternating regions of hydrophobic and hydrophilic groups. Treating SMA as a detergent allows the pseudophase model to be applied to provide a thermodynamic description of nanodisc self-assembly.[213]

The pseudophase model describes the transition of lipid and surfactants between bilayer and micellar phases. At a given concentration of lipid, c_L, with no surfactant present, all lipids will exist in a bilayer phase. Increasing the concentration of surfactant, c_s, leads to a transition from the bilayer range to the coexistence range, which contains a mixture of lipids and surfactant in the bilayer and micellar phases in equilibrium. The phase transition boundary between these two phases is the saturation (SAT) boundary, where all bilayers are embedded with the maximum quantity of surfactant before transitioning to the micellar phase. Increasing c_L further leads to a second phase transition from the coexistence range to the micellar range, where the solubilization (SOL) boundary defines the minimum amount of surfactant required for a given concentration of lipid to be entirely in the micellar phase. This scheme allows the construction of a phase diagram where the phase SAT and SOL phase boundaries are described by linear equations in the form of:

$$c_s^{SAT} = c_s^{aq,0} + R_s^{b,SAT} c_L$$

$$c_s^{SOL} = c_s^{aq,0} + R_s^{m,SOL} c_L$$

Where c_s^{SAT} and c_s^{SOL} describe the surfactant concentrations at the SAT and SOL boundaries, respectively. $R_s^{b,SAT}$ and $R_s^{m,SOL}$ describe the molar ratios of surfactant to lipid at each phase boundary. $c_s^{aq,0}$ describes the concentration of monomeric surfactant in solution in equilibrium with the bilayer and micellar phases:

$$c_s^{aq,0} = CMC \cdot \frac{R_s^{m,SOL}}{R_s^{b,SAT}}$$

The above molar ratios are identically equal to the ratio of mole fractions of surfactant to lipid at the saturating or solubilizing breakpoint:

$$R_s^{b,SAT} = \frac{c_s^{SAT}}{c_L^{SAT}} \equiv \frac{\chi_s^{b,SAT}}{\chi_L^{b,SAT}}$$

$$R_s^{m,SOL} = \frac{c_s^{SOL}}{c_L^{SOL}} \equiv \frac{\chi_s^{b,SOL}}{\chi_L^{b,SOL}}$$

Rearrangement of this identity allows calculation of mole fractions of the surfactant in the bilayer and micellar phases at the saturating and solubilizing break points:

$$\chi_s^{b,SAT} = \frac{R_s^{b,SAT}}{1 + R_s^{b,SAT}}$$

$$\chi_s^{m,SOL} = \frac{R_s^{m,SOL}}{1 + R_s^{m,SOL}}$$

This in turn allows the calculation of the equilibrium molar partition coefficients describing the ratios of surfactant, $K_s^{b\to m}$, or lipid, $K_L^{b\to m}$, between the micellar and bilayer phases at equilibrium:

$$K_s^{b\to m} = \frac{\chi_s^{m,SOL}}{\chi_s^{b,SAT}}$$

$$K_L^{b\to m} = \frac{1 - \chi_s^{m,SOL}}{1 - \chi_s^{b,SAT}}$$

As micelle self-assembly is spontaneous, the micellar phase is favoured over the bilayer phase, therefore $K_S^{b\to m} > 1$ and $K_L^{b\to m} < 1$. From these equilibrium partition coefficients, the molar Gibbs energy changes associated with the micelle to bilayer transition can be calculated for the surfactant, $\Delta G_s^{b\to m}$, and the lipid, $\Delta G_L^{b\to m}$:

$$\Delta G_s^{b\to m} = -RTln(K_s^{b\to m})$$

$$\Delta G_L^{b\to m} = -RTln(K_L^{b\to m})$$

Where the universal gas constant, R = 8.314 J·mol^{-1}·K^{-1}, T is the temperature in Kelvin, and the Gibbs energy change is defined as the sum of the enthalpic and entropic changes at a given temperature:

$$\Delta G = \Delta H - T\Delta S$$

For a thermodynamically favourable process $\Delta G < 0$ while for a thermodynamically unfavourable process, $\Delta G > 0$.

The pseudophase model has been shown to adequately describe the solubilization of phospholipid vesicles by SMA, treating the nanodisc phase as the micellar phase. By titrating large unilamellar vesicles of 1-palmitoyl-2-oleyol-*sn*-phosphatidylcholine (POPC) [213] or DMPC [214] with SMA, it has been shown that independently of the lipids acyl chain length or degree of unsaturation, SMALP self-assembly is driven by a negative Gibbs energy of the polymer interacting with phospholipids. Phospholipids show a small positive Gibbs energy change upon solubilization into nanodiscs, indicating a less favourable free-energy environment experienced within nanodiscs compared to that experienced in vesicles. However, the negative energy change associated with SMA is enough to negate the unfavorability of lipid incorporation. As SMA concentration is increased above c_s^{SOL}, the diameter of SMALPs decreases from ~ 50 to ~ 10 nm, as the increased polymer partitions amongst the available phospholipid to maximize the SMA-lipid interactions. However, the phospholipid composition of the membrane does influence the favourability of SMALP self-assembly. Tail unsaturation results in larger negative $\Delta G_s^{b\to m}$ values, as does the increased proportion of PE to PC headgroups.[214] This supports kinetic studies discussed above in suggesting reduced lipid packing order results in more efficient solubilization. In comparison to kinetic studies, where SMA-mediated solubilization of gel-phase membranes resulted in slower solubilization into nanodiscs, the Gibbs energy of transitions for both lipids and polymer were more favourable when below the T_m of the lipids.

1.5.4 Membrane properties within SMALP nanodiscs

In assessing how close of a mimic an SMA-encapsulated lipid membrane is compared to a native membrane, a useful parameter is whether membranes within SMALPs retain the phase transition

temperatures as experienced in vesicular preparations. In differential scanning calorimetry measurements, DMPC SMALPs show a slight decrease in the T_m from 24 to 23°C, although show a substantial broadening.[208] This has been proposed to be a result of decreased cooperativity within the restricted number of lipids within the bilayer and interactions between SMA and DMPC. Interestingly, ^{31}P-NMR measurements have shown when solubilizing $L_{\beta'}$ phase membranes, phosphorous in DMPC headgroups experience a downstream chemical shift more akin to that experienced in L_α membranes.[214] This is suggestive of an SMA-induced phase transition, possibly to an L_O-like phase as a result of styrene intercalation.

Vesicular membranes have been long known to undergo membrane fusion events and lipid exchange between membranes. The first evidence that lipid exchange occurs in SMALPs was observed when investigating SMALP adsorption to lipid monolayers at the air-water or silicon-water interfaces using neutron reflectometry.[215] While changes in scattering intensity were observed, these could not be modelled by an increased interfacial thickness as would be expected for SMALP adsorption. Rather, the changes in scattering intensity could be accounted for by changing the isotopic contrast of the originally deuterated lipid monolayers to incorporate hydrogenous lipids from the nanodiscs. Subsequent studies have characterized lipid exchange in more detail and shown lipid exchange occurs between nanodiscs in solution much faster than for either vesicular membranes or MSP-nanodiscs.[216] It has also been observed that the rate of lipid exchange varies as a function of ionic strength in solution, where increased Coulombic shielding at higher ionic strengths leads to an increase in the rate of exchange.[217] The kinetics of lipid exchange between SMALPs can be described by a combination of a first-order rate constant describing monomeric lipid diffusion in aqueous solution between SMALPs and a second-order rate constant describing the rate of collisions between SMALPs, the latter of which is dominant with increasing SMALP concentration.[216]

1.5.5 Influence of SMA chemistry on SMALP properties

To date, there has been a broad range of SMA copolymers which have been used in the solubilization of synthetic and biological membranes. The majority of these have been commercially available

statistical copolymers synthesized by a radical polymerization of styrene and maleic anhydride (MAnh), forming poly(styrene-*co*-maleic anhydride) (SMAnh). SMAnh is then hydrolyzed under basic conditions resulting in conversion of anhydride groups to acid groups, yielding functional SMA. The continually stirring tank reactor (CSTR) method of SMAnh synthesis continually adds monomeric precursors whilst continually removing products. This results in a statistical arrangement of styrene and maleic anhydride along the length of the chain which is, in theory, equal to the ratio of monomeric precursors introduced to the reaction. Due to the increased reactivity of styrene radicals relative to MAnh radicals, a styrene end group can react with either another styrene or a maleic anhydride, however a MAnh end group can only react with styrene monomers. This results in a limited number of permitted monomeric triads in the resultant polymer, irrespective of the monomer ratio. An additional effect of the CSTR radical polymerization method is the broad polydispersity index (PDI) of the resultant polymer formulations, where PDI is defined as the ratio of the weight-averaged molecular weight, M_w, to the number averaged molecular weight, M_n:

$$PDI = \frac{M_w}{M_n}$$

SMA synthesis conditions therefore result in three variable factors which may influence the membrane solubilization properties: monomer ratio, chain length and polydispersity. While the effect of PDI is undoubtably important, limited control is available over the PDI of CSTR-synthesized polymers.

The majority of studies using SMA to date have utilized SMA polymers containing either a 2:1 or 3:1 ratio of styrene:maleic acid (SMA(2:1) or SMA(3:1), respectively). By increasing the styrene to maleic acid ratio, the hydrophobicity of the polymer is also increased. Not unsurprisingly, this has shown to lead to a more favourable $\Delta G_S^{b\rightarrow m}$ for SMA(3:1) than SMA(2:1) in SMALP self-assembly.[218] This is likely due to the increased influence of the hydrophobic effect in driving SMALP formation. However, in assessing the properties of the membrane encapsulated within the SMALP, $\Delta G_L^{b\rightarrow m}$ is more relevant in describing the thermodynamic perturbations experienced by the lipids during SMALP self-assembly. Here, a smaller thermodynamic penalty is experienced by lipids during SMALP self-assembly using

SMA(2:1) than SMA(3:1). Combined with reports that the lipid T_m is shifted to a lesser extent in SMA(2:1) nanodiscs than with more hydrophobic polymers, this suggests that the most native-like bilayer environment is provided by SMA(2:1) nanodiscs.[219] In terms of kinetic efficiency, SMA(2:1) is the most efficient solubilize of phospholipid vesicles when compared to the more hydrophobic SMA(3:1) and SMA(4:1) polymers.[220] Interestingly, the more hydrophilic SMA(1.4:1) is only able to solubilize vesicles at low pH, when the polymer is only partially charged.[220] This suggests that effective solubilization requires a balance between hydrophobicity and charged groups. The emergence of SMA(2:1) as the most efficient and least detrimental nanodisc-forming polymer has been corroborated in their application to the solubilization of biological membranes and proteins, where SMA(2:1) was the most efficient in the solubilization of *E. coli* membranes.[221]

The length of the SMA polymer chains also has a substantial influence on solubilization characteristics. It was observed that polymers where $M_w \geq 30$ kDa were ineffective in solubilizing *E. coli* membranes and extracting membrane proteins, regardless of the monomer ratio.[221] Given the broad PDI of commercially available polymers, a recent study has investigated the efficacy of different length polymers within commercial formulations. By fractionating polymers of different lengths by their relative solubility within acetone and hexane, it was shown that all SMA(2:1) polymers between 1.1 and 4.6 kDa, and all SMA(3:1) polymers between 1.6 and 6.5 kDa were able to solubilize DMPC vesicles into nanodiscs. Interestingly, while the kinetic efficiency of solubilization and the rate of lipid exchange between nanodiscs is greatest for shorter polymers, longer polymers induce a smaller shift in the T_m of the encapsulated bilayer compared to nanodiscs formed with shorter chain polymers.

1.5.6 Limitations of SMALP nanodiscs

As with other membrane mimetic systems discussed above, SMALPs also have inherent limitations. Due to SMA requiring at least partial ionisation of the maleic acid groups for aqueous solubility, decreased pH below the lowest pKa of maleic acid (~ 6.0) leads to precipitation of both free SMA and SMALPs as the acid groups become protonated and the polymers aggregate into large globular

structures.[222] This results in SMALPs, with or without encapsulated proteins, being limited to basic solution conditions.

Secondly, coordination of divalent cations by the anionic acid groups of SMA has been proposed to lead to ionic cross-linking between polymer chains. This results in precipitation of both SMA and SMALPs. SMALPs have been shown to tolerate low concentrations (< 2 mM) of divalent cations in solution, and an increased ionic strength can increase tolerance to divalent cations to a limited extent. Nonetheless, this is particularly limiting for many functional studies of SMALP encapsulated membrane proteins where divalent cations are an essential cofactor.

A limitation to solubilization of larger proteins and complexes is the restricted diameter of the lipid bilayer encapsulated within SMALPs. Based on structural parameters of DMPC SMALP nanodiscs obtained by SANS, it has been estimated that a limit of ~ 40 TM helices can be accommodated by the lipid bilayer. In support of this initial estimate, cryo-EM reconstructions of AcrB (containing a total of 36 TM helices) encapsulated within a SMALP have resolved a narrow belt of density surrounding the trimeric TM bundle, proposed to represent SMA with limited density resolved to accommodate lipids. While it has been shown that the diameter of SMALPs can be modified by varying the polymer:lipid ratio, only small changes in diameter have been experimentally observed.

1.5.7 Modifications to SMA and new nanodisc-forming polymers

With the limitations described above, there has been a recent development of modified or new polymers which are functional in nanodisc self-assembly in an attempt to circumvent specific limitations.

With evidence that different length polymers within a commercial SMA formulation can display different characteristics in the resultant polymers, SMA polymers have been synthesized using reversible addition-fragmentation chain transfer (RAFT) polymerization. RAFT polymerization utilizes a radical initiator to activate the monomers that can then polymerize as in conventional radical polymerization. By including a RAFT-agent, typically a trithiocarbonate, a growing, active chain can react with the

RAFT agent, yielding a non-polymerizing 'dormant' polymer. This releases a radical leaving group from the RAFT-agent, which can re-initiate further radical polymerizations. As chains grow via radical polymerization, RAFT agents can be transferred between active and dormant polymers. Given the correct conditions, the rate of addition or fragmentation of chains from the RAFT agent is higher than the rate of radical monomer polymerization. This process results in an even growth experienced by all chains, until 'dead' chains are formed by bimolecular radical termination, at which point the polymerization ceases.[223] The benefit of RAFT polymerization is in the control offered over the polymers molecular weight and the narrow PDI of the resulting polymers.[224]

In an attempt to overcome the functional diversity of polydisperse commercial SMA polymers, SMA polymers have been synthesized by RAFT-polymerization (termed RAFT-SMA, Figure 1.12). In contrast to CSTR-synthesized SMAnh, RAFT-SMAnh containing an excess of styrene monomers contains an initial alternating block of styrene and maleic anhydride groups which tends towards longer poly(styrene) stretches as monomeric maleic anhydride is depleted as polymerization progresses. Should the polymerization be permitted to progress to completion, this will result in an extended poly(styrene) tail.[224] Initial evidence suggests that RAFT-SMAs containing monomer ratios of 2:1, 3:1 and 4:1 are capable of solubilizing lipids into particles of different sizes.[225] Subsequent studies have shown that the solubilization efficiency of RAFT-SMAs have a dependence on both the polymer length, the monomer ratio and the presence or absence of a poly(styrene) tail.[224] This suggests that polymer architecture and chain topology can have a significant, and potentially exploitable, influence on SMALP formation. However, there is currently limited evidence of the efficacy of RAFT-SMAs in the solubilization of biological membranes.

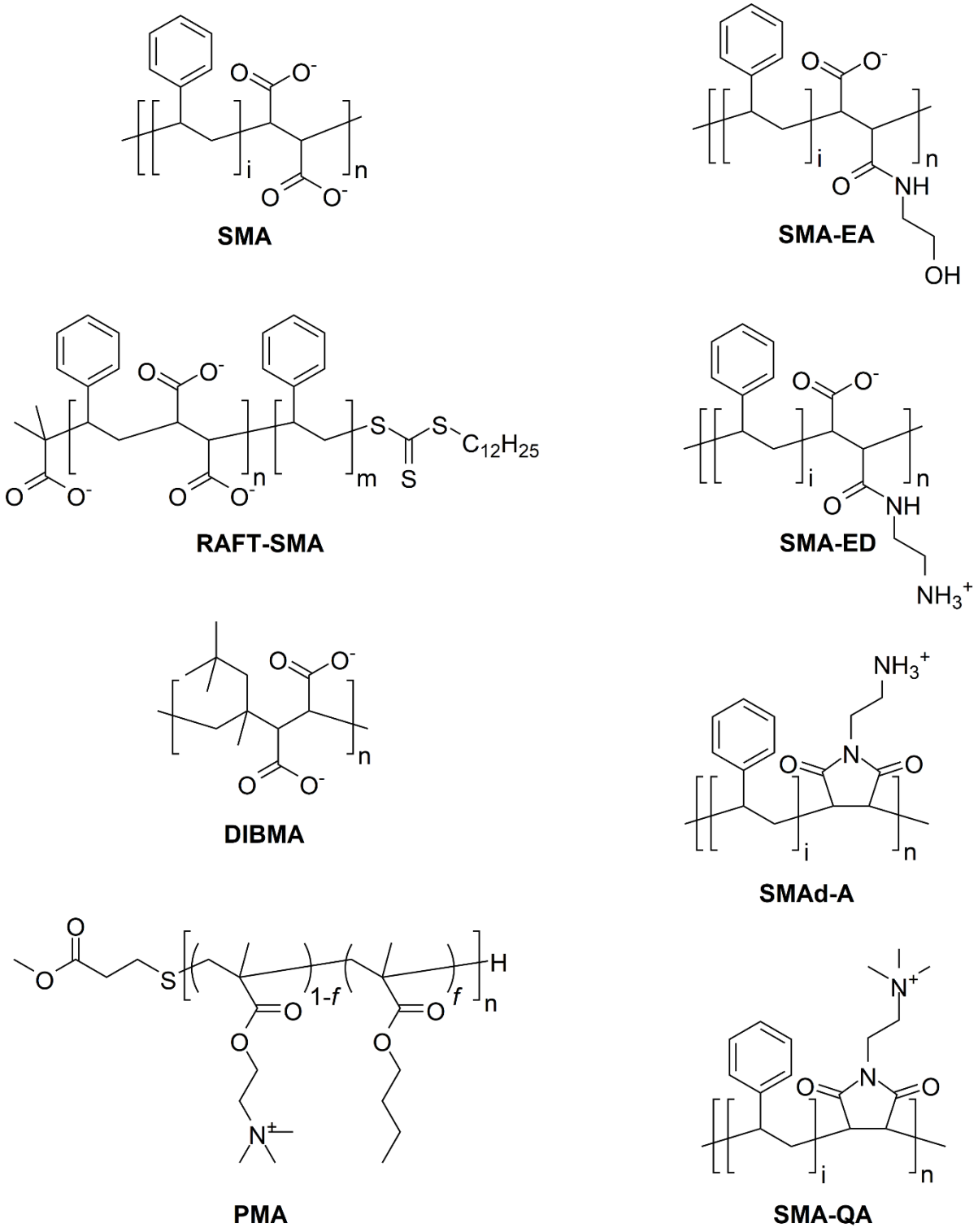

Figure 1.12. Chemical structures of SMA and some other nanodisc-forming polymers.

In addition to *de novo* synthesis of SMA polymers, several studies have reported modification of existing SMA polymers. In order to add customized functionality to SMALPs, SMAnh(2:1) polymers have been modified to contain cysteamine-modified maleic anhydride. This is then cleaved to the acid form under mildly alkaline conditions to yield SMA containing exposed reactive sulfhydryl groups, termed SMA-SH (Figure 1.12).[226] Compared to un-modified SMA(2:1), SMA-SH is capable of solubilizing phospholipids with comparable kinetic efficiency to form nanodiscs of a similar size distribution.[226] The exposed sulfhydryl group allows conjugation to a range of functional groups, including fluorophores and biotin, which can in turn bind to streptavidin-conjugated substrates.[226,227]

In a similar modification strategy to SMA-SH, modification of a low molecular weight (M_n = 1.6 kDa) SMA(1.3:1) has yielded a range of polymers which have improved pH compatibility and improved tolerance to divalent cations (Figure 1.12). Functionalization of SMA(1.3:1) with ethanolamine yields SMA-EA.[228] Similarly, modification with ethylenediamine yields the SMA-ED, which is zwitterionic except at neutral pH. SMA-ED can then be dehydrated to yield SMAd-A which is positively charged at acidic pH.[229] The final polymer in this series was formed by modification of SMA(1.3:1) with (2-aminoethyl)trimethylammonium, yielding a polymer with a permanent positive charge thanks to the presence of a quaternary ammonium, termed SMA-QA.[230] While all these polymers are functional in lipid nanodisc formation, by modifying the polymer:lipid ratio, it has been demonstrated that SMA-EA can solubilize a range of lipids to form nanodiscs of 10 nm to 50 nm diameter (termed macro-nanodiscs).[228,231] While this effect has also been observed for both SMA(3:1)[213] and SMA(2:1),[218] the range of obtainable diameters is much narrower than for nanodiscs formed with SMA-EA. The pH range over which each polymer is effective is dependent on the pH at which they retain net charge. While both SMA-ED and SMAd-A are functional at acidic pH, SMA-ED will precipitate between pH 4 and pH 7, and SMAd-A will precipitate above pH 6.[229] Due to the permanent positive charge present on SMA-QA being independent of pH, SMA-QA is functional across all pH values tested.[230] While none of these low-M_n modified SMA(1.3:1) polymers have been shown to extract proteins directly from native membranes, SMA-QA has been shown to retain activity of a reconstituted cytochrome P450 which is inactivated in SMA(1.3:1) and SMA-EA. This has been proposed to be a result of the electrostatic

repulsion between positively charged SMA-QA and cytochrome P450 preventing non-specific polymer-protein interactions.[232]

Finally, there has been a limited number of non-SMA polymers which have recently been shown to be functional in nanodisc formation. The first of these is poly(diisobutylene-*alt*-maleic acid) (DIBMA, Figure 1.12).[233] In contrast to SMA, DIBMA contains aliphatic diisobutylene in place of aromatic styrene groups, which are strictly alternating with maleic acid groups. This has the advantage that DIBMA has a much lower absorbance in the UV region overlapping with that from aromatic residues in proteins than SMA, enabling spectroscopic techniques such as UV-CD spectroscopy to be performed on encapsulated proteins without high absorbance arising from the polymer belt.[233] DIBMA is capable of solubilizing phospholipids of different chain lengths into nanodiscs.[234] From a thermodynamic perspective, DIBMA is milder than SMA(3:1) with less positive $\Delta G_L^{b\rightarrow m}$ and more negative $\Delta G_S^{b\rightarrow m}$, whilst better preserving the thermotropic properties of encapsulated membranes.[233] Crucially, DIBMA has been shown to be capable of extracting membrane proteins directly from *E. coli* membranes with comparable efficiency.[233]

More recently, a series of amphipathic poly(methacrylate) (PMA, Figure 1.12) based polymers have been synthesized which are functional in lipid nanodisc formation. Structurally, these polymers bear more resemblance to amphipols than SMA/ DIBMA.[235] While PMAs have not been shown to be capable of extracting proteins from native membranes, the properties of polymers which lead to amphipol vs nanodisc behaviour remain unknown. Like DIBMA, PMA polymers lack aromatic styrene moieties so have been utilized in CD measurements where PMA-nanodiscs have been shown to inhibit amyloid fibrilisation.[235]

1.6 AIMS AND SCOPE OF THIS THESIS

This study aims to better understand the properties of SMA polymers which can influence the self-assembly of SMALP nanodiscs and their resultant properties, whilst developing new polymers and

methodologies to expand the application of polymer-stabilized phoshpholipid nanodiscs in membrane and membrane protein research.

As discussed above, there is clearly a complicated interplay between the polymer hydrophobicity and monomer architecture which can modify SMALP self-assembly properties. To investigate the influence of polymer architecture on SMALP self-assembly, Chapter 2 investigates the thermodynamics of SMALP self-assembly by two related polymers, compares their structural properties, stability and application to the solubilization of biological membranes. The two polymers utilized in this study are the popular SMA2000, a CSTR-synthesized SMA(2:1) and a RAFT-SMA(2:1) of similar polymer length, but decreased polydispersity and better defined monomer topology.

While the limitations of SMA in terms of pH stability and sensitivity to divalent cations have been addressed by modifications to SMA, as described above, none of these polymers are commercially available. Polymer synthesis will likely be inhibitory to many protein-focused laboratories. Furthermore, none of the low-M_n modified SMA polymers with enhanced pH stability have been shown to be capable of solubilizing membrane proteins directly from cell membranes. To this end, Chapter 3 investigates the application of a commercially available, positively charged poly(styrene-*co*-maleimide) (SMI) in nanodisc formation. The thermodynamics of self-assembly, structural properties of the resultant nanodiscs, stability and biological application of SMI are investigated.

When introduced to planar phospholipid membranes at either the air-water or silicon-water interfaces, SMALPs show a drastically different behaviour to MSP-nanodiscs. While MSP-nanodiscs adsorb to the interface, SMALPs undergo a rapid lipid exchange. While the mechanism of lipid exchange between SMALPs in solution is now well understood, this is still unknown for lipid exchange between SMALPs and pre-existing planar membranes. Chapter 4 investigates this phenomenon by measuring the kinetics of lipid exchange and the structural properties of membranes at the air-water and silicon-water interfaces before and after nanodisc interaction. Furthermore, in assessing whether the kinetics and extent of lipid-exchange at interfaces is polymer dependent, the interaction between planar membranes and nanodiscs formed with SMA2000, RAFT-SMA and SMI are characterized.

Finally, one application where SMALPs have not yet been utilized is in the characterization of lipid-protein interactions between peripheral membrane proteins and membranes. While MSP nanodiscs have been successfully utilized in the investigation of peripheral membrane protein-membrane interactions, to the best of our knowledge, SMALPs have not been used for this purpose. Therefore, Chapter 5 investigates the potential of SMALPs in providing a soluble membrane surface for structural characterization of peripheral membrane protein-lipid interactions. As a test-case, the *E. coli* peripheral membrane protein, YraP is utilized. While well structurally characterized, the function of YraP is unknown. Therefore, by using SMALPs as a membrane surface, the interaction of YraP with membranes in solution is structurally characterized in order to provide hints as to YraP function.

1.7 REFERENCES

(1) Lombard, J. Once upon a Time the Cell Membranes: 175 Years of Cell Boundary Research. *Biol. Direct* **2014**, *9*. https://doi.org/10.1186/s13062-014-0032-7.

(2) Uings, I. J.; Farrow, S. N. Cell Receptors and Cell Signalling. *Mol. Pathol.* **2000**, *53* (6), 295–299.

(3) Marat, A. L.; Haucke, V. Phosphatidylinositol 3-phosphates—at the Interface between Cell Signalling and Membrane Traffic. *EMBO J.* **2016**, *35* (6), 561–579. https://doi.org/10.15252/embj.201593564.

(4) Wilson, J.; Schurr, M.; LeBlanc, C.; Ramamurthy, R.; Buchanan, K.; Nickerson, C. Mechanisms of Bacterial Pathogenicity. *Postgrad. Med. J.* **2002**, *78* (918), 216–224. https://doi.org/10.1136/pmj.78.918.216.

(5) Van Baarlen, P.; Van Belkum, A.; Summerbell, R. C.; Crous, P. W.; Thomma, B. P. H. J. Molecular Mechanisms of Pathogenicity: How Do Pathogenic Microorganisms Develop Cross-Kingdom Host Jumps? *FEMS Microbiol. Rev.* **2007**, *31* (3), 239–277. https://doi.org/10.1111/j.1574-6976.2007.00065.x.

(6) Blair, J. M. A.; Webber, M. A.; Baylay, A. J.; Ogbolu, D. O.; Piddock, L. J. V. Molecular Mechanisms of Antibiotic Resistance. *Nat. Rev. Microbiol.* **2015**, *13* (1), 42–51. https://doi.org/10.1038/nrmicro3380.

(7) Sun, J.; Deng, Z.; Yan, A. Bacterial Multidrug Efflux Pumps: Mechanisms, Physiology and Pharmacological Exploitations. *Biochem. Biophys. Res. Commun.* **2014**, *453* (2), 254–267. https://doi.org/10.1016/j.bbrc.2014.05.090.

(8) Dimitrov, D. S. Virus Entry: Molecular Mechanisms and Biomedical Applications. *Nat. Rev. Microbiol.* **2004**, *2* (2), 109–122. https://doi.org/10.1038/nrmicro817.

(9) Cosset, F.-L.; Lavillette, D. Cell Entry of Enveloped Viruses. *Adv. Genet.* **2011**, *73*, 121–183. https://doi.org/10.1016/B978-0-12-380860-8.00004-5.

(10) Grove, J.; Marsh, M. The Cell Biology of Receptor-Mediated Virus Entry. *J Cell Biol* **2011**, *195* (7), 1071–1082. https://doi.org/10.1083/jcb.201108131.

(11) Lorizate, M.; Kräusslich, H.-G. Role of Lipids in Virus Replication. *Cold Spring Harb. Perspect. Biol.* **2011**, *3* (10). https://doi.org/10.1101/cshperspect.a004820.

(12) Garnacho, C. Intracellular Drug Delivery: Mechanisms for Cell Entry. *Curr. Pharm. Des.* **2016**, *22* (9), 1210–1226.

(13) Cleal, K.; He, L.; Watson, P. D.; Jones, A. T. Endocytosis, Intracellular Traffic and Fate of Cell Penetrating Peptide Based Conjugates and Nanoparticles. *Curr. Pharm. Des.* **2013**, *19* (16), 2878–2894.
(14) Hillaireau, H.; Couvreur, P. Nanocarriers' Entry into the Cell: Relevance to Drug Delivery. *Cell. Mol. Life Sci. CMLS* **2009**, *66* (17), 2873–2896. https://doi.org/10.1007/s00018-009-0053-z.
(15) Strasser, A.; Wittmann, H.-J.; Seifert, R. Binding Kinetics and Pathways of Ligands to GPCRs. *Trends Pharmacol. Sci.* **2017**. https://doi.org/10.1016/j.tips.2017.05.005.
(16) Shoichet, B. K.; Kobilka, B. K. Structure-Based Drug Screening for G-Protein-Coupled Receptors. *Trends Pharmacol. Sci.* **2012**, *33* (5), 268–272. https://doi.org/10.1016/j.tips.2012.03.007.
(17) Romantsov, T.; Guan, Z.; Wood, J. M. Cardiolipin and the Osmotic Stress Responses of Bacteria. *Biochim. Biophys. Acta BBA - Biomembr.* **2009**, *1788* (10), 2092–2100. https://doi.org/10.1016/j.bbamem.2009.06.010.
(18) van Meer, G.; Voelker, D. R.; Feigenson, G. W. Membrane Lipids: Where They Are and How They Behave. *Nat. Rev. Mol. Cell Biol.* **2008**, *9* (2), 112–124. https://doi.org/10.1038/nrm2330.
(19) Whitfield, C.; Trent, M. S. Biosynthesis and Export of Bacterial Lipopolysaccharides. *Annu. Rev. Biochem.* **2014**, *83* (1), 99–128. https://doi.org/10.1146/annurev-biochem-060713-035600.
(20) Ingólfsson, H. I.; Melo, M. N.; van Eerden, F. J.; Arnarez, C.; Lopez, C. A.; Wassenaar, T. A.; Periole, X.; de Vries, A. H.; Tieleman, D. P.; Marrink, S. J. Lipid Organization of the Plasma Membrane. *J. Am. Chem. Soc.* **2014**, *136* (41), 14554–14559. https://doi.org/10.1021/ja507832e.
(21) Fadeel, B.; Xue, D. The Ins and Outs of Phospholipid Asymmetry in the Plasma Membrane: Roles in Health and Disease. *Crit. Rev. Biochem. Mol. Biol.* **2009**, *44* (5), 264–277. https://doi.org/10.1080/10409230903193307.
(22) Bernardino de la Serna, J.; Schütz, G. J.; Eggeling, C.; Cebecauer, M. There Is No Simple Model of the Plasma Membrane Organization. *Front. Cell Dev. Biol.* **2016**, *4*. https://doi.org/10.3389/fcell.2016.00106.
(23) The Challenges of Understanding Glycolipid Functions: An Open Outlook Based on Molecular Simulations. *Biochim. Biophys. Acta BBA - Mol. Cell Biol. Lipids* **2014**, *1841* (8), 1130–1145. https://doi.org/10.1016/j.bbalip.2013.12.016.
(24) Marquardt, D.; Geier, B.; Pabst, G.; Marquardt, D.; Geier, B.; Pabst, G. Asymmetric Lipid Membranes: Towards More Realistic Model Systems. *Membranes* **2015**, *5* (2), 180–196. https://doi.org/10.3390/membranes5020180.
(25) Malanovic, N.; Lohner, K. Gram-Positive Bacterial Cell Envelopes: The Impact on the Activity of Antimicrobial Peptides. *Biochim. Biophys. Acta BBA - Biomembr.* **2016**, *1858* (5), 936–946. https://doi.org/10.1016/j.bbamem.2015.11.004.
(26) Percy, M. G.; Gründling, A. Lipoteichoic Acid Synthesis and Function in Gram-Positive Bacteria. *Annu. Rev. Microbiol.* **2014**, *68* (1), 81–100. https://doi.org/10.1146/annurev-micro-091213-112949.
(27) Sohlenkamp, C.; Geiger, O. Bacterial Membrane Lipids: Diversity in Structures and Pathways. *FEMS Microbiol. Rev.* **2016**, *40* (1), 133–159. https://doi.org/10.1093/femsre/fuv008.
(28) Henderson, J. C.; Zimmerman, S. M.; Crofts, A. A.; Boll, J. M.; Kuhns, L. G.; Herrera, C. M.; Trent, M. S. The Power of Asymmetry: Architecture and Assembly of the Gram-Negative Outer Membrane Lipid Bilayer. *Annu. Rev. Microbiol.* **2016**, *70*, 255–278. https://doi.org/10.1146/annurev-micro-102215-095308.
(29) Ekiert, D. C.; Bhabha, G.; Isom, G. L.; Greenan, G.; Ovchinnikov, S.; Henderson, I. R.; Cox, J. S.; Vale, R. D. Architectures of Lipid Transport Systems for the Bacterial Outer Membrane. *Cell* **2017**, *169* (2), 273-285.e17. https://doi.org/10.1016/j.cell.2017.03.019.
(30) Delcour, A. H. Outer Membrane Permeability and Antibiotic Resistance. *Biochim. Biophys. Acta* **2009**, *1794* (5), 808–816. https://doi.org/10.1016/j.bbapap.2008.11.005.
(31) Maget-Dana, R. The Monolayer Technique: A Potent Tool for Studying the Interfacial Properties of Antimicrobial and Membrane-Lytic Peptides and Their Interactions with Lipid Membranes. *Biochim. Biophys. Acta* **1999**, *1462* (1–2), 109–140.

(32) Ma, G.; Allen, H. C. DPPC Langmuir Monolayer at the Air−Water Interface: Probing the Tail and Head Groups by Vibrational Sum Frequency Generation Spectroscopy. *Langmuir* **2006**, *22* (12), 5341–5349. https://doi.org/10.1021/la0535227.
(33) Dynarowicz-Latka, P.; Dhanabalan, A.; Oliveira, O. N. Modern Physicochemical Research on Langmuir Monolayers. *Adv. Colloid Interface Sci.* **2001**, *91* (2), 221–293.
(34) Stefaniu, C.; Brezesinski, G. Grazing Incidence X-Ray Diffraction Studies of Condensed Double-Chain Phospholipid Monolayers Formed at the Soft Air/Water Interface. *Adv. Colloid Interface Sci.* **2014**, *207*, 265–279. https://doi.org/10.1016/j.cis.2014.01.005.
(35) Baoukina, S.; Monticelli, L.; Risselada, H. J.; Marrink, S. J.; Tieleman, D. P. The Molecular Mechanism of Lipid Monolayer Collapse. *Proc. Natl. Acad. Sci.* **2008**, *105* (31), 10803–10808. https://doi.org/10.1073/pnas.0711563105.
(36) Levental, I.; Janmey, P. A.; Cēbers, A. Electrostatic Contribution to the Surface Pressure of Charged Monolayers Containing Polyphosphoinositides. *Biophys. J.* **2008**, *95* (3), 1199–1205. https://doi.org/10.1529/biophysj.107.126615.
(37) Kranenburg, M.; Smit, B. Phase Behavior of Model Lipid Bilayers. *J. Phys. Chem. B* **2005**, *109* (14), 6553–6563. https://doi.org/10.1021/jp0457646.
(38) McIntosh, T. J. Differences in Hydrocarbon Chain Tilt between Hydrated Phosphatidylethanolamine and Phosphatidylcholine Bilayers. A Molecular Packing Model. *Biophys. J.* **1980**, *29* (2), 237–245. https://doi.org/10.1016/S0006-3495(80)85128-9.
(39) Chapman, D.; Urbina, J. Biomembrane Phase Transitions. Studies of Lipid-Water Systems Using Differential Scanning Calorimetry. *J. Biol. Chem.* **1974**, *249* (8), 2512–2521.
(40) Papahadjopoulos, D.; Jacobson, K.; Nir, S.; Isac, I. Phase Transitions in Phospholipid Vesicles Fluorescence Polarization and Permeability Measurements Concerning the Effect of Temperature and Cholesterol. *Biochim. Biophys. Acta BBA - Biomembr.* **1973**, *311* (3), 330–348. https://doi.org/10.1016/0005-2736(73)90314-3.
(41) Saez, R.; Goñi, F. M.; Alonso, A. The Effect of Bilayer Order and Fluidity on Detergent-Induced Liposome Fusion. *FEBS Lett.* **1985**, *179* (2), 311–315. https://doi.org/10.1016/0014-5793(85)80541-X.
(42) Allhusen, J. S.; Conboy, J. C. The Ins and Outs of Lipid Flip-Flop. *Acc. Chem. Res.* **2017**, *50* (1), 58–65. https://doi.org/10.1021/acs.accounts.6b00435.
(43) Aricha, B.; Fishov, I.; Cohen, Z.; Sikron, N.; Pesakhov, S.; Khozin-Goldberg, I.; Dagan, R.; Porat, N. Differences in Membrane Fluidity and Fatty Acid Composition between Phenotypic Variants of Streptococcus Pneumoniae. *J. Bacteriol.* **2004**, *186* (14), 4638–4644. https://doi.org/10.1128/JB.186.14.4638-4644.2004.
(44) Russell, N. J. The Regulation of Membrane Fluidity in Bacteria by Acyl Chain Length Changes. In *Membrane Fluidity*; Kates, M., Manson, L. A., Eds.; Biomembranes; Springer US, 1984; pp 329–347. https://doi.org/10.1007/978-1-4684-4667-8_10.
(45) Singer, S. J.; Nicolson, G. L. The Fluid Mosaic Model of the Structure of Cell Membranes. *Science* **1972**, *175* (4023), 720–731.
(46) Marsh, D. Liquid-Ordered Phases Induced by Cholesterol: A Compendium of Binary Phase Diagrams. *Biochim. Biophys. Acta BBA - Biomembr.* **2010**, *1798* (3), 688–699. https://doi.org/10.1016/j.bbamem.2009.12.027.
(47) Sodt, A. J.; Sandar, M. L.; Gawrisch, K.; Pastor, R. W.; Lyman, E. The Molecular Structure of the Liquid-Ordered Phase of Lipid Bilayers. *J. Am. Chem. Soc.* **2014**, *136* (2), 725–732. https://doi.org/10.1021/ja4105667.
(48) Meyer, F. de; Smit, B. Effect of Cholesterol on the Structure of a Phospholipid Bilayer. *Proc. Natl. Acad. Sci.* **2009**, *106* (10), 3654–3658. https://doi.org/10.1073/pnas.0809959106.
(49) Dufourc, E. J. Sterols and Membrane Dynamics. *J. Chem. Biol.* **2008**, *1* (1–4), 63–77. https://doi.org/10.1007/s12154-008-0010-6.
(50) Sezgin, E.; Levental, I.; Mayor, S.; Eggeling, C. The Mystery of Membrane Organization: Composition, Regulation and Roles of Lipid Rafts. *Nat. Rev. Mol. Cell Biol.* **2017**, *18* (6), 361–374. https://doi.org/10.1038/nrm.2017.16.

(51) Raghunathan, K.; Kenworthy, A. K. Dynamic Pattern Generation in Cell Membranes: Current Insights into Membrane Organization. *Biochim. Biophys. Acta BBA - Biomembr.* **2018**. https://doi.org/10.1016/j.bbamem.2018.05.002.
(52) Cordeiro, R. M. Molecular Structure and Permeability at the Interface between Phase-Separated Membrane Domains. *J. Phys. Chem. B* **2018**, *122* (27), 6954–6965. https://doi.org/10.1021/acs.jpcb.8b03406.
(53) Kulkarni, C. V.; Wachter, W.; Iglesias-Salto, G.; Engelskirchen, S.; Ahualli, S. Monoolein: A Magic Lipid? *Phys. Chem. Chem. Phys.* **2011**, *13* (8), 3004–3021. https://doi.org/10.1039/C0CP01539C.
(54) McMahon, H. T.; Boucrot, E. Membrane Curvature at a Glance. *J Cell Sci* **2015**, *128* (6), 1065–1070. https://doi.org/10.1242/jcs.114454.
(55) Pinot, M.; Vanni, S.; Pagnotta, S.; Lacas-Gervais, S.; Payet, L.-A.; Ferreira, T.; Gautier, R.; Goud, B.; Antonny, B.; Barelli, H. Polyunsaturated Phospholipids Facilitate Membrane Deformation and Fission by Endocytic Proteins. *Science* **2014**, *345* (6197), 693–697. https://doi.org/10.1126/science.1255288.
(56) Jarsch, I. K.; Daste, F.; Gallop, J. L. Membrane Curvature in Cell Biology: An Integration of Molecular Mechanisms. *J Cell Biol* **2016**, *214* (4), 375–387. https://doi.org/10.1083/jcb.201604003.
(57) Graham, T. R.; Kozlov, M. M. Interplay of Proteins and Lipids in Generating Membrane Curvature. *Curr. Opin. Cell Biol.* **2010**, *22* (4), 430–436. https://doi.org/10.1016/j.ceb.2010.05.002.
(58) Katritch, V.; Cherezov, V.; Stevens, R. C. Structure-Function of the G-Protein-Coupled Receptor Superfamily. *Annu. Rev. Pharmacol. Toxicol.* **2013**, *53*, 531–556. https://doi.org/10.1146/annurev-pharmtox-032112-135923.
(59) Rosenbaum, D. M.; Rasmussen, S. G. F.; Kobilka, B. K. The Structure and Function of G-Protein-Coupled Receptors. *Nature* **2009**, *459* (7245), 356–363. https://doi.org/10.1038/nature08144.
(60) Farber, P. J.; Mittermaier, A. Side Chain Burial and Hydrophobic Core Packing in Protein Folding Transition States. *Protein Sci. Publ. Protein Soc.* **2008**, *17* (4), 644–651. https://doi.org/10.1110/ps.073105408.
(61) Zhou, Y.; Morais-Cabral, J. H.; Kaufman, A.; MacKinnon, R. Chemistry of Ion Coordination and Hydration Revealed by a K^+ Channel–Fab Complex at 2.0 Å Resolution. *Nature* **2001**, *414* (6859), 43–48. https://doi.org/10.1038/35102009.
(62) Sula, A.; Booker, J.; Ng, L. C. T.; Naylor, C. E.; DeCaen, P. G.; Wallace, B. A. The Complete Structure of an Activated Open Sodium Channel. *Nat. Commun.* **2017**, *8*, 14205. https://doi.org/10.1038/ncomms14205.
(63) Cuello, L. G.; Cortes, D. M.; Perozo, E. The gating cycle of a K+ channel at atomic resolution https://elifesciences.org/articles/28032 (accessed Aug 29, 2018). https://doi.org/10.7554/eLife.28032.
(64) Rühle, T.; Leister, D. Assembly of F1F0-ATP Synthases. *Biochim. Biophys. Acta BBA - Bioenerg.* **2015**, *1847* (9), 849–860. https://doi.org/10.1016/j.bbabio.2015.02.005.
(65) Sobti, M.; Smits, C.; Wong, A. S.; Ishmukhametov, R.; Stock, D.; Sandin, S.; Stewart, A. G. Cryo-EM Structures of the Autoinhibited E. Coli ATP Synthase in Three Rotational States. *eLife* **2016**, *5*, e21598. https://doi.org/10.7554/eLife.21598.
(66) Pérez, A.; Poza, M.; Fernández, A.; Fernández, M. del C.; Mallo, S.; Merino, M.; Rumbo-Feal, S.; Cabral, M. P.; Bou, G. Involvement of the AcrAB-TolC Efflux Pump in the Resistance, Fitness, and Virulence of Enterobacter Cloacae. *Antimicrob. Agents Chemother.* **2012**, *56* (4), 2084–2090. https://doi.org/10.1128/AAC.05509-11.
(67) Amaral, L.; Martins, A.; Spengler, G.; Molnar, J. Efflux Pumps of Gram-Negative Bacteria: What They Do, How They Do It, with What and How to Deal with Them. *Front. Pharmacol.* **2014**, *4*. https://doi.org/10.3389/fphar.2013.00168.

(68) Murakami, S.; Nakashima, R.; Yamashita, E.; Yamaguchi, A. Crystal Structure of Bacterial Multidrug Efflux Transporter AcrB. *Nature* **2002**, *419* (6907), 587–593. https://doi.org/10.1038/nature01050.

(69) Seeger, M. A.; Schiefner, A.; Eicher, T.; Verrey, F.; Diederichs, K.; Pos, K. M. Structural Asymmetry of AcrB Trimer Suggests a Peristaltic Pump Mechanism. *Science* **2006**, *313* (5791), 1295–1298. https://doi.org/10.1126/science.1131542.

(70) Du, D.; Wang, Z.; James, N. R.; Voss, J. E.; Klimont, E.; Ohene-Agyei, T.; Venter, H.; Chiu, W.; Luisi, B. F. Structure of the AcrAB–TolC Multidrug Efflux Pump. *Nature* **2014**, *509* (7501), 512–515. https://doi.org/10.1038/nature13205.

(71) Wang, Z.; Fan, G.; Hryc, C. F.; Blaza, J. N.; Serysheva, I. I.; Schmid, M. F.; Chiu, W.; Luisi, B. F.; Du, D. An allosteric transport mechanism for the AcrAB-TolC multidrug efflux pump https://elifesciences.org/articles/24905 (accessed Aug 29, 2018). https://doi.org/10.7554/eLife.24905.

(72) Fairman, J. W.; Noinaj, N.; Buchanan, S. K. The Structural Biology of β-Barrel Membrane Proteins: A Summary of Recent Reports. *Curr. Opin. Struct. Biol.* **2011**, *21* (4), 523–531. https://doi.org/10.1016/j.sbi.2011.05.005.

(73) Gessmann, D.; Mager, F.; Naveed, H.; Arnold, T.; Weirich, S.; Linke, D.; Liang, J.; Nussberger, S. Improving the Resistance of a Eukaryotic β-Barrel Protein to Thermal and Chemical Perturbations. *J. Mol. Biol.* **2011**, *413* (1), 150–161. https://doi.org/10.1016/j.jmb.2011.07.054.

(74) Noinaj, N.; Kuszak, A. J.; Buchanan, S. K. Heat Modifiability of Outer Membrane Proteins from Gram-Negative Bacteria. *Methods Mol. Biol. Clifton NJ* **2015**, *1329*, 51–56. https://doi.org/10.1007/978-1-4939-2871-2_4.

(75) Galdiero, S.; Pedone, M. G. and C. β-Barrel Membrane Bacterial Proteins: Structure, Function, Assembly and Interaction with Lipids http://www.eurekaselect.com/77804/article (accessed Aug 30, 2018).

(76) Tian, W.; Lin, M.; Tang, K.; Liang, J.; Naveed, H. High-Resolution Structure Prediction of β-Barrel Membrane Proteins. *Proc. Natl. Acad. Sci.* **2018**, 201716817. https://doi.org/10.1073/pnas.1716817115.

(77) Cowan, S. W.; Schirmer, T.; Rummel, G.; Steiert, M.; Ghosh, R.; Pauptit, R. A.; Jansonius, J. N.; Rosenbusch, J. P. Crystal Structures Explain Functional Properties of Two E. Coli Porins. *Nature* **1992**, *358* (6389), 727–733. https://doi.org/10.1038/358727a0.

(78) Lou, K.-L.; Saint, N.; Prilipov, A.; Rummel, G.; Benson, S. A.; Rosenbusch, J. P.; Schirmer, T. Structural and Functional Characterization of OmpF Porin Mutants Selected for Larger Pore Size I. CRYSTALLOGRAPHIC ANALYSIS. *J. Biol. Chem.* **1996**, *271* (34), 20669–20675. https://doi.org/10.1074/jbc.271.34.20669.

(79) Kefala, G.; Ahn, C.; Krupa, M.; Esquivies, L.; Maslennikov, I.; Kwiatkowski, W.; Choe, S. Structures of the OmpF Porin Crystallized in the Presence of Foscholine-12. *Protein Sci.* **2010**, *19* (5), 1117–1125. https://doi.org/10.1002/pro.369.

(80) Balasubramaniam, D.; Arockiasamy, A.; Kumar, P. D.; Sharma, A.; Krishnaswamy, S. Asymmetric Pore Occupancy in Crystal Structure of OmpF Porin from Salmonella Typhi. *J. Struct. Biol.* **2012**, *178* (3), 233–244. https://doi.org/10.1016/j.jsb.2012.04.005.

(81) Yamashita, E.; Zhalnina, M. V.; Zakharov, S. D.; Sharma, O.; Cramer, W. A. Crystal Structures of the OmpF Porin: Function in a Colicin Translocon. *EMBO J.* **2008**, *27* (15), 2171–2180. https://doi.org/10.1038/emboj.2008.137.

(82) Konovalova, A.; Kahne, D. E.; Silhavy, T. J. Outer Membrane Biogenesis. *Annu. Rev. Microbiol.* **2017**, *71* (1), 539–556. https://doi.org/10.1146/annurev-micro-090816-093754.

(83) Iadanza, M. G.; Higgins, A. J.; Schiffrin, B.; Calabrese, A. N.; Brockwell, D. J.; Ashcroft, A. E.; Radford, S. E.; Ranson, N. A. Lateral Opening in the Intact β-Barrel Assembly Machinery Captured by Cryo-EM. *Nat. Commun.* **2016**, *7*, 12865. https://doi.org/10.1038/ncomms12865.

(84) Gu, Y.; Li, H.; Dong, H.; Zeng, Y.; Zhang, Z.; Paterson, N. G.; Stansfeld, P. J.; Wang, Z.; Zhang, Y.; Wang, W.; et al. Structural Basis of Outer Membrane Protein Insertion by the BAM Complex. *Nature* **2016**, *531* (7592), 64–69. https://doi.org/10.1038/nature17199.

(85) Höhr, A. I. C.; Lindau, C.; Wirth, C.; Qiu, J.; Stroud, D. A.; Kutik, S.; Guiard, B.; Hunte, C.; Becker, T.; Pfanner, N.; et al. Membrane Protein Insertion through a Mitochondrial β-Barrel Gate. *Science* **2018**, *359* (6373), eaah6834. https://doi.org/10.1126/science.aah6834.
(86) Denisov, I. G.; Shih, A. Y.; Sligar, S. G. Structural Differences between Soluble and Membrane Bound Cytochrome P450s. *J. Inorg. Biochem.* **2012**, *108*, 150–158. https://doi.org/10.1016/j.jinorgbio.2011.11.026.
(87) Linder, M. E.; Deschenes, R. J. Palmitoylation: Policing Protein Stability and Traffic. *Nat. Rev. Mol. Cell Biol.* **2007**, *8* (1), 74–84. https://doi.org/10.1038/nrm2084.
(88) McTaggart, S. J. Isoprenylated Proteins. *Cell. Mol. Life Sci. CMLS* **2006**, *63* (3), 255–267. https://doi.org/10.1007/s00018-005-5298-6.
(89) Wright, M. H.; Heal, W. P.; Mann, D. J.; Tate, E. W. Protein Myristoylation in Health and Disease. *J. Chem. Biol.* **2009**, *3* (1), 19–35. https://doi.org/10.1007/s12154-009-0032-8.
(90) Paulick, M. G.; Bertozzi, C. R. The Glycosylphosphatidylinositol Anchor: A Complex Membrane-Anchoring Structure for Proteins. *Biochemistry* **2008**, *47* (27), 6991–7000. https://doi.org/10.1021/bi8006324.
(91) Resh, M. D. Covalent Lipid Modifications of Proteins. *Curr. Biol. CB* **2013**, *23* (10), R431–R435. https://doi.org/10.1016/j.cub.2013.04.024.
(92) Dennis, E. A.; Cao, J.; Hsu, Y.-H.; Magrioti, V.; Kokotos, G. Phospholipase A2 Enzymes: Physical Structure, Biological Function, Disease Implication, Chemical Inhibition, and Therapeutic Intervention. *Chem. Rev.* **2011**, *111* (10), 6130–6185. https://doi.org/10.1021/cr200085w.
(93) Habermann, B. The BAR-Domain Family of Proteins: A Case of Bending and Binding? *EMBO Rep.* **2004**, *5* (3), 250–255. https://doi.org/10.1038/sj.embor.7400105.
(94) Nakamura, K.; Man, Z.; Xie, Y.; Hanai, A.; Makyio, H.; Kawasaki, M.; Kato, R.; Shin, H.-W.; Nakayama, K.; Wakatsuki, S. Structural Basis for Membrane Binding Specificity of the Bin/Amphiphysin/Rvs (BAR) Domain of Arfaptin-2 Determined by Arl1 GTPase. *J. Biol. Chem.* **2012**, *287* (30), 25478–25489. https://doi.org/10.1074/jbc.M112.365783.
(95) Arkhipov, A.; Yin, Y.; Schulten, K. Membrane-Bending Mechanism of Amphiphysin N-BAR Domains. *Biophys. J.* **2009**, *97* (10), 2727–2735. https://doi.org/10.1016/j.bpj.2009.08.051.
(96) Frost, A.; Perera, R.; Roux, A.; Spasov, K.; Destaing, O.; Egelman, E. H.; Camilli, P. D.; Unger, V. M. Structural Basis of Membrane Invagination by F-BAR Domains. *Cell* **2008**, *132* (5), 807–817. https://doi.org/10.1016/j.cell.2007.12.041.
(97) Berman, H. M.; Westbrook, J.; Feng, Z.; Gilliland, G.; Bhat, T. N.; Weissig, H.; Shindyalov, I. N.; Bourne, P. E. The Protein Data Bank. *Nucleic Acids Res.* **2000**, *28* (1), 235–242.
(98) Membrane Proteins of Known Structure http://blanco.biomol.uci.edu/mpstruc/ (accessed Sep 3, 2018).
(99) Gupta, K.; Donlan, J. A. C.; Hopper, J. T. S.; Uzdavinys, P.; Landreh, M.; Struwe, W. B.; Drew, D.; Baldwin, A. J.; Stansfeld, P. J.; Robinson, C. V. The Role of Interfacial Lipids in Stabilizing Membrane Protein Oligomers. *Nature* **2017**, *541* (7637), 421–424. https://doi.org/10.1038/nature20820.
(100) Martens, C.; Stein, R. A.; Masureel, M.; Roth, A.; Mishra, S.; Dawaliby, R.; Konijnenberg, A.; Sobott, F.; Govaerts, C.; Mchaourab, H. S. Lipids Modulate the Conformational Dynamics of a Secondary Multidrug Transporter. *Nat. Struct. Mol. Biol.* **2016**, *23* (8), 744–751. https://doi.org/10.1038/nsmb.3262.
(101) Baylon, J. L.; Vermaas, J. V.; Muller, M. P.; Arcario, M. J.; Pogorelov, T. V.; Tajkhorshid, E. Atomic-Level Description of Protein-Lipid Interactions Using an Accelerated Membrane Model. *Biochim. Biophys. Acta* **2016**, *1858* (7 Pt B), 1573–1583. https://doi.org/10.1016/j.bbamem.2016.02.027.
(102) Hedger, G.; Sansom, M. S. P. Lipid Interaction Sites on Channels, Transporters and Receptors: Recent Insights from Molecular Dynamics Simulations. *Biochim. Biophys. Acta* **2016**, *1858* (10), 2390–2400. https://doi.org/10.1016/j.bbamem.2016.02.037.
(103) Arnold, T.; Linke, D. The Use of Detergents to Purify Membrane Proteins. *Curr. Protoc. Protein Sci.* **2008**, *Chapter 4*, Unit 4.8.1-4.8.30. https://doi.org/10.1002/0471140864.ps0408s53.

(104) Carpenter, E. P.; Beis, K.; Cameron, A. D.; Iwata, S. Overcoming the Challenges of Membrane Protein Crystallography. *Curr. Opin. Struct. Biol.* **2008**, *18* (5), 581–586. https://doi.org/10.1016/j.sbi.2008.07.001.
(105) Smith, S. M. Strategies for the Purification of Membrane Proteins. *Methods Mol. Biol. Clifton NJ* **2011**, *681*, 485–496. https://doi.org/10.1007/978-1-60761-913-0_29.
(106) Opekarová, M.; Tanner, W. Specific Lipid Requirements of Membrane Proteins—a Putative Bottleneck in Heterologous Expression. *Biochim. Biophys. Acta BBA - Biomembr.* **2003**, *1610* (1), 11–22. https://doi.org/10.1016/S0005-2736(02)00708-3.
(107) Seddon, A. M.; Curnow, P.; Booth, P. J. Membrane Proteins, Lipids and Detergents: Not Just a Soap Opera. *Biochim. Biophys. Acta BBA - Biomembr.* **2004**, *1666* (1–2), 105–117. https://doi.org/10.1016/j.bbamem.2004.04.011.
(108) Bogdanov, M.; Mileykovskaya, E.; Dowhan, W. Lipids in the Assembly of Membrane Proteins and Organization of Protein Supercomplexes. *Subcell. Biochem.* **2008**, *49*, 197–239. https://doi.org/10.1007/978-1-4020-8831-5_8.
(109) Lorent, J. H.; Levental, I. Structural Determinants of Protein Partitioning into Ordered Membrane Domains and Lipid Rafts. *Chem. Phys. Lipids* **2015**, *192*, 23–32. https://doi.org/10.1016/j.chemphyslip.2015.07.022.
(110) Laganowsky, A.; Reading, E.; Allison, T. M.; Ulmschneider, M. B.; Degiacomi, M. T.; Baldwin, A. J.; Robinson, C. V. Membrane Proteins Bind Lipids Selectively to Modulate Their Structure and Function. *Nature* **2014**, *510* (7503), 172–175. https://doi.org/10.1038/nature13419.
(111) Long, S. B.; Tao, X.; Campbell, E. B.; MacKinnon, R. Atomic Structure of a Voltage-Dependent K+ Channel in a Lipid Membrane-like Environment. *Nature* **2007**, *450* (7168), 376–382. https://doi.org/10.1038/nature06265.
(112) Palsdottir, H.; Hunte, C. Lipids in Membrane Protein Structures. *Biochim. Biophys. Acta BBA - Biomembr.* **2004**, *1666* (1–2), 2–18. https://doi.org/10.1016/j.bbamem.2004.06.012.
(113) Krishnamani, V.; Lanyi, J. K. Molecular Dynamics Simulation of the Unfolding of Individual Bacteriorhodopsin Helices in Sodium Dodecyl Sulfate Micelles. *Biochemistry* **2012**, *51* (6), 1061–1069. https://doi.org/10.1021/bi201770y.
(114) Geertsma, E. R.; Nik Mahmood, N. A. B.; Schuurman-Wolters, G. K.; Poolman, B. Membrane Reconstitution of ABC Transporters and Assays of Translocator Function. *Nat. Protoc.* **2008**, *3* (2), 256–266. https://doi.org/10.1038/nprot.2007.519.
(115) Schulze, R. J.; Komar, J.; Botte, M.; Allen, W. J.; Whitehouse, S.; Gold, V. A. M.; Lycklama a Nijeholt, J. A.; Huard, K.; Berger, I.; Schaffitzel, C.; et al. Membrane Protein Insertion and Proton-Motive-Force-Dependent Secretion through the Bacterial Holo-Translocon SecYEG?SecDF?YajC?YidC. *Proc. Natl. Acad. Sci.* **2014**, *111* (13), 4844–4849. https://doi.org/10.1073/pnas.1315901111.
(116) Zakharian, E. Recording of Ion Channel Activity in Planar Lipid Bilayer Experiments. In *Ion Channels*; Gamper, N., Ed.; Humana Press: Totowa, NJ, 2013; Vol. 998, pp 109–118. https://doi.org/10.1007/978-1-62703-351-0_8.
(117) Merz, C.; Knoll, W.; Textor, M.; Reimhult, E. Formation of Supported Bacterial Lipid Membrane Mimics. *Biointerphases* **2008**, *3* (2), FA41–FA50. https://doi.org/10.1116/1.2896119.
(118) Tanaka, M.; Sackmann, E. Polymer-Supported Membranes as Models of the Cell Surface. *Nature* **2005**, *437* (7059), 656–663. https://doi.org/10.1038/nature04164.
(119) Aristotelous, T.; Hopkins, A. L.; Navratilova, I. Surface Plasmon Resonance Analysis of Seven-Transmembrane Receptors. *Methods Enzymol.* **2015**, *556*, 499–525. https://doi.org/10.1016/bs.mie.2015.01.016.
(120) Patching, S. G. Surface Plasmon Resonance Spectroscopy for Characterisation of Membrane Protein-Ligand Interactions and Its Potential for Drug Discovery. *Biochim. Biophys. Acta* **2014**, *1838* (1 Pt A), 43–55. https://doi.org/10.1016/j.bbamem.2013.04.028.
(121) Chu, R.; Reczek, D.; Brondyk, W. Capture-Stabilize Approach for Membrane Protein SPR Assays. *Sci. Rep.* **2014**, *4*. https://doi.org/10.1038/srep07360.

(122) Zhou, W.; Wang, Y. Y.; Lim, T.-S.; Pham, T.; Jain, D.; Burke, P. J. Detection of Single Ion Channel Activity with Carbon Nanotubes. *Sci. Rep.* **2015**, *5* (1). https://doi.org/10.1038/srep09208.
(123) Clifton, L. A.; Neylon, C.; Lakey, J. H. Examining Protein–Lipid Complexes Using Neutron Scattering. In *Lipid-Protein Interactions*; Kleinschmidt, J. H., Ed.; Humana Press: Totowa, NJ, 2013; Vol. 974, pp 119–150. https://doi.org/10.1007/978-1-62703-275-9_7.
(124) Shen, H.-H.; Leyton, D. L.; Shiota, T.; Belousoff, M. J.; Noinaj, N.; Lu, J.; Holt, S. A.; Tan, K.; Selkrig, J.; Webb, C. T.; et al. Reconstitution of a Nanomachine Driving the Assembly of Proteins into Bacterial Outer Membranes. *Nat. Commun.* **2014**, *5*, ncomms6078. https://doi.org/10.1038/ncomms6078.
(125) Clifton, L. A.; Holt, S. A.; Hughes, A. V.; Daulton, E. L.; Arunmanee, W.; Heinrich, F.; Khalid, S.; Jefferies, D.; Charlton, T. R.; Webster, J. R. P.; et al. An Accurate In Vitro Model of the E. Coli Envelope. *Angew. Chem. Int. Ed.* **2015**, *54* (41), 11952–11955. https://doi.org/10.1002/anie.201504287.
(126) Paracini, N.; Clifton, L. A.; Skoda, M. W. A.; Lakey, J. H. Liquid Crystalline Bacterial Outer Membranes Are Critical for Antibiotic Susceptibility. *Proc. Natl. Acad. Sci.* **2018**, *115* (32), E7587–E7594. https://doi.org/10.1073/pnas.1803975115.
(127) Sanders, C. R.; Landis, G. C. Reconstitution of Membrane Proteins into Lipid-Rich Bilayered Mixed Micelles for NMR Studies. *Biochemistry* **1995**, *34* (12), 4030–4040.
(128) Dürr, U. H. N.; Soong, R.; Ramamoorthy, A. When Detergent Meets Bilayer: Birth and Coming of Age of Lipid Bicelles. *Prog. Nucl. Magn. Reson. Spectrosc.* **2013**, *69*, 1–22. https://doi.org/10.1016/j.pnmrs.2013.01.001.
(129) Ujwal, R.; Bowie, J. U. Crystallizing Membrane Proteins Using Lipidic Bicelles. *Methods* **2011**, *55* (4), 337–341. https://doi.org/10.1016/j.ymeth.2011.09.020.
(130) Faham, S.; Bowie, J. U. Bicelle Crystallization: A New Method for Crystallizing Membrane Proteins Yields a Monomeric Bacteriorhodopsin Structure11Edited by D. Rees. *J. Mol. Biol.* **2002**, *316* (1), 1–6. https://doi.org/10.1006/jmbi.2001.5295.
(131) Poulos, S.; Morgan, J. L. W.; Zimmer, J.; Faham, S. Chapter Nineteen - Bicelles Coming of Age: An Empirical Approach to Bicelle Crystallization. In *Methods in Enzymology*; Shukla, A. K., Ed.; Membrane Proteins—Engineering, Purification and Crystallization; Academic Press, 2015; Vol. 557, pp 393–416. https://doi.org/10.1016/bs.mie.2014.12.024.
(132) Rasmussen, S. G. F.; Choi, H.-J.; Rosenbaum, D. M.; Kobilka, T. S.; Thian, F. S.; Edwards, P. C.; Burghammer, M.; Ratnala, V. R. P.; Sanishvili, R.; Fischetti, R. F.; et al. Crystal Structure of the Human β_2 Adrenergic G-Protein-Coupled Receptor. *Nature* **2007**, *450* (7168), 383–387. https://doi.org/10.1038/nature06325.
(133) Payandeh, J.; Scheuer, T.; Zheng, N.; Catterall, W. A. The Crystal Structure of a Voltage-Gated Sodium Channel. *Nature* **2011**, *475* (7356), 353–358. https://doi.org/10.1038/nature10238.
(134) Lenaeus, M. J.; El-Din, T. M. G.; Ing, C.; Ramanadane, K.; Pomès, R.; Zheng, N.; Catterall, W. A. Structures of Closed and Open States of a Voltage-Gated Sodium Channel. *Proc. Natl. Acad. Sci.* **2017**, *114* (15), E3051–E3060. https://doi.org/10.1073/pnas.1700761114.
(135) Noinaj, N.; Kuszak, A. J.; Gumbart, J. C.; Lukacik, P.; Chang, H.; Easley, N. C.; Lithgow, T.; Buchanan, S. K. Structural Insight into the Biogenesis of β-Barrel Membrane Proteins. *Nature* **2013**, *501* (7467), 385–390. https://doi.org/10.1038/nature12521.
(136) Nakane, T.; Hanashima, S.; Suzuki, M.; Saiki, H.; Hayashi, T.; Kakinouchi, K.; Sugiyama, S.; Kawatake, S.; Matsuoka, S.; Matsumori, N.; et al. Membrane Protein Structure Determination by SAD, SIR, or SIRAS Phasing in Serial Femtosecond Crystallography Using an Iododetergent. *Proc. Natl. Acad. Sci.* **2016**, *113* (46), 13039–13044. https://doi.org/10.1073/pnas.1602531113.
(137) Dürr, U. H. N.; Gildenberg, M.; Ramamoorthy, A. The Magic of Bicelles Lights Up Membrane Protein Structure. *Chem. Rev.* **2012**, *112* (11), 6054–6074. https://doi.org/10.1021/cr300061w.
(138) Harroun, T. A.; Koslowsky, M.; Nieh, M.-P.; de Lannoy, C.-F.; Raghunathan, V. A.; Katsaras, J. Comprehensive Examination of Mesophases Formed by DMPC and DHPC Mixtures. *Langmuir* **2005**, *21* (12), 5356–5361. https://doi.org/10.1021/la050018t.

(139) Yamamoto, K.; Soong, R.; Ramamoorthy, A. Comprehensive Analysis of Lipid Dynamics Variation with Lipid Composition and Hydration of Bicelles Using Nuclear Magnetic Resonance (NMR) Spectroscopy. *Langmuir* **2009**, *25* (12), 7010–7018. https://doi.org/10.1021/la900200s.
(140) Beaugrand, M.; Arnold, A. A.; Hénin, J.; Warschawski, D. E.; Williamson, P. T. F.; Marcotte, I. Lipid Concentration and Molar Ratio Boundaries for the Use of Isotropic Bicelles. *Langmuir* **2014**, *30* (21), 6162–6170. https://doi.org/10.1021/la5004353.
(141) Tribet, C.; Audebert, R.; Popot, J.-L. Amphipols: Polymers That Keep Membrane Proteins Soluble in Aqueous Solutions. *Proc. Natl. Acad. Sci.* **1996**, *93* (26), 15047–15050.
(142) Le Bon, C.; Marconnet, A.; Masscheleyn, S.; Popot, J.-L.; Zoonens, M. Folding and Stabilizing Membrane Proteins in Amphipol A8-35. *Methods* **2018**. https://doi.org/10.1016/j.ymeth.2018.04.012.
(143) Giusti, F.; Popot, J.-L.; Tribet, C. Well-Defined Critical Association Concentration and Rapid Adsorption at the Air/Water Interface of a Short Amphiphilic Polymer, Amphipol A8-35: A Study by Förster Resonance Energy Transfer and Dynamic Surface Tension Measurements. *Langmuir* **2012**, *28* (28), 10372–10380. https://doi.org/10.1021/la300774d.
(144) Charvolin, D.; Picard, M.; Huang, L.-S.; Berry, E. A.; Popot, J.-L. Solution Behavior and Crystallization of Cytochrome bc_1 in the Presence of Amphipols. *J. Membr. Biol.* **2014**, *247* (9–10), 981–996. https://doi.org/10.1007/s00232-014-9694-4.
(145) Zoonens, M.; Popot, J.-L. Amphipols for Each Season. *J. Membr. Biol.* **2014**, *247* (0), 759–796. https://doi.org/10.1007/s00232-014-9666-8.
(146) Arunmanee, W.; Harris, J. R.; Lakey, J. H. Outer Membrane Protein F Stabilised with Minimal Amphipol Forms Linear Arrays and LPS-Dependent 2D Crystals. *J. Membr. Biol.* **2014**, *247* (9–10), 949–956. https://doi.org/10.1007/s00232-014-9640-5.
(147) Tribet, C.; Diab, C.; Dahmane, T.; Zoonens, M.; Popot, J.-L.; Winnik, F. M. Thermodynamic Characterization of the Exchange of Detergents and Amphipols at the Surfaces of Integral Membrane Proteins. *Langmuir* **2009**, *25* (21), 12623–12634. https://doi.org/10.1021/la9018772.
(148) Nagy, J. K.; Kuhn Hoffmann, A.; Keyes, M. H.; Gray, D. N.; Oxenoid, K.; Sanders, C. R. Use of Amphipathic Polymers to Deliver a Membrane Protein to Lipid Bilayers. *FEBS Lett.* **2001**, *501* (2–3), 115–120.
(149) Tehei, M.; Perlmutter, J. D.; Giusti, F.; Sachs, J. N.; Zaccai, G.; Popot, J.-L. Thermal Fluctuations in Amphipol A8-35 Particles: A Neutron Scattering and Molecular Dynamics Study. *J. Membr. Biol.* **2014**, *247* (9–10), 897–908. https://doi.org/10.1007/s00232-014-9725-1.
(150) Pocanschi, C. L.; Popot, J.-L.; Kleinschmidt, J. H. Folding and Stability of Outer Membrane Protein A (OmpA) from Escherichia Coli in an Amphipathic Polymer, Amphipol A8-35. *Eur. Biophys. J. EBJ* **2013**, *42* (2–3), 103–118. https://doi.org/10.1007/s00249-013-0887-z.
(151) Popot, J.-L.; Althoff, T.; Bagnard, D.; Banères, J.-L.; Bazzacco, P.; Billon-Denis, E.; Catoire, L. J.; Champeil, P.; Charvolin, D.; Cocco, M. J.; et al. Amphipols from A to Z. *Annu. Rev. Biophys.* **2011**, *40*, 379–408. https://doi.org/10.1146/annurev-biophys-042910-155219.
(152) Picard, M.; Dahmane, T.; Garrigos, M.; Gauron, C.; Giusti, F.; le Maire, M.; Popot, J.-L.; Champeil, P. Protective and Inhibitory Effects of Various Types of Amphipols on the Ca2+-ATPase from Sarcoplasmic Reticulum: A Comparative Study. *Biochemistry* **2006**, *45* (6), 1861–1869. https://doi.org/10.1021/bi051954a.
(153) Liao, M.; Cao, E.; Julius, D.; Cheng, Y. Structure of the TRPV1 Ion Channel Determined by Electron Cryo-Microscopy. *Nature* **2013**, *504* (7478), 107–112. https://doi.org/10.1038/nature12822.
(154) Lu, P.; Bai, X.; Ma, D.; Xie, T.; Yan, C.; Sun, L.; Yang, G.; Zhao, Y.; Zhou, R.; Scheres, S. H. W.; et al. Three-Dimensional Structure of Human γ-Secretase. *Nature* **2014**, *512* (7513), 166–170. https://doi.org/10.1038/nature13567.
(155) Polovinkin, V.; Gushchin, I.; Sintsov, M.; Round, E.; Balandin, T.; Chervakov, P.; Schevchenko, V.; Utrobin, P.; Popov, A.; Borshchevskiy, V.; et al. High-Resolution Structure of a Membrane Protein Transferred from Amphipol to a Lipidic Mesophase. *J. Membr. Biol.* **2014**, *247* (9–10), 997–1004. https://doi.org/10.1007/s00232-014-9700-x.

(156) Giusti, F.; Rieger, J.; Catoire, L. J.; Qian, S.; Calabrese, A. N.; Watkinson, T. G.; Casiraghi, M.; Radford, S. E.; Ashcroft, A. E.; Popot, J.-L. Synthesis, Characterization and Applications of a Perdeuterated Amphipol. *J. Membr. Biol.* **2014**, *247* (9–10), 909–924. https://doi.org/10.1007/s00232-014-9656-x.

(157) Gohon, Y.; Dahmane, T.; Ruigrok, R. W. H.; Schuck, P.; Charvolin, D.; Rappaport, F.; Timmins, P.; Engelman, D. M.; Tribet, C.; Popot, J.-L.; et al. Bacteriorhodopsin/Amphipol Complexes: Structural and Functional Properties. *Biophys. J.* **2008**, *94* (9), 3523–3537. https://doi.org/10.1529/biophysj.107.121848.

(158) Charvolin, D.; Perez, J.-B.; Rouvière, F.; Giusti, F.; Bazzacco, P.; Abdine, A.; Rappaport, F.; Martinez, K. L.; Popot, J.-L. The Use of Amphipols as Universal Molecular Adapters to Immobilize Membrane Proteins onto Solid Supports. *Proc. Natl. Acad. Sci. U. S. A.* **2009**, *106* (2), 405–410. https://doi.org/10.1073/pnas.0807132106.

(159) Giusti, F.; Kessler, P.; Hansen, R. W.; Della Pia, E. A.; Le Bon, C.; Mourier, G.; Popot, J.-L.; Martinez, K. L.; Zoonens, M. Synthesis of a Polyhistidine-Bearing Amphipol and Its Use for Immobilizing Membrane Proteins. *Biomacromolecules* **2015**, *16* (12), 3751–3761. https://doi.org/10.1021/acs.biomac.5b01010.

(160) Pocanschi, C. L.; Dahmane, T.; Gohon, Y.; Rappaport, F.; Apell, H.-J.; Kleinschmidt, J. H.; Popot, J.-L. Amphipathic Polymers: Tools To Fold Integral Membrane Proteins to Their Active Form. *Biochemistry* **2006**, *45* (47), 13954–13961. https://doi.org/10.1021/bi0616706.

(161) Bechara, C.; Bolbach, G.; Bazzaco, P.; Sharma, K. S.; Durand, G.; Popot, J.-L.; Zito, F.; Sagan, S. MALDI-TOF Mass Spectrometry Analysis of Amphipol-Trapped Membrane Proteins. *Anal. Chem.* **2012**, *84* (14), 6128–6135. https://doi.org/10.1021/ac301035r.

(162) Bayburt, T. H.; Grinkova, Y. V.; Sligar, S. G. Self-Assembly of Discoidal Phospholipid Bilayer Nanoparticles with Membrane Scaffold Proteins. *Nano Lett.* **2002**, *2* (8), 853–856. https://doi.org/10.1021/nl025623k.

(163) Bayburt, T. H.; Carlson, J. W.; Sligar, S. G. Reconstitution and Imaging of a Membrane Protein in a Nanometer-Size Phospholipid Bilayer. *J. Struct. Biol.* **1998**, *123* (1), 37–44. https://doi.org/10.1006/jsbi.1998.4007.

(164) Denisov, I. G.; Grinkova, Y. V.; Lazarides, A. A.; Sligar, S. G. Directed Self-Assembly of Monodisperse Phospholipid Bilayer Nanodiscs with Controlled Size. *J. Am. Chem. Soc.* **2004**, *126* (11), 3477–3487. https://doi.org/10.1021/ja0393574.

(165) Nakano, M.; Fukuda, M.; Kudo, T.; Miyazaki, M.; Wada, Y.; Matsuzaki, N.; Endo, H.; Handa, T. Static and Dynamic Properties of Phospholipid Bilayer Nanodiscs. *J. Am. Chem. Soc.* **2009**, *131* (23), 8308–8312. https://doi.org/10.1021/ja9017013.

(166) Bibow, S.; Polyhach, Y.; Eichmann, C.; Chi, C. N.; Kowal, J.; Albiez, S.; McLeod, R. A.; Stahlberg, H.; Jeschke, G.; Güntert, P.; et al. Solution Structure of Discoidal High-Density Lipoprotein Particles with a Shortened Apolipoprotein A-I. *Nat. Struct. Mol. Biol.* **2017**, *24* (2), 187–193. https://doi.org/10.1038/nsmb.3345.

(167) Pourmousa, M.; Pastor, R. W. Molecular Dynamics Simulations of Lipid Nanodiscs. *Biochim. Biophys. Acta BBA - Biomembr.* **2018**. https://doi.org/10.1016/j.bbamem.2018.04.015.

(168) Denisov, I. G.; Sligar, S. G. Nanodiscs in Membrane Biochemistry and Biophysics. *Chem. Rev.* **2017**, *117* (6), 4669–4713. https://doi.org/10.1021/acs.chemrev.6b00690.

(169) Grinkova, Y. V.; Denisov, I. G.; Sligar, S. G. Engineering Extended Membrane Scaffold Proteins for Self-Assembly of Soluble Nanoscale Lipid Bilayers. *Protein Eng. Des. Sel. PEDS* **2010**, *23* (11), 843–848. https://doi.org/10.1093/protein/gzq060.

(170) Bayburt, T. H.; Sligar, S. G. Membrane Protein Assembly into Nanodiscs. *FEBS Lett.* **2010**, *584* (9), 1721–1727. https://doi.org/10.1016/j.febslet.2009.10.024.

(171) Shaw, A. W.; McLean, M. A.; Sligar, S. G. Phospholipid Phase Transitions in Homogeneous Nanometer Scale Bilayer Discs. *FEBS Lett.* **2004**, *556* (1–3), 260–264.

(172) Mi, L.-Z.; Grey, M. J.; Nishida, N.; Walz, T.; Lu, C.; Springer, T. A. Functional and Structural Stability of the Epidermal Growth Factor Receptor in Detergent Micelles and Phospholipid Nanodiscs. *Biochemistry* **2008**, *47* (39), 10314–10323. https://doi.org/10.1021/bi801006s.

(173) Moon, C. P.; Fleming, K. G. Side-Chain Hydrophobicity Scale Derived from Transmembrane Protein Folding into Lipid Bilayers. *Proc. Natl. Acad. Sci.* **2011**, *108* (25), 10174–10177. https://doi.org/10.1073/pnas.1103979108.
(174) Dominik, P. K.; Borowska, M. T.; Dalmas, O.; Kim, S. S.; Perozo, E.; Keenan, R. J.; Kossiakoff, A. A. Conformational Chaperones for Structural Studies of Membrane Proteins Using Antibody Phage Display with Nanodiscs. *Structure* **2016**, *24* (2), 300–309. https://doi.org/10.1016/j.str.2015.11.014.
(175) Borowska, M. T.; Dominik, P. K.; Anghel, S. A.; Kossiakoff, A. A.; Keenan, R. J. A YidC-like Protein in the Archaeal Plasma Membrane. *Structure* **2015**, *23* (9), 1715–1724. https://doi.org/10.1016/j.str.2015.06.025.
(176) Shaw, A. W.; Pureza, V. S.; Sligar, S. G.; Morrissey, J. H. The Local Phospholipid Environment Modulates the Activation of Blood Clotting. *J. Biol. Chem.* **2007**, *282* (9), 6556–6563. https://doi.org/10.1074/jbc.M607973200.
(177) Bocquet, N.; Kohler, J.; Hug, M. N.; Kusznir, E. A.; Rufer, A. C.; Dawson, R. J.; Hennig, M.; Ruf, A.; Huber, W.; Huber, S. Real-Time Monitoring of Binding Events on a Thermostabilized Human A2A Receptor Embedded in a Lipid Bilayer by Surface Plasmon Resonance. *Biochim. Biophys. Acta BBA - Biomembr.* **2015**, *1848* (5), 1224–1233. https://doi.org/10.1016/j.bbamem.2015.02.014.
(178) Wadsäter, M.; Simonsen, J. B.; Lauridsen, T.; Tveten, E. G.; Naur, P.; Bjørnholm, T.; Wacklin, H.; Mortensen, K.; Arleth, L.; Feidenhans'l, R.; et al. Aligning Nanodiscs at the Air–Water Interface, a Neutron Reflectivity Study. *Langmuir* **2011**, *27* (24), 15065–15073. https://doi.org/10.1021/la203100n.
(179) Wadsäter, M.; Barker, R.; Mortensen, K.; Feidenhans'l, R.; Cárdenas, M. Effect of Phospholipid Composition and Phase on Nanodisc Films at the Solid–Liquid Interface as Studied by Neutron Reflectivity. *Langmuir* **2013**, *29* (9), 2871–2880. https://doi.org/10.1021/la3024698.
(180) Wadsäter, M.; Laursen, T.; Singha, A.; Hatzakis, N. S.; Stamou, D.; Barker, R.; Mortensen, K.; Feidenhans'l, R.; Møller, B. L.; Cárdenas, M. Monitoring Shifts in the Conformation Equilibrium of the Membrane Protein Cytochrome P450 Reductase (POR) in Nanodiscs. *J. Biol. Chem.* **2012**, *287* (41), 34596–34603. https://doi.org/10.1074/jbc.M112.400085.
(181) Denisov, I. G.; Sligar, S. G. Nanodiscs for Structural and Functional Studies of Membrane Proteins. *Nat. Struct. Mol. Biol.* **2016**, *23* (6), 481–486. https://doi.org/10.1038/nsmb.3195.
(182) Ding, Y.; Fujimoto, L. M.; Yao, Y.; Marassi, F. M. Solid-State NMR of the Yersinia Pestis Outer Membrane Protein Ail in Lipid Bilayer Nanodiscs Sedimented by Ultracentrifugation. *J. Biomol. NMR* **2015**, *61* (3–4), 275–286. https://doi.org/10.1007/s10858-014-9893-4.
(183) Kucharska, I.; Edrington, T. C.; Liang, B.; Tamm, L. K. Optimizing Nanodiscs and Bicelles for Solution NMR Studies of Two β-Barrel Membrane Proteins. *J. Biomol. NMR* **2015**, *61* (3–4), 261–274. https://doi.org/10.1007/s10858-015-9905-z.
(184) Hagn, F.; Etzkorn, M.; Raschle, T.; Wagner, G. Optimized Phospholipid Bilayer Nanodiscs Facilitate High-Resolution Structure Determination of Membrane Proteins. *J. Am. Chem. Soc.* **2013**, *135* (5), 1919–1925. https://doi.org/10.1021/ja310901f.
(185) Frauenfeld, J.; Gumbart, J.; Sluis, E. O. van der; Funes, S.; Gartmann, M.; Beatrix, B.; Mielke, T.; Berninghausen, O.; Becker, T.; Schulten, K.; et al. Cryo-EM Structure of the Ribosome–SecYE Complex in the Membrane Environment. *Nat. Struct. Mol. Biol.* **2011**, *18* (5), 614–621. https://doi.org/10.1038/nsmb.2026.
(186) Gao, Y.; Cao, E.; Julius, D.; Cheng, Y. TRPV1 Structures in Nanodiscs Reveal Mechanisms of Ligand and Lipid Action. *Nature* **2016**, *534* (7607), 347–351. https://doi.org/10.1038/nature17964.
(187) Jin, P.; Bulkley, D.; Guo, Y.; Zhang, W.; Guo, Z.; Huynh, W.; Wu, S.; Meltzer, S.; Cheng, T.; Jan, L. Y.; et al. Electron Cryo-Microscopy Structure of the Mechanotransduction Channel NOMPC. *Nature* **2017**, *547* (7661), 118–122. https://doi.org/10.1038/nature22981.
(188) Roh, S.-H.; Stam, N. J.; Hryc, C. F.; Couoh-Cardel, S.; Pintilie, G.; Chiu, W.; Wilkens, S. The 3.5-Å CryoEM Structure of Nanodisc-Reconstituted Yeast Vacuolar ATPase Vo Proton Channel. *Mol. Cell* **2018**, *69* (6), 993-1004.e3. https://doi.org/10.1016/j.molcel.2018.02.006.

(189) Nikolaev, M.; Round, E.; Gushchin, I.; Polovinkin, V.; Balandin, T.; Kuzmichev, P.; Shevchenko, V.; Borshchevskiy, V.; Kuklin, A.; Round, A.; et al. Integral Membrane Proteins Can Be Crystallized Directly from Nanodiscs. *Cryst. Growth Des.* **2017**, *17* (3), 945–948. https://doi.org/10.1021/acs.cgd.6b01631.

(190) McLean, M. A.; Gregory, M. C.; Sligar, S. G. Nanodiscs: A Controlled Bilayer Surface for the Study of Membrane Proteins. *Annu. Rev. Biophys.* **2018**, *47* (1), 107–124. https://doi.org/10.1146/annurev-biophys-070816-033620.

(191) Ye, X.; McLean, M. A.; Sligar, S. G. Conformational Equilibrium of Talin Is Regulated by Anionic Lipids. *Biochim. Biophys. Acta BBA - Biomembr.* **2016**, *1858* (8), 1833–1840. https://doi.org/10.1016/j.bbamem.2016.05.005.

(192) Viennet, T.; Wördehoff, M. M.; Uluca, B.; Poojari, C.; Shaykhalishahi, H.; Willbold, D.; Strodel, B.; Heise, H.; Buell, A. K.; Hoyer, W.; et al. Structural Insights from Lipid-Bilayer Nanodiscs Link α-Synuclein Membrane-Binding Modes to Amyloid Fibril Formation. *Commun. Biol.* **2018**, *1* (1), 44. https://doi.org/10.1038/s42003-018-0049-z.

(193) Mazhab-Jafari, M. T.; Marshall, C. B.; Smith, M. J.; Gasmi-Seabrook, G. M. C.; Stathopulos, P. B.; Inagaki, F.; Kay, L. E.; Neel, B. G.; Ikura, M. Oncogenic and RASopathy-Associated K-RAS Mutations Relieve Membrane-Dependent Occlusion of the Effector-Binding Site. *Proc. Natl. Acad. Sci.* **2015**, *112* (21), 6625–6630. https://doi.org/10.1073/pnas.1419895112.

(194) Miyazaki, M.; Nakano, M.; Fukuda, M.; Handa, T. Smaller Discoidal High-Density Lipoprotein Particles Form Saddle Surfaces, but Not Planar Bilayers. *Biochemistry* **2009**, *48* (32), 7756–7763. https://doi.org/10.1021/bi900785x.

(195) Knowles, T. J.; Finka, R.; Smith, C.; Lin, Y.-P.; Dafforn, T.; Overduin, M. Membrane Proteins Solubilized Intact in Lipid Containing Nanoparticles Bounded by Styrene Maleic Acid Copolymer. *J. Am. Chem. Soc.* **2009**, *131* (22), 7484–7485. https://doi.org/10.1021/ja810046q.

(196) Lee, S. C.; Knowles, T. J.; Postis, V. L. G.; Jamshad, M.; Parslow, R. A.; Lin, Y.-P.; Goldman, A.; Sridhar, P.; Overduin, M.; Muench, S. P.; et al. A Method for Detergent-Free Isolation of Membrane Proteins in Their Local Lipid Environment. *Nat. Protoc.* **2016**, *11* (7), 1149–1162. https://doi.org/10.1038/nprot.2016.070.

(197) Jamshad, M.; Lin, Y.-P.; Knowles, T. J.; Parslow, R. A.; Harris, C.; Wheatley, M.; Poyner, D. R.; Bill, R. M.; Thomas, O. R. T.; Overduin, M.; et al. Surfactant-Free Purification of Membrane Proteins with Intact Native Membrane Environment. *Biochem. Soc. Trans.* **2011**, *39* (3), 813–818. https://doi.org/10.1042/BST0390813.

(198) Long, A. R.; O'Brien, C. C.; Malhotra, K.; Schwall, C. T.; Albert, A. D.; Watts, A.; Alder, N. N. A Detergent-Free Strategy for the Reconstitution of Active Enzyme Complexes from Native Biological Membranes into Nanoscale Discs. *BMC Biotechnol.* **2013**, *13*, 41. https://doi.org/10.1186/1472-6750-13-41.

(199) Paulin, S.; Jamshad, M.; Dafforn, T. R.; Garcia-Lara, J.; Foster, S. J.; Galley, N. F.; Roper, D. I.; Rosado, H.; Taylor, P. W. Surfactant-Free Purification of Membrane Protein Complexes from Bacteria: Application to the Staphylococcal Penicillin-Binding Protein Complex PBP2/PBP2a. *Nanotechnology* **2014**, *25* (28), 285101. https://doi.org/10.1088/0957-4484/25/28/285101.

(200) Routledge, S. J.; Mikaliunaite, L.; Patel, A.; Clare, M.; Cartwright, S. P.; Bawa, Z.; Wilks, M. D. B.; Low, F.; Hardy, D.; Rothnie, A. J.; et al. The Synthesis of Recombinant Membrane Proteins in Yeast for Structural Studies. *Methods* **2016**, *95*, 26–37. https://doi.org/10.1016/j.ymeth.2015.09.027.

(201) Swainsbury, D. J. K.; Scheidelaar, S.; van Grondelle, R.; Killian, J. A.; Jones, M. R. Bacterial Reaction Centers Purified with Styrene Maleic Acid Copolymer Retain Native Membrane Functional Properties and Display Enhanced Stability. *Angew. Chem. Int. Ed Engl.* **2014**, *53* (44), 11803–11807. https://doi.org/10.1002/anie.201406412.

(202) Prabudiansyah, I.; Kusters, I.; Caforio, A.; Driessen, A. J. M. Characterization of the Annular Lipid Shell of the Sec Translocon. *Biochim. Biophys. Acta* **2015**, *1848* (10 Pt A), 2050–2056. https://doi.org/10.1016/j.bbamem.2015.06.024.

(203) Jamshad, M.; Charlton, J.; Lin, Y.-P.; Routledge, S. J.; Bawa, Z.; Knowles, T. J.; Overduin, M.; Dekker, N.; Dafforn, T. R.; Bill, R. M.; et al. G-Protein Coupled Receptor Solubilization and

Purification for Biophysical Analysis and Functional Studies, in the Total Absence of Detergent. *Biosci. Rep.* **2015**, *35* (2), e00188. https://doi.org/10.1042/BSR20140171.

(204) Parmar, M.; Rawson, S.; Scarff, C. A.; Goldman, A.; Dafforn, T. R.; Muench, S. P.; Postis, V. L. G. Using a SMALP Platform to Determine a Sub-Nm Single Particle Cryo-EM Membrane Protein Structure. *Biochim. Biophys. Acta BBA - Biomembr.* **2018**, *1860* (2), 378–383. https://doi.org/10.1016/j.bbamem.2017.10.005.

(205) Sun, C.; Benlekbir, S.; Venkatakrishnan, P.; Wang, Y.; Hong, S.; Hosler, J.; Tajkhorshid, E.; Rubinstein, J. L.; Gennis, R. B. Structure of the Alternative Complex III in a Supercomplex with Cytochrome Oxidase. *Nature* **2018**, *557* (7703), 123–126. https://doi.org/10.1038/s41586-018-0061-y.

(206) Bersch, B.; Dörr, J. M.; Hessel, A.; Killian, J. A.; Schanda, P. Proton-Detected Solid-State NMR Spectroscopy of a Zinc Diffusion Facilitator Protein in Native Nanodiscs. *Angew. Chem. Int. Ed Engl.* **2017**, *56* (9), 2508–2512. https://doi.org/10.1002/anie.201610441.

(207) Broecker, J.; Eger, B. T.; Ernst, O. P. Crystallogenesis of Membrane Proteins Mediated by Polymer-Bounded Lipid Nanodiscs. *Structure* **2017**, *25* (2), 384–392. https://doi.org/10.1016/j.str.2016.12.004.

(208) Jamshad, M.; Grimard, V.; Idini, I.; Knowles, T. J.; Dowle, M. R.; Schofield, N.; Sridhar, P.; Lin, Y.; Finka, R.; Wheatley, M.; et al. Structural Analysis of a Nanoparticle Containing a Lipid Bilayer Used for Detergent-Free Extraction of Membrane Proteins. *Nano Res.* **2015**, *8* (3), 774–789. https://doi.org/10.1007/s12274-014-0560-6.

(209) Kučerka, N.; Liu, Y.; Chu, N.; Petrache, H. I.; Tristram-Nagle, S.; Nagle, J. F. Structure of Fully Hydrated Fluid Phase DMPC and DLPC Lipid Bilayers Using X-Ray Scattering from Oriented Multilamellar Arrays and from Unilamellar Vesicles. *Biophys. J.* **2005**, *88* (4), 2626–2637. https://doi.org/10.1529/biophysj.104.056606.

(210) Scheidelaar, S.; Koorengevel, M. C.; Pardo, J. D.; Meeldijk, J. D.; Breukink, E.; Killian, J. A. Molecular Model for the Solubilization of Membranes into Nanodisks by Styrene Maleic Acid Copolymers. *Biophys. J.* **2015**, *108* (2), 279–290. https://doi.org/10.1016/j.bpj.2014.11.3464.

(211) Dominguez Pardo, J. J.; Dörr, J. M.; Iyer, A.; Cox, R. C.; Scheidelaar, S.; Koorengevel, M. C.; Subramaniam, V.; Killian, J. A. Solubilization of Lipids and Lipid Phases by the Styrene-Maleic Acid Copolymer. *Eur. Biophys. J. EBJ* **2017**, *46* (1), 91–101. https://doi.org/10.1007/s00249-016-1181-7.

(212) Xue, M.; Cheng, L.; Faustino, I.; Guo, W.; Marrink, S. J. Molecular Mechanism of Lipid Nanodisk Formation by Styrene-Maleic Acid Copolymers. *Biophys. J.* **2018**. https://doi.org/10.1016/j.bpj.2018.06.018.

(213) Vargas, C.; Arenas, R. C.; Frotscher, E.; Keller, S. Nanoparticle Self-Assembly in Mixtures of Phospholipids with Styrene/Maleic Acid Copolymers or Fluorinated Surfactants. *Nanoscale* **2015**, *7* (48), 20685–20696. https://doi.org/10.1039/c5nr06353a.

(214) Cuevas Arenas, R.; Klingler, J.; Vargas, C.; Keller, S. Influence of Lipid Bilayer Properties on Nanodisc Formation Mediated by Styrene/Maleic Acid Copolymers. *Nanoscale* **2016**, *8* (32), 15016–15026. https://doi.org/10.1039/c6nr02089e.

(215) Hazell, G.; Arnold, T.; Barker, R. D.; Clifton, L. A.; Steinke, N.-J.; Tognoloni, C.; Edler, K. J. Evidence of Lipid Exchange in Styrene Maleic Acid Lipid Particle (SMALP) Nanodisc Systems. *Langmuir* **2016**, *32* (45), 11845–11853. https://doi.org/10.1021/acs.langmuir.6b02927.

(216) Cuevas Arenas, R.; Danielczak, B.; Martel, A.; Porcar, L.; Breyton, C.; Ebel, C.; Keller, S. Fast Collisional Lipid Transfer Among Polymer-Bounded Nanodiscs. *Sci. Rep.* **2017**, *7*, 45875. https://doi.org/10.1038/srep45875.

(217) Grethen, A.; Glueck, D.; Keller, S. Role of Coulombic Repulsion in Collisional Lipid Transfer Among SMA(2:1)-Bounded Nanodiscs. *J. Membr. Biol.* **2018**, *251* (3), 443–451. https://doi.org/10.1007/s00232-018-0024-0.

(218) Grethen, A.; Oluwole, A. O.; Danielczak, B.; Vargas, C.; Keller, S. Thermodynamics of Nanodisc Formation Mediated by Styrene/Maleic Acid (2:1) Copolymer. *Sci. Rep.* **2017**, *7* (1), 11517. https://doi.org/10.1038/s41598-017-11616-z.

(219) Dominguez Pardo, J. J.; Dörr, J. M.; Renne, M. F.; Ould-Braham, T.; Koorengevel, M. C.; van Steenbergen, M. J.; Killian, J. A. Thermotropic Properties of Phosphatidylcholine Nanodiscs Bounded by Styrene-Maleic Acid Copolymers. *Chem. Phys. Lipids* **2017**, *208*, 58–64. https://doi.org/10.1016/j.chemphyslip.2017.08.010.

(220) Scheidelaar, S.; Koorengevel, M. C.; van Walree, C. A.; Dominguez, J. J.; Dörr, J. M.; Killian, J. A. Effect of Polymer Composition and PH on Membrane Solubilization by Styrene-Maleic Acid Copolymers. *Biophys. J.* **2016**, *111* (9), 1974–1986. https://doi.org/10.1016/j.bpj.2016.09.025.

(221) Morrison, K. A.; Akram, A.; Mathews, A.; Khan, Z. A.; Patel, J. H.; Zhou, C.; Hardy, D. J.; Moore-Kelly, C.; Patel, R.; Odiba, V.; et al. Membrane Protein Extraction and Purification Using Styrene-Maleic Acid (SMA) Copolymer: Effect of Variations in Polymer Structure. *Biochem. J.* **2016**, *473* (23), 4349–4360. https://doi.org/10.1042/BCJ20160723.

(222) Dörr, J. M.; Scheidelaar, S.; Koorengevel, M. C.; Dominguez, J. J.; Schäfer, M.; van Walree, C. A.; Killian, J. A. The Styrene–Maleic Acid Copolymer: A Versatile Tool in Membrane Research. *Eur. Biophys. J.* **2016**, *45*, 3–21. https://doi.org/10.1007/s00249-015-1093-y.

(223) Perrier, S. 50th Anniversary Perspective: RAFT Polymerization—A User Guide. *Macromolecules* **2017**, *50* (19), 7433–7447. https://doi.org/10.1021/acs.macromol.7b00767.

(224) Smith, A. A. A.; Autzen, H. E.; Laursen, T.; Wu, V.; Yen, M.; Hall, A.; Hansen, S. D.; Cheng, Y.; Xu, T. Controlling Styrene Maleic Acid Lipid Particles through RAFT. *Biomacromolecules* **2017**, *18* (11), 3706–2713. https://doi.org/10.1021/acs.biomac.7b01136.

(225) Craig, A. F.; Clark, E. E.; Sahu, I. D.; Zhang, R.; Frantz, N. D.; Al-Abdul-Wahid, M. S.; Dabney-Smith, C.; Konkolewicz, D.; Lorigan, G. A. Tuning the Size of Styrene-Maleic Acid Copolymer-Lipid Nanoparticles (SMALPs) Using RAFT Polymerization for Biophysical Studies. *Biochim. Biophys. Acta BBA - Biomembr.* **2016**, *1858* (11), 2931–2939. https://doi.org/10.1016/j.bbamem.2016.08.004.

(226) Lindhoud, S.; Carvalho, V.; Pronk, J. W.; Aubin-Tam, M.-E. SMA-SH: Modified Styrene-Maleic Acid Copolymer for Functionalization of Lipid Nanodiscs. *Biomacromolecules* **2016**, *17* (4), 1516–1522. https://doi.org/10.1021/acs.biomac.6b00140.

(227) Schmidt, V.; Sturgis, J. N. Modifying Styrene-Maleic Acid Co-Polymer for Studying Lipid Nanodiscs. *Biochim. Biophys. Acta BBA - Biomembr.* **2018**, *1860* (3), 777–783. https://doi.org/10.1016/j.bbamem.2017.12.012.

(228) Ravula Thirupathi; Ramadugu Sudheer Kumar; Di Mauro Giacomo; Ramamoorthy Ayyalusamy. Bioinspired, Size-Tunable Self-Assembly of Polymer–Lipid Bilayer Nanodiscs. *Angew. Chem. Int. Ed.* **2017**, *56* (38), 11466–11470. https://doi.org/10.1002/anie.201705569.

(229) Ravula, T.; Hardin, N. Z.; Ramadugu, S. K.; Ramamoorthy, A. PH Tunable and Divalent Metal Ion Tolerant Polymer Lipid Nanodiscs. *Langmuir* **2017**, *33* (40), 10655–10662. https://doi.org/10.1021/acs.langmuir.7b02887.

(230) Ravula, T.; Hardin, N. Z.; Ramadugu, S. K.; Cox, S. J.; Ramamoorthy, A. Formation of PH-Resistant Monodispersed Polymer-Lipid Nanodiscs. *Angew. Chem. Int. Ed Engl.* **2018**, *57* (5), 1342–1345. https://doi.org/10.1002/anie.201712017.

(231) Ramadugu, V. S. K.; Mauro, G. M. D.; Ravula, T.; Ramamoorthy, A. Polymer Nanodiscs and Macro-Nanodiscs of a Varying Lipid Composition. *Chem. Commun.* **2017**, *53* (78), 10824–10826. https://doi.org/10.1039/C7CC06409H.

(232) Ravula, T.; Hardin, N. Z.; Bai, J.; Im, S.-C.; Waskell, L.; Ramamoorthy, A. Effect of Polymer Charge on Functional Reconstitution of Membrane Proteins in Polymer Nanodiscs. *Chem. Commun.* **2018**, *54* (69), 9615–9618. https://doi.org/10.1039/C8CC04184A.

(233) Oluwole, A. O.; Danielczak, B.; Meister, A.; Babalola, J. O.; Vargas, C.; Keller, S. Solubilization of Membrane Proteins into Functional Lipid-Bilayer Nanodiscs Using a Diisobutylene/Maleic Acid Copolymer. *Angew. Chem. Int. Ed Engl.* **2017**, *56* (7), 1919–1924. https://doi.org/10.1002/anie.201610778.

(234) Oluwole, A. O.; Klingler, J.; Danielczak, B.; Babalola, J. O.; Vargas, C.; Pabst, G.; Keller, S. Formation of Lipid-Bilayer Nanodiscs by Diisobutylene/Maleic Acid (DIBMA) Copolymer. *Langmuir* **2017**, *33* (50), 14378–14388. https://doi.org/10.1021/acs.langmuir.7b03742.

(235) Yasuhara, K.; Arakida, J.; Ravula, T.; Ramadugu, S. K.; Sahoo, B.; Kikuchi, J.; Ramamoorthy, A. Spontaneous Lipid Nanodisc Fomation by Amphiphilic Polymethacrylate Copolymers. *J. Am. Chem. Soc.* **2017**, *139* (51), 18657–18663. https://doi.org/10.1021/jacs.7b10591.

CHAPTER 2

INFLUENCE OF POLY(STYRENE-*CO*-MALEIC ACID) COPOLYMER STRUCTURE ON THE PROPERTIES AND SELF-ASSEMBLY OF SMALP NANODISCS

Published Article

Stephen C.L. Hall[†‡], Cecilia Tognoloni[§,‖], Gareth J. Price[§], Bert Klumperman[Δ], Karen J. Edler[§], Tim R. Dafforn[†] and Thomas Arnold[‡]

Biomacromolecules, **2018**, 19 (3), pp 761–762
DOI: 10.1021/acs.biomac.7b01539

† School of Biosciences, University of Birmingham, Edgbaston, Birmingham, B15 2TT, UK

‡ Diamond Light Source, Harwell Science and Innovation Campus, Didcot, OX11 ODE, UK

§ Department of Chemistry, University of Bath, Claverton Down, Bath, BA2 7AY, UK

‖ ISIS Neutron and Muon Source, Science and Technology Facilities Council Rutherford Appleton Laboratory, Harwell, Didcot, OX11 0QX, UK

Δ Department of Chemistry and Polymer Science, Division of Polymer Science, Stellenbosch University, De Beers Street, Stellenbosch 7600, South Africa

Author contribution statement

S.C.L.H conceived and designed the study, prepared the samples, performed the experiments (unless otherwise stated), analysed and interpreted the data, prepared and edited the manuscript. C.T synthesized the altSMA used within this study and confirmed synthesis by ^{1}H-NMR spectroscopy. G.J.P and B.K assisted in altSMA synthesis and edited the manuscript. K.J.E conceived the study, edited the manuscript and supervised C.T. T.R.D and T.A conceived the study, interpreted the data, edited the manuscript and supervised S.C.L.H.

Signed:

Stephen Hall

Thomas Arnold

2.1 ABSTRACT

Polymer stabilized nanodiscs are self-assembled structures composed of a polymer belt that wraps around a segment of lipid bilayer, and as such are capable of encapsulating membrane proteins directly from the cell membrane. To date, most studies on these nanodiscs have used poly(styrene-*co*-maleic acid) (SMA) with the term SMA-lipid particles (SMALPs) coined to describe them. In this study, we have determined the physical and thermodynamic properties of such nanodiscs made with two different SMA copolymers. These include a widely used and commercially available statistical poly(styrene-*co*-maleic acid) copolymer (coSMA) and a RAFT-synthesized copolymer with narrow molecular weight distribution and alternating styrene and maleic acid groups with a polystyrene tail, (altSMA). We define phase diagrams for each polymer, and show that, regardless of polymer topological structure, self-assembly is driven by the free energy change associated with the polymers. We also show that nanodisc size is polymer dependent, but can be modified by varying polymer concentration. The thermal stability of each nanodisc type is similar and both can effectively solubilize proteins from the *E. coli* membrane. These data show the potential for the development of different SMA polymers with controllable properties to produce nanodiscs that can be optimized for specific applications and will enable more optimized and widespread use of the SMA-based nanodiscs in membrane protein research.

2.1 INTRODUCTION

With the ever increasing interest in biological membrane research, there is a need for appropriate model systems to study these large, multi-component, dynamic systems without perturbing the very properties that make biological membranes so essential and fascinating. Membrane proteins represent around 30% of the proteome [1–3] and constitute > 70% of therapeutic targets [4]. While knowledge of membrane proteins has been increasing [5–7], there is still a limited amount of structural and functional information available compared to soluble proteins, largely due to their inherent insolubility and instability in aqueous media. One traditional strategy in membrane research is the use of detergents to aid solubilization. They replace the lipid annulus around the hydrophobic core to solubilize the protein inside a detergent micelle, whilst keeping it relatively stable so that structural and functional information can be obtained [8,9]. The principal problem with these methods is that detergents are a poor replacement for lipids [10]. Recent work has shown that the lipid annulus can have specific interactions with the membrane protein and has roles in stability and function of many transmembrane proteins[11,12]. While a detergent is amphipathic like a phospholipid, it lacks the specific chemical moieties which interact with the protein of interest.

Attempts to overcome these problems led to the development of membrane mimetic systems such as amphipols, bicelles and nanodiscs (for more information, see [13]). Nanodiscs are self-assembled structures comprising a planar 'disc' shaped segment of phospholipid bilayer which is stabilized by a surrounding protein or polymer belt. The first nanodiscs were formed by the amphipathic membrane scaffold protein (MSP) which wraps around the hydrophobic lipid tails to stabilize the nanodisc structure [14]. These MSP-nanodiscs have proven effective in membrane protein solubilization [15] and have been amenable to structural studies using a range of techniques [16–22]. However, while the protein is kept in a stable environment, the production of MSP-nanodiscs requires the protein first to be extracted within a detergent micelle and then reconstituted into a nanodisc.

Polymer-stabilized nanodiscs, commonly termed (SMA) lipid particles (SMALPs) use the amphipathic poly(styrene-*co*-maleic acid) SMA copolymer (Figure 2.1a) to wrap around the lipid tails

to stabilize the lipids within a nanodisc structure. The SMA copolymer has statistically arranged styrene and maleic acid groups which are thought to self-assemble into nanodisc structures by intercalating the planar styrene rings into the lipid tails (perpendicular to the plane of the bilayer, analogous to the incorporation of cholesterol into a lipid bilayer) with the maleic acid groups allowing solubilization through hydrogen bonding and ionic interactions with the aqueous solvent [23]. SMALPs have the advantage over MSP-nanodiscs that the protein can be extracted straight from the native membrane by SMA, without having to be reconstituted into a detergent micelle thus keeping the essential lipid annulus present [24–31]. Since their discovery SMALPs have also proven to be effective in structural studies of membrane proteins utilizing techniques such as circular dichroism, analytical ultracentrifugation, electron microscopy, solid state NMR spectroscopy and X-ray crystallography [24,32–34]. SMALPs have also been shown to maintain both the structural stability and function of the encapsulated membrane proteins far more effectively than detergent alternatives [26]. Studies have also shown that the local environment within a SMALP is very similar in terms of physical properties to the native environment of the membrane proteins [35].

Recent work investigating the thermodynamic properties of the statistical SMA(3:1) polymer (with a styrene:maleic acid ratio of 3:1) and its assembly into nanodiscs has shown that the phase behavior of the solubilization can be approximated by a pseudophase model [36] (Figure 2.1b). Traditionally, the pseudophase model has been used to characterize the solubilization of phospholipids by surfactants [36,37]. When applied to SMA, the pseudophase model shows that upon increasing the concentration of SMA at a fixed concentration of lipid vesicles, three ranges can be identified: the bilayer range, the coexistence range and the micellar range (in the case of solubilization by SMA, the nanodisc range). The boundaries between these ranges are termed the saturation (SAT) and solubilization (SOL) boundaries. To allow comparison between SMA and classical surfactants, SAT and SOL boundaries can be expressed in terms of the molar ratio of surfactant to lipid at the phase boundary: $R_S^{b,SAT}$ and $R_S^{m,SOL}$ respectively (representing the gradient of the phase boundary line) [38]. From these values the Gibbs free energy change

for the vesicle to nanodisc transition for lipids, $\Delta G_{Lipid}^{b\rightarrow m,0}$, and for the solution to nanodisc transition for polymer, $\Delta G_{Polymer}^{b\rightarrow m,0}$ can be calculated.

Since the first use of an SMA polymer (SMA2000, with a 2:1 ratio of S:MA) in membrane protein isolation[39], a number of other SMA polymers have been shown to be effective in membrane solubilization [40,36,41–43]. These polymers have utilized different S:MA ratios and chain lengths. A recent side-by-side comparison of membrane protein solubilization by a number of these polymers has shown that their effectiveness varies significantly with the most effective remaining the original SMA2000 2:1 ratio polymer [43].

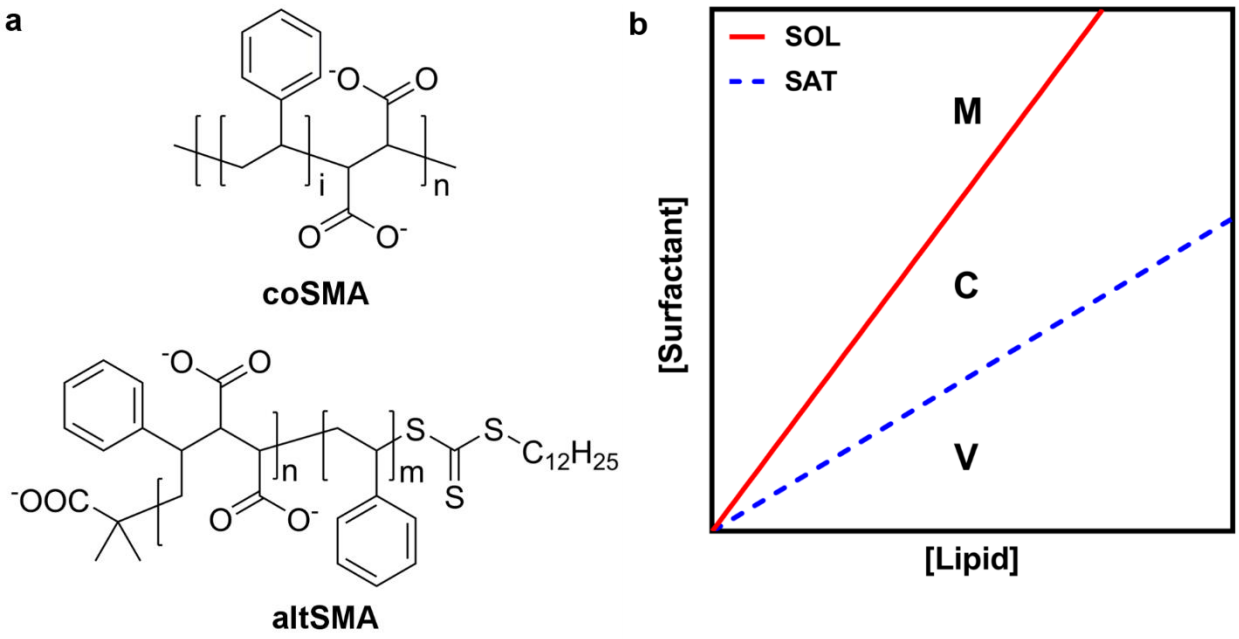

Figure 2.1. a. Structures of coSMA, where on average <i> = 2, corresponding to the 2:1 ratio of styrene to maleic acid, and altSMA. The altSMA has an overall 2:1 ratio of styrene to maleic acid, but comprises a block of alternating S – MA with the excess styrene forming a polystyrene tail which is terminated by the DDMAT RAFT agent. b. A model phase diagram schematic for a generic surfactant solubilizing a lipid, which we have applied to SMA solubilizing lipids into nanodiscs. At low surfactant concentrations, all the lipid exists in the bilayer phase as vesicles (V).

In addition to effectiveness in membrane protein solubilization, thermodynamic studies of the solubilization of DMPC and POPC large unilamellar vesicles (LUVs) by an SMA(2:1) polymer have been reported [44]. These results demonstrated that this SMA(2:1) (Tradename Xiran SZ30010) is more efficient in membrane solubilization than the SMA(3:1) and this efficiency increases with increasing pH. These data, in combination with other studies [45,46], have led to the emergence of SMA(2:1) polymers as the most effective solubilizer of membranes and membrane proteins.

In this work we have therefore determined phase diagrams for the solubilization of DMPC vesicles using the acid forms of two SMA(2:1) polymers of differing chain length and chain topology, to investigate the effect of polymer structural properties on phospholipid solubilization. We compare the acid form of the commercially available and frequently utilized SMA2000 and a 2:1 SMA polymer synthesized using reversible addition-fragmentation chain transfer (RAFT) polymerization. RAFT-synthesized SMA has recently been shown to form nanodiscs with tunable properties based on the high degree of control over the polymerization that RAFT offers [41]. While SMA2000 is a statistical copolymer, RAFT-SMA has an alternating styrene-maleic acid block with the styrene excess forming a polystyrene tail terminating in the RAFT agent. This diblock approximation has however been shown to be an oversimplification of the RAFT-polymer structure. In reality, RAFT-synthesized SMA will display a gradient from alternating styrene-maleic acid towards polystyrene along the length of the polymer chain [47]. The polymers herein will be referred to as coSMA (SMA2000, acid form) and altSMA (RAFT-SMA, acid form). In addition to topological differences, these polymers also exhibit differences in chain length distribution to each other and to the Xiran SZ30010 SMA(2:1) studied by others. Here we have characterized the self-assembly and properties of SMALPs formed by coSMA and altSMA and compared to those formed by Xiran SZ30010 (as studied by others) in order to understand the factors that define the function of these materials.

Finally, we have confirmed that both polymers effectively solubilize membrane proteins directly from the *E. coli* cell membrane and assessed their performance in this regard relative to each other and to commonly used detergent alternatives.

2.2 MATERIALS AND METHODS

2.2.1 Materials

Figure 2.1a shows the structure of SMA2000 at pH 8.0 (poly(styrene-*co*-maleic acid)), purchased from Cray Valley (UK) as poly(styrene-*co*-maleic anhydride) (coSMAnh). All buffer components, chloroform and 1,2-dimyristoyl-***sn***-glycero-3-phosphocholine (DMPC) were purchased from Sigma-Aldrich (UK) at >98% purity and used without further purification.

2.2.2 Methods

2.2.2.1 Synthesis of altSMAnh

altSMAnh with a styrene:maleic anhydride ratio of 2:1, and a molar mass of 6 kDa was synthesized using reversible addition-fragmentation chain-transfer (RAFT) polymerization as described by Harrisson and Wooley [48]. altSMA was synthesized in one step by mixing initial reagents of styrene and maleic anhydride in a 2.34:1 ratio. Specifically, 1.0 g (9.6 mmol) styrene and 0.404 g maleic anhydride (4.1 mmol) were added in a molar ratio of 2.34:1 with 4.8 mg (0.03 mmol) azobisisobutyronitrile (AIBN) and 72.2 mg (0.20 mmol) 2-(dodecylthiocarbonothioylthio)-2-methylpropionic acid (DDMAT) were mixed in 4.4 mL 1,4-dioxane and degassed by three freeze-pump-thaw cycles. The flask was slightly over pressured with nitrogen and maintained at 60°C for 20 hours. The viscous solution obtained was diluted in a minimal volume of tetrahydrofuran (THF) and precipitated in diethyl ether before recovery by filtration. The redissolution and precipitation procedure was repeated three times and the resulting copolymer dried at 70°C for 16 hours. The molecular weight distribution was measured by size exclusion chromatography (Appendix A, Figure A.1) and styrene:maleic anhydride ratio determined by NMR spectroscopy (Appendix A, Figure A.2).

2.2.2.2 Nanodisc preparation

coSMAnh and altSMAnh copolymers were hydrolyzed from the anhydride to the acid forms using a previously published procedure [24]. For a complete description, refer to the supporting information.

Nanodiscs were prepared essentially as previously described [35]. In brief, DMPC was dissolved in chloroform and dried under nitrogen to create a multilamellar lipid film on the surface of the glass vial. Trace solvent was removed by placing overnight in a desiccator attached to a vacuum pump. DMPC was re-suspended in 50 mM sodium phosphate pH 8 containing 200 mM NaCl to the required concentration for titration and concentration dependent experiments. Suspensions were sonicated for 30 minutes in a water bath at 35°C to form small unilamellar vesicles (SUVs - presence confirmed by dynamic light scattering). DMPC SUV suspensions were kept at room temperature and used within 3 days.

The molecular weight averaged molar mass (M_w) and number average molar mass (M_n) of the copolymers used in this study are shown in Table 2.1. We assume no changes of molecular weight on hydrolysis. Copolymer stock solutions were made in 50 mM sodium phosphate, 200 mM NaCl pH 8 to the required molar concentration required for titration experiments (calculated using the M_n value) or to 3 % (w/v) if being used to make nanodiscs at excess copolymer concentration.

Nanodiscs were made by mixing 10 mg/mL DMPC suspension and 3% (w/v) copolymer solutions (or as required for titration and concentration dependent experiments) in a 1:1 ratio at room temperature. Nanodiscs were left at 25°C for at least 24 hours to equilibrate before use. For temperature stability experiments and freeze-thaw stability experiments, the resultant nanodiscs were purified using a Superdex S200 16/600 size exclusion chromatography column to remove large aggregates and excess polymer. Purified nanodiscs were concentrated using a 10 kDa MWCO spin concentrator to a copolymer concentration of 1.5 % (w/v) determined by constructing a calibration curve of UV-absorbance at 254 nm for polymer solutions of known concentration.

Table 2.1. Thermodynamic values obtained for coSMA and altSMA compared to SMA(3:1) and SMA(2:1) (Xiran SZ30010) mediated phospholipid nanodisc self-assembly.

	coSMA (SMA2000)	**altSMA**	**SMA(2:1) (Xiran SZ30010)** [44]	**SMA(3:1) (Xiran SL25010 S25)** [49]
M_w (kg·mol^{-1})	7.50	6.85	6.50	10.00
M_n (kg·mol^{-1})	3.00	6.00	2.70	4.00
$R_S^{b,SAT}$	0.050 ± 0.003	0.024 ± 0.002	0.087 ± 0.006	0.078 ± 0.002
$R_S^{m,SOL}$	0.133 ± 0.004	0.137 ± 0.007	0.130 ± 0.004	0.144 ± 0.001
$\Delta G_{Lipid}^{b\rightarrow m,0}$ **(kJ·mol^{-1})**	+0.19 ± 0.06	+0.26 ± 0.08	+0.10 ± 0.02	+0.15 ± 0.05
$\Delta G_{Polymer}^{b\rightarrow m,0}$ **(kJ·mol^{-1})**	-2.23 ± 0.08	-4.11 ± 0.11	-0.91 ± 0.23	-1.36 ± 0.45

2.2.2.3 ^{31}P NMR

Lipid-polymer mixtures were prepared as described above with DMPC concentrations of 7.50, 5.00, 2.50 and 1.25 mM. For coSMA and altSMA experiments, instead of phosphate buffer (which would compromise the ^{31}P NMR signal from the lipids), 50 mM Tris pH 8.0, 200 mM NaCl was prepared in D_2O. All ^{31}P NMR experiments were performed using an Avance III 400MHz NMR spectrometer (Bruker, Coventry, UK). Spectra were acquired at 298 K at 161.98 MHz using ^{1}H decoupling. 256 scans were performed per measurement with an acquisition time of 1.022 s over a sweep width of 32051 Hz. A pre-scan delay of 6.5 s, a relaxation delay of 5 s and a pulse width of 7.25 µs was required to observe sufficient signal on which to perform analysis. An external reference of 85% H_3PO_4 in 10% D_2O was measured and set to 0 ppm to correct for any drift of the magnetic field between experiments.

2.2.2.4 ^{31}P NMR data analysis

TopSpin software (Bruker, Coventry, UK) was used to perform peak integration. Absolute integrals were then normalized to the largest and smallest value across all experiments. Peak area data were fitted using least-squares non-linear regression [50]. In order to determine the saturating and solubilizing concentrations of copolymer for a given lipid concentration, fits to the experimental data were performed simultaneously to the following scenario:

$$A({c_S} \leq {c_S}^{SAT}) = 0$$

$$A({c_S}^{SAT} \leq {c_S} \leq {c_S}^{SOL}) = f{c_L} \cdot \frac{{c_S} - {c_S}^{SAT}}{{c_S}^{SOL} - {c_S}^{SAT}}$$

$$A({c_S}^{SOL} \leq {c_S}) = f{c_L}$$

Where A represents peak area and ${c_S}$ is the molar polymer concentration. ${c_S}^{SAT}$ and ${c_S}^{SOL}$ are the saturating and solubilizing concentrations of polymer for a given lipid concentration, ${c_L}$. f is a scaling factor dependent on data acquisition parameters.

Phase diagrams were constructed by plotting ${c_S}^{SAT}$ and ${c_S}^{SOL}$ as lipid concentration versus polymer concentration. Linear regression was performed to fit the following equations to the experimental data:

$${c_S}^{SAT} = {c_S} + \ R_S^{b,SAT}{c_L}$$

$${c_S}^{SOL} = {c_S} + \ R_S^{m,SOL}{c_L}$$

Where $R_S^{b,SAT}$ and $R_S^{m,SOL}$ represent the molar ratios of polymer to lipid at the SAT and SOL phase boundaries respectively. This allows calculation of the partitioning coefficients:

$$K_{Lipid}^{b \to m} = \frac{1 + R_S^{b,SAT}}{1 + R_S^{m,SOL}}$$

$$K_{Polymer}^{b \to m} = K_{Lipid}^{b \to m} \cdot \frac{R_S^{m,SOL}}{R_S^{b,SAT}}$$

for the lipid and polymer, respectively, between the vesicular bilayer phase (b) and the 'micellar' (m) nanodisc phase. From this, the Gibbs free energy for the transfer from vesicular bilayer to nanodisc phase can be calculated for both the lipid:

$$\Delta G_{Lipid}^{b \to m,0} = -RT \cdot ln(K_{Lipid}^{b \to m})$$

And the polymer:

$$\Delta G^{b\rightarrow m,0}_{Polymer} = -RT \cdot ln(K^{b\rightarrow m}_{Polymer})$$

For a more complete theoretical description, see [36].

2.2.2.5 Dynamic Light Scattering

Dynamic light scattering (DLS) experiments were performed with a Zetasizer Nano S (Malvern Instruments, Worcestershire, UK) using a He-Ne laser at 633 nm with a detector angle of 178° relative to the incident beam. Samples were loaded into 45 µL quartz cuvettes with a 3 × 3 mm light path (Hellma Analytics, Müllheim, Germany). All measurements were performed after equilibrating the sample at 25°C for 60 seconds and each sample measured 3 times with the attenuator position automatically optimized for size determination. Each measurement consists of 11 scans of 10 seconds. Samples prepared for the concentration dependence of polymer were left to equilibrate for at least 3 hours before the measurement. Freeze-thaw stability was performed by flash freezing the nanodisc solution in liquid N_2 for 5 min and then thawing at room temperature before being loaded into the cuvette. Temperature stability was performed by increasing the temperature from 4 to 80°C in 1°C increments. Again, each sample was measured three times at each temperature after equilibrating at that temperature for 2 minutes.

2.2.2.6 Size exclusion chromatography with multi-angled light scattering

SEC-MALS experiments were performed using a Superdex 200 increase 10/300 GL size exclusion column attached to an Äkta purification system (GE Healthcare Life Sciences, Buckinghamshire, UK). In line absorbance measurements at 280 and 254 nm were used to calibrate the delay volume between the column and the MALS detector. MALS measurements were performed using a Dawn Helios II (Wyatt Technologies, Suffolk, UK) equipped with a 633 nm He-Ne laser with static light scattering detectors positioned at 18 angles radially about the flow cell. The MALS detector at 110 ° has been replaced with a DLS detector in order to obtain information on the hydrodynamic radius of particles more accurately than using MALS alone. Samples were prepared as described above and centrifuged at

10,000 × *g* for 10 minutes to remove any contaminant particulate matter. 70 µL of each sample was loaded onto the column which was run with a flow rate of 0.7 mL/min.

2.2.2.7 Solubilization of membrane proteins from *E. coli* BL21 (DE3) membranes

Membranes were resuspended to 60 mg/mL in 50 mM Na_2HPO_4, 0.2 M NaCl, 10 % v/v glycerol pH 8 and homogenized. Stocks of 4% (w/v) Triton X-100, 2 % (w/v) DDM, 2 % (w/v) β-OG, 16 mM coSMA and 16 mM altSMA were prepared in 50 mM Na_2HPO_4, 0.2 M NaCl, 10 % v/v glycerol pH 8. Membrane suspensions were mixed 1:1 with detergent or polymer samples and a control was performed where membranes were diluted to 30 mg/mL within the same buffer but no detergent or polymer was added. All samples were incubated for 2 hours (4°C for control and detergent samples, 20°C for polymer samples as per published protocols [24]). Samples were centrifuged at 100,000 × *g* for 45 minutes at 4°C. The supernatant was removed containing the soluble fraction and the insoluble pellet resuspended in an equal volume of the same buffer. Soluble and insoluble fractions were then precipitated by the addition of 25 % (w/v) trichloroacetic acid (TCA). After 10 minutes incubation at 4°C, samples were centrifuged at 14,000 × *g* for 5 minutes to pellet precipitated protein. The protein pellet was washed three times by vortexing in 200 µL ice cold acetone and repeating the centrifugation step. The protein pellet was dried under vacuum for 10 minutes before resuspension in the starting volume of buffer. The samples were analysed by SDS polyacrylamide gel electrophoresis (PAGE) using precast Criterion XT graduated 4 – 12 % acrylamide bis-tris gels (Bio-Rad Laboratorie Ltd., Hertfordshire, UK) using standard procedures and stained overnight using InstantBlue protein stain (Expedeon Ltd., Cambridgeshire, UK).

2.3 RESULTS AND DISCUSSION

2.3.1 Thermodynamics of nanodisc self-assembly

In order to consistently compare measurements of nanodiscs formed from different polymers and lipids using different techniques, a thorough initial characterization of the nanodiscs is required. Vargas *et al.* [36] showed that ^{31}P NMR experiments could be used to determine the phase diagram of SMA(3:1) solubilizing vesicles of 1-palmitoyl-2-oleoyl-*sn*-glycero-3-phosphocholine (POPC). Similar

experiments have also been performed by measuring the solubilization of DMPC vesicles by SMA(3:1) [49] and SMA(2:1) (Xiran SZ30010) [44].

We performed ^{31}P NMR experiments at 298 K to examine the phase diagram of coSMA and altSMA mediated solubilization of fluid phase DMPC small unilamellar vesicles (SUVs). The ^{31}P NMR peak from the phosphate group in DMPC did not broaden beyond detection as it does in the data published in reference 36 (Appendix A, Figure A.4). This is due to the use of SUVs rather than large unilamellar vesicles (LUVs) as in the previous study.

Our data suggest the scenario proposed for the solubilization of POPC or DMPC LUVs by SMA(3:1) [36,49] and SMA(2:1) (Xiran SZ30010) [44] can also explain the solubilization of DMPC SUVs by coSMA and altSMA. At polymer concentrations below c_s^{SAT}, the ^{31}P peak broadens beyond detection as the polymers embed in the vesicular bilayer. The initial decrease in peak area suggests that the rearrangement of SUVs into larger, slower tumbling structures, occurs through individual polymer chains crosslinking vesicles, or polymer chains adsorbing into the vesicular bilayer leading to a swelling of the vesicle. As c_s^{SAT} is surpassed, the polymer molecules are able to initiate the bilayer to nanodisc phase transition. This leads to a sharp, linear increase in ^{31}P NMR peak area as lipids become solubilized into small, fast tumbling nanodiscs. Above c_s^{SOL}, there is sufficient polymer present to solubilize all lipids into nanodiscs, so further increases in peak areas are not observed.

In all experiments, fitting of the ^{31}P peak area yields c_s^{SAT} and c_s^{SOL} values, which are proportional to the DMPC concentration. Therefore, plotting these breakpoints as polymer concentration vs DMPC concentration allows us to obtain phase diagrams (Figure 2.2b, d). From these, we calculated the molar ratios of polymer to lipid at each of the phase boundaries (Table 2.1). coSMA has a noticeably larger $R_S^{b,SAT}$ value (steeper gradient of blue lines in Figure 2.2b) compared to altSMA (Figure 2.2d), indicating that over twice the molar concentration is required to saturate a given quantity of DMPC. In contrast, coSMA and altSMA have almost identical $R_S^{m,SOL}$ values (the gradients of the red lines in Figures 2b & 2d). This means that, although altSMA is more effective at starting the solubilization of DMPC, both polymers ultimately require similar concentrations to achieve complete solubilization. It is

worth noting that all of the values derived for these polymers, including $R_S^{m,SOL}$, are lower than previously determined for SMA(3:1). This means that the statistical SMA(3:1) is less effective in nanodisc self-assembly than both SMA(2:1) polymers investigated. SMA(2:1) Xiran SZ30010 shows very similar molar ratios of polymer to lipid at the solubilization boundary to both coSMA and altSMA. This points at an overriding influence of chemical composition of the SMA copolymers compared to chain topology.

Table 2.1 also shows the Gibbs free energy change for the vesicle to nanodisc transition. In all cases, the relatively large negative free energy change associated with this transition for each polymer indicates that the polymer:lipid complex is significantly thermodynamically favored. It also shows that altSMA exhibits a more negative free-energy change associated with the vesicle to nanodisc transition than coSMA. This is probably due to the topological differences between the polymers. We expect that the hydrophobic polystyrene tail present on altSMA experiences a larger driving force to bury itself in a hydrophobic environment than the statistical ordering of styrene and maleic acid moieties on coSMA.

The RAFT agent used to make this polymer may also have an effect here, although we don't have any data to quantify such an effect. Further, altSMA has a much narrower mass distribution than the commercial copolymers. Therefore, there are far fewer, less thermodynamically favourable small chains present which could account for the larger thermodynamic driving force compared to the commercial copolymers.

The relatively small positive Gibbs energy change for DMPC undergoing the vesicle to nanodisc transition in all cases shows that from the lipids' perspective there is little energetic cost in going from a vesicle into a SMALP and the major driving force for this process is the large gain from the polymer. Comparing this with SMA(3:1) (where DMPC LUVs were solubilized at 30°C) suggests that while DMPC molecules are in a more favorable free-energy environment within SMA(3:1)-SMALPs, the SMA(3:1) polymer has a much smaller thermodynamic driving force for self-assembly into SMALPs.

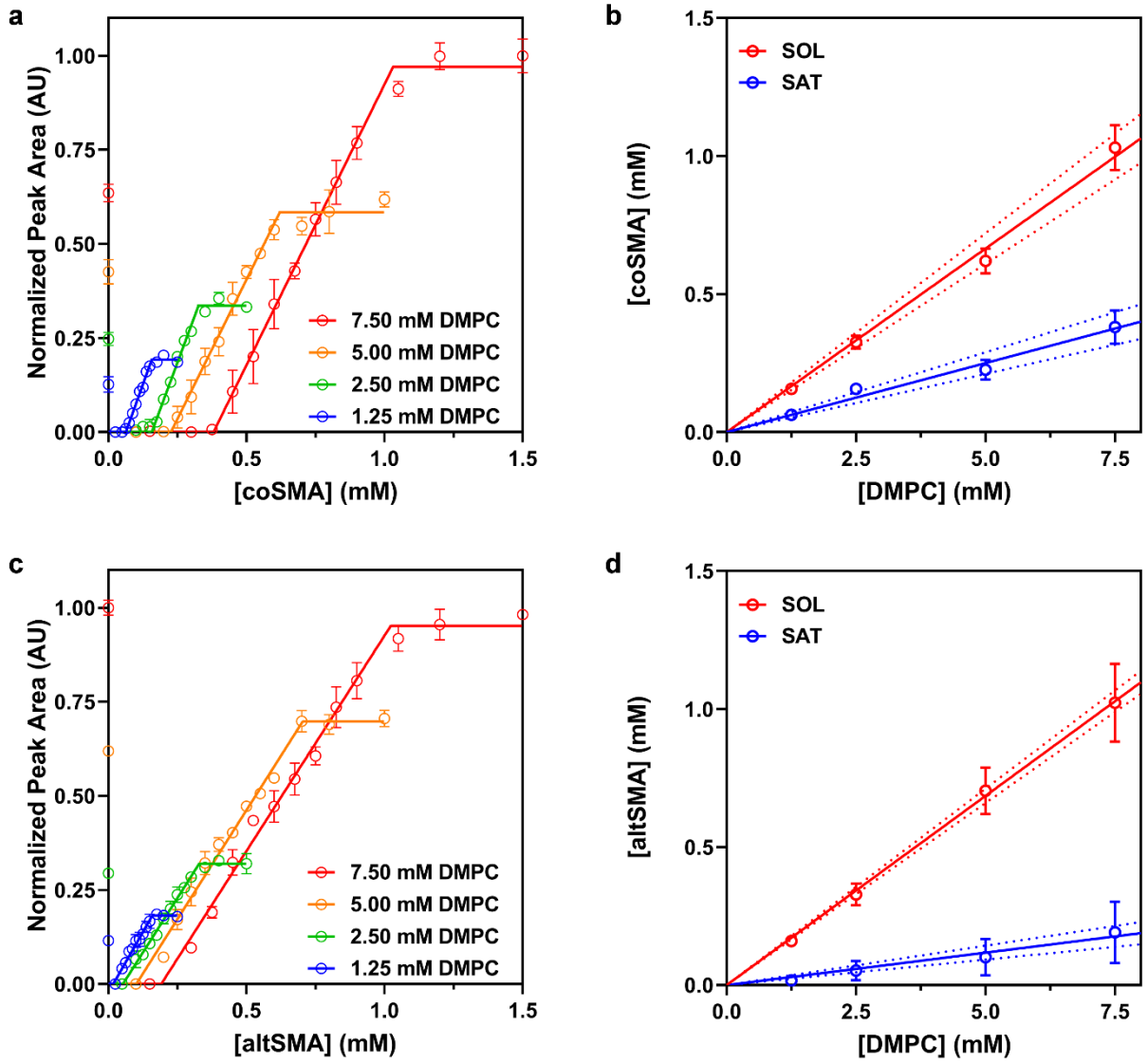

Figure 2.2. ^{31}P NMR Data for coSMA (a, b) and altSMA (c, d) solubilizing DMPC SUVs. **a, c.** Normalized ^{31}P NMR peak area plotted as a function of polymer concentration with corresponding fits to the experimental data to obtain SAT and SOL break points. Each point is the mean of three separate measurements with error bars representing ± 1 standard error. **b, d.** Phase diagrams constructed using SAT and SOL breakpoints determined from **a** and **c**. The SAT boundary is shown as a blue line and the SOL boundary is shown as a red line. Points represent c_s^{SAT} and c_s^{SOL} breakpoints with error bars representing the standard error determined from the fitting procedure in **a** and **c**. Dashed lines represent the 95 % confidence bands associated with linear regression.

It is particularly notable that the magnitude of the free energy change for the two polymers studied here is significantly larger than that seen in previous studies, and particularly in comparison with Xiran SZ30010 (where again, DMPC LUVs were solubilized at 30°C) which has the same ratio of styrene to malic acid. When taking into account the molar mass distributions of the copolymers, Xiran SZ30010 has the smallest M_n and M_w compared to coSMA, altSMA and SMA(3:1), and it is the least thermodynamically efficient polymer of those tested. This points to an interplay between the more efficient 2:1 styrene to maleic acid ratio, and the more thermodynamically effective longer copolymer chains and topologies for optimum phospholipid solubilization. This may explain why in comparisons of SMALP solubilisation effectiveness and downstream stability, coSMA is more effective than other related polymers [43].

2.3.2 Controlling the size of nanodiscs formed by coSMA and altSMA

Next, we undertook structural characterization of nanodiscs by dynamic light scattering to monitor Z-average diameters, associated polydispersity indices and volume weighted particle size distributions as a function of polymer concentration. Both coSMALP and altSMALP self-assembly show very similar trends across the measured polymer concentration range. Initially, where $c_s \leq c_s^{SAT}$, both coSMA and altSMA show an increase in Z-average diameter and corresponding drop in polydispersity. This is in agreement with volume weighted particle size distribution (PSD) data (Appendix A, Figure A.5) which show a shift towards larger diameters upon the addition of 0.1 mM of polymer to a 7.5 mM DMPC SUV suspension. This occurs below c_s^{SAT}, correlating to the previously discussed broadening of ^{31}P NMR peak, so a possible explanation is incomplete polymer insertion leading to polymer chain crosslinking between vesicles and thereby forming an effectively larger species. Interestingly, coSMA induces aggregation of vesicles leading to a Z-average diameter > 100 nm, whereas altSMA induces aggregation < 80 nm. In both cases, as c_s^{SOL} is approached the Z-average diameter shrinks as the vesicles become solubilized. AltSMA induces a much more gradual decrease in Z-average diameter compared to coSMA. However, both polymers lead to a gradual increase in polydispersity beyond c_s^{SAT}. These data show that there are no well-defined structural changes occurring at each of the previously determined

thermodynamic breakpoints. A similar phenomenon was observed with SMA(3:1) solubilizing POPC vesicles [36]. Under the conditions used, ^{31}P NMR is sensitive only to small, fast-tumbling particles so exclusively monitors the formation of SMALPs, while DLS is able to track the net changes in particle diameter and is most sensitive to larger particles, which can mask the onset of SMALP formation where the majority of lipid is not present within a smaller nanodisc structure.

Increasing c_s beyond c_s^{SOL} leads to a steady decrease in Z-average diameter (Figure 2.3a, c) and shifting of the PSD towards smaller diameters (Figure 2.3b, d) over the concentration range measured. From c_s^{SOL} to 5 mM polymer concentration, coSMALPs decreased in diameter from 14.6 ± 0.3 to 10.0 ± 0.8 nm, a 31% decrease in size, while altSMALPs decreased in diameter from 30.3 ± 1.9 nm to 16.1 ± 0.3 nm, decreasing in diameter by 53%. This trend has been observed with other SMA polymers [36,44], although occurs to a greater extent with altSMA to previously studied polymers.

The increasing polydispersity index (PDI) above c_s^{SOL} is related to the addition of excess polymer. Polymer can either remain free in solution or interact with existing nanodiscs, both of which would modify the PDI. altSMA should also be able to self-assemble into micelles in the absence of lipid due to the presence of the hydrophobic polystyrene tail which could again influence the PDI. We believe that the dominant factor in decreasing the Z-average diameter upon increasing polymer concentration is not the presence of particulate free polymer in solution, but the formation of an increased number of nanodiscs. This is because, for both polymers, as the polymer concentration is increased, we see a clear shift in the peak position without an associated broadening. This indicates a decrease in the disc diameter but only a small change in polydispersity. Furthermore, the negative Gibbs free energy change associated with the polymers during nanodisc self-assembly indicates that the polymers will preferentially interact with lipids over self-interaction.

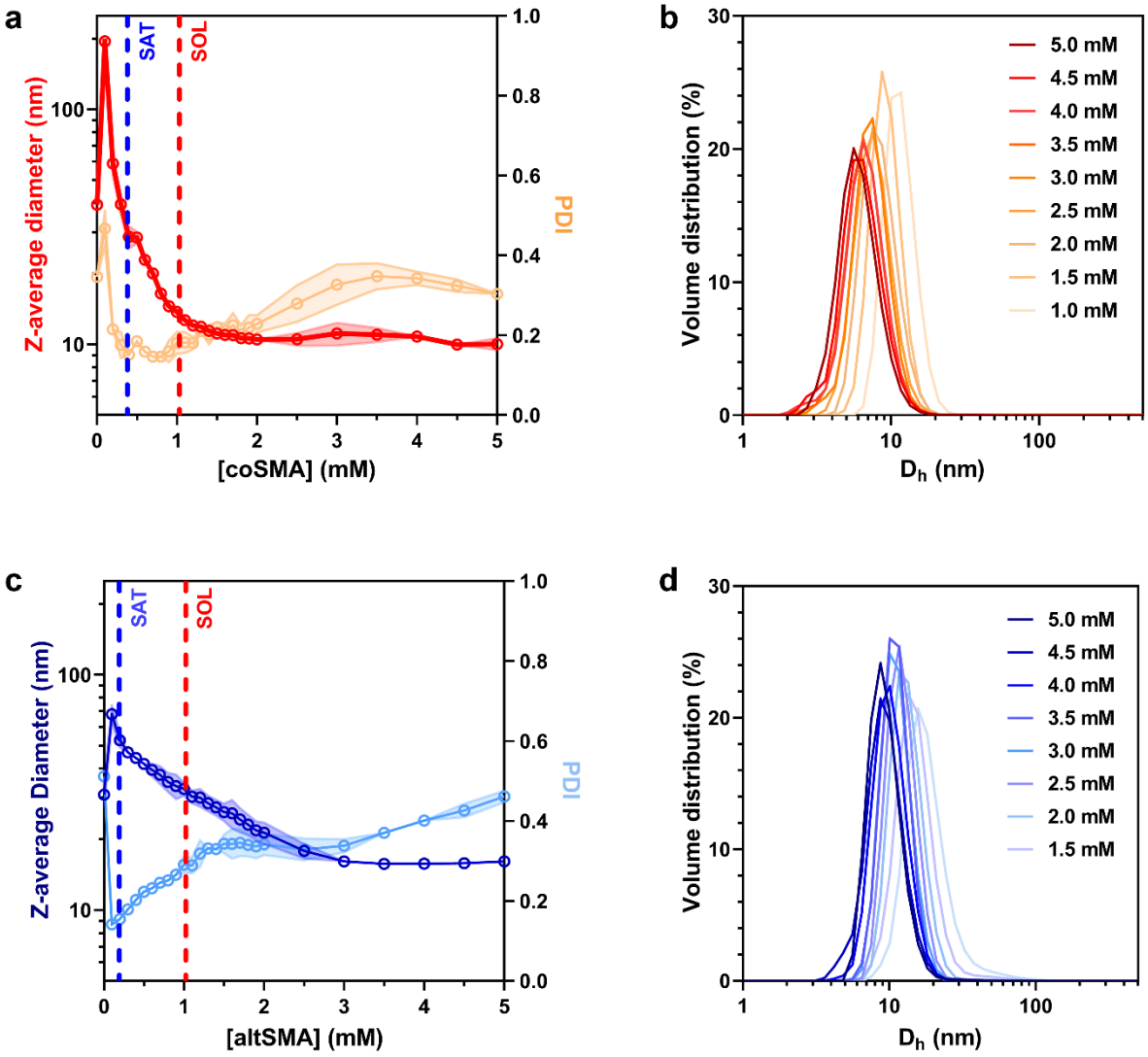

Figure 2.3 a, c. DLS data showing the effect of coSMA (**a**), altSMA (**c**) concentration on Z-average diameter (dark line) and polydispersity Index (PDI -light line). SAT and SOL boundaries obtained from ^{31}P NMR are shown as dashed blue and red lines respectively. Points represent the mean and shaded regions indicate the standard error obtained from three separate experiments. **b, d.** Volume weighted particle size distribution (PSD) data showing the hydrodynamic diameter (D_h) for SMALPs formed at coSMA (**b**) and altSMA (**d**) concentrations above c_s^{SOL}. Lines represent the mean PSD of three separate experiments. Error bars are not shown for clarity.

If this interpretation is correct, it means that we see the formation of a greater number of nanodiscs at polymer concentrations above c_s^{SOL}. We believe lipid reorganization between nanodiscs is a dynamic process because lipid exchange has been observed elsewhere [51,52] and we have no reason to believe that is not the case here. Therefore for higher polymer concentrations we would expect the available lipids to be distributed among the polymer in such a way as to minimize the Gibbs free energy, and this would result in fewer lipids being present per nanodisc, explaining the observed decrease in size. This interpretation would also explain our assertion (mentioned earlier) that the chemical shift seen with ^{31}P NMR data is partly due to interaction of a greater number of DMPC head-groups with the polymer belt beyond c_s^{SOL}.

Previous experiments have shown that one can vary the size of nanodiscs by changing the styrene:maleic acid ratio of the SMA polymer [41]. The data presented here indicate polymers with the same styrene:maleic acid ratio are able to form nanodiscs with different size ranges; altSMALPs appear larger than coSMALPs at equivalent molar polymer concentrations beyond c_s^{SOL}. However, these data do not confirm whether it is the chain topology which leads to the observed differences in diameter because changes in polymer chain length may also lead to this effect. coSMA has a broader chain length distribution and a far greater proportion of small chains compared to altSMA (Table 2.1). The larger proportion of shorter chains in coSMA could also lead to the observed difference in size distributions. However, a recent investigation of RAFT-synthesized SMA polymers found no significant change in SMALP diameter formed using polymers of the same monomer ratio but different chain lengths [41]. This indicates that the observed size difference between coSMALPs and altSMALPs is due to differences in polymer topology rather than size distribution. When comparing SMALPs assembled using statistical 2:1 and 3:1 SMA polymers, the nanodiscs are of a similar size. This is a different trend to that seen with RAFT-synthesized polymers where 3:1 polymers have been shown to have a decreased diameter when compared to 2:1 polymers [41]. SMALP size is therefore likely driven by the relative proportion of poly(styrene) and poly(styrene-*alt*-maleic acid) blocks of the polymer chain. Nonetheless, these data provide evidence that the nanodisc size can be tuned by simply changing the polymer concentration above c_s^{SOL}.

2.3.3 Molecular weight determination of nanodiscs

DLS data suggest that at polymer concentrations beyond c_s^{SOL}, excess polymer may exist as free polymer in solution or may associate with existing SMALPs. We therefore performed SEC-MALS measurements to assess what populations of species are present in solution at polymer concentrations in excess of c_S^{SOL} with the same number of monomer units (5 mg·mL^{-1} DMPC, 1.5 % (w/v) polymer), and to determine molecular weights of coSMALP and altSMALP nanodiscs (Figure 2.4).

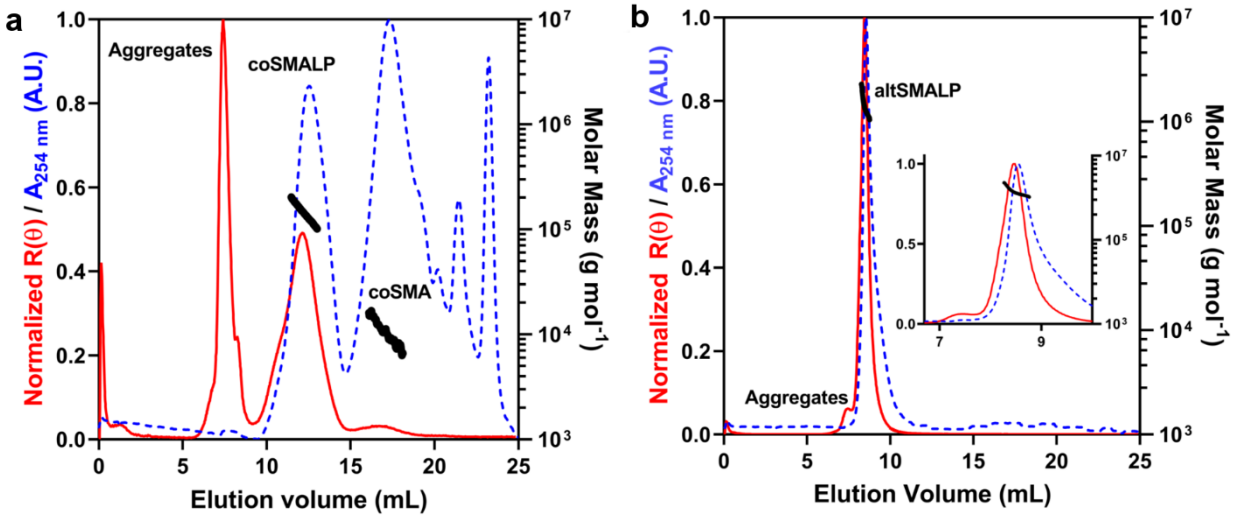

Figure 2.4. SEC-MALS chromatograms corresponding to **a.** coSMALP and **b.** altSMALP nanodiscs containing DMPC. Traces show the normalized Rayleigh ratio (red) and UV absorbance at 254 nm (blue, dashed) with overlaid mass calculations (black points). **b.** Inset displays an expanded X-axis to allow for clearer distinction between the aggregate and altSMALP peak.

Table 2.2. Parameters determined by analysis of SEC-MALS data collected from DMPC coSMALPs and altSMALPs.

	coSMALPs		**altSMALPs**
	coSMALP peak	coSMA peak	altSMALP peak
Hydrodynamic diameter (nm)	9.45 ± 0.13	3.67 ± 0.23	25.00 ± 0.36
R_g (nm)	5.50 ± 0.64	8.17 ± 0.92	13.93 ± 0.49
R_g/R_h	1.16 ± 0.12	4.45 ± 0.39	1.11 ± 0.03
M_w (kDa)	146.13 ± 2.93	11.29 ± 0.51	1512 ± 84
M_n (kDa)	142.70 ± 2.93	10.89 ± 0.63	1488 ± 88
$Đ$	1.02 ± 0.01	1.04 ± 0.01	1.02 ± 0.01

SEC-MALS analysis of coSMALPs (Figure 2.4a) show three principal features that appear with increasing elution volume. The first large aggregate peak (at 8 mL elution volume just after the void volume) detected by light scattering has no UV absorbance at 254 nm. The lack of UV absorbance suggests that this peak is due only to aggregated DMPC in a state which does not interact with the polymer. The second feature (which we have designated as "coSMALP" in Figure 4a) is detected by both light scattering and UV absorbance, showing a symmetric Gaussian-like shape. Analysis of in-line DLS data (Table 2.2) indicates a hydrodynamic diameter of ~ 10 nm, similar to that determined by DLS independently. Analysis of MALS data (Table 2.2) shows a large mass and low polydispersity. Furthermore, ratio of the radius of gyration (R_g) from MALS and the hydrodynamic radius (R_h) from in-line DLS gives information on particle shape [53]. For this peak the ratio is in the range of oblate spheroids, consistent with a disc structure proposed. However, this conclusion should be treated with some caution because the small size of the particles means that the R_g determined by MALS is not wholly reliable as an absolute value and should only be considered indicative of the particle shape. We therefore assign this peak to DMPC/coSMALP nanodiscs. The final feature in the SEC-MALS chromatogram

(designated as "coSMA" in Figure 2.4a) shows a large UV absorbance but only a small scattering intensity. The hydrodynamic diameter is smaller and has a significantly lower mass than the coSMALP peak, with an R_g/R_h ratio in the range of a prolate spheroid or rod, which is consistent with bundled, extended polymer chains. This is supported by SEC-MALS analysis of coSMA in the absence of lipids (Appendix A, Figure A.6a, Table A.1) which gives similar results. Here, a larger polymer aggregate is present in addition to the peak we have assigned as rod-like polymer bundles. Further downstream peaks show no scattering intensity with only UV absorbance and are highly convoluted. These peaks are also present for coSMA in the absence of lipids. We propose that these peaks are due to excess polymer that has not formed higher order structures in solution.

In contrast, altSMALPs show much cleaner SEC-MALS chromatogram (Figure 2.4b). There is only a small peak at the void volume (Inset to Figure 2.4b) detected by light scattering (assigned to lipid aggregates) followed by a single sharp peak detected by UV-absorbance and light scattering, which we assign to nanodiscs. Again, this assignment is supported by an R_g/R_h ratio, very similar to that of coSMALPs, in the range of oblate spheroids. At higher elution volumes, there are only very minor UV peaks corresponding to excess free polymer in solution. As altSMA was added in excess of c_s^{SOL}, one would expect to see a large UV signal arising from free polymer in solution. The absence of this signal suggests that either all altSMA is associating with nanodiscs, or excess altSMA is forming lipid-free structures of a similar size to DMPC/altSMALPs that cannot be resolved. SEC-MALS analysis of altSMA in the absence of lipids shows a peak detected by light scattering and UV-absorbance that does indeed elute at the same elution volume as altSMALPs. The R_g/R_h ratio across this peak is consistent with a spherical particle (Appendix A, Figure A.6b). The peak corresponding to altSMALP nanodiscs shows a hydrodynamic radius of 25 nm which is in the range measured using stand-alone DLS discussed above. The measured molecular weight is on the order of ten-fold higher than calculated for coSMALPs. Assuming a cylindrical structure, the mass of altSMALPs would be expected to be 7-fold higher than coSMALPs given the measured hydrodynamic radii of the two particles. This suggests that in the case of altSMALPs, altSMA in solution will associate with the available DMPC to form nanodiscs and thereby minimize the Gibbs free energy, rather than remain as spherical micelle-like particles. Such a

conclusion is supported by the R_g/R_h values. The polydispersity for the altSMALP peak gives the same value as measured for coSMALPs.

2.3.4 Stability of nanodiscs

A lot of recent interest in SMALPs from the membrane protein community is due to the increased stability of the solubilized target protein over classical 'head and tail' detergents [26,43]. It is therefore of interest to understand how robust these nanodiscs are to temperature and particularly to the freezing process. We used DLS to measure changes in z-average diameter as a function of temperature between 4°C to 80°C (Figure 2.5a, Appendix A, Figure A.7).

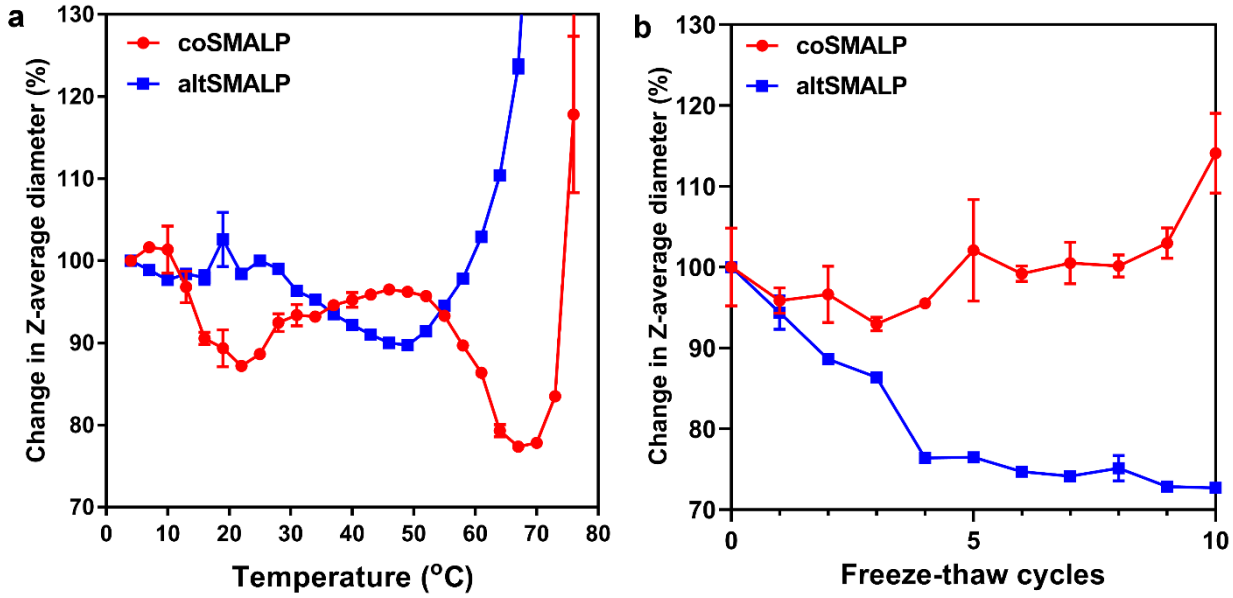

Figure 2.5. DLS data showing the effect of temperature (**a**), for clarity every third data point is plotted) and freeze-thaw cycles (**b**) on Z-average diameter of SEC purified coSMALP (red circles) and altSMALP (blue squares) nanodiscs containing DMPC. Points represent the mean value taken from three separate experiments with error bars displaying ± 1 standard error. In order to highlight changes, the data are plotted as percentage change, rather than the absolute diameter (which are plotted in Appendix A, Figure A.7).

At low temperatures (from 4 to 12°C) DMPC coSMALPs appear at a Z-average diameter of 10.6 ± 0.5 nm. Between 13°C and 20°C they then show a gradual decrease in diameter to 9.3 ± 0.2 nm. The onset of this decrease in size is of interest as 13°C is known to be the pre-transition temperature for pure DMPC (gel to ripple phase) [54,55]. From 20 to 50°C, the nanodiscs slowly increase in diameter to 10.1 ± 0.1 nm. It is again worth noting that this increase begins approximately after the melting phase transition for pure DMPC at 24°C. From 50 to 68°C, coSMALPs significantly shrink in size by about 20% (to 8.0 ± 0.03 nm) and then above 68°C, we observe a rapid increase in z-average diameter.

It is difficult to fully explain these observations on a microscopic level, though we can speculate. The initial decrease in diameter may be related to small losses of lipids from the nanodiscs that result from increased thermal motion of the DMPC tails. Above 24°C, DMPC is in the liquid phase, so increased mobility of DMPC molecules may exert outward pressure on the polymer belt that more than compensates for any losses of lipids from the discs and so lead to an increase in size. At higher temperatures still, this can no longer compensate for lipid loss and so the discs shrink again until they start to aggregate above 68°C.

At low temperature, the altSMALPs are observed to be 21.0 ± 0.03 nm and, in contrast to coSMALPs do not show any significant change in diameter until 24°C. Above this temperature a gradual decrease in size is observed to a minimum of 18.7 ± 0.1 nm at 47°C. We have no reason to suspect the mechanism leading to this diameter change is different to coSMALPs. Above this temperature, the size of the altSMALPs increase significantly with increasing temperature. Z-average diameter data could not be measured above 75°C for coSMALPs or altSMALPs as a precipitated lipid film deposited on the inside of the cuvette. Lowering the temperature did not result in re-solubilization of this precipitate. While high temperature destabilizes both coSMALPs and altSMALPs, both occur above usual working ranges, within which they are of comparable thermal stability.

We have also used DLS to characterize changes in coSMALPs and altSMALPs as a function of the number of freeze-thaw cycles (Figure 2.5b, Appendix A, Figure A.7). Volume PSD data for all nanodiscs clearly show that there are no aggregation effects or large changes in hydrodynamic diameter

after 10 freeze-thaw cycles (Appendix A, Figure A.8**)**. Looking at Z-average diameter data (Figure 2.5b, Appendix A, Figure A.7) there is a broad trend of increasing diameter for coSMALPs through repeated freeze-thaw cycles. This trend is quite poorly defined; the diameter shows an initial small decrease but is approximately constant until 8-10 cycles where the increase becomes more obvious. The coSMALP diameter is 114 % of the original size after 10 freeze-thaw cycles, increasing from 11.45 ± 0.95 nm to 13.06 ± 0.97 nm. In contrast, the altSMALPs show a much more pronounced decreasing diameter with increasing number of cycles, with an altSMALP diameter of 76% of their original size after 10 freeze-thaw cycles, decreasing from 17.93 ± 0.14 nm to 13.03 ± 0.16 nm. The majority of the size reduction appears over the first few cycles and the particle size appears to show relatively much smaller changes thereafter. To explain these observations, we speculate that multiple freeze-thaw cycles could lead to a minor lipid loss in altSMALPs as discussed above. coSMALPs seem to be much less affected by freeze-thaw cycles. This leads us to suspect that it is the poly(styrene) tail of altSMA which is expected to bury in the core of the nanodisc and could disrupt the lipids to a greater extent than coSMA, leading to the observed increased susceptibility to structural changes upon multiple freeze-thaw cycles.

It is worth noting that analysis of DLS data assumes a spherical particle and since we believe that neither coSMALPs or altSMALPs are spherical structures, the validity of the assumptions used to draw conclusions on the size of the particles is somewhat limited. The apparent small changes in diameter from DLS could alternatively be due to more complicated changes in the overall particle dimensions, swelling of the bilayer region, for example.

2.3.5 Solubilization of membrane proteins

Thus far, we have only characterized the various nanodiscs using a model DMPC bilayer. As a primary use of these polymers will be to solubilize membrane proteins, we have also tested their ability to solubilize proteins from isolated *Escherichia coli* BL21(DE3) membranes. As controls we have compared the polymers to some common traditional detergents: Triton X-100, n-dodecyl β-D-maltopyranoside (DDM) and octyl β-D-glucopyranoside (β-OG) as well as a sample where no detergent was added (Figure 2.6).

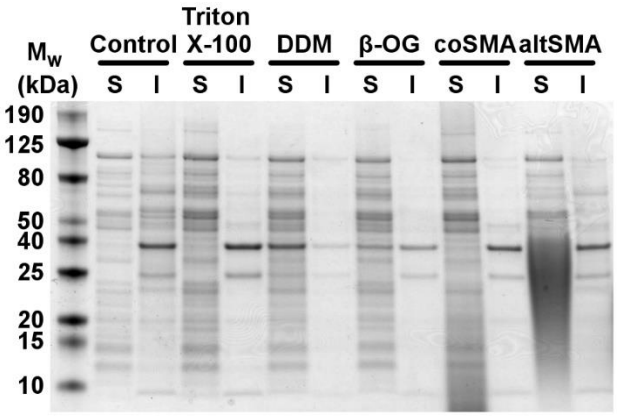

Figure 2.6. Coomassie stained SDS-PAGE showing the range of proteins that have been solubilized (S) and remained insoluble (I) after the incubation of *E. coli* membranes with coSMA and altSMA compared to three traditional detergents (Triton X-100, DDM and β-OG) and a control where no detergent was added to the membrane extract.

The experiment shows that coSMA is able to solubilize the membrane proteome with comparable efficiency to traditional detergents and significantly better than the control experiment without detergent. altSMA also shows a clear improvement over the detergent-free control though it is less effective than coSMA and traditional detergents. Interestingly, altSMA induces a loss of resolution on SDS-PAGE. We speculate that this is due to altSMA forming larger polymer aggregates which migrate through the gel and thus leads to a loss of resolution.

Given the different sizes of nanodisc formed by each polymer, there does not appear to be any selectivity towards proteins of different masses, with each polymer effectively solubilizing proteins across the whole mass range. However, given that altSMA displays a decreased extraction efficiency, it appears that the alternating topology combined with the hydrophobic polystyrene tail is, in this case, less effective when extracting membrane proteins from native *E.coli* membranes. We speculate that the polystyrene tail present on altSMA may bury itself within the acyl region of the lipid bilayer and could therefore interact with hydrophobic membrane spanning regions of certain membrane proteins. This interaction could prevent a clean solubilization of membrane proteins. This hypothesis is supported by previous observations where RAFT-synthesized SMA copolymers with a long polystyrene tail have been ineffective in solubilizing membrane proteins [47]. Nonetheless, altSMA is able to form nanodiscs up to twice the diameter of coSMA (as shown above). Previous analysis of SMALP structure formed by

coSMA has led to the estimate of a maximum of 40 α-helices being able to pack into the lipid core of a SMALP [23]. If one assumes that the lipid core of altSMALPs increases in diameter proportionately to the overall particle diameter, then altSMA may have useful application in the extraction of larger membrane protein complexes which are too large to be encapsulated by coSMA.

2.4 CONCLUSIONS

It is becoming increasingly clear that the SMALP system offers significant advantages over detergent-based systems for membrane protein production. The retention of the membrane solvating the membrane protein assures near native structure, function and stability. In addition, unlike detergent systems there is no need to maintain a concentration of free SMA above a nominal CMC meaning less issues with interference with downstream applications. However, it is clear that the rapid adoption of the SMALP method has outreached our fundamental understanding of the process of SMALP formation. While pragmatically this is not an issue as a number of SMA 3:1 and 2:1 polymers function adequately as membrane protein solubilizers, it is likely that at some point improved polymers are going to be required. To generate these polymers in a targeted fashion, an understanding of the SMALP formation process and the influence of polymer structure is going to be required. In this study we have applied methods developed for the study of other SMA polymers to the original SMA polymer (SMA2000) used in the first demonstration of SMALPs in membrane protein isolation [39] that has remained the most effective membrane protein solubilization polymer [43]. With the addition of data from a related RAFT polymer and in combination with data from three other studies of related polymers [36,44,49] we can begin to correlate polymer structure with effectiveness in membrane protein solubilization.

Both coSMA and altSMA exhibit a stronger thermodynamic driving force for nanodisc self-assembly than the SMA(2:1) (Xiran SZ30010) and SMA(3:1). This has demonstrated that at least four parameters (polymer chain length, chain length distribution, topology and monomer ratio) have influence on the SMALP self-assembly process. This correlates well with published data which show that these parameters have influence on the capability of the SMA to extract membrane proteins [43]. We have identified SMA polymers with a 2:1 styrene:maleic acid ratio being the most efficient in membrane

solubilization and polymers of larger length displaying the more favorable free energy change associated with SMALP formation amongst those tested. We have shown that changing the topological structure of polymers with the same 2:1 styrene:maleic acid ratio causes large differences in SMALP size and molecular weight. Furthermore, by simply increasing the polymer concentration beyond c_s^{SOL}, the final size of the nanodiscs can be further tuned. We have shown that coSMALPs and altSMALPs are of comparable stability, and able to effectively solubilize membrane proteins from the *E. coli* membrane, though with subtle differences. Previous studies have found that SMA polymers with a lower styrene content, similar to the poly(styrene-*alt*-maleic acid) block of altSMA, have been ineffective in forming SMALPs and extracting membrane proteins [43,47]. This leads us to believe that the presence of the polystyrene tail on altSMA is driving the differences observed in comparison to coSMA. The *S*-dodecyl trithiocarbonate end group is likely to hydrolyze under the conditions employed for ring-opening of the maleic anhydride (2 hr, 100°C, 1 M NaOH), and yield a thiol end group. It can however not be ruled out that a certain fraction of the dodecyl end groups are retained at the chain end, and contribute to the hydrophobicity of the polystyrene tail of the copolymer. Lack of trithiocarbonate end group hydrolysis has previously been reported, albeit under milder conditions (16 hr, room temperature, 0.1 M NaOH) [41]. Other classes of RAFT agent could be used [56] which could potentially be exploited to modify the properties of resultant SMALPs. This work indicates that SMALPs can be formed with varying properties, which can be applied to membrane and membrane protein research. These, and further modifications to the SMA polymer will expand the capabilities of the SMA toolkit.

2.5 REFERENCES

(1) Almén, M. S.; Nordström, K. J. V.; Fredriksson, R.; Schiöth, H. B. Mapping the Human Membrane Proteome: A Majority of the Human Membrane Proteins Can Be Classified According to Function and Evolutionary Origin. *BMC Biol.* **2009**, *7*, 50.

(2) Tan, S.; Tan, H. T.; Chung, M. C. M. Membrane Proteins and Membrane Proteomics. *PROTEOMICS* **2008**, *8* (19), 3924–3932.

(3) Fagerberg, L.; Jonasson, K.; von Heijne, G.; Uhlén, M.; Berglund, L. Prediction of the Human Membrane Proteome. *PROTEOMICS* **2010**, *10* (6), 1141–1149.

(4) Overington, J. P.; Al-Lazikani, B.; Hopkins, A. L. How Many Drug Targets Are There? *Nat. Rev. Drug Discov.* **2006**, *5* (12), 993–996.

(5) Stansfeld, P. J.; Goose, J. E.; Caffrey, M.; Carpenter, E. P.; Parker, J. L.; Newstead, S.; Sansom, M. S. P. MemProtMD: Automated Insertion of Membrane Protein Structures into Explicit Lipid Membranes. *Structure* **2015**, *23* (7), 1350–1361.

(6) Carpenter, E. P.; Beis, K.; Cameron, A. D.; Iwata, S. Overcoming the Challenges of Membrane Protein Crystallography. *Curr. Opin. Struct. Biol.* **2008**, *18* (5), 581–586.
(7) Moraes, I.; Evans, G.; Sanchez-Weatherby, J.; Newstead, S.; Stewart, P. D. S. Membrane Protein Structure Determination — The next Generation. *Biochim. Biophys. Acta BBA - Biomembr.* **2014**, *1838* (1), 78–87.
(8) Smith, S. M. Strategies for the Purification of Membrane Proteins. In *Protein Chromatography*; Walls, D., Loughran, S. T., Eds.; Humana Press: Totowa, NJ, **2011**; Vol. 681, pp 485–496.
(9) Arnold, T.; Linke, D. The Use of Detergents to Purify Membrane Proteins. In *Current Protocols in Protein Science*; Coligan, J. E., Dunn, B. M., Speicher, D. W., Wingfield, P. T., Eds.; John Wiley & Sons, Inc.: Hoboken, NJ, USA, **2008**; pp 4.8.1-4.8.30.
(10) Privé, G. G. Lipopeptide Detergents for Membrane Protein Studies. *Curr. Opin. Struct. Biol.* **2009**, *19* (4), 379–385.
(11) Baylon, J. L.; Vermaas, J. V.; Muller, M. P.; Arcario, M. J.; Pogorelov, T. V.; Tajkhorshid, E. Atomic-Level Description of Protein–Lipid Interactions Using an Accelerated Membrane Model. *Biochim. Biophys. Acta BBA - Biomembr.* **2016**, *1858* (7), 1573–1583.
(12) Hedger, G.; Sansom, M. S. P. Lipid Interaction Sites on Channels, Transporters and Receptors: Recent Insights from Molecular Dynamics Simulations. *Biochim. Biophys. Acta BBA - Biomembr.* **2016**.
(13) Parmar, M. J.; Lousa, C. D. M.; Muench, S. P.; Goldman, A.; Postis, V. L. G. Artificial Membranes for Membrane Protein Purification, Functionality and Structure Studies. *Biochem. Soc. Trans.* **2016**, *44* (3), 877–882.
(14) Bayburt, T. H.; Grinkova, Y. V.; Sligar, S. G. Self-Assembly of Discoidal Phospholipid Bilayer Nanoparticles with Membrane Scaffold Proteins. *Nano Lett.* **2002**, *2* (8), 853–856.
(15) Bayburt, T. H.; Sligar, S. G. Membrane Protein Assembly into Nanodiscs. *FEBS Lett.* **2010**, *584* (9), 1721–1727.
(16) Skar-Gislinge, N.; Arleth, L. Small-Angle Scattering from Phospholipid Nanodiscs: Derivation and Refinement of a Molecular Constrained Analytical Model Form Factor. *Phys Chem Chem Phys* **2011**, *13* (8), 3161–3170.
(17) Skar-Gislinge, N.; Kynde, S. A. R.; Denisov, I. G.; Ye, X.; Lenov, I.; Sligar, S. G.; Arleth, L. Small-Angle Scattering Determination of the Shape and Localization of Human Cytochrome P450 Embedded in a Phospholipid Nanodisc Environment. *Acta Crystallogr. D Biol. Crystallogr.* **2015**, *71* (12), 2412–2421.
(18) Pandit, A.; Shirzad-Wasei, N.; Wlodarczyk, L. M.; van Roon, H.; Boekema, E. J.; Dekker, J. P.; de Grip, W. J. Assembly of the Major Light-Harvesting Complex II in Lipid Nanodiscs. *Biophys. J.* **2011**, *101* (10), 2507–2515.
(19) Frauenfeld, J.; Gumbart, J.; Sluis, E. O. van der; Funes, S.; Gartmann, M.; Beatrix, B.; Mielke, T.; Berninghausen, O.; Becker, T.; Schulten, K.; et al. Cryo-EM Structure of the Ribosome–SecYE Complex in the Membrane Environment. *Nat. Struct. Mol. Biol.* **2011**, *18* (5), 614–621.
(20) Wang, X.; Mu, Z.; Li, Y.; Bi, Y.; Wang, Y. Smaller Nanodiscs Are Suitable for Studying Protein Lipid Interactions by Solution NMR. *Protein J.* **2015**, *34* (3), 205–211.
(21) Mörs, K.; Roos, C.; Scholz, F.; Wachtveitl, J.; Dötsch, V.; Bernhard, F.; Glaubitz, C. Modified Lipid and Protein Dynamics in Nanodiscs. *Biochim. Biophys. Acta BBA - Biomembr.* **2013**, *1828* (4), 1222–1229.
(22) Nikolaev, M.; Round, E.; Gushchin, I.; Polovinkin, V.; Balandin, T.; Kuzmichev, P.; Shevchenko, V.; Borshchevskiy, V.; Kuklin, A.; Round, A.; et al. Integral Membrane Proteins Can Be Crystallized Directly from Nanodiscs. *Cryst. Growth Des.* **2017**, *17* (3), 945–948.
(23) Jamshad, M.; Grimard, V.; Idini, I.; Knowles, T. J.; Dowle, M. R.; Schofield, N.; Sridhar, P.; Lin, Y.; Finka, R.; Wheatley, M.; et al. Structural Analysis of a Nanoparticle Containing a Lipid Bilayer Used for Detergent-Free Extraction of Membrane Proteins. *Nano Res.* **2015**, *8* (3), 774–789.
(24) Lee, S. C.; Knowles, T. J.; Postis, V. L. G.; Jamshad, M.; Parslow, R. A.; Lin, Y.; Goldman, A.; Sridhar, P.; Overduin, M.; Muench, S. P.; et al. A Method for Detergent-Free Isolation of Membrane Proteins in Their Local Lipid Environment. *Nat. Protoc.* **2016**, *11* (7), 1149–1162.

(25) Routledge, S. J.; Mikaliunaite, L.; Patel, A.; Clare, M.; Cartwright, S. P.; Bawa, Z.; Wilks, M. D. B.; Low, F.; Hardy, D.; Rothnie, A. J.; et al. The Synthesis of Recombinant Membrane Proteins in Yeast for Structural Studies. *Methods* **2016**, *95*, 26–37.

(26) Jamshad, M.; Charlton, J.; Lin, Y.; Routledge, S. J.; Bawa, Z.; Knowles, T. J.; Overduin, M.; Dekker, N.; Dafforn, T. R.; Bill, R. M.; et al. G-Protein Coupled Receptor Solubilization and Purification for Biophysical Analysis and Functional Studies, in the Total Absence of Detergent. *Biosci. Rep.* **2015**, *35* (2), 1–10.

(27) Paulin, S.; Jamshad, M.; Dafforn, T. R.; Garcia-Lara, J.; Foster, S. J.; Galley, N. F.; Roper, D. I.; Rosado, H.; Taylor, P. W. Surfactant-Free Purification of Membrane Protein Complexes from Bacteria: Application to the Staphylococcal Penicillin-Binding Protein Complex PBP2/PBP2a. *Nanotechnology* **2014**, *25* (28), 285101.

(28) Gulati, S.; Jamshad, M.; Knowles, T. J.; Morrison, K. A.; Downing, R.; Cant, N.; Collins, R.; Koenderink, J. B.; Ford, R. C.; Overduin, M.; et al. Detergent-Free Purification of ABC (ATP-Binding-Cassette) Transporters. *Biochem. J.* **2014**, *461* (2), 269–278.

(29) Jamshad, M.; Lin, Y.-P.; Knowles, T. J.; Parslow, R. A.; Harris, C.; Wheatley, M.; Poyner, D. R.; Bill, R. M.; Thomas, O. R. T.; Overduin, M.; et al. Surfactant-Free Purification of Membrane Proteins with Intact Native Membrane Environment. *Biochem. Soc. Trans.* **2011**, *39* (3), 813–818.

(30) Long, A. R.; O'Brien, C. C.; Malhotra, K.; Schwall, C. T.; Albert, A. D.; Watts, A.; Alder, N. N. A Detergent-Free Strategy for the Reconstitution of Active Enzyme Complexes from Native Biological Membranes into Nanoscale Discs. *BMC Biotechnol.* **2013**, *13* (1), 41.

(31) Prabudiansyah, I.; Kusters, I.; Caforio, A.; Driessen, A. J. M. Characterization of the Annular Lipid Shell of the Sec Translocon. *Biochim. Biophys. Acta BBA - Biomembr.* **2015**, *1848* (10), 2050–2056.

(32) Postis, V.; Rawson, S.; Mitchell, J. K.; Lee, S. C.; Parslow, R. A.; Dafforn, T. R.; Baldwin, S. A.; Muench, S. P. The Use of SMALPs as a Novel Membrane Protein Scaffold for Structure Study by Negative Stain Electron Microscopy. *Biochim. Biophys. Acta BBA - Biomembr.* **2015**, *1848* (2), 496–501.

(33) Bersch, B.; Dörr, J. M.; Hessel, A.; Killian, J. A.; Schanda, P. Proton-Detected Solid-State NMR Spectroscopy of a Zinc Diffusion Facilitator Protein in Native Nanodiscs. *Angew. Chem. Int. Ed.* **2017**, *56* (9), 2508–2512.

(34) Broecker, J.; Eger, B. T.; Ernst, O. P. Crystallogenesis of Membrane Proteins Mediated by Polymer-Bounded Lipid Nanodiscs. *Structure* **2017**, *25* (2), 384–392.

(35) Jamshad, M.; Grimard, V.; Idini, I.; Knowles, T.; Dowle, M.; Schofield, N.; Sridhar, P.; Lin, Y.; Finka, R.; Wheatley, M.; et al. Structural Analysis of a Nanoparticle Containing a Lipid Bilayer Used for Detergent-Free Extraction of Membrane Proteins. *Nano Res.* **2014**, 1–16.

(36) Vargas, C.; Arenas, R. C.; Frotscher, E.; Keller, S. Nanoparticle Self-Assembly in Mixtures of Phospholipids with Styrene/Maleic Acid Copolymers or Fluorinated Surfactants. *Nanoscale* **2015**, *7* (48), 20685–20696.

(37) Helenius, A.; Simons, K. Solubilization of Membranes by Detergents. *Biochim. Biophys. Acta* **1975**, *415* (1), 29–79.

(38) Heerklotz, H. Interactions of Surfactants with Lipid Membranes. *Q. Rev. Biophys.* **2008**, *41* (3–4), 205.

(39) Knowles, T. J.; Finka, R.; Smith, C.; Lin, Y.-P.; Dafforn, T.; Overduin, M. Membrane Proteins Solubilized Intact in Lipid Containing Nanoparticles Bounded by Styrene Maleic Acid Copolymer. *J. Am. Chem. Soc.* **2009**, *131* (22), 7484–7485.

(40) Orwick, M. C.; Judge, P. J.; Procek, J.; Lindholm, L.; Graziadei, A.; Engel, A.; Gröbner, G.; Watts, A. Detergent-Free Formation and Physicochemical Characterization of Nanosized Lipid–Polymer Complexes: Lipodisq. *Angew. Chem. Int. Ed.* **2012**, *51* (19), 4653–4657.

(41) Craig, A. F.; Clark, E. E.; Sahu, I. D.; Zhang, R.; Frantz, N. D.; Al-Abdul-Wahid, M. S.; Dabney-Smith, C.; Konkolewicz, D.; Lorigan, G. A. Tuning the Size of Styrene-Maleic Acid Copolymer-Lipid Nanoparticles (SMALPs) Using RAFT Polymerization for Biophysical Studies. *Biochim. Biophys. Acta BBA - Biomembr.* **2016**, *1858* (11), 2931–2939.

(42) Lindhoud, S.; Carvalho, V.; Pronk, J. W.; Aubin-Tam, M.-E. SMA-SH: Modified Styrene-Maleic Acid Copolymer for Functionalization of Lipid Nanodiscs. *Biomacromolecules* **2016**, *17* (4), 1516–1522.
(43) Morrison, K. A.; Akram, A.; Mathews, A.; Khan, Z. A.; Patel, J. H.; Zhou, C.; Hardy, D. J.; Moore-Kelly, C.; Patel, R.; Odiba, V.; et al. Membrane Protein Extraction and Purification Using Styrene-Maleic Acid (SMA) Copolymer: Effect of Variations in Polymer Structure. *Biochem. J.* **2016**, *473* (23), 4349–4360.
(44) Grethen, A.; Oluwole, A. O.; Danielczak, B.; Vargas, C.; Keller, S. Thermodynamics of Nanodisc Formation Mediated by Styrene/Maleic Acid (2:1) Copolymer. *Sci. Rep.* **2017**, *7* (1).
(45) Scheidelaar, S.; Koorengevel, M. C.; van Walree, C. A.; Dominguez, J. J.; Dörr, J. M.; Killian, J. A. Effect of Polymer Composition and PH on Membrane Solubilization by Styrene-Maleic Acid Copolymers. *Biophys. J.* **2016**, *111* (9), 1974–1986.
(46) Dominguez Pardo, J. J.; Dörr, J. M.; Renne, M. F.; Ould-Braham, T.; Koorengevel, M. C.; van Steenbergen, M. .; Killian, J. A. Thermotropic Properties of Phosphatidylcholine Nanodiscs Bounded by Styrene-Maleic Acid Copolymers. *Chem. Phys. Lipids* **2017**, *208*, 58–64.
(47) Smith, A. A. A.; Autzen, H. E.; Laursen, T.; Wu, V.; Yen, M.; Hall, A.; Hansen, S. D.; Cheng, Y.; Xu, T. Controlling Styrene Maleic Acid Lipid Particles through RAFT. *Biomacromolecules* **2017**, *18* (11), 3706–2713.
(48) Harrisson, S.; Wooley, K. L. Shell-Crosslinked Nanostructures from Amphiphilic AB and ABA Block Copolymers of Styrene-Alt-(Maleic Anhydride) and Styrene: Polymerization, Assembly and Stabilization in One Pot. *Chem. Commun.* **2005**, *26*, 3259–3261.
(49) Arenas, R. C.; Klingler, J.; Vargas, C.; Keller, S. Influence of Lipid Bilayer Properties on Nanodisc Formation Mediated by Styrene/Maleic Acid Copolymers. *Nanoscale* **2016**, *8* (32), 15016–15026.
(50) Kemmer, G.; Keller, S. Nonlinear Least-Squares Data Fitting in Excel Spreadsheets. *Nat. Protoc.* **2010**, *5* (2), 267–281.
(51) Hazell, G.; Arnold, T.; Barker, R. D.; Clifton, L. A.; Steinke, N.-J.; Tognoloni, C.; Edler, K. J. Evidence of Lipid Exchange in Styrene Maleic Acid Lipid Particle (SMALP) Nanodisc Systems. *Langmuir* **2016**, *32* (45), 11845–11853.
(52) Cuevas Arenas, R.; Danielczak, B.; Martel, A.; Porcar, L.; Breyton, C.; Ebel, C.; Keller, S. Fast Collisional Lipid Transfer Among Polymer-Bounded Nanodiscs. *Sci. Rep.* **2017**, *7*, 45875.
(53) Brewer, A. K.; Striegel, A. M. Characterizing the Size, Shape, and Compactness of a Polydisperse Prolate Ellipsoidal Particle via Quadruple-Detector Hydrodynamic Chromatography. *Analyst* **2011**, *136* (3), 515–519.
(54) Heimburg, T. A Model for the Lipid Pretransition: Coupling of Ripple Formation with the Chain-Melting Transition. *Biophys. J.* **2000**, *78* (3), 1154–1165.
(55) Blume, A. Apparent Molar Heat Capacities of Phospholipids in Aqueous Dispersion. Effects of Chain Length and Head Group Structure. *Biochemistry* **1983**, *22* (23), 5436–5442.
(56) Keddie, D. J.; Moad, G.; Rizzardo, E.; Thang, S. H. RAFT Agent Design and Synthesis. *Macromolecules* **2012**, *45* (13), 5321–5342.

CHAPTER 3

AN ACID-COMPATIBLE CO-POLYMER FOR THE SOLUBILIZATION OF MEMBRANES AND PROTEINS INTO LIPID BILAYER-CONTAINING NANOPARTICLES

Published Article

Stephen C.L. Hall[†‡], Cecilia Tognoloni[§], Jack Charlton[†], Éilís C. Bragginton[‖], Alice J. Rothnie[Δ], Pooja Sridhar[†], Mark Wheatley[†], Timothy J. Knowles[†], Thomas Arnold[‡§⊥], Karen J. Edler[§] and Tim R. Dafforn[†]

Nanoscale, **2018**, 22 (**10**), pp 10609–10619
DOI: 10.1039/C8NR01322E

† School of Biosciences, University of Birmingham, Edgbaston, Birmingham, B15 2TT, UK

‡ Diamond Light Source, Harwell Science and Innovation Campus, Didcot, OX11 ODE, UK

§ Department of Chemistry, University of Bath, Claverton Down, Bath, BA2 7AY, UK

‖ School of Cellular and Molecular Medicine, University of Bristol, University Walk, Bristol, UK

Δ School of Life & Health Sciences, Aston University, Aston Triangle, Birmingham, B4 7ET, UK

⊥ European Spallation Source, ERIC, P.O Box 176, SE-221 00 Lund, Sweden

Author contribution statement

S.C.L.H conceived and designed the study, prepared the samples, performed the experiments (unless otherwise stated), analyzed and interpreted the data, prepared and edited the manuscript. C.T performed and analyzed SAXS experiments. J.C performed GPCR solubilization experiments. É.C.B collected TEM data. A.J.R performed SMILP-ZipA protein purification experiments. P.S provided SMI copolymer stocks. M.W conceived GPCR solubilization experiments, edited the manuscript, supervised J.C. T.J.K conceived the study, provided SMA2000I resin and materials for *E. coli* solubilization experiments. K.J.E conceived the study, interpreted the data, responsible for SAXS beamtime, analyzed SAXS data, edited the manuscript and supervised C.T. T.A and T.R.D conceived the study, interpreted the data, edited the manuscript and supervised S.C.L.H. Methods which have not been performed by S.C.L.H. are described in Appendix B.

Signed:

Stephen Hall

Tim Dafforn

Abstract

The fundamental importance of membrane proteins in drug discovery has meant that membrane mimetic systems for studying membrane proteins is of increasing interest. One such system has been the amphipathic, negatively charged poly(styrene-co-maleic acid) (SMA) polymer to form "SMA Lipid Particles" (SMALPs) which have been widely adopted to solubilize membrane proteins directly from the cell membrane. However, SMALPs are only soluble under basic conditions and precipitate in the presence of divalent cations required for many downstream applications. Here, we show that the positively charged poly(styrene-co-maleimide) (SMI) forms similar nanoparticles with comparable efficiency to SMA, whilst remaining functional at acidic pH and compatible with high concentrations of divalent cations. We have performed a detailed characterization of the performance of SMI that enables a direct comparison with similar data published for SMA. We also demonstrate that SMI is capable of extracting proteins directly from the cell membrane and can solubilize functional human G-protein coupled receptors (GPCRs) expressed in cultured HEK 293T cells. "SMILPs" thus provide an alternative membrane solubilization method that successfully overcomes some of the limitations of the SMALP method.

3.1 INTRODUCTION

With an increasing interest in membrane proteins due to their physiological and pharmacological significance[1–4], recent developments have yielded alternative solutions to the solubilization bottleneck often limiting purification and characterization.[5–10] A commonly adopted method involves the use of the amphipathic, helical membrane scaffold proteins (MSP),[11] or peptides inspired by the amino acid residue sequence of the MSP helix,[12–14] to solubilise phospholipid vesicles containing reconstituted membrane proteins into so-called 'nanodiscs'. These MSP or peptide-stabilized nanodiscs have proven a valuable tool for stabilizing membrane proteins within a planar, nanoscale segment of lipid bilayer surrounded by an proteinaceous belt. MSP nanodiscs have been used extensively for a variety of targets and applications.[10,15,16] While it has been observed that peptide-stabilized nanodiscs are potentially more amenable to studying protein complexes within the nanodisc environment,[17,18] they have been shown to have a higher polydispersity than the MSP variety.[14] However, both these protein-stabilized nanodisc systems still suffer from the limitation that encapsulated membrane proteins need to be extracted using detergent-mediated solubilization before reconstitution into nanodiscs which can lead to instability and disruption of protein-protein interactions. In addition, the peptide nature of the stabilizing belt can lead to spectroscopic interference in downstream applications such as UV circular dichroism (UV-CD) spectroscopy.

An alternate strategy is the use of poly(styrene-*co*-maleic acid) (SMA) (Figure 3.1a) to extract nanodiscs containing a segment of native cell bilayer, encapsulated by the SMA polymer (termed SMA lipid particles, SMALPs).[19–22] Since the first report of SMA-mediated solubilization[19] the method has been successfully employed to solubilize a wide variety of targets directly from a range of biological membranes.[23–28] SMALPs have also proven useful in downstream functional[23,25,29] and structural characterization.[22,24,30–32]

The commonly used variants of the SMA polymer have now been investigated thoroughly,[21,33–39] showing that the first used polymer (SMA2000) is the best performing of the polymers so far studied. However, SMA has its limitations. Firstly, the nanodiscs formed by commercially available SMA have

a diameter of ~10 nm[20] which potentially limits the size of proteins that can be solubilized. Secondly, the styrene moiety shows significant absorption of UV light,[40] which overlaps with the absorption from aromatic residues within proteins. This interferes with spectroscopic techniques to study solubilized proteins. Thirdly, SMALPs have been shown to be unstable in the presence of divalent cations such as Mg^{2+}, with precipitation of the polymer occurring under such conditions. Although this can be a useful property under certain circumstances, it can also be a limitation for many potential downstream applications where divalent cations are necessary for membrane protein function.[41,42] Finally, SMA is pH sensitive; at acidic pH values, maleic acid groups become protonated and the polymer becomes insoluble.[39] This limits the SMALP method to proteins that are stable at basic pHs.

It is both the success and the limitations of the SMA polymer which has spawned a drive to investigate other amphipathic polymers which are capable of solubilizing lipid bilayers into colloidal disc-shaped particles.[43–45] Given the high UV absorbance of styrene, recent advances have been made in establishing the use of styrene-free polymers for nanodisc formation. The first of these copolymers to be investigated was poly(diisobutylene-co-maleic acid) (DIBMA) shown to be successful in the solubilization of phospholipid membranes and membrane proteins whilst providing a more native-like phospholipid environment than SMALP nanodiscs.[40,46] Additionally, poly(methacrylate) (PMA) polymers, inspired by the amphiphilic nature of the MSP helix, have been shown to be functional in nanodisc formation.[47] PMA-stabilised nanodiscs have been applied to stabilization of helical intermediates of amyloid proteins in the presence of a phospholipid membrane. Currently, the efficiency of PMA for solubilization of biological membranes is unknown. In order to address the limited size range of nanodiscs formed by SMA, modification of a low-molecular weight SMA polymer by an amination reaction to form SMA-EA has been shown to form so-called 'macro nanodiscs'.[48,49] SMA-EA stabilized nanodiscs have been shown to have diameters up to ~60 nm whilst exhibiting alignment properties in external magnetic fields with demonstrated applications in 2D solid state NMR spectroscopy.

While these new polymers have addressed the issues of UV absorbance, tolerance to low concentrations of divalent cations in solution and size limitations, they are still limited by the same pH constraints as SMA. Two SMA-derived polymers have recently been developed to allow nanodisc formation under acidic conditions. The first such polymer to be developed, SMAd-A, involves modification of SMA with a primary amine. SMAd-A can tolerate low pH and is functional in the solubilization of phospholipids into nanodiscs[50]. SMAd-A stabilized nanodiscs have been demonstrated to provide an encapsulation platform for the solubilization of hydrophobic drugs in aqueous media. Most recently, modification of SMA with a quaternary ammonium has yielded a polymer (SMA-QA) which is capable of forming nanodiscs.[51] SMA-QA-stabilized nanodiscs have been shown to remain soluble between pH 2.5 and pH 10, offering a substantial improvement in pH-stability compared to the original SMA polymers. Furthermore, SMA-QA is also able to form macro-nanodiscs of ~30 nm diameter to overcome the size limitation of SMA-stabilized nanodiscs. However, neither SMAd-A or SMA-QA is commercially available, requiring synthesis through modification of an SMA backbone, and neither have been shown to be compatible with membrane protein solubilization.

Given the limitations discussed above, we have investigated whether an alternative polymer with a similar structure to SMA; poly(styrene-*co*-maleimide) (SMI) (Figure 3.1a) can be used in the self-assembly of phospholipid nanodiscs under acidic conditions. SMI is a commercially available amphipathic copolymer of styrene and dimethylaminopropylamine maleimide in a 2:1 ratio. SMI has been used to create nanoparticles[52] capable of oil microencapsulation[53] and as a surface coating with application to printing[54]. Despite exploitation of the amphipathic properties of SMI, there have been no reports on SMI-mediated phospholipid solubilization.

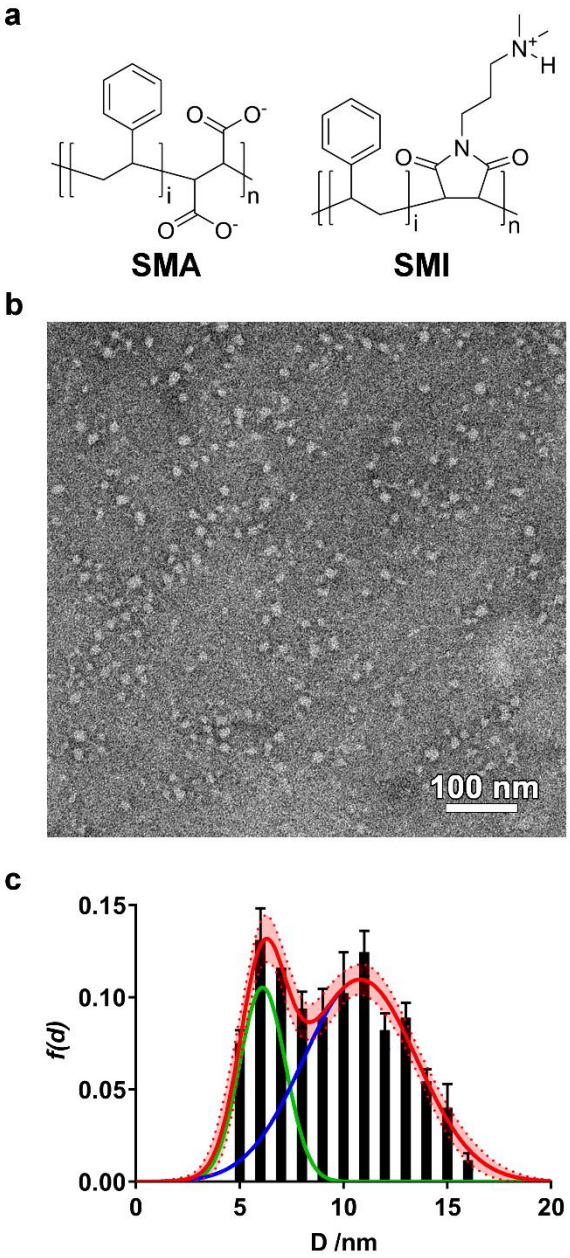

Figure 3.1. a. Structures of SMA and SMI. In both cases, i=2n. **b**. Representative transmission electron micrograph (TEM) of DMPC-SMILPs negatively stained with phosphotungstic acid. **c.** Frequency distribution of SMILP diameters imaged with TEM. Bars represent the mean frequency associated with analysis of three separate micrographs with error bars representing ± 1 standard deviation. The data fit to the sum of two Gaussian populations of particles (red curve, dashed curve and shaded region represents the standard error associated with nonlinear regression) with maxima at diameters of 6 nm (green line) and 11 nm (blue line).

Here, we demonstrate that SMI is capable of solubilizing phospholipids by self-assembling in the same way as seen for SMA. We refer to the resulting nanodisc particles as SMI lipid particles (SMILPs). SMI exhibits high thermodynamic efficiency in nanodisc self-assembly which is comparable with SMA. Furthermore, we demonstrate that the size of the lipid core of SMILPs can be tuned as a function of polymer:lipid ratio. SMI circumvents some of the limitations of SMA-mediated solubilization by being tolerant to high concentrations of divalent cations and is soluble in acidic conditions. As SMA is widely used in membrane protein solubilization, we present data to show that SMI is also capable of extracting functional membrane proteins directly from cell membranes without laborious reconstitution following detergent solubilization. These data establish SMI and SMILPs as an alternative to SMA that is an efficient and effective platform for membrane and protein solubilization under acidic conditions.

3.2 MATERIALS AND METHODS

3.2.1 Materials

SMI was purchased as SMA2000I resin from Cray Valley (UK). SMA2000I has a weight averaged molecular weight, M_w of 7500 and a number averaged molecular weight, M_n of 2700. SMA was purchased as SMA2000 (poly(styrene-*co*-maleic anhydride) SMAnh) from Cray Valley (UK) with an M_w of 7500 and an M_n of 3000. 1,2-dimyristoyl-*sn*-glycero-3-phosphocholine (DMPC) was purchased as a powder from Avanti Polar Lipids (USA). 400 mesh carbon coated Cu grids were purchased from Agar Scientific (UK). Precast Criterion XT graduated 4 – 12 % bis-tris poly(acrylamide) gels were purchased from Bio-Rad Laboratories Ltd. (UK). InstantBlue protein stain was purchased from Expedion (UK). [^{3}H]ZM241385 (specific activity 50 Ci/mmol) was purchased from American Radiolabelled Chemicals (Cardiff, UK). [Phe-3,4,5-^{3}H]AVP (specific activity 68 Ci/mmol) was supplied by PerkinElmer (Stevenage, UK). ZM241385 (4-(2-[7-amino-2-(2-furyl)[1,2,4]triazolo[2,3-a][1,3,5]triazin-5-yl amino]ethyl)phenol) was purchased from Tocris (Bristol, UK) and AVP was from Bachem (Weil am Rhine, Germany). The standard HEK 293T cell line was provided as a kind gift from Professor John Heath (University of Birmingham, UK). All other chemicals and reagents were purchased from Sigma-Aldrich (UK) at > 98 % purity and used without further purification.

3.2.2 Methods

3.2.2.1 Solubilization of SMI and SMAnh

SMA2000I resin was solubilized by following the manufacturer's instructions. In brief, concentrated HCl was added dropwise to a 10 % suspension of SMA2000I in ultrapure water to a concentration of 1 M. This solution was heated under reflux at 125 °C for 2 – 4 hours until the solution has clarified. Solubilized SMI was then precipitated by the addition of 5 M NaOH to pH 9.0 and washed three times in ultrapure water. Precipitated SMI was dissolved in a minimal volume of 0.6 M HCl, the pH adjusted to as required and lyophilized. SMI stocks were made directly from the dried powder.

SMAnh (poly(styrene-*co*-maleic anhydride)) was hydrolyzed from SMA2000 resin as previously described [22]. Briefly, a 10 % w/v suspension of SMA2000 resin in 1 M sodium hydroxide was heated under reflux at 125 °C for 2 hours until the solution clarified. Solubilized copolymer was precipitated after cooling by lowering the pH to 5.0 with the drop-wise addition of concentrated hydrochloric acid and then washed 3 times in ultra-pure water. Washed, precipitated SMA was re-dissolved in 0.6 M NaOH overnight and the precipitation and washing procedure repeated. Finally, SMA was dissolved in a minimal volume of 0.6 M NaOH, pH adjusted to 8.0 and lyophilized. SMA stocks were made directly from the dried powder.

3.2.2.2 Nanodisc preparation

DMPC was weighed and dissolved in chloroform in glass vials. A lipid film was deposited on the surface of the vials by evaporating chloroform with N_2 and then desiccating overnight to remove trace solvent. DMPC was hydrated to 10 mg/mL with buffer (50 mM NaOAc, 200 mM NaCl, pH 5 for SMILPs and 50 mM sodium phosphate, 200 mM NaCl, pH 8 for SMALPs) at 25 °C and sonicated in a water bath for 30 minutes until the suspensions turned clear, indicating the formation of small unilamellar vesicles (SUVs). DMPC SUV suspensions were stored at room temperature and used within 3 days.

SMI stock solutions were made in 50 mM sodium acetate, 200 mM NaCl, pH 5 to the required molar concentration (assuming no changes in molecular weight distribution upon copolymer solubilization) based on the M_n value for titration experiments. For experiments using nanodiscs made at excess copolymer concentration, SMI stock solutions were made to 3 % w/v in the same buffer. SMA stock solutions were made to 3 % w/v in 50 mM sodium phosphate, 200 mM NaCl pH 8.

3.2.2.3 ^{31}P NMR

^{31}P NMR was carried out essentially as previously described,[33] but with the following modifications. SMI and DMPC mixtures were prepared as described above in 50 mM sodium acetate, 200 mM NaCl, pD 5.0 using DMPC concentrations of 7.50, 5.00, 2.50 and 1.25 mM. The M_n value for SMA2000I was used to calculate molar concentrations of SMI, as the distribution was assumed to remain unchanged throughout the solubilization procedure described above. ^{31}P NMR spectra were recorded at 298 K using an Avance III 400 MHz NMR spectrometer (Bruker, UK) operating with an excitation frequency of 161.98 MHz using ^{1}H-decoupling. 256 scans were recorded per measurement over a sweep width of 32051 Hz, with an acquisition time of 1.022 s, a pre scan delay of 6.5 s, a relaxation delay of 5 s and a pulse width of 7.25 µs. Spectra were referenced to an external standard of 85 % H_3PO_4 in 10 % D_2O to correct for any changes in field strength between measurements.

3.2.2.4 Thermodynamic calculations

The thermodynamic analysis performed is based on the work of Vargas et al.[21], and has been described by them and us[33] previously. Briefly, to obtain saturation and soluilization breakpoints (c_S^{SAT} and c_S^{SOL}, respectively) the 31P-NMR peaks were integrated using TopSpin software (Bruker, UK) and the absolute integrals normalized to the largest and smallest value in each data set. Normalized integrals were then averaged from three independent measurements, plotted as a function of SMI molar concentration and fit to the scenario described previously[21,33,34,37,40]. This fitting procedure yields c_s^{SAT} and c_S^{SOL} breakpoints, ie, the concentration of SMI required for the onset and completion of solubilization at each DMPC concentration. Plotting these breakpoints as molar concentrations of SMI against DMPC yields the phase boundary lines. The gradient of each of these lines describes the molar

ratio of SMI to DMPC required for the vesicle saturation, $R_S^{b,\,SAT}$, and solubilization, $R_S^{m,\,SOL}$. These molar ratios allow the calculation of partitioning coefficients for SMI and DMPC which in turn allow for the calculation of the free-energy of transition of both DMPC, $\Delta G_{Lipid}^{b\rightarrow m,0}$, and SMI, $\Delta G_{Polymer}^{b\rightarrow m,0}$, transitioning from a vesicle/aggregate to a nanodisc. A detailed description of this analysis has been published previously[21].

3.2.2.5 Dynamic light scattering

Dynamic light scattering experiments were performed as previously described [33]. In brief, samples were loaded into 45 µL quartz cuvettes with a 3 × 3 mm light path (Hellma Analytics, Germany). Measurements were taken using a Zetasizer Nano S (Malvern Instruments, Worcestershire, UK) equipped with a He-Ne laser at 633 nm with a detector angle of 178° relative to the incident beam. All measurements were performed after equilibrating the sample at 25°C for 60 seconds. Each sample measured 3 times with the attenuator position automatically optimized for size determination. Each measurement consists of 11 scans of 10 seconds. Freeze-thaw stability was performed by flash freezing the nanodisc solution in liquid N_2 for 5 min and then thawing at room temperature before taking the sample to load into the cuvette. Temperature stability was performed by increasing the temperature from 4 to 80°C in 1°C increments. The samples were measured at each temperature after equilibrating at that temperature for 2 minutes. Data analysis was performed after taking into account the viscosity and refractive index of all buffer constituents by fitting a non-negatively constrained least squares function to the measured autocorrelation function. This gives an intensity weighted particle distribution assuming spherical particles, which is converted to a volume weighted particle size distribution using Mie scattering theory[55,56]**.** A volume weighted PSD takes into account the increased scattering of light by larger particles to give a more realistic representation of the particles present. Cumulant analysis was also performed to obtain the Z-average diameter and polydispersity index[57]**.** The polydispersity index (PDI) is defined as the square of the ratio of the peak value to the width of the Gaussian distribution obtained from cumulant analysis.

3.2.2.6 Size exclusion chromatography with multi-angled light scattering

SEC-MALS experiments were performed as previously described[33]. A Superdex 200 increase 10/300 GL size exclusion column attached to an Äkta purification system (GE Healthcare Life Sciences, UK) was equilibrated with 2 column volumes of 50 mM sodium acetate pH 5, 200 mM NaCl. In line absorbance measurements at 280 and 254 nm were used to calibrate the delay volume between the column and the MALS detector. MALS measurements were performed using a Dawn Helios II (Wyatt Technologies, UK) equipped with a 633 nm He-Ne laser with static light scattering detectors positioned at 18 angles radially about the flow cell. The MALS detector at 110° has been replaced with a quasi-elastic light scattering (QELS) detector. DMPC SMILPs were prepared as described above and centrifuged at 16,000 × *g* for 10 minutes to remove any contaminant particulate matter. 70 µL of each sample was loaded onto the column which was run with a flow rate of 0.7 mL/min.

The analysis of SEC-MALS data has been discussed in detail elsewhere. We analyzed the data for DMPC SMILPs using a refractive index increment, *dn/dc*, value of 0.16 for saturated phospholipids. As a large proportion of the scattering volume of DMPC SMILPs comprises of SMI, as determined by SAXS, the masses obtained are estimations for an equivalent particle composed purely of DMPC. Analysis was performed using ASTRA software (Wyatt Technologies, Suffolk, UK) to obtain weight averaged and number averaged molar masses, M_w and M_n, respectively using the Zimm equation[62,63]. The polydispersity index is defined as the ratio of M_w/M_n. Hydrodynamic radii were calculated by measuring the autocorrelation function across the peak and analyzing each curve by cumulant analysis[57] to give a mean Z-average R_h.

3.2.2.7 Turbidity measurements

Turbidity measurements were used to measure the solubility of DMPC SMILPs and DMPC SMALPs as a function of the concentration of divalent cations and pH.

For divalent cation stability measurements, DMPC SMILPs and DMPC SMALPs were prepared as described above using 50 mM sodium acetate, 200 mM NaCl, pH 5.0 for SMILPs and 50 mM tris, 200

mM NaCl, pH 8.0 for DMPC SMALPs. Nanodiscs were diluted to 3.22 mg/mL DMPC and 0.5 % (w/v) copolymers in the appropriate buffers. A dilution series was prepared of $MgCl_2$ and $CaCl_2$ from 200 to 2 mM in acetate (for SMILPs) and tris (for SMALPs) buffers as described above. Both the nanodisc solutions and the divalent cation dilution series were centrifuged at 14,000 × *g* for 10 minutes to remove any large contaminating matter. 100 µL of diluted nanodiscs were mixed with 100 µL of the divalent cation dilution series in a flat-bottomed 96-well plate and incubated, shaking, at room temperature for 30 mins. The OD was measured at 620 nm for each sample and a background OD subtracted for an identical solution containing no nanodiscs.

To measure the turbidity of DMPC SMILPs and SMALPs as a function of pH, nanodiscs were prepared as described above in 50 mM sodium phosphate, 200 mM NaCl at pH 5.0 for SMILPs and pH 8.0 for SMALPs in order to negate buffer-dependent effects. Nanodiscs were diluted to 0.33 mg/mL DMPC, 0.1 % (w/v) copolymer. 0.2 M HCl or 0.2 M NaCl was added dropwise to SMILPs and SMALPs, respectively, with the solution stirring at room temperature. The pH was measured with a probe and equilibrated for 5 minutes at each pH point. Three 1 mL aliquots of the solution wwere transferred to separate 1 cm path length, optically clear poly(styrene) disposable cuvettes and the OD measured in triplicate at 620 nm using a Ultrospec™ 2100 UV-Vis spectrophotometer (GE Healthcare, UK). All turbidity experiments were performed in triplicate.

3.2.2.8 Preparation of *E. coli* BL21 (DE3) membranes

E. coli BL21 (DE3) cultures were inoculated from a single colony on an LB-agar plate and grown in 15 mL LB at 37°C for 16 hours. A 1 % (v/v) inoculum was used to inoculate 1 L LB. This culture was grown at 37°C until stationary phase was reached, monitored by measuring optical density at 600 nm. Cells were isolated by centrifugation at 7000 × *g* for 10 minutes at 4°C. Pelleted cells were washed in phosphate buffered saline (PBS) and resuspended in 3.5 mL lysis buffer (50 mM Tris, 5 % (w/v) glycerol, 2 mM EDTA pH 7.5 containing 1 Pearce EDTA-free protease inhibitor tablet per 50 mL) per gram of cells at 4°C. Cells were lysed by 5 passes through an Emmulsiflex C3 cell disruptor at 4°C. Cell debris is removed by centrifugation at 11000 × *g* for 30 minutes at 4°C. Supernatant was removed and

membranes isolated by centrifugation at 100,000 × *g* for 60 minutes at 4°C. Supernatant was removed and the wet weight of membranes weighed.

3.2.2.9 Solubilization of *E. coli* membranes

E. coli membranes were washed 3 times in PBS to remove trace soluble components. Membranes were resuspended to a concentration of 60 mg/mL in either 50 mM sodium acetate, 200 mM NaCl, pH 5.0 or 50 mM sodium phosphate, 200 mM NaCl, pH 7.0. n-Dodecyl β-D-maltoside (DDM) and copolymer stock solutions were made under the same buffering conditions to 2 % (w/v) for DDM and 5 % (w/v) for both SMA and SMI. Membrane resuspensions were mixed with the DDM/ copolymer stocks in a 1:1 ratio and allowed to equilibrate for 2 hours at room temperature. In addition, membranes were diluted to 30 mg/mL with each of the buffers containing no solubilization agent as a control. Insoluble material was removed by ultracentrifugation at 100,000 ×*g* for 45 minutes at 4 °C. The supernatant, corresponding to the solubilized material, was removed. The insoluble pellets were washed three times in PBS and then resuspended in the same volume of 2 % (w/v) sodium dodecyl sulfate (SDS). The soluble and insoluble fractions were then analyzed by SDS-poly(acrylamide) gel electrophoresis (PAGE) using Criterion XT graduated 4 – 12 % acrylamide bis-tris gels following standard protocols. Gels were stained overnight using InstantBlue protein stain.

3.3 RESULTS

3.3.1 SMI-mediated nanodisc self-assembly

We initially investigated whether SMI in the presence of phospholipids is able to self-assemble into discoidal structures. SMI was added to a suspension of 1,2-dimyristoyl-sn-glycero-3-phosphocholine (DMPC) vesicles and analyzed by negative stain transmission electron microscopy (TEM) (Figure 3.1b). The absence of vesicles and the clear presence of discrete particles suggests lipid has been solubilized by SMI. A Gaussian analysis of the size distribution in multiple TEM images (Figure 3.1c) shows a distribution of diameters with two maxima at 6 ± 1 nm and 11 ± 3 nm. This distribution is similar to that previously determined for SMALP nanodiscs by TEM[19,20].

Having confirmed the capability of SMI to form nanoparticles which conform to the size of previously observed nanodiscs[19,20] we tested the thermodynamic efficiency of SMILP self-assembly using ^{31}P-NMR spectroscopy, the principles of which have been described previously [34,40,37,21] (see Figure 3.2). DMPC small unilamellar vesicles (SUVs) alone gave a broad ^{31}P peak. Upon addition of SMI at concentrations below that required for the onset of solubilization (the saturation boundary, c_S^{SAT}) this peak broadened beyond detection. This, we believe, is due to low concentrations of SMI causing aggregation of DMPC, rather than solubilization, as previously reported for SMA(3:1)[21,37], SMA(2:1) [34] and DIBMA [40] polymers. Increasing SMI concentration beyond c_S^{SAT} led to the appearance of an isotropic ^{31}P peak (Figure 3.2a) which linearly increased in area with increasing SMI concentration, corresponding to the proportion of lipids solubilized. Beyond the SMI concentration at which all lipids are solubilized, c_S^{SOL}, all the lipids are present within a nanodisc phase. Plotting ^{31}P peak area against SMI concentration (Figure 3.2b) allowed determination of the c_S^{SAT} and c_S^{SOL} breakpoints at different DMPC concentrations. Plotting the breakpoints obtained as SMI concentration against DMPC concentration (Figure 3.2c), enabled definition of the phase diagram for SMI-mediated solubilization of DMPC SUVs. This phase diagram gives the molar ratios of SMI:DMPC required for saturation, $R_S^{b,\,SAT}$, and solubilization, $R_S^{m,\,SOL}$, from which we can calculate the free energy changes for the vesicle to nanodisc transition associated with DMPC, $\Delta G_{Lipid}^{b\rightarrow m,0}$, and SMI, $\Delta G_{Polymer}^{b\rightarrow m,0}$ [21]. These values are compared (Table 3.1) with equivalent values obtained for two other polymers known to form nanodiscs; SMA2000 and DIBMA. SMA2000 is the SMA polymer variant most similar to SMI structurally and DIBMA is a recently developed polymer[40].

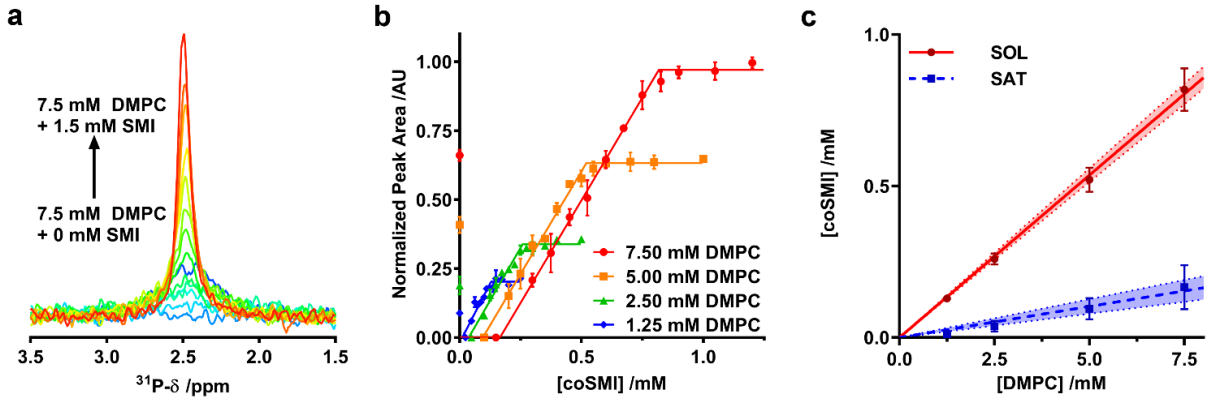

Figure 3.2. Thermodynamics of SMILP self-assembly. **a**. Representative ^{31}P-NMR spectra showing an increasing peak area as 7.5 mM DMPC small unilamellar vesicle suspensions are solubilized by increasing SMI concentration from 0 mM SMI (dark blue spectrum) to 1.5 mM SMI (red spectrum). **b.** Normalized ^{31}P-NMR peak area plotted as a function of polymer concentration with corresponding fits to the experimental data to obtain saturation (SAT) and solubilization (SOL) break points. Each point is the mean of three separate measurements with error bars representing ± standard error. **c**. The phase diagram for SMI solubilizing DMPC constructed using SAT and SOL breakpoints determined from b. The SAT boundary is shown as a blue line and the SOL boundary is shown as a red line. Points represent c_s^{SAT} and c_s^{SOL} breakpoints with error bars representing standard error determined from the fitting procedure in a and b. The shaded region bound by dashed lines represent the 95 % confidence bands associated with linear regression

Table 3.1 Thermodynamic parameters obtained for DMPC-SMILP nanodiscs compared with equivalent data from other nanodisc forming polymers SMA2000[33] and DIBMA.[40]

	SMI	SMA2000	DIBMA
$R_S^{b,\,SAT}$	0.021 ± 0.002	0.050 ± 0.003	0.03 ± 0.005
$R_S^{m,\,SOL}$	0.107 ± 0.013	0.133 ± 0.004	0.062 ± 0.004
$\Delta G_{Lipid}^{b\rightarrow m,0}$ / kJ.mol^{-1}	0.20 ± 0.07	0.19 ± 0.06	0.077 ± 0.01
$\Delta G_{Polymer}^{b\rightarrow m,0}$ / kJ.mol^{-1}	-3.90 ± 0.11	-2.23 ± 0.08	-1.76 ± 0.09

3.3.2 Structural characterization of SMILP nanodiscs

To this point we have assumed that the structure adopted by SMI-DMPC aggregates is, by analogy to SMA, that of a "nanodisc". This conclusion is supported by the provisional structural data presented here.

We have monitored particle size over the self-assembly process using dynamic light scattering (DLS) (Figure 3.3a, Appendix B, Figure B.1). Below the saturation boundary, a large z-average diameter was observed. This agrees well with ^{31}P-NMR data discussed above, and with previous reports using the SMA(2:1) [33,34], SMA(3:1)[21,37] and DIBMA[40] polymers. As polymer concentration increases beyond the SAT boundary, a rapid decrease of z-average diameter and polydispersity index (PDI) is observed (Figure 3.3a). As mentioned above, we believe this corresponds to the solubilization of the large non-uniform vesicles into SMILPs. Beyond the solubilization boundary, the remaining SMILP aggregates continue to decrease in size by 48 % from 11.99 ± 0.26 nm at the SOL boundary to 6.23 ± 0.29 nm diameter at the highest concentration measured. When monitoring the particle size distributions above c_S^{SOL} (Figure 3.3b), a clear shift can be seen towards smaller diameters. These data combined with a relatively constant PDI, suggests that this shift in diameter is not being skewed by excess free polymer in solution. This capacity of SMILPs to be tuneable in size could be beneficial to numerous applications where size is an important parameter.

To improve the structural detail provided by the low resolution DLS data, we have performed small angle X-ray scattering (SAXS) using beamline B21 at Diamond Light Source. We examined SMILPs formed using different polymer:lipid ratios above c_S^{SOL} (Figure 3.3c). The data were fitted with to a polydisperse core-shell bicelle model (Appendix B, Table B.1, Figure B.2) which has been used previously to gain structural insight into SMALP nanodiscs[20], but with a summed ellipsoid model to account for excess SMI. As can be seen in Figure 3.3c, this summed model provided a good fit to the SMILPs. The corresponding fit parameters are shown in Table 3.2. The structural parameters for DMPC (headgroup and tail sizes and scattering lengths) were fixed based on values from comparable studies [20].

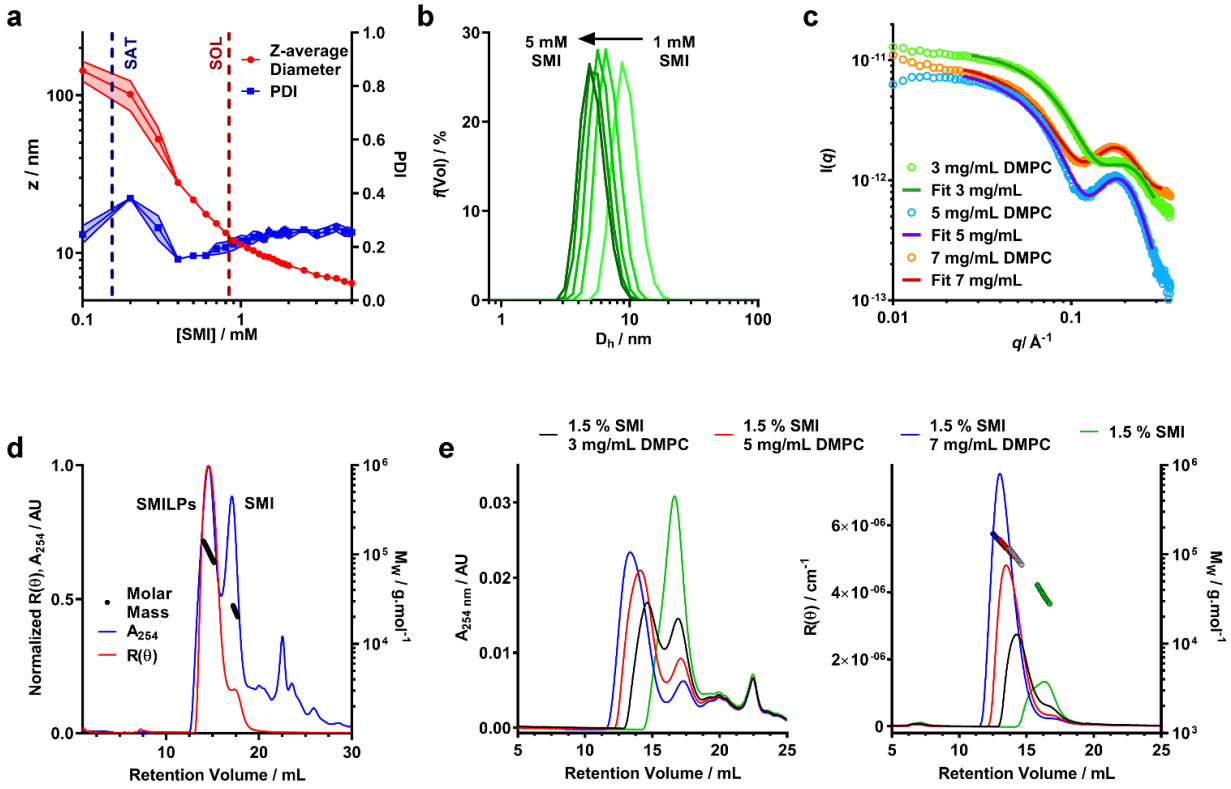

Figure 3.3. Structural characterization of DMPC-SMILP nanodiscs. **a.** DLS data showing the effect of SMI concentration on Z-average diameter (red) and polydispersity Index (PDI - blue). SAT and SOL boundaries obtained from ^{31}P NMR are shown as dashed blue and red lines respectively. Points represent the mean and shaded regions indicate the standard error obtained from three separate experiments. **b.** Volume weighted particle size distribution (PSD) data showing the hydrodynamic diameter (D_h) for SMILPs formed at SMI concentrations above c_s^{SOL}. Lines represent the mean PSD of three separate experiments. Error bars are not shown for clarity. **c.** Small angle X-ray scattering (SAXS) curves for DMPC-SMILPs made with 1.5 % (w/v) SMI with 3, 5 and 7 mg.mL^{-1} DMPC (green, blue and red respectively). Points represent the measured scattering intensity, while lines represent the fit to the experimental data. **d.** SEC-MALS chromatogram corresponding to SMI-DMPC nanodiscs made with 1.5 % (w/v) SMI and 5 mg ml^{-1} DMPC. Traces show the normalized Rayleigh ratio (red trace) and UV absorbance at 254 nm (blue trace) with overlaid mass calculations (black trace). **e.** SEC-MALS chromatograms obtained for SMI (green traces) and SMILPs made with 1.5 % (w/v) SMI and 3, 5 and 7 mg.mL^{-1} (black, red and blue traces, respectively). UV absorbance traces at 254 nm are shown in the left hand graph any Rayleigh ratio traces with overlaid mass calculations (colored circles) are shown in the right hand graph.

Table 3.2. Structural Parameters obtained through fitting of SAXS data for DMPC-SMILP nanodiscs made with fixed SMI concentration (5.56 mM, 1.5 % w/v) and varying DMPC concentrations, in 50 mM sodium acetate, 200 mM NaCl, pH 5. All ratios are above the SOL boundary. Parameters labelled with * were held constant through fitting, using values previously determined for DMPC bilayers[61]. The full list of fit parameters is provided in Appendix B (Table B.1).

DMPC concentration /mg ml^{-1}	3	5	7
Molar ratio [SMI]:[DMPC]	1.26	0.75	0.54
DMPC core diameter/ nm	1.3 ± 0.2	1.9 ± 0.2	2.3 ± 0.2
SMI belt thickness/ nm	1.7 ± 0.2	1.8 ± 0.2	1.6 ± 0.2
DMPC tail length/ nm	2.76 *	2.76 *	2.76 *
DMPC headgroup length/ nm	0.8 *	0.8 *	0.8 *
Overall diameter /nm	4.7 ± 0.6	5.5 ± 0.6	5.6 ± 0.6

The mass of the SMILP nanodiscs was also investigated by size exclusion chromatography with multiple angle light scattering (SEC-MALS)[63] (Figure 3.3d). These data show negligible aggregated material since there is no strong signal eluting from the column at the 8 mL void volume. After this, two major peaks eluted, the first of which shows both strong light scattering intensity, indicating the presence of large particles, and UV absorption signals, indicating the presence of styrene from SMI. We have assigned this peak to SMILPs. It gives a mass averaged M_w of 104.7 ± 0.8 kDa, a number averaged M_n of 102.8 ± 4.4 kDa, resulting in a PDI of 1.02. In-line DLS further confirms the presence of SMILPs; giving a hydrodynamic diameter of 8.68 ± 0.87 nm, consistent with the range of SMILP diameters observed by stand-alone DLS. The second peak shows a strong UV absorbance yet low scattering intensity. The M_w and M_n of this peak are 26.7 ± 3.5 kDa and 26.3 ± 3.31 kDa respectively, giving a PDI of 1.01. A hydrodynamic radius was measured to be 7.44 nm. This peak has been assigned to excess SMI polymer aggregates in solution by account of the decreased scattering intensity yet strong UV absorption. Further downstream peaks were also seen with UV yet gave no discernible scattering

intensity. We propose these peaks are due to the presence of short oligomeric polymers which are present as a by-product of SMI synthesis.

To provide further evidence of the size-tuneability of SMILPs, SEC-MALS was performed on 1.5% SMI and SMILPs made at the same SMI:DMPC ratios as measured by SAXS (Figure 3.3e). SEC-MALS of SMI in the absence phospholipids confirms our earlier assignment of the second peak in Figure 3.3d being due to SMI aggregates. SMILPs formed at higher SMI:DMPC ratios show the same trend as observed by SAXS and DLS, exhibiting higher retention volumes on the column, indicating formation of smaller particles. The M_W calculations from light scattering data and hydrodynamic diameter measured by in-line DLS also agree with this assertion, with SMILPs formed at a higher SMI:DMPC ratio having a both a lower mass and smaller diameter (Appendix B, Table B.2). In addition, the ratio of the UV peaks corresponding to SMILPs and SMI decreases indicating that at higher DMPC concentrations, more SMI associates with the nanodiscs while the proportion of SMI forming lipid-free aggregates in solution decreases.

3.3.3 Stability of SMILPs

A limitation of SMA in many downstream biological applications is the low tolerance to divalent cations and insolubility at low pH. The polyimide structure of SMI inherently means that it behaves differently to SMA. We therefore directly compared the stability of SMALPs and SMILPs in the presence of Ca^{2+} or Mg^{2+} or as a function of pH (Figure 3.4). This was done by measuring the turbidity of nanodisc solutions (Figure 3.4a & 3.b). The data show that SMALPs begin to precipitate at 5 mM Mg^{2+} and 4 mM Ca^{2+}, as indicated by an increased turbidity, with severe precipitation occurring above 10 mM in both cases. SMILPs, however, can tolerate concentrations of Mg^{2+} and Ca^{2+} in excess of 100 mM. The pH dependence for the two polymers shows an intuitive trend; SMALPs are only soluble at pH values above 5.8, but SMILPs are only soluble below pH 7.8. This gives SMILPs a broad working pH range, and importantly allows studies at physiological pH (7.4).

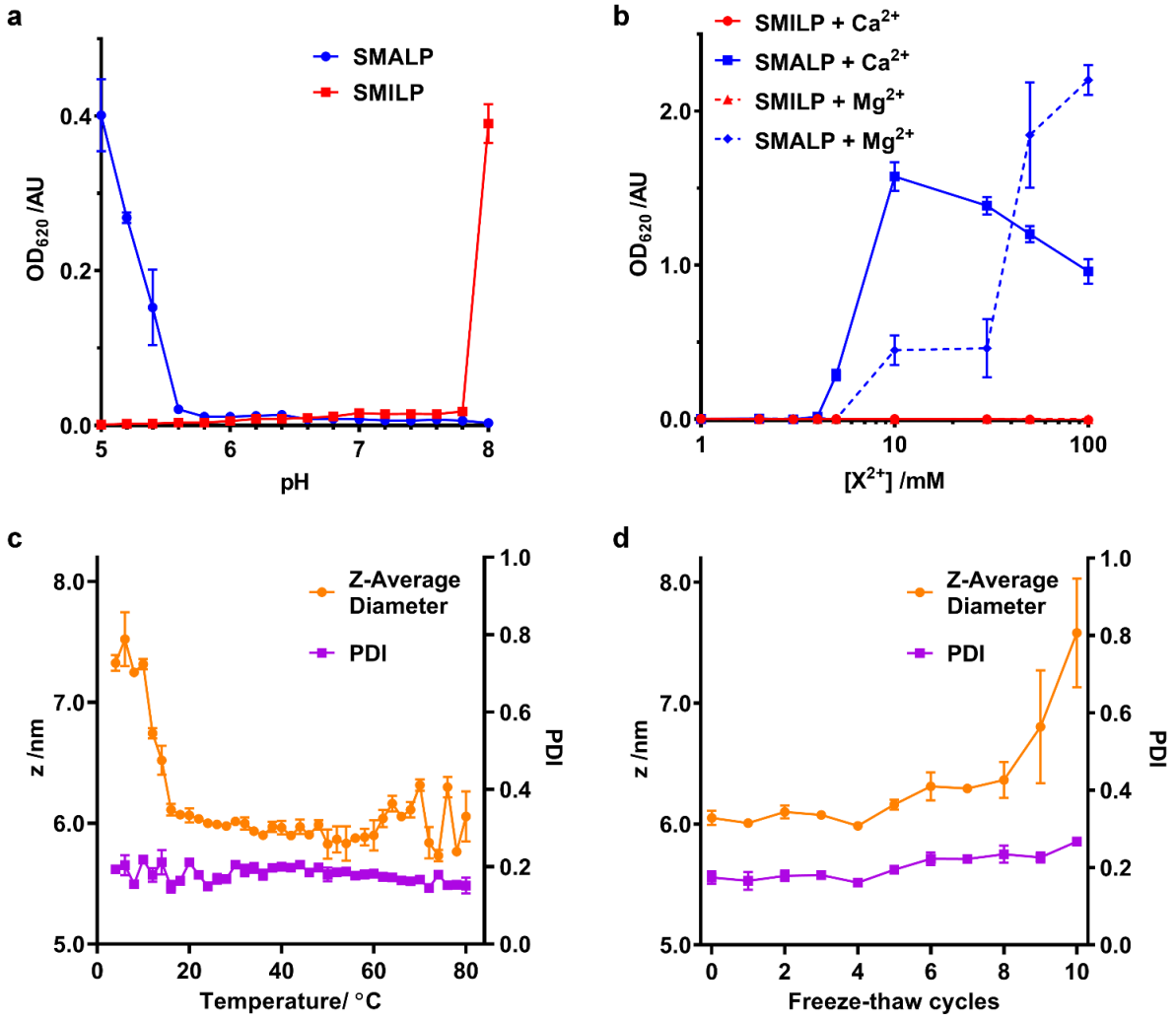

Figure 3.4. Stability of SMILPs. **a.** The turbidity of SMALP and SMILP solutions as a function of pH. Data were recorded at concentrations of 0.33 mg/mL DMPC, 0.1 % w/v SMA or SMI for SMALPs and SMILPs respectively, in 50 mM sodium phosphate, 200 mM NaCl. **b.** The turbidity of SMALP and SMILP solutions in response to increasing concentrations of Mg^{2+} or Ca^{2+}. **c.** DLS data showing the effect of temperature on Z-average diameter (orange) and PDI (magneta) of DMPC-SMILPs (1.5 % w/v SMI, 5 $mg.mL^{-1}$ DMPC, 50 mM sodium acetate, 200 mM NaCl, pH 5). Points represent the mean value taken from three separate experiments with error bars displaying ± 1 standard error. **d.** DLS data showing the effect of freeze-thaw cycles on Z-average diameter (orange) and PDI (magenta) of DMPC-SMILPs (1.5 % w/v SMI, 5 $mg.mL^{-1}$ DMPC, 50 mM sodium acetate, 200 mM NaCl, pH 5). Points represent the mean value taken from three separate experiments with error bars displaying ± 1 standard error.

In addition, SMILPs exhibit high thermal stability as monitored by DLS (Figure 3.4c & d). We observed no significant changes to polydispersity up to 80 ℃ and no changes in diameter over a wide temperature range (16 ℃ - 80 ℃) However, there was a decrease in diameter between 10 ℃ and 16 ℃. Importantly, we observed no signs of aggregation or precipitation at elevated temperature. We also observed that the diameter of the particles increased from 6.05 ± 0.10 nm to 7.58 ± 0.78 nm after multiple freeze-thaw cycles. This is not enough to suggest aggregation or precipitation and no peaks of larger diameter were observed in the associated particle size distributions (Appendix B, Figure B.3). These data indicate that SMILPs are a stable platform which is ideal for applications involving the presence of divalent cations and acidic pH.

3.3.4 SMILP solubilization of membrane proteins from biological membranes

SMA has been widely utilized for the solubilization of membrane proteins. We therefore investigated the efficiency of SMI to solubilize membrane proteins directly from native *Escherichia coli* (*E. coli*) membranes. The solubilizing capability of SMI was compared to that of SMA2000 and to the detergent n-dodecyl β-D-maltoside (DDM), which is commonly employed for solubilizing functional membrane proteins. A control where no solubilizing agent was added to the membranes was also included (Figure 3.5a). Soluble and insoluble fractions were separated by ultracentrifugation and analyzed by SDS-PAGE. SMILP-solubilized samples show a diffuse low molecular weight band that results from the presence of polymer in the soluble fractions at pH 5 and pH 7. Despite this, it is clear that both SMI and DDM effectively solubilize *E. coli* membrane proteins, which are evident in the supernatant fraction (S) at both pH values (Figure 3.5a). In contrast, SMA is ineffective at pH 5. At pH 7 however, both SMI and SMA effectively solubilized membrane proteins, consistent with the pH-dependence data of SMILP and SMALP stability presented in Figure 3.4a. However at pH 7, SMI is less effective than SMA or DDM.

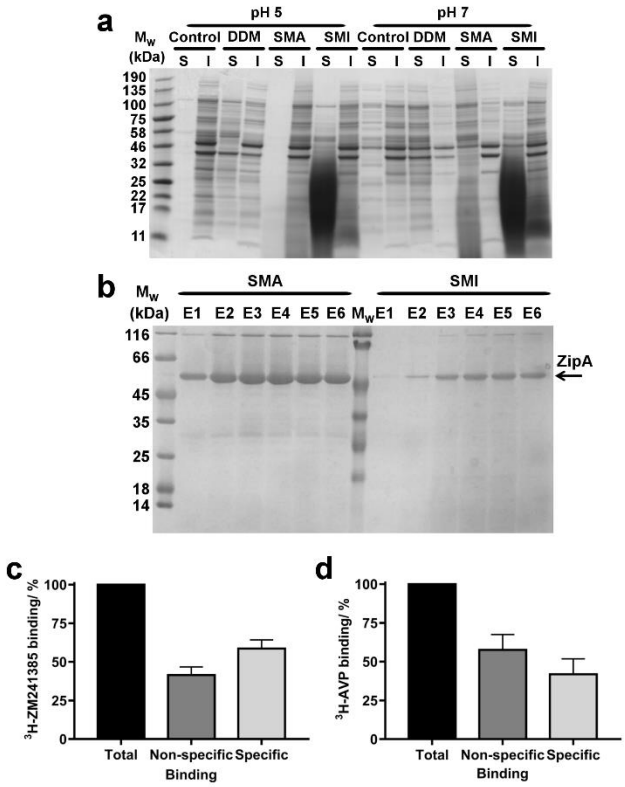

Figure 3.5. The solubilization of membrane proteins using SMI. **a.** Coomassie stained SDS-PAGE showing the range of proteins that have been solublized (S) and remained insoluble (I) after the incubation of *E. coli* membranes with SMI compared to DDM SMA2000 at pH 5 and pH 7. A control using membranes without the addition of SMI, DDM or SMA is also shown. **b.** Coomassie stained SDS-PAGE showing the relative yield and purity of *E.coli* His_6-ZipA extracted with SMA compared with SMI over six elutions (E1 – E6) from Ni^{2+}-NTA IMAC purification. **c.** Binding of [^{3}H]ZM241385 to A_{2A}R-SMILP extracted from HEK 293T cells expressing human A_{2A}R. Non-specific binding was defined by a saturating concentration (1 μM) of ZM241385. **d.** Binding of [^{3}H]vasopressin ([^{3}H]AVP) to V_{1a}R-SMILP extracted from HEK 293T cells expressing human V1aR. Non-specific binding was defined by a saturating concentration (1 μM) of AVP. Binding data are mean ± s.e.m. of three separate experiments performed in triplicate with total binding, non-specific binding and specific binding shown in each case.

In order to be widely adopted, SMILP-solubilized proteins must be amenable to purification techniques. To investigate the yield and purity of SMILP-solubilized compared to SMALP-solubilized proteins, Ni^{2+}-NTA immobilized metal affinity chromatography (IMAC) was performed on *E. coli* ZipA, which has been previously used to determine the efficiency of different SMA polymers[38], after extraction with SMA and SMI (Figure 3.5b). The yield obtained when extracting ZipA using SMI is marginally less than when using SMA, which is corroborated by whole membrane extractions discussed above. Importantly, SMILP-ZipA can be obtained at a higher purity than SMALP-ZipA.

To investigate if the functional capability of membrane proteins was preserved following encapsulation in a SMILP, two G-protein-coupled receptors (GPCRs) were SMILP-solubilized. The human adenosine A_{2A} receptor ($A_{2A}R$) and the human V_{1a} vasopressin receptor ($V_{1a}R$) were each transiently expressed in HEK 293T cells and the cells solubilized by SMI. The binding capability of the SMI-solubilized membranes containing GPCR-SMILPs was determined by radio-ligand binding assays using [^{3}H]ZM241385 as tracer ligand for the $A_{2A}R$ encapsulated in a SMILP ($A_{2A}R$-SMILP) and [^{3}H]vasopressin ([^{3}H]AVP) as tracer ligand for the $V_{1a}R$-SMILP. Non-specific binding was determined in each case by a saturating concentration (1 μM) of unlabeled ligand. The SMILP-solubilized $A_{2A}R$ and $V_{1a}R$ were both functional as specific binding to the receptor was observed for both the $A_{2A}R$-SMILP (Figure 3.5c) and the $V_{1a}R$-SMILP (Figure 3.5d), with 59 ± 6 % and 42 ± 10 % (mean ± s.e.m.) of total binding being specific binding, respectively.

3.4 DISCUSSION

The similarity in the thermodynamic parameters for SMALP self-assembly to those obtained for SMI show that there is a similar thermodynamic driving force for the formation of both SMALPs and SMILPs. In both cases it is the polymer that drives this process, despite the electrostatic differences between SMI and SMA. SMI shows a slightly larger negative free energy change upon interaction with the lipids than SMA, indicating a more favorable self-assembly. As with all other polymers so far studied (SMA(2:1) [33,34], SMA(3:1) [21,37] and DIBMA [40]) there is a small positive free energy change associated with DMPC moving from vesicle to nanodisc. This means that SMI can be thought of as a mild

membrane solubilizer, since it effectively keeps the lipid molecules in a free-energy environment similar to that experienced in vesicles.

When comparing SMI to DIBMA, SMI is more efficient at initiating the onset of solubilization, although higher concentrations of SMI are required for completion of solubilization than that of DIBMA. The free energy change associated with DMPC during nanodisc formation is slightly less positive in "DIBMALPs" than in SMILPs. The driving force for SMI to self-assemble into nanodiscs is over twice as strong as DIBMA, indicating SMILP formation is overall more thermodynamically favored in comparison to DIBMALPs.

SMALPs have been widely reported to have diameters of approximately 10 nm. Data presented here suggest that SMILPs appear slightly smaller. By comparison, pH-resistant SMA-QA polymers form 'macro-nanodiscs' with substantially larger diameters up to approximately 30 nm[51] while the acid-soluble SMAd-A has been observed to form nanodiscs slightly smaller than observed for SMALPs: between 5 – 10 nm[50]. Values from TEM, DLS and SEC-MALS suggest SMILPs have diameters ranging from 12 to 6 nm, similar to SMAd-A nanodiscs. A more in-depth structural investigation of SMILPs using SAXS suggests a smaller overall particle diameter of around 5 nm. This discrepancy in SMILPs analyzed by TEM appearing larger is likely due to negative staining by PTA coating the particles, leading to a larger apparent diameter. DLS and SEC-MALS are similarly affected by the hydration shell around SMILPs, with analysis assuming a spherical particle. SAXS is insensitive to these limitations, providing a more accurate estimation of size, whilst also showing that the adopted structure is consistent with the 'nanodisc' model proposed for SMALPs. The presence of free SMI as determined by SAXS and SEC-MALS may also explain the particle size distribution seen by TEM. The population of smaller particles is most likely due to aggregates formed by excess SMI. This is similar to previous studies of oil microencapsulation by SMI. However, it is also possible that the second population also represents the second dimension of the SMILP nanodisc structure (i.e. it is slightly bigger than the "thickness" of the nanodiscs determined by SAXS: lipid tail + lipid head is ~ 3.5 nm).

The parameters obtained from fitting SAXS data, taking into account the presence of free SMI, indicate that SMILPs are smaller than SMALPs due to a decreased diameter of the phospholipid core. The diameter of the core, however, increases slightly with an increased DMPC:SMI ratio while the thickness of the SMI belt remains unchanged. These data are in agreement with DLS data, suggesting that phospholipid partitions between the available polymer, leading to changes in particle diameter for different relative ratios of DMPC:SMI. Interestingly, SEC-MALS data collected for SMILPs formed at different SMI:DMPC ratios indicate that once formed, excess SMI aggregates can be removed and the different sizes of SMILPs can be maintained through purification. This could have important application to membrane protein solubilization whereby the size of the SMILP can be tuned to optimally accommodate the target protein.

Two of the major limitations of SMALPs have been their insolubility at acidic pH and their very low tolerance of divalent cations. SMILPs display the opposite pH dependence to SMALPs, whilst being able to tolerate higher concentrations of divalent cations than SMALPs and DIBMALPs. Meanwhile, SMILPs show improved thermal stability relative to SMALPs[33], with demonstrated stability up to 80 ℃ and over many freeze-thaw cycles. While a decrease in diameter is observed between 10 and 16 ℃, the mechanism behind this change remains unclear. While it could be indicative of minor lipid loss from increased thermal motion of either the lipids or the polymer, it is also possible that more subtle structural rearrangements occur to which the DLS technique is insensitive. However, regardless of the mechanism of this small change in SMILP size, the absence of any large aggregates and relatively constant PDI up to 80 ℃ indicate SMILPs provide a stable platform for membrane protein solubilization.

When used to solubilize membrane proteins from biological membranes, SMI is effective below pH 7.8 and importantly is effective at the physiological relevant pH of 7.4. This is an important attribute as it allows membrane proteins that cannot tolerate low pH to be studied using SMILPs. The decreased solubilization efficiency of SMI compared to SMA at pH 7 may be due to the size of SMILPs. With such a small lipid core, it is unclear how much native lipid can remain in the SMILP in addition to a membrane protein. SMI does not exhibit any selectivity towards the size of the proteins which are

solubilized within SMILPs, with both high and low M_w proteins being equally represented. This is surprising given the smaller diameter of the lipid core as determined by SAXS. Although SMI forms nanodisc structures in the presence of phospholipids alone, the addition of membrane proteins may lead to SMI acting more as an amphipol rather than a nanodisc, but with the benefit of being able to extract proteins directly from cell membranes. Irrespective of the solubilization mechanism, it is clear that the SMILP-solubilized GPCRs investigated here retain a conformation capable of ligand binding. The $A_{2A}R$ and the $V_{1a}R$ have different binding modes in that the $A_{2A}R$ binds small biogenic amine ligands within the transmembrane helical bundle whereas the $V_{1a}R$ binds larger nonapeptides to a binding site comprising extracellular elements in addition to the helical bundle[64]. Despite differences in their binding modes, both $A_{2A}R$-SMILP and $V_{1a}R$-SMILP retained ligand binding capability. In each case non-specific binding of radio-ligand was expected, resulting from low level ligand partitioning into the lipid bilayer, or the SMI polymer belt. However, the degree of non-specific binding when using GPCR-SMILPs is similar to previously observed for GPCR-SMALPs and low enough to allow accurate measurement of specific binding. The non-specific binding of [^{3}H]ZM241385 to $A_{2A}R$-SMILP was 41 ± 5.3% of total binding, compared to 39 ± 3.8% observed for [^{3}H]ZM241385 binding to the same receptor in a SMALP ($A_{2A}R$-SMALP)[23]. Consequently, using GPCRs as an example, it has been shown that SMI-solubilized membrane proteins remain functional. Furthermore, SMILP-solubilized ZipA can be obtained to a higher degree of purity than SMALP-solubilized ZipA, albeit at a slightly lower yield. This could have important implications for applications such as electron microscopy, where only micrograms of sample are required but at a very high level of purity.

3.5 CONCLUSIONS

Nanodisc technology is becoming widely adopted as a membrane and membrane protein solubilization strategy. The recent development of SMALP nanodiscs provides benefits over other alternative solubilization strategies by being able to solubilize membrane proteins directly from the host cell membrane whilst keeping the annular lipids present within the nanodisc to maintain the native

environment of the membrane protein[29]. SMALPs however are limited by two predominant factors: insolubility at low pH and precipitation in the presence of divalent cations.

We have presented data showing that the positively charged SMI polymer can self-assemble in the presence of phospholipids in acidic conditions to form SMI lipid particle (SMILP) nanodiscs which are both thermally stable and stable in the presence of divalent cations. SMI is also capable of extracting functional membrane proteins directly from biological membranes.

Recent developments in nanodisc-forming polymers have resulted in a range of polymers capable of forming nanodiscs which can solubilize membrane proteins. These polymers, now with the addition of SMI, provide a nanodisc toolbox for the study of membrane proteins, where the nanodisc can be tuned to application. For example, SMA has been successfully utilised for structural studies of membrane proteins by electron microscopy[24,32], X-ray crystallography[31], and solid-state NMR[30] as well as functional studies[23,25,29]. However, the limitations discussed above still apply. For solubilization of larger membrane proteins or complexes, a larger nanodisc may be required. High resolution cryo-transmission electron microscopy also benefits from a larger particle. It has been demonstrated that SMA polymers synthesised by random addition fragmentation chain transfer (RAFT) polymerisation can form larger nanodiscs[43] which would be suited for these studies. Similarly, macro-nanodiscs formed by SMA-QA[51] and SMA-EA[48,49] may prove advantageous for study of membrane proteins by electron microscopy. In addition, structural studies of membrane proteins by 2D solid-state NMR could benefit from the demonstrated magnetic alignment properties of SMA-QA and SMA-EA nanodiscs. For downstream spectroscopic applications such as circular dichroism, DIBMA[40] and PMA[47] are ideal polymers due to the absence of the styrene moiety leading to non-overlapping UV-absorbance signals from the polymer and solubilized proteins. Sulfhydryl-modified SMA (SMA-SH)[44] is capable of solubilizing membrane proteins and is ideal for fluorescence studies and surface-coupling applications such as surface plasmon resonance, where specific chemistries can be easily added to the polymer. Now, we have shown that SMI is the ideal polymer for the solubilization of membrane proteins that require acidic pH or the presence of high concentrations of divalent cations directly from biological membranes. For example,

membrane-associated ATPase enzymes[41] and the calcium-dependant potassium channel superfamily[42] require Mg^{2+} or Ca^{2+} for activity, which would be incompatible with the SMALP system.

Having demonstrated the potential of SMILPs, we will continue our studies of this system to obtain more detail on the structure, function and the mechanism by which it operates. As a first step we have already performed neutron small angle scattering measurements (data currently under analysis) that will provide improved structural detail on the size and shape of SMILPs.

Taken together these data show that SMILPs address some of the long-standing limitations of SMALPs and other existing nanodisc forming polymers. Together this makes SMILPs and important addition to the membrane nanodisc toolbox.

3.6 REFERENCES

(1) Fagerberg, L.; Jonasson, K.; von Heijne, G.; Uhlén, M.; Berglund, L. Prediction of the Human Membrane Proteome. *Proteomics* **2010**, *10* (6), 1141–1149.

(2) Almén, M. S.; Nordström, K. J. V.; Fredriksson, R.; Schiöth, H. B. Mapping the Human Membrane Proteome: A Majority of the Human Membrane Proteins Can Be Classified According to Function and Evolutionary Origin. *BMC Biol.* **2009**, *7*, 50.

(3) Yildirim, M. A.; Goh, K.-I.; Cusick, M. E.; Barabási, A.-L.; Vidal, M. Drug-Target Network. *Nat. Biotechnol.* **2007**, *25* (10), 1119–1126.

(4) Bakheet, T. M.; Doig, A. J. Properties and Identification of Human Protein Drug Targets. *Bioinforma. Oxf. Engl.* **2009**, *25* (4), 451–457.

(5) Arnold, T.; Linke, D. The Use of Detergents to Purify Membrane Proteins. *Curr. Protoc. Protein Sci.* **2008**, *Chapter 4*, Unit 4.8.1-4.8.30.

(6) Smith, S. M. Strategies for the Purification of Membrane Proteins. *Methods Mol. Biol. Clifton NJ* **2011**, *681*, 485–496.

(7) Dürr, U. H. N.; Gildenberg, M.; Ramamoorthy, A. The Magic of Bicelles Lights Up Membrane Protein Structure. *Chem. Rev.* **2012**, *112* (11), 6054–6074.

(8) Popot, J.-L.; Althoff, T.; Bagnard, D.; Banères, J.-L.; Bazzacco, P.; Billon-Denis, E.; Catoire, L. J.; Champeil, P.; Charvolin, D.; Cocco, M. J.; et al. Amphipols from A to Z. *Annu. Rev. Biophys.* **2011**, *40*, 379–408.

(9) Popot, J.-L. Amphipols, Nanodiscs, and Fluorinated Surfactants: Three Nonconventional Approaches to Studying Membrane Proteins in Aqueous Solutions. *Annu. Rev. Biochem.* **2010**, *79*, 737–775.

(10) Denisov, I. G.; Sligar, S. G. Nanodiscs in Membrane Biochemistry and Biophysics. *Chem. Rev.* **2017**, *117* (6), 4669–4713.

(11) Bayburt, T. H.; Grinkova, Y. V.; Sligar, S. G. Self-Assembly of Discoidal Phospholipid Bilayer Nanoparticles with Membrane Scaffold Proteins. *Nano Lett.* **2002**, *2* (8), 853–856.

(12) Mishra, V. K.; Anantharamaiah, G. M.; Segrest, J. P.; Palgunachari, M. N.; Chaddha, M.; Sham, S. W. S.; Krishna, N. R. Association of a Model Class A (Apolipoprotein) Amphipathic α Helical Peptide with Lipid HIGH RESOLUTION NMR STUDIES OF PEPTIDE·LIPID DISCOIDAL COMPLEXES. *J. Biol. Chem.* **2006**, *281* (10), 6511–6519.

(13) Mishra, V. K.; Palgunachari, M. N.; Krishna, R.; Glushka, J.; Segrest, J. P.; Anantharamaiah, G. M. Effect of Leucine to Phenylalanine Substitution on the Nonpolar Face of a Class A Amphipathic Helical Peptide on Its Interaction with Lipid: High Resolution Solution NMR Studies of 4F-Dimyristoylphosphatidylcholine Discoidal Complex. *J. Biol. Chem.* **2008**, *283* (49), 34393–34402.

(14) Midtgaard, S. R.; Pedersen, M. C.; Kirkensgaard, J. J. K.; Sørensen, K. K.; Mortensen, K.; Jensen, K. J.; Arleth, L. Self-Assembling Peptides Form Nanodiscs That Stabilize Membrane Proteins. *Soft Matter* **2014**, *10* (5), 738–752.

(15) Bayburt, T. H.; Sligar, S. G. Membrane Protein Assembly into Nanodiscs. *FEBS Lett.* **2010**, *584* (9), 1721–1727.

(16) Denisov, I. G.; Sligar, S. G. Nanodiscs for Structural and Functional Studies of Membrane Proteins. *Nat. Struct. Mol. Biol.* **2016**, *23* (6), 481–486.

(17) Zhang Meng; Huang Rui; Ackermann Rose; Im Sang-Choul; Waskell Lucy; Schwendeman Anna; Ramamoorthy Ayyalusamy. Reconstitution of the Cytb5–CytP450 Complex in Nanodiscs for Structural Studies Using NMR Spectroscopy. *Angew. Chem. Int. Ed.* **2016**, *55* (14), 4497–4499.

(18) Ravula, T.; Barnaba, C.; Mahajan, M.; Anantharamaiah, G. M.; Im, S.-C.; Waskell, L.; Ramamoorthy, A. Membrane Environment Drives Cytochrome P450's Spin Transition and Its Interaction with Cytochrome B5. *Chem. Commun.* **2017**, *53* (95), 12798–12801.

(19) Knowles, T. J.; Finka, R.; Smith, C.; Lin, Y.-P.; Dafforn, T.; Overduin, M. Membrane Proteins Solubilized Intact in Lipid Containing Nanoparticles Bounded by Styrene Maleic Acid Copolymer. *J. Am. Chem. Soc.* **2009**, *131* (22), 7484–7485.

(20) Jamshad, M.; Grimard, V.; Idini, I.; Knowles, T. J.; Dowle, M. R.; Schofield, N.; Sridhar, P.; Lin, Y.; Finka, R.; Wheatley, M.; et al. Structural Analysis of a Nanoparticle Containing a Lipid Bilayer Used for Detergent-Free Extraction of Membrane Proteins. *Nano Res.* **2015**, *8* (3), 774–789.

(21) Vargas, C.; Arenas, R. C.; Frotscher, E.; Keller, S. Nanoparticle Self-Assembly in Mixtures of Phospholipids with Styrene/Maleic Acid Copolymers or Fluorinated Surfactants. *Nanoscale* **2015**, *7* (48), 20685–20696.

(22) Lee, S. C.; Knowles, T. J.; Postis, V. L. G.; Jamshad, M.; Parslow, R. A.; Lin, Y.-P.; Goldman, A.; Sridhar, P.; Overduin, M.; Muench, S. P.; et al. A Method for Detergent-Free Isolation of Membrane Proteins in Their Local Lipid Environment. *Nat. Protoc.* **2016**, *11* (7), 1149–1162.

(23) Jamshad, M.; Charlton, J.; Lin, Y.-P.; Routledge, S. J.; Bawa, Z.; Knowles, T. J.; Overduin, M.; Dekker, N.; Dafforn, T. R.; Bill, R. M.; et al. G-Protein Coupled Receptor Solubilization and Purification for Biophysical Analysis and Functional Studies, in the Total Absence of Detergent. *Biosci. Rep.* **2015**, *35* (2), e00188.

(24) Postis, V.; Rawson, S.; Mitchell, J. K.; Lee, S. C.; Parslow, R. A.; Dafforn, T. R.; Baldwin, S. A.; Muench, S. P. The Use of SMALPs as a Novel Membrane Protein Scaffold for Structure Study by Negative Stain Electron Microscopy. *Biochim. Biophys. Acta BBA - Biomembr.* **2015**, *1848* (2), 496–501.

(25) Swainsbury, D. J. K.; Scheidelaar, S.; van Grondelle, R.; Killian, J. A.; Jones, M. R. Bacterial Reaction Centers Purified with Styrene Maleic Acid Copolymer Retain Native Membrane Functional Properties and Display Enhanced Stability. *Angew. Chem. Int. Ed Engl.* **2014**, *53* (44), 11803–11807.

(26) Paulin, S.; Jamshad, M.; Dafforn, T. R.; Garcia-Lara, J.; Foster, S. J.; Galley, N. F.; Roper, D. I.; Rosado, H.; Taylor, P. W. Surfactant-Free Purification of Membrane Protein Complexes from Bacteria: Application to the Staphylococcal Penicillin-Binding Protein Complex PBP2/PBP2a. *Nanotechnology* **2014**, *25* (28), 285101.

(27) Long, A. R.; O'Brien, C. C.; Malhotra, K.; Schwall, C. T.; Albert, A. D.; Watts, A.; Alder, N. N. A Detergent-Free Strategy for the Reconstitution of Active Enzyme Complexes from Native Biological Membranes into Nanoscale Discs. *BMC Biotechnol.* **2013**, *13*, 41.

(28) Routledge, S. J.; Mikaliunaite, L.; Patel, A.; Clare, M.; Cartwright, S. P.; Bawa, Z.; Wilks, M. D. B.; Low, F.; Hardy, D.; Rothnie, A. J.; et al. The Synthesis of Recombinant Membrane Proteins in Yeast for Structural Studies. *Methods* **2016**, *95*, 26–37.

(29) Prabudiansyah, I.; Kusters, I.; Caforio, A.; Driessen, A. J. M. Characterization of the Annular Lipid Shell of the Sec Translocon. *Biochim. Biophys. Acta* **2015**, *1848* (10 Pt A), 2050–2056.

(30) Bersch, B.; Dörr, J. M.; Hessel, A.; Killian, J. A.; Schanda, P. Proton-Detected Solid-State NMR Spectroscopy of a Zinc Diffusion Facilitator Protein in Native Nanodiscs. *Angew. Chem. Int. Ed Engl.* **2017**, *56* (9), 2508–2512.

(31) Broecker, J.; Eger, B. T.; Ernst, O. P. Crystallogenesis of Membrane Proteins Mediated by Polymer-Bounded Lipid Nanodiscs. *Structure* **2017**, *25* (2), 384–392.

(32) Parmar, M.; Rawson, S.; Scarff, C. A.; Goldman, A.; Dafforn, T. R.; Muench, S. P.; Postis, V. L. G. Using a SMALP Platform to Determine a Sub-Nm Single Particle Cryo-EM Membrane Protein Structure. *Biochim. Biophys. Acta BBA - Biomembr.* **2017**.

(33) Hall, S. C. L.; Tognoloni, C.; Price, G. J.; Klumperman, B.; Edler, K. J.; Dafforn, T. R.; Arnold, T. The Influence of Poly(Styrene-Co-Maleic Acid) Copolymer Structure on the Properties and Self-Assembly of SMALP Nanodiscs. *Biomacromolecules* **2017**.

(34) Grethen, A.; Oluwole, A. O.; Danielczak, B.; Vargas, C.; Keller, S. Thermodynamics of Nanodisc Formation Mediated by Styrene/Maleic Acid (2:1) Copolymer. *Sci. Rep.* **2017**, *7* (1).

(35) Dominguez Pardo, J. J.; Dörr, J. M.; Renne, M. F.; Ould-Braham, T.; Koorengevel, M. C.; van Steenbergen, M. .; Killian, J. A. Thermotropic Properties of Phosphatidylcholine Nanodiscs Bounded by Styrene-Maleic Acid Copolymers. *Chem. Phys. Lipids* **2017**, *208*, 58–64.

(36) Swainsbury, D. J. K.; Scheidelaar, S.; Foster, N.; van Grondelle, R.; Killian, J. A.; Jones, M. R. The Effectiveness of Styrene-Maleic Acid (SMA) Copolymers for Solubilisation of Integral Membrane Proteins from SMA-Accessible and SMA-Resistant Membranes. *Biochim. Biophys. Acta BBA - Biomembr.* **2017**, *1859* (10), 2133–2143.

(37) Cuevas Arenas, R.; Klingler, J.; Vargas, C.; Keller, S. Influence of Lipid Bilayer Properties on Nanodisc Formation Mediated by Styrene/Maleic Acid Copolymers. *Nanoscale* **2016**, *8* (32), 15016–15026.

(38) Morrison, K. A.; Akram, A.; Mathews, A.; Khan, Z. A.; Patel, J. H.; Zhou, C.; Hardy, D. J.; Moore-Kelly, C.; Patel, R.; Odiba, V.; et al. Membrane Protein Extraction and Purification Using Styrene-Maleic Acid (SMA) Copolymer: Effect of Variations in Polymer Structure. *Biochem. J.* **2016**, *473* (23), 4349–4360.

(39) Scheidelaar, S.; Koorengevel, M. C.; van Walree, C. A.; Dominguez, J. J.; Dörr, J. M.; Killian, J. A. Effect of Polymer Composition and PH on Membrane Solubilization by Styrene-Maleic Acid Copolymers. *Biophys. J.* **2016**, *111* (9), 1974–1986.

(40) Oluwole, A. O.; Danielczak, B.; Meister, A.; Babalola, J. O.; Vargas, C.; Keller, S. Solubilization of Membrane Proteins into Functional Lipid-Bilayer Nanodiscs Using a Diisobutylene/Maleic Acid Copolymer. *Angew. Chem. Int. Ed Engl.* **2017**, *56* (7), 1919–1924.

(41) Møller, J. V.; Juul, B.; le Maire, M. Structural Organization, Ion Transport, and Energy Transduction of P-Type ATPases. *Biochim. Biophys. Acta BBA - Rev. Biomembr.* **1996**, *1286* (1), 1–51.

(42) Guéguinou, M.; Chantôme, A.; Fromont, G.; Bougnoux, P.; Vandier, C.; Potier-Cartereau, M. KCa and Ca2+ Channels: The Complex Thought. *Biochim. Biophys. Acta BBA - Mol. Cell Res.* **2014**, *1843* (10), 2322–2333.

(43) Craig, A. F.; Clark, E. E.; Sahu, I. D.; Zhang, R.; Frantz, N. D.; Al-Abdul-Wahid, M. S.; Dabney-Smith, C.; Konkolewicz, D.; Lorigan, G. A. Tuning the Size of Styrene-Maleic Acid Copolymer-Lipid Nanoparticles (SMALPs) Using RAFT Polymerization for Biophysical Studies. *Biochim. Biophys. Acta BBA - Biomembr.* **2016**, *1858* (11), 2931–2939.

(44) Lindhoud, S.; Carvalho, V.; Pronk, J. W.; Aubin-Tam, M.-E. SMA-SH: Modified Styrene-Maleic Acid Copolymer for Functionalization of Lipid Nanodiscs. *Biomacromolecules* **2016**, *17* (4), 1516–1522.

(45) Stroud, Z.; Hall, S. C. L.; Dafforn, T. R. Purification of Membrane Proteins Free from Conventional Detergents: SMA, New Polymers, New Opportunities and New Insights. *Methods* **2018**.
(46) Oluwole, A. O.; Klingler, J.; Danielczak, B.; Babalola, J. O.; Vargas, C.; Pabst, G.; Keller, S. Formation of Lipid-Bilayer Nanodiscs by Diisobutylene/Maleic Acid (DIBMA) Copolymer. *Langmuir* **2017**, *33* (50), 14378–14388.
(47) Yasuhara, K.; Arakida, J.; Ravula, T.; Ramadugu, S. K.; Sahoo, B.; Kikuchi, J.; Ramamoorthy, A. Spontaneous Lipid Nanodisc Fomation by Amphiphilic Polymethacrylate Copolymers. *J. Am. Chem. Soc.* **2017**, *139* (51), 18657–18663.
(48) Ravula, T.; Ramadugu, S. K.; Di Mauro, G.; Ramamoorthy, A. Bioinspired, Size-Tunable Self-Assembly of Polymer-Lipid Bilayer Nanodiscs. *Angew. Chem. Int. Ed Engl.* **2017**, *56* (38), 11466–11470.
(49) Ramadugu, V. S. K.; Mauro, G. M. D.; Ravula, T.; Ramamoorthy, A. Polymer Nanodiscs and Macro-Nanodiscs of a Varying Lipid Composition. *Chem. Commun.* **2017**, *53* (78), 10824–10826.
(50) Ravula, T.; Hardin, N. Z.; Ramadugu, S. K.; Ramamoorthy, A. PH Tunable and Divalent Metal Ion Tolerant Polymer Lipid Nanodiscs. *Langmuir* **2017**, *33* (40), 10655–10662.
(51) Ravula, T.; Hardin, N. Z.; Ramadugu, S. K.; Cox, S. J.; Ramamoorthy, A. Formation of PH-Resistant Monodispersed Polymer-Lipid Nanodiscs. *Angew. Chem. Int. Ed Engl.* **2018**, *57* (5), 1342–1345.
(52) Samyn, P.; Deconinck, M.; Schoukens, G.; Stanssens, D.; Vonck, L.; Van den Abbeele, H. Synthesis and Characterization of Imidized Poly(Styrene-Maleic Anhydride) Nanoparticles in Stable Aqueous Dispersion. *Polym. Adv. Technol.* **2012**, *23* (3), 311–325.
(53) Samyn, P.; Van Nieuwkerke, D.; Schoukens, G.; Stanssens, D.; Vonck, L.; Van den Abbeele, H. Hybrid Palm-Oil/Styrene-Maleimide Nanoparticles Synthesized in Aqueous Dispersion under Different Conditions. *J. Microencapsul.* **2015**, *32* (4), 336–348.
(54) Rastogi, V. K.; Stanssens, D.; Samyn, P. Reaction Efficiency and Retention of Poly(Styrene-Co-Maleimide) Nanoparticles Deposited on Fibrillated Cellulose Surfaces. *Carbohydr. Polym.* **2016**, *141*, 244–252.
(55) Mie, G. Beiträge zur Optik trüber Medien, speziell kolloidaler Metallösungen. *Ann. Phys.* **1908**, *330* (3), 377–445.
(56) Hassan, P. A.; Rana, S.; Verma, G. Making Sense of Brownian Motion: Colloid Characterization by Dynamic Light Scattering. *Langmuir* **2015**, *31* (1), 3–12.
(57) Koppel, D. E. Analysis of Macromolecular Polydispersity in Intensity Correlation Spectroscopy: The Method of Cumulants. *J. Chem. Phys.* **1972**, *57* (11), 4814.
(58) Zimm, B. H. The Scattering of Light and the Radial Distribution Function of High Polymer Solutions. *J. Chem. Phys.* **1948**, *16* (12), 1093–1099.
(59) Wyatt, P. Light Scattering and the Absolute Characterization of Macromolecules. *Anal. Chim. Acta* **1993**, *272*, 1–40.
(60) Kučerka, N.; Kiselev, M. A.; Balgavý, P. Determination of Bilayer Thickness and Lipid Surface Area in Unilamellar Dimyristoylphosphatidylcholine Vesicles from Small-Angle Neutron Scattering Curves: A Comparison of Evaluation Methods. *Eur. Biophys. J.* **2004**, *33* (4), 328–334.
(61) Wheatley, M.; Wootten, D.; Conner, M. T.; Simms, J.; Kendrick, R.; Logan, R. T.; Poyner, D. R.; Barwell, J. Lifting the Lid on GPCRs: The Role of Extracellular Loops. *Br. J. Pharmacol.* **2012**, *165* (6), 1688–1703.

CHAPTER 4

A STRUCTURAL AND KINETIC INVESTIGATION OF THE INTERACTIONS OF POLYMER-STABILIZED PHOSPHOLIPID NANODISCS WITH INTERFACIAL PHOSPHOLIPID MEMBRANES

Stephen C. L. Hall[†‡], Luke A. Clifton[‖], Cecilia Tognoloni[§], Richard Campbell[○], Kerrie A. Morrison[§], Sophie Meredith[‡], Timothy J. Knowles[†], Tim R. Dafforn[†], Karen J. Edler[§] and Thomas Arnold[‡‖§Δ].

† School of Biosciences, University of Birmingham, Edgbaston, Birmingham, B15 2TT, U.K.

‡ Diamond Light Source, Harwell Science and Innovation Campus, Didcot, OX11 ODE, U.K.

§ Department of Chemistry, University of Bath, Claverton Down, Bath, BA2 7AY, U.K.

‖ ISIS Neutron and Muon Source, Rutherford Appleton Laboratory, Didcot, OX11 0QX, UK

○ Institut Laue-Langevin, 71 Avenue des Martyrs, CS-20156, 38042 Grenoble, France

Δ European Spallation Source ERIC, P.O Box 176, SE-221 00 Lund, Sweden

Author contribution statement

SCLH designed and performed experiments, prepared the samples, analyzed the data and prepared the manuscript. LAC assisted with NR data collection at the Si-water interface, assisted with ATR-FTIR data collection, NR substrate preparation, instrument set-up and provided advice regarding data analysis. CT provided the RAFT-SMA copolymer and assisted with NR data collection at the air-water interface. RC assisted with NR data collection at the air-water interface, performed instrument setup and provided advice regarding data analysis. KAM assisted with NR data collection at the Si-water interface. SM performed preliminary measurements to assist in determining conditions under which to perform NR experiments. TJK assisted with beam time proposals and ATR-FTIR data collection. TRD provided funding, proof read the manuscript and supervised SCLH. KJE conceived the study, assisted with NR data collection at the air-water interface and supervised CT and KAM. TA conceived the study, assisted with NR experimental design and data collection, provided advice on data analysis, proof read the manuscript and supervised SCLH.

Signed:

Stephen Hall

Thomas Arnold 

4.1 ABSTRACT

Over recent years, there has been a rapid development of membrane-mimetic systems to encapsulate and stabilize planar segments of phospholipid bilayers in solution. One such system has been the use of amphipathic copolymers to solubilize lipid bilayers into nanodiscs. The attractiveness of this system, in part, stems from the capability of these polymers to solubilize membrane proteins directly from the host cell membrane. The assumption has been that the native lipid annulus remains intact, with nanodiscs providing a snapshot of the lipid environment. Recent studies have provided evidence that phospholipids can exchange from the nanodiscs with either lipids at interfaces, or with other nanodiscs in bulk solution. Here we investigate kinetics of lipid exchange between three recently studied polymer-stabilized nanodiscs and model lipid membranes at the air-water and silicon-water interfaces. We show that lipid and polymer exchange occurs in all nanodiscs tested, though the rate differs between different nanodisc types and interfaces. This has important implications in applications of polymer-stabilized nanodiscs to membrane protein research.

4.2 INTRODUCTION

The inherent amphiphilic nature of biological membranes has been a persistent challenge when attempting to study membrane proteins (MPs). These molecules represent an important class of biological macromolecules, as exemplified by representing approximately 30% of the protein-coding regions of the human genome and 60% of therapeutic drug targets.[1–3] MPs require stabilization of a hydrophobic, transmembrane core for solubility in aqueous media. This has traditionally been achieved by the use of 'head and tail' surfactants which act by assembling a micelle around the MP of interest, with hydrophobic tails stabilizing the transmembrane regions of the protein, and hydrophilic head groups allowing interactions with the aqueous solvent.[4–6] However, this leads to issues with stability, denaturation and suppression of conformational flexibility which is frequently a bottleneck when attempting *in vitro* studies of isolated MPs.[7,8]

Over the past 20 years there has been a rapid development of alternative solubilization strategies attempting to overcome the limitations of classical surfactant mediated MP solubilization.[9–12] One such solution has been nanodiscs: nanoscale discoidal colloidal particles which consist of a central core of a planar phospholipid bilayer which is stabilized by a 'belt' of a helical amphiphilic membrane scaffold protein (MSP). MSP-nanodiscs have been shown to self-assemble in the presence of synthetic phospholipid vesicles to form a highly monodisperse population of particles whilst allowing precise control over nanodisc diameters.[13,14] When applied to MPs, MSP-nanodiscs have been shown to provide stability and structural homogeneity, superior to surfactant-solubilized MPs, which has allowed for extensive functional and structural studies of nanodiscs both with and without an encapsulated MP using a broad range of techniques.[15–23]

Despite the success of MSP-nanodiscs, MPs still require solubilization using a classical surfactant prior to reconstitution into MSP-nanodiscs. To overcome this bottleneck, an alternative nanodisc technology has been more recently developed. An amphipathic copolymer, poly(styrene-*co*-maleic acid) (SMA), has been shown to self-assemble in the presence of phospholipids to form nanodiscs.[24] These polymer-stabilized nanodiscs, structurally analogous to MSP-nanodiscs but with the lipid core stabilized

by a polymer belt [25], have been termed SMA lipid particles (SMALPs). SMA has the advantage of being able to solubilize MPs directly from the cell membrane, without the need for classical surfactants at any stage.[26] SMALPs have been reported to both maintain protein function and improve stability over classical surfactant solubilized MPs and also MPs in native membranes.[27,28] Furthermore, the capability of SMA to extract MPs directly from the cell membrane maintains a more native-like lipid environment, facilitating functional [29,28,30] and structural [31–34] studies of SMALP-solubilized MPs .

There have now been a number of studies detailing the self-assembly and structure of SMALP nanodiscs from a range of commercially available SMA copolymers.[35–39] This has spawned a drive to develop new nanodisc-forming polymers which are able to form nanodiscs with increased stability, enhanced buffer compatibility, modified size and improved properties for a larger range of downstream applications.[40] One example is the synthesis of SMA polymers by reversible addition-fragmentation chain transfer polymerization (RAFT) polymerization. These polymers have a narrower size distribution than commercial SMA polymers and have a substantially different monomer architecture along the polymer chain, whereby the styrene and maleic acid monomers are initially alternating, tending towards longer poly(styrene) stretches along the length of the chain as maleic acid is consumed throughout the synthesis reaction.[41] RAFT-SMA has been shown to form nanodiscs in a similar manner to commercial SMAs but forming nanodiscs of increased size and with greater thermodynamic efficiency.[39,42]

Another polymer, poly(styrene-*co*-maleimide) (SMI) has recently been shown to form nanodiscs termed SMI lipid particles (SMILPs).[43] In contrast to SMA, SMI contains positively charged dimethylaminopropylamine maleimide in place of maleic acid as the hydrophilic component. This has a number of advantages over SMA, including solubility under acidic conditions and a high tolerance to divalent cations. While SMI is capable of efficiently solubilizing phospholipids to form nanodiscs, SMILPs are somewhat smaller than SMALPs and SMI is less efficient at MP solubilization from biological membranes.

Due to the therapeutic importance of MPs, nanodiscs have gained significant interest in application to characterizing MP-ligand interactions and drug discovery. An increasingly adopted strategy involves

adsorption of the MP of interest to interfaces allowing interaction screens against large compound libraries to be performed using techniques such as surface plasmon resonance (SPR).[44] MSP-nanodiscs have been shown to adsorb to the air-water and Si-water interfaces where the plane of the membrane lies parallel to the surface under investigation.[45] Further studies have shown that MSP-nanodiscs containing cytochrome P450 reductase align at the Si-water interface in a similar manner whilst retaining dynamic conformational flexibility and solvent accessibility of globular, soluble domains.[46,47]

Inspired by this work, the interaction of SMALP nanodiscs containing a phospholipid bilayer with a net-negative charge to synthetic lipid monolayers containing positively charged surfactants was studied using neutron reflectometry. It was hoped that an electrostatic interaction between nanodiscs and lipid interfaces would aid the adsorption process. However, the data could not be fit assuming a meaningful coverage of adsorbed nanodiscs, but instead lipid exchange between the lipids in the monolayers and nanodiscs was found to be the only explanation, providing the first evidence of the phenomenon of lipid exchange occurring with SMALPs.[48]

Lipid exchange between SMALP nanodiscs in solution has since been investigated in more detail. These studies revealed a combination of a rapid collisional and slower monomer diffusion mechanism underlying the transfer of lipids between nanodiscs in solution where the rate of lipid exchange is increased further with increasing ionic strength.[49,50] Furthermore, lipid exchange is not unique to an individual SMA polymer, where RAFT-SMA [48], SMA(2:1) [50] (containing a 2:1 ratio of styrene:maleic acid monomers, tradename Xiran SZ30010) and SMA(3:1) [49] (tradename Xiran SL25010 S25) have now been shown to exhibit rapid lipid exchange between nanodiscs.

While much research has been conducted characterizing lipid exchange between nanodiscs in solution, the interaction with different nanodisc types and model membranes remains relatively unknown. Here, we have investigated the interactions between nanodiscs and lipid monolayers and bilayers at the air-water and Si-water interfaces, respectively as mimics of biological membranes. We have use nanodiscs formed of three polymers: SMA2000 (SMA), SMA2000I (SMI) and a RAFT-synthesized SMA (RAFT-SMA), each containing a 2:1 ratio of styrene:maleic acid (or maleimide in the

case of SMI).[39,43] While lipid exchange at interfaces has been reported for nanodiscs bound by RAFT-SMA,[48] there have been no such reports for SMA2000 or SMI. We determine the kinetics of lipid exchange at these two interfaces using a combination of neutron reflectometry and attenuated total reflection Fourier transform infrared (ATR-FTIR) spectroscopy and show that each nanodisc type exhibits different kinetics for deposition and removal of lipids at each interface measured. Furthermore, contrary to earlier studies, in the process of carrying out these measurements we have observed an adsorption of SMALPs formed by RAFT-SMA to phospholipid bilayers at the Si-water interface in addition to lipid exchange, an unexpected result. While this was not observed at the air-water interface, both interfaces show a localization of polymers at the membrane with each nanodisc system. This provides evidence of a mechanism through which lipid exchange may occur between nanodiscs and planar membranes. The results presented here have important implications in membrane and membrane protein research, challenging the viewpoint of polymer-bound nanodiscs representing a static and kinetically trapped snapshot of a native cell-membrane environment.

4.3 MATERIALS AND METHODS

4.3.1 Materials

Fully hydrogenated 1,2-dimyristoyl-d_{54}-*sn*-glycero-3-phosphocholine (hDMPC) and tail-deuterated d_{54}-DMPC (dDMPC) were purchased from Avanti Polar Lipids. SMA2000 and SMA2000I resin was purchased from Cray Valley. All other chemicals were purchased from Sigma-Aldrich at > 98% purity and used without further purification.

4.3.2 Methods

4.3.2.1 Polymer solubilization

Both RAFT-SMAnh (synthesized as previously described [39,51]) and SMAnh require hydrolysis from the anhydride to the acid forms to become soluble in aqueous solution, and for functionality in SMALP nanodisc self-assembly. Copolymer hydrolysis was performed as previously described.[39] In brief, a 10% w/v suspension of either SMAnh or RAFT-SMAnh in 1 M NaOH was heated under reflux for 2 hrs.

Once the clarified solution had cooled, soluble SMA was precipitated by the dropwise addition of concentrated HCl until pH < 5.0. Precipitated SMA was pelleted by centrifugation at 10,000 ×*g* and washed 3 times in water. After washing, precipitated SMA was dissolved in 0.6 M NaOH and incubated at 37°C for 16 hours before repeating the precipitation and washing procedure. The final hydrolyzed SMAs were again dissolved in a minimal volume of 0.6 M NaOH, adjusted to pH 8.0 by dropwise addition of concentrated HCl, lyophilized and used without further purification.

Similarly SMI was solubilized as previously described [43]. This was essentially performed in the same manner as for both SMA copolymers, except 10% w/v SMA2000I resin in 1 M HCl was heated under reflux for 2 hours. The precipitation and washing procedure was identical as for SMA, except the polymer was precipitated by the dropwise addition of 5 M NaOH until pH > 9.0 prior to redissolution in 0.6 M HCl. After washing, precipitated, solubilized SMI was dissolved in a minimal volume of 0.6 M HCl, adjusted to pH 5.0 by dropwise addition of 5 M NaOH, lyophilized and used without further purification.

4.3.2.2 Nanodisc preparation

hDMPC or dDMPC powder was dissolved in $CHCl_3$ and dried under a stream of N_2 to create a multilamellar lipid film around a glass vial. Vials were desiccated for at least 2 hours to remove residual solvent. For experiments using SMA, lipids were rehydrated in 50 mM sodium phosphate, 200 mM NaCl, pH 8.0 to 5 mg/mL. For experiments using SMI, lipids were rehydrated in 50 mM sodium acetate, 200 mM NaCl, pH 5.0. In all cases, the buffer was warmed to 30°C and lipids hydrated to 10 mg/mL. Vesicles were formed by sonication at 30°C for 30 minutes. 3% w/v polymer was prepared in the appropriate buffer (SMA - 50 mM sodium phosphate, 200 mM NaCl, pH 8.0; SMI - 50 mM sodium acetate (NaOAc), 200 mM NaCl, pH 5.0) and added to vesicles at a 1:1 v/v ratio to a final volume of 10 mL. The nanodisc solutions were allowed to equilibrate at room temperature for 24 hours. Nanodiscs were concentrated in 10,000 MWCO centrifugal concentrator tubes to a volume of 3 mL. Concentrated nanodiscs were purified by size exclusion chromatography (SEC) using a HiLoad Superdex 200 26/600 column, equilibrated in the same buffer, attached to an Äkta purification system (GE Healthcare Life

Sciences, Buckinghamshire, UK) monitoring absorbance at 254 nm (Appendix C, Figure C.1). Fractions containing nanodiscs, as confirmed by dynamic light scattering (Appendix C, Figure C.2), were pooled, flash frozen in liquid nitrogen and stored at -80°C.

4.3.2.3 Langmuir trough measurements

Buffer was made as described above (Na_2HPO_4 pH 8.0 for SMAs and NaOAc pH 5.0 for SMI) in H_2O or D_2O. Buffers were made in air-contrast-matched water (ACMW) by the addition of 8.9% w/w deuterated buffer to hydrogenated buffer. A Teflon Langmuir trough was cleaned with EtOH and $CHCl_3$ before the addition of ACMW buffer. Temperature was maintained at 25°C. After sufficient wetting of the Wilhelmy plate, 45 µL of 0.5 mg/mL hDMPC or dDMPC in $CHCl_3$ was spread on the surface and $CHCl_3$ allowed to evaporate for 10 minutes. Three compression-expansion cycles were performed between 0 and 40 $mN \cdot m^{-1}$ before the surface area was compressed to a surface pressure of 10 $mN \cdot m^{-1}$ and the surface area maintained. Nanodiscs in ACMW were injected into the subphase to a final polymer concentration of 0.5 µM and the surface pressure monitored as a function of time.

4.3.2.4 Neutron reflectometry (NR) at the air-water interface

Neutron reflectometry (NR) was performed using the FIGARO reflectometer at the Institut Laue-Langevin.[52] Detailed descriptions of the theoretical basis of NR, instrumental details and applications to soft-matter have been described in depth elsewhere,[53–55] so here we will only include a brief description of the technique. NR measures the specular reflection of neutrons as a function of the scattering vector perpendicular to the surface normal (Q_z), defined by:

$$Q_z = \frac{4\pi \sin\theta}{\lambda}$$

where θ represents the angle of reflection and λ represents the wavelength of the reflected neutrons. The reflected intensity is dependent on the structure and scattering length density (SLD) of the material at the interface, as well as the scattering length density of the bulk phases through an inverse Fourier transform. The SLD of a molecule is defined as:

$$\rho = \frac{\sum_{i=1}^{n} b_c}{V_m}$$

where SLD, ρ, is given by the sum of the coherent scattering lengths, b_c, for each atomic nuclei, n, within a given molecular volume, V_m. Due to the distinctly different neutron scattering lengths of deuterium and hydrogen (-3.74 × 10^{-5} Å and 6.67 × 10^{-5} Å, respectively), NR is very sensitive to the incorporation of hydrogenated material from nanodiscs into a deuterated monolayer, or *vice versa*. As FIGARO is a time-of-flight instrument, the reflectivity was measured at two fixed angles, θ = 0.62 and 3.8° with a wavelength range of 2 – 30 Å covering an effective Q_z range of 0.01 to 0.3 $Å^{-1}$ with a wavelength resolution (δλ/λ) of 7%. Structural measurements covering the full obtainable Q_z range were collected before the injection of nanodiscs, and 2 hours after nanodisc injection. Specular reflectivity was measured for 10 minutes at θ = 0.62° and 30 minutes at θ = 3.8°. The resulting reflectivity curves were normalized against the direct beam and "stitched" together. For kinetic measurements, only θ = 0.62° was collected, measuring for 30 seconds for the first 15 minutes after nanodisc injection, and then measuring for 2 minutes for a further 100 minutes.

4.3.2.5 Analysis of Langmuir monolayer structure at the air-water interface

Full-Q NR data were analyzed using RasCAL software running within MATLAB.[56] Due to the loss of phase information upon measuring the reflected neutron intensity, it is not possible to directly transform the experimental data to obtain the interfacial structure. Instead, a theoretical reflectometry pattern was back-calculated for a model scattering length density profile, and iteratively, simultaneously fit to the experimental data for monolayers of hDMPC and dDMPC on ACMW. Within the model, lipid tails and lipid headgroups were treated as individual homogenous layers, each with an SLD, thickness, interfacial roughness and solvent volume fraction. The models were constrained such that the surface excess of phospholipid tails matches that of the head groups to represent a physically relevant monolayer. This was achieved by calculating a mean molecular area from the thickness of the phospholipid tail layer, where

$$A_{Tails} = \frac{V_{m,Tails}}{d_{Tails}}$$

Here, A_{Tails} represents the mean molecular area associated with the phospholipid tails, $V_{m,Tails}$ represents the partial specific molecular volume of the phospholipid tails and d_{Tails} corresponds to the fitted thickness of the tail layer. Solvent penetration into the tail layer was assumed to be negligible. Similarly the apparent hydrated area of the lipid headgroups, $A_{Heads,Hyd}$, can be calculated as

$$A_{Heads,Hyd} = \frac{V_{m,Heads}}{d_{Heads}}$$

Where $V_{m,Heads}$ represents the partial specific molecular volume of headgroups as d_{Heads} represents the fitted thickness of the headgroup layer. As the mean molecular area of the headgroups must equal that of the phospholipid tails, the volume fraction of 'dry' lipid headgroups, χ_{Heads}, within the layer can be calculated as

$$\chi_{Heads} = \frac{A_{Heads,Hyd}}{A_{Tails}}$$

Allowing calculation of the volume fraction of solvent, $\chi_{Solvent}$, in the headgroup layer from

$$\chi_{Solvent} = 1 - \chi_{Heads}$$

This allows direct calculation of headgroup hydration throughout the fitting procedure to ensure the model describes a physically feasible monolayer. Furthermore, d_{Tails} and d_{Heads} were constrained to not exceed the maximum thickness for a fully extended conformation. These values were calculated using the trigonometric law of cosines from ideal bond angles and bond lengths as 16 and 12 Å, respectively. We made the assumption that DMPC remains in the liquid expanded (LE) phase throughout the measurement (π = 10 mN·m^{-1}, T = 25°C) such that the molecular volumes, and therefore SLDs, remain unchanged for pure hDMPC and dDMPC. Literature values for the partial specific molecular volumes of PC headgroups (281.9 Å^3) and dimyristoyl tails (779.0 Å^3) were used to calculate the SLD throughout.[57] Additionally surface roughness between layers held constant to account for surface capillary waves at fluid interfaces with surfactant-induced decreased surface tension.[58] After

injection of nanodiscs, the SLD of the tail region was allowed to vary through the fitting procedure to allow for the incorporation of different isotopically labelled molecules into the monolayer from the nanodiscs. Due to the lack of available contrasts, and restricted Q_z range to accurately model subtle structural changes to the monolayer upon nanodisc interactions, the remainder of the parameters were fixed according to the structural model fit prior to nanodisc injection. The error associated with each fitted parameter was estimated using Markov chain Monte Carlo (MCMC) methods implemented within RasCAL to account for the covariance between parameters. We assumed a Gaussian prior distribution for each parameter. The posterior distribution was determined by performing 50,000 iterations with 5,000 burn-in points to allow for location of the global minima. The 95% confidence interval was then calculated from the posterior distribution obtained after three independent repeat runs. For any individual contrast, the smallest real space structures which can be resolved by defined features in the data is given by $d_{min} = 2\pi/Q_{max}$, though structures smaller than this limit can be inferred by using multiple contrasts, either interfacial or bulk. Throughout this work, we have quoted fit parameters and errors to the nearest ångström to account for both the limited contrasts and Q_z range.

4.3.2.6 Analysis of lipid exchange kinetics at the air-water interface

The application of specular NR to perform kinetic studies has been recently described in detail elsewhere.[59,53] Therefore, here only a brief description will be given. At low *Q,* the reflected intensity is dependent solely on the scattering excess, defined as product of total layer thickness (d) and the total SLD (ρ), with no contribution of interfacial structure. By restricting the measured Q_z range to 0.01 Å^{-1} – 0.04 Å^{-1}, and maximizing neutron flux at the expense of Q_z-resolution, the scattering excess can be monitored in real time without sacrificing time resolution. From, the scattering excess, the surface excess, Γ, can be calculated:

$$\Gamma = \frac{\rho d}{N_A b_i}$$

where N_A represents Avogadro's constant and b_i represents the coherent scattering length. In this case, the total scattering excess is governed by a combination of the surface excess of two components:

hDMPC and d_{54}DMPC, from either the spread monolayer (Γ_M), or the nanodiscs in solution (Γ_N). For each of the two measured contrasts (d_{54}DMPC nanodiscs exchanging with hDMPC monolayer and *vice versa*), the measured scattering excess is governed by a combination of the surface excess of each of the two components, the scattering lengths of d_{54}DMPC and hDMPC (b_D and b_H, respectively) and Avogadro's constant:

$$\rho d_{c1} = (\Gamma_M b_H + \Gamma_N b_D) N_A$$

$$\rho d_{c2} = (\Gamma_M b_D + \Gamma_N b_H) N_A$$

The scattering excess at each time point was obtained by fitting the scattering length density of the tail layer within the model obtained with full-Q data. This allows, at each measured time point, calculation of the surface excess of the lipids originating from the nanodiscs in solution:

$$\Gamma_N = \frac{b_D \rho d_{c1} - b_H \rho d_{c2}}{N_A({b_D}^2 - {b_H}^2)}$$

and lipids originating from the spread monolayer:

$$\Gamma_M = (\frac{\rho d_{c1}}{N_A} - \Gamma_N b_D){b_H}^{-1}$$

Surface excess values were then plotted with respect to time and kinetic equations fit to these data by non-linear regression. Lipid exchange at the air-water interface from nanodiscs to DMPC monolayers was modelled by a two-phase, first order process which was fit to the experimental surface excess data for lipid originating in the nanodiscs (Γ_N):

$$\Gamma_{N,t} = \Gamma_{N,0} + \Delta\Gamma^{eq}_{N,0,Fast}(1 - e^{-k_{N\rightarrow M,Fast}\cdot t}) + \Delta\Gamma^{eq}_{N,0,Slow}(1 - e^{-k_{N\rightarrow M,Slow}\cdot t})$$

where the surface excess of lipid from the nanodiscs at the air-water interface at time t, $\Gamma_{N,t}$, can be described by two first order rate constants for a fast and slow lipid exchange from the nanodiscs to the monolayer, $k_{N\rightarrow M,Fast}$ and $k_{N\rightarrow M,Slow}$, respectively. Each process is responsible for a proportion of the

decrease from the initial surface excess, $\Gamma_{N,0}$, to that at equilibrium , $\Gamma_{N,eq}$, described by $\Delta\Gamma^{eq}_{N,0,Fast}$ and $\Delta\Gamma^{eq}_{N,0,Slow}$ for the fast and slow processes, respectively.

Single-phase first order kinetic equations were fit to the experimental data showing the decrease in surface excess of lipids originating in the monolayer (Γ_M):

$$\Gamma_{M,t} = (\Gamma_{M,0} - \Gamma_{M,eq})e^{-k_{M\rightarrow N,Diss}\cdot t} + \Gamma_{M,eq}$$

where the rate of decrease in surface excess of lipids originating at the monolayer at time *t*, $\Gamma_{M,t}$, between the initial surface excess, $\Gamma_{M,0}$, and the surface excess at equilibrium, $\Gamma_{M,eq}$, can be described by a single dissociative first-order rate constant, $k_{M\rightarrow N,Diss}$. In the case of exchange from the monolayer to SMALP nanodiscs, a single dissociative rate constant was not sufficient to provide satisfactory fits to the experimental data. Here, a combination of first-order decay and first-order association was applied:

$$\Gamma_{M,t} = (\Gamma_{M,0} - \Gamma_{M,eq,Diss})e^{-k_{M\rightarrow N,Diss}\cdot t} + (\Gamma_{M,eq,Ass}(1 - e^{-k_{M\rightarrow N,Ass}\cdot t})$$

where $k_{M\rightarrow N,Diss}$ is the dissociative rate constant, $\Gamma_{M,eq,Diss}$ is the equilibrium position of the dissociation process, $k_{M\rightarrow N,Ass}$ is the associative rate constant and $\Gamma_{M,eq,Ass}$ is the equilibrium position of the associative process.

4.3.2.7 ATR-FTIR at the silicon-water interface

Attenuated total reflection Fourier transform infrared spectroscopy (ATR-FTIR) provides a qualitative analysis of the chemical bonds present at a surface. An infrared (IR) beam is totally internally reflected through a substrate in contact with bulk solvent, where the refractive index of the substrate, n_1, must be higher than that of the solvent, n_2, to allow for total internal reflection. As the beam is reflected from the substrate-solvent interface, the beam penetrates into the solvent, with a depth, d, given by:

$$d = \frac{\lambda}{2\pi\sqrt{sin^2\theta - (n_1/n_2)^2}}$$

where λ is the wavelength of the IR light and θ is the angle of incidence of the beam at the interface.[60] This penetration depth is on the order of a few microns, resulting in sensitivity to material adsorbed to

the substrate. The absorption of IR light within the penetration depth occurs when the characteristic frequency of vibrational modes of a given chemical bond matches the frequency of the incident light. As deuterium has a higher mass than hydrogen, the vibrational frequency of deuterium-containing bonds is higher than hydrogen-containing bonds, resulting in absorption of higher frequency IR light.

ATR-FTIR spectra were collected using a ThermoNicolet Nexus instrument fitted with an ATR flow cell accessory (Specac) attached to a calibrated syringe pump, a cryo-cooled mercury cadmium telluride detector and a dry-air purge operating at a flow rate of 40 L/min in order to minimize absorbance from residual water vapor in the beam path. All spectra were collected with a resolution of 4 cm^{-1} and 128 interferograms collected for each spectra. Throughout the measurements, temperature was maintained at 25°C by a temperature controlled water cooling loop passing through hollow aluminium blocks in direct contact with the Si substrate and the aqueous superphase.

Silicon ATR substrates were cleaned by sonication in 2% (w/v) SDS for 30 minutes before rinsing extensively with ultrapure water and drying under a stream of nitrogen. Substrates were then UV-ozone cleaned for 10 minutes, washed with ultrapure water and then UV-ozone cleaned a final time for 10 minutes. The substrate was mounted in a dry flow cell and the volume filled with either 50 mM Na_2HPO_4, 200 mM NaCl, pD 8.0 in D_2O for measurements using SMALPs and RAFT-SMALPs, or 50 mM NaOAc, 200 mM NaCl, pD 5.0 in D_2O for measurements using SMILPs. A background spectra was taken of the bare Si substrate in the appropriate buffer and subtraction spectra collected for later removal of water vapor absorbance. 20 µL d_{54}DMPC as a 10 mg/mL stock in $CHCl_3$ (Avanti) was transferred to a clean glass vial and dried under a stream of nitrogen. Lipid films were rehydrated in either Na_2HPO_4 or NaOAc buffer as described above to a concentration of 0.1 mg/mL. The lipid suspension was sonicated in a sonic bath for 30 minutes leading to small unilamellar vesicle (SUV) formation prior to centrifugation at 14,000 × *g*, 25°C for 10 minutes to pellet large aggregates. A 2 mL dDMPC SUV suspension was manually injected into the flow cell and incubated for 20 minutes with continuous spectra collection to allow for deposition of the d_{54}DMPC bilayer until no further spectral changes were observed. The flow cell was then flushed with 2 mL buffer at a flow rate of 0.5 mL/min

and a spectrum collected of the supported d_{54}DMPC bilayer at the Si-water interface. Nanodiscs were diluted to 50 μM polymer concentration and 2 mL manually injected into the flow cell over the d_{54}DMPC bilayer. The deuterated bilayer was incubated with the hDMPC nanodiscs for 300 minutes. Spectra were continuously recorded with a time resolution of 80 s.

Fourier self-deconvolution was performed automatically by the OMNIC data acquisition software with a constant amplitude and bandwidth applied for all spectra. All spectra were corrected for removal of water vapor absorbance bands by scaling and subtraction of spectra collected before the deposition of the d_{54}DMPC bilayer from the bilayer spectra. No further processing was performed.

ATR-FTIR peak integrations were preformed over the aliphatic C-H stretching and aliphatic C-D stretching regions from 2990 – 2810 cm^{-1} and 2230 – 2050 cm^{-1}, respectively. This includes contributions from the symmetric and asymmetric C-H_2/ C-D_2 stretching vibrations and the C-H_3/ C-D_3 stretching vibrations arising primarily from the aliphatic phospholipid tails. Due to the different frequencies and amplitudes of C-H and C-D bond vibrations, this allows the relative changes in hydrogenated and deuterated material at the Si-water to be compared as a function of time.

4.3.2.8 Analysis of lipid exchange kinetics at the Si-water interface

Analogously to our NR measurements at the air-water interface, the exchange of d_{54}DMPC from bilayers at the Si-water interface to nanodiscs in bulk solution was modelled by a two-phase first order process which was fit to the experimental data by non-linear regression:

$$I_t = I_{eq} + \Delta I^{eq}_{0,Fast} e^{-k_{B\rightarrow N,\ Fast}\cdot t} + \Delta I^{eq}_{0,Slow} e^{-k_{B\rightarrow N,\ Slow}\cdot t}$$

where the Integrated area at time t, I_t, can be described by two relative first order rate constants for a fast and slow process, k_{Fast} and k_{Slow}, respectively and the proportion of the decrease of the initial integrated area, I_0, to that at equilibrium, I_{eq}, for which each process is responsible, $\Delta I^{eq}_{0,Fast}$ and $\Delta I^{eq}_{0,Slow}$.

The exchange of hDMPC from the nanodiscs to the bilayer showed more variation between different nanodisc systems. Therefore, each process was modelled by both a single-phase first order process:

$$I_t = I_0 + \left(I_{eq} - I_0\right) \cdot (1 - e^{-k \cdot t})$$

and two-phase first order process:

$$I_t = I_0 + \Delta I_{0,Fast}^{eq}(1 - e^{-k_{Fast} \cdot t}) + \Delta I_{0,Slow}^{eq}(1 - e^{-k_{Slow} \cdot t})$$

which were fit to the experimental data by nonlinear regression. The model with the highest probability of being correct was then selected by performing the Akaike's Information Criteria (AIC) test implemented within GraphPad Prism.

4.3.2.9 NR at the Si-water interface

Polished single crystal silicon blocks with surface dimensions of 50 × 80 mm were cleaned by immersion in piranha solution (5:3:1 H_2O:H_2SO_4:H_2O_2 heated to 80°C) followed by two cycles of extensive washing in ultrapure water and ozone cleaning. Clean Si blocks were then mounted in sealed PTFE lamellar flow cells underwater to avoid introduction of air bubbles during cell assembly.

Data for the interaction of SMALPs and RAFT-SMALPs with d_{54}DMPC bilayers at the Si-water interface were collected using the Polref reflectometer (ISIS neutron and muon source, UK) in TOF-NR setup in event mode. NR was measured at three angles: 0.5, 1.2 and 2.5 ° with a neutron wavelength range of 1 – 14 Å covering an effective Q_z-range of 0.01 – 0.3 $Å^{-1}$ where δQ/Q is 2.88%. Data for the interaction of SMILPs with d_{54}DMPC bilayers at the Si-water interface were measured using the Surf reflectometer (ISIS neutron and muon source, UK) using time-of-flight-NR setup in event mode. NR was measured at three incident angles: 0.35, 0.65 and 1.5 ° with a neutron wavelength range of 0.55 – 6.8 Å covering a similar Q_z-range of 0.012 – 0.3 $Å^{-1}$. In both instruments, Si crystal flow cells were mounted on a horizontal geometry translation stage and connected to a HPLC pump in order to change solution contrasts. The measured reflected neutron intensity was normalized to the incident neutron flux measured in transmission through each substrate.

Si crystal substrates were initially characterized by NR in H_2O and D_2O buffers (50 mM Na_2HPO_4, 200 mM NaCl, pH 8 for substrates to be injected with SMALP and RAFT-SMALP nanodiscs and 50

mM NaOAc, 200 mM NaCl pH 5 for substrates to be injected with SMILP nanodiscs). dDMPC in chloroform was transferred to a clean glass vial and dried under a stream of nitrogen. Lipids were rehydrated to 0.3 mg/mL in 20 mM HEPES pH 7 and small unilamellar vesicles (SUVs) formed by sonication in a water bath for 30 min. 10 mL of d_{54}DMPC was manually injected into each flow cell and incubated for 40 min to allow for vesicular rupture and bilayer deposition on the Si substrates. Resultant bilayers were characterized by NR in H_2O, D_2O and silicon-matched water (SiMW, 38% v/v D_2O) buffers as described above. SEC-purified Nanodiscs were diluted to 50 μM polymer concentration in the appropriate deuterated buffer and 15 mL flowed over the supported bilayers at a flow rate of 1.2 mL/min. Nanodiscs were incubated for 5 hours and NR measured to characterize the bilayer structure before removing nanodiscs in the bulk solution. Excess nanodiscs in bulk solution were removed by flushing the flow cells with deuterated buffer and the final interfacial structure characterized in H_2O, D_2O and SiMW.

4.3.2.10 Analysis of lipid bilayer structure at the Si-water interface

As with structural analysis of lipid monolayers at the air-water interface, NR data corresponding to lipid bilayers at the Si-water interface were analyzed using RasCAL[56] by generating a model SLD profile from which a theoretical reflectometry pattern is calculated and iteratively fit to the experimental data in order to minimize the χ^2 value. Data for each Si substrate before bilayer deposition were simultaneously analyzed using two solution contrasts of H_2O and D_2O using a single layer model corresponding to SiO_2. The SLD of Si and SiO_2 were fixed based on literature values and the only parameter which varied between the individual contrasts is the SLD of the bulk solution to account for different isotopic contrasts measured. This model was then fit to the experimental data in order to define the thickness, hydration and roughness of the SiO_2 layer. These parameters were then held as a constant throughout subsequent fitting procedures. Following this, NR data corresponding to d_{54}DMPC bilayers characterized in three solution contrasts (H_2O, SiMW and D_2O) were analyzed. A five-layer model was fit to the experimental data with layers corresponding to SiO_2, inner leaflet phosphatidylcholine headgroups, two identical layers corresponding to dimyristoyl tails and outer leaflet phosphatidylcholine

headgroups. We made the assumption that the bilayer was symmetrical across each leaflet and applied the same constraints as described above for analysis of lipid monolayer structure at the air-water interface, such that the mean molecular area is consistent for both headgroup and tail layers ensuring that the resulting model represents a physically feasible bilayer structure. However, due to the high likelihood for incomplete bilayer coverage, an additional parameter was included in the initial calculation of the mean molecular area accounting for the solvent volume fraction within the tail layer, $\chi_{Solvent}$, where the area per molecule is calculated as

$$A_{Tails} = \frac{V_{m,Tails}}{d_{Tails}(1 - \chi_{Solvent})}$$

Subsequent calculation of the lipid headgroup hydration was performed identically to that described above for the lipid monolayer case with the same constraints applied. SLD values for the headgroups were calculated based on literature values for partial specific molecular volumes[57] and held as a constant. Fixing the SLD of the deuterated phospholipid tails was unable to produce satisfactory fits to the measured data, therefore the SLD was fit to take into account incomplete acyl chain deuteration. Several studies have previously reported incomplete deuteration of phospholipid tails, providing justification for relaxing this constraint.[25,61] Surface roughness was fit and constrained to be equal for all layers within the lipid bilayer, taking into account the physical coupling between the layers.

In order to analyze the bilayer structure after nanodisc interaction, data corresponding to the bilayer after interaction with nanodiscs characterized in three solution contrasts (H_2O, SiMW and D_2O) were simultaneously analyzed. Here, the only parameter fit was the mole fraction of hydrogenated tails within the bilayer to account for lipid exchange between the bilayer and nanodiscs. All other parameters describing the bilayer structure were held as constant. While subtle structural changes to the lipid bilayer were able to produce slight improvements in the fits, we opted for the simplest model as the resolution of the data is insensitive to minor changes to bilayer structure at the precision implied by the fitting parameters.

In the case of analysis of lipid bilayer structure after interaction of RAFT-SMA, in order to model the appearance of Keissig fringes in the data, an additional two layers were required to fit the data. These two layers correspond to two orientations of nanodiscs: the first layer with the plane of the bilayer within the nanodisc parallel to the initial bilayer, and the second perpendicular. The thickness, hydration and surface roughness of these layers were fit. The same SLD was used for both these layers, where volume fractions of each component (lipid headgroups, lipid tails and polymer) were calculated from SMALP dimensions determined previously by SANS.[25] The SLDs of the individual components were fixed based on literature values (or on the SLD of the phospholipid tails determined by analysis of the original bilayer structure), except for the SLD of the phospholipid tails within the nanodisc, $\rho_{Nanodisc\ Tails}$. This was fit to account for lipid exchange between the bilayer and adsorbed nanodiscs where

$$\rho_{Nanodisc\ Tails} = (\chi_{hDMPC}\rho_{hDM\ Tails}) + (\chi_{dDMPC}\rho_{dDM\ Tails})$$

And the SLD of the entire nanodisc is calculated as

$$\rho_{Nanodisc} = (\chi_{Nanodisc\ Tails}\rho_{Nanodisc\ Tails}) + (\chi_{Headgroups}\rho_{Headgroups}) + (\chi_{Polymer}\rho_{Polymer})$$

Retaining the bilayer structure before and after nanodisc interaction was unable to produce satisfactory fits to the experimental data, therefore the bilayer structure was fit independently after nanodisc interaction, albeit with the same constraints applied as described above such that the model represents a physically feasible bilayer. The error associated with each parameter in all resulting models was estimated by MCMC analysis implemented within RasCAL as described for the lipid monolayer case.

4.4 RESULTS

4.4.1 Structural changes to phospholipid Langmuir monolayers at the air-water interface upon incubation with phospholipid nanodiscs

As discussed above, there is currently limited information on the interaction of nanodiscs stabilized by different polymers with interfacial lipid membranes. In order to determine the nature of these interactions, we first investigated the structural changes to phospholipid monolayers at the air-water interface using neutron reflectometry (NR). Initially, we characterized monolayers of either hDMPC or dDMPC spread on the air contrast matched water (ACMW) subphase to a surface pressure of 10 mN m^{-1}. This ensures that the monolayers are in the liquid-expanded phase,[62] which allows for non-stoichiometric lipid exchange to occur without collapse of the monolayer,[63] or insufficient neutron scattering intensity due to low surface coverage. Fitting of two-layer models to these data (Figure 4.1), with layers corresponding to DMPC tails and headgroups provide satisfactory fits to the experimental data. Parameters obtained from these models indicate that the monolayers formed have a structure which is expected of LE phase monolayers (Table 4.1, 4.2, 4.3). The thickness of the tail regions are 9 ± 1 Å and 10 ± 1 Å for monolayers formed on phosphate buffers (for SMALP and RAFT-SMALP interactions, respectively; Table 4.1, 4.3) and 8 ± 1 Å for monolayers formed on acetate buffers (for SMILP interactions; Table 4.2). These thicknesses are thinner than both the theoretical maximum thickness given fully extended, saturated C_{14} chains.[64,65] This suggests a high degree of chain tilt, indicative of lipids within the LE phase, and consistent with previous studies. [66]

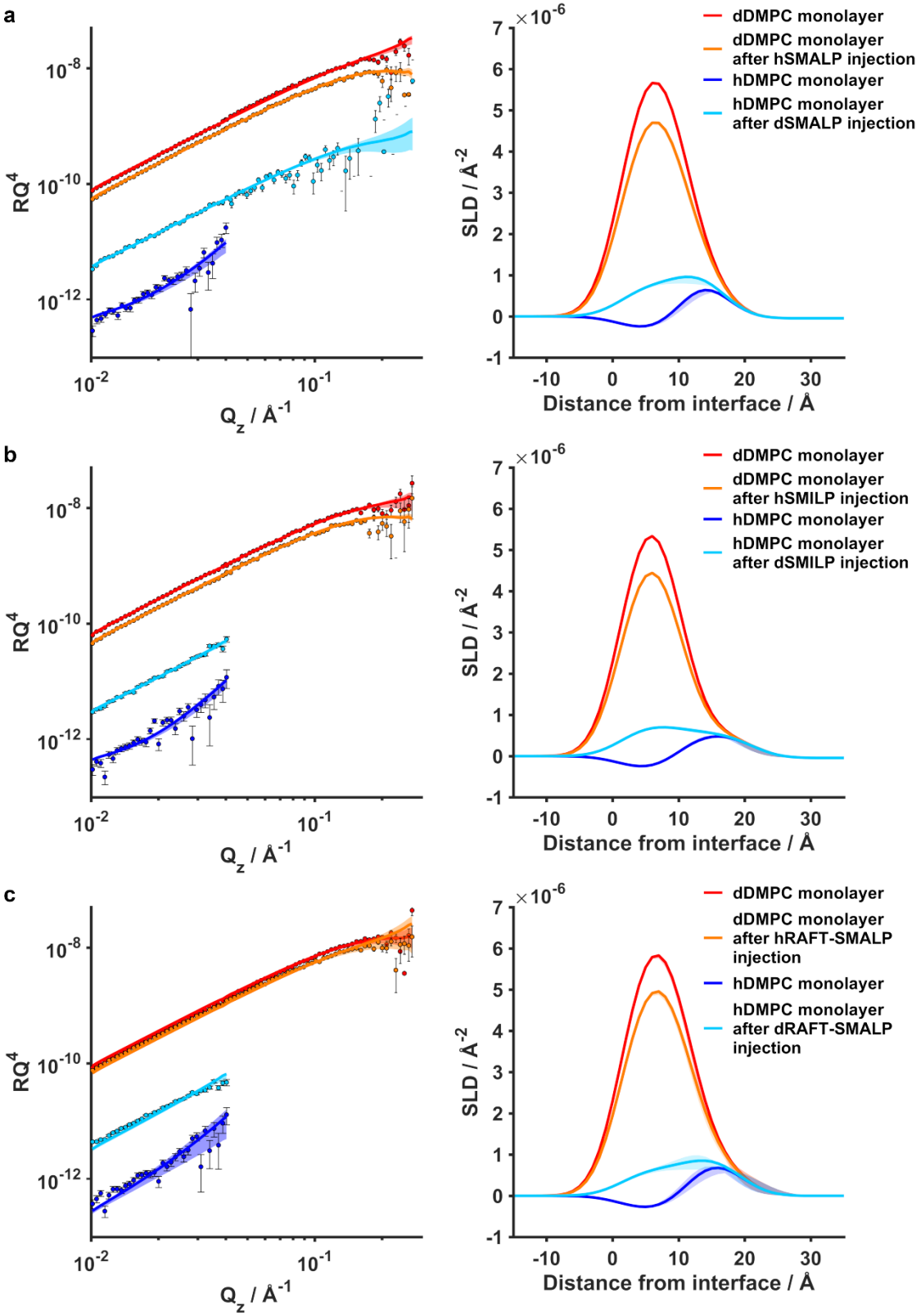

Figure 4.1. Full-Q NR data (points) and fits (solid lines) plotted as RQ^4 (left panels) with corresponding SLD profiles (right panels) of SMALP (a), SMILP (b) and RAFT-SMALP (c) nanodisc interactions with phospholipid Langmuir monolayers at the air-water interface. Colored shaded regions represent the 95% confidence interval associated with the fit and model SLD profiles determined by Bayesian MCMC error estimation routines.

Table 4.1. Structural parameters obtained by fitting NR data of DMPC monolayers at the air-water interface before and after introduction of DMPC SMALPs into the subphase. Values marked * were held as a constant throughout the fitting procedure. Values in italics were obtained after fitting NR data of a dDMPC monolayer after incubation with dDMPC SMALPs. Values in parentheses indicate the 95% confidence intervals estimated from Bayesian MCMC error estimation.

Layer	Parameter	Monolayer before SMALP injection	Monolayer after SMALP injection
Air	SLD / $\times 10^{-6}$ Å^{-2}	0*	
DMPC tails	SLD / $\times 10^{-6}$ Å^{-2}	6.84*	5.65 (5.63, 5.67)
		-0.37*	0.81 (0.79, 0.83)
			6.43 (6.35, 6.50)
	Thickness / Å	9 (8, 10)	
	Hydration / %	0*	
	Roughness / Å	3.5*	
DMPC headgroup	SLD / $\times 10^{-6}$ Å^{-2}	2.14*	
	Thickness / Å	6 (5, 7)	
	Hydration / %	41 (33, 51)	
	Roughness / Å	3.5 *	
Subphase	SLD / $\times 10^{-6}$ Å^{-2}	0*	
	Roughness / Å	3.5*	

Table 4.2. Structural parameters obtained by fitting NR data of DMPC monolayers at the air-water interface before and after introduction of DMPC SMILPs into the subphase. Values marked * were held as a constant throughout the fitting procedure. Values in italics were obtained after fitting NR data of a dDMPC monolayer after incubation with dDMPC SMILPs. Values in parentheses indicate the 95% confidence intervals estimated from Bayesian MCMC error estimation.

Layer	Parameter	Monolayer before SMILP injection	Monolayer after SMILP injection
Air	SLD / $\times 10^{-6}$ Å^{-2}	0*	
DMPC tails	SLD / $\times 10^{-6}$ Å^{-2}	6.84*	5.68 (5.66, 5.70)
		-0.37*	0.79 (0.76, 0.80)
			6.53 (6.49, 6.57)
	Thickness / Å	8 (8, 9)	
	Hydration / %	0*	
	Roughness / Å	3.5*	
DMPC headgroup	SLD / $\times 10^{-6}$ Å^{-2}	2.14*	
	Thickness / Å	10 (8, 12)	
	Hydration / %	71 (67, 74)	
	Roughness / Å	3.5 *	
Subphase	SLD / $\times 10^{-6}$ Å^{-2}	0*	
	Roughness / Å	3.5*	

Table 4.3. Structural parameters obtained by fitting NR data of DMPC monolayers at the air-water interface before and after introduction of DMPC RAFT-SMALPs into the subphase. Values marked * were held as a constant throughout the fitting procedure. Values in italics were obtained after fitting NR data of a dDMPC monolayer after incubation with dDMPC RAFT-SMALPs. Values in parentheses indicate the 95% confidence intervals estimated from Bayesian MCMC error estimation.

Layer	Parameter	Monolayer before RAFT-SMALP injection	Monolayer after RAFT-SMALP injection
Air	SLD / $\times 10^{-6}$ Å^{-2}	0*	
DMPC tails	SLD / $\times 10^{-6}$ Å^{-2}	6.84*	5.80 (5.76, 5.83)
		-0.37*	0.67 (0.63, 0.81)
			6.59 (6.56, 6.62)
	Thickness / Å	10 (9, 10)	
	Hydration / %	0*	
	Roughness / Å	3.5*	
DMPC headgroup	SLD / $\times 10^{-6}$ Å^{-2}	2.14*	
	Thickness / Å	8 (5, 11)	
	Hydration / %	53 (30, 68)	
	Roughness / Å	3.5*	
Subphase	SLD / $\times 10^{-6}$ Å^{-2}	0*	
	Roughness / Å	3.5*	

Following initial characterization of the monolayers, nanodiscs containing phospholipids of the opposite isotopic labelling were injected into the subphase, i.e., hDMPC nanodiscs were injected beneath a dDMPC monolayer and *vice versa*. The system was allowed to equilibrate for 2 hours and the NR measured again (Figure 4.1). In all cases, the reflected intensity of the originally deuterated monolayers decreased, and the reflected intensity from the originally hydrogenated monolayer increased. No additional layers were required to be added to the model to fit the data, with the only parameters requiring modification to achieve satisfactory fits being the SLD of the phospholipid tails (Table 4.1, 4.2, 4.3), consistent with lipid exchange occurring.

Importantly, the absence of any strong Keissig fringes in the measured data or additional layers in the model required to fit the data can rule out adsorption of nanodiscs to the interfacial lipids. However, due to the similarity of SLDs for the polymers and lipid head groups, we remain insensitive to polymer incorporation into the monolayer. Here, we have constrained the model such that the structural parameters of the monolayer, apart from the tail SLD, are fixed to that determined prior to nanodisc injection. While the data can be fit by a model allowing subtle structural changes, no improvement in

the fit was observed, thus we opted for the simpler model. Nonetheless, we cannot rule out structural changes occurring as a result of either polymer interaction with the monolayer, or changes to the total surface excess as a result of non-stoichiometric lipid exchange.

In order to investigate to the extent of polymer incorporation into the monolayers, an additional contrast was collected where dDMPC nanodiscs bound by hydrogenated polymer were injected beneath a dDMPC monolayer (Figure 4.2). Co-refinement of these contrasts with those discussed above was not possible due to uncertainty in the absolute magnitude of scaling factors applied to data collected at different beam time allocations. However, from these measurements it is clear that, for all systems measured, there is a decrease in SLD of the phospholipid tails, albeit less than observed for hDMPC nanodiscs injected beneath dDMPC monolayers. In this case, as both lipids at the monolayer and lipids within nanodiscs are both deuterium labelled, this indicates hydrogenated polymer incorporation into the phospholipid tails, in addition to the hypothesized lipid exchange. These differences in SLD of the phospholipid tails for each of the measured contrasts allow us to estimate the percentage of volume of the monolayer occupied by lipids and polymers from nanodiscs after the interactions have occurred (Table 4.5). Due to the similarity in SLD between the polymers (1.84×10^{-6} Å^{-2}) and the phosphatidylcholine headgroups (2.14×10^{-6} Å^{-2}), we remain insensitive to polymer incorporation within the headgroup region. Therefore, this estimate is likely an underestimation of the volume fraction of the monolayer occupied by polymers. Nonetheless, this suggests that the change in SLD is due to a large proportion of polymer incorporation into the monolayer in addition to lipid exchange.

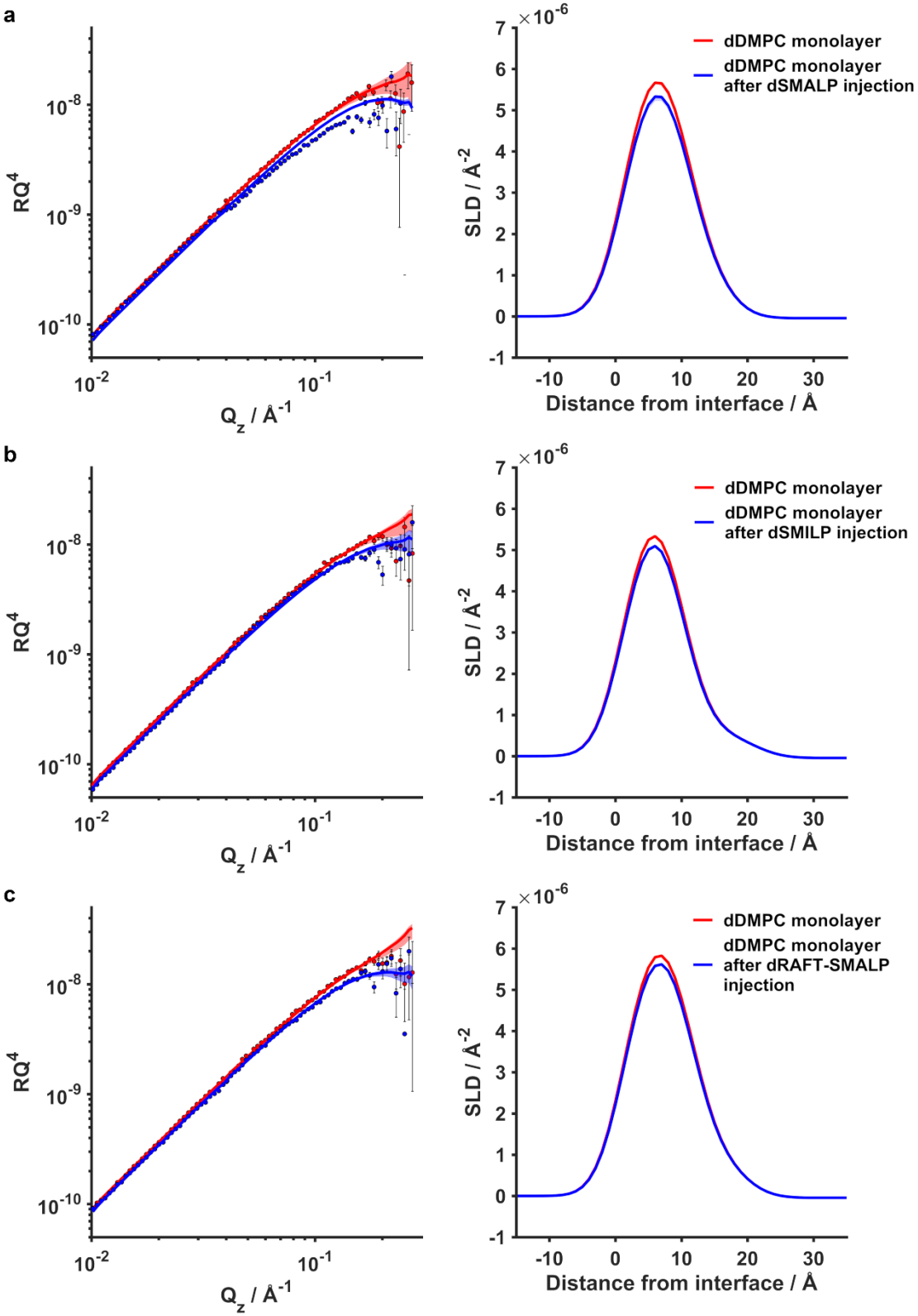

Figure 4.2. Full-Q NR data (points) and fits (solid lines) plotted as RQ^4 (left panels) with corresponding SLD profiles (right panels) of dDMPC monolayers after incubation with (a) dDMPC SMALPs, (b) dDMPC SMILPs and (c) dDMPC RAFT-SMALPs. Colored shaded regions represent the 95% confidence interval associated with the fit and model SLD profiles determined by Bayesian MCMC error estimation routines.

Polymer presence within the monolayer presents the question as to what extent the nanodiscs themselves are surface-active. To gauge the effect of surface activity of nanodiscs, we injected dDMPC SMALP nanodiscs (where the incorporation of polymers into the monolayer is most pronounced) into an ACMW subphase with no monolayer present. After a 2 hour incubation, reflectometry was measured (Figure 4.3, Table 4.4). From the limited structural information available from the single contrast we were able to collect within the allocated beamtime, we are able to fit a model consistent with a phospholipid monolayer with a decreased SLD of the dDMPC tails compared to the theoretical value. This suggests that SMALPs will disassemble when in contact with the air-water interface resulting in a large proportion of the volume of the phospholipid tails being occupied by polymers, confirming surface activity.

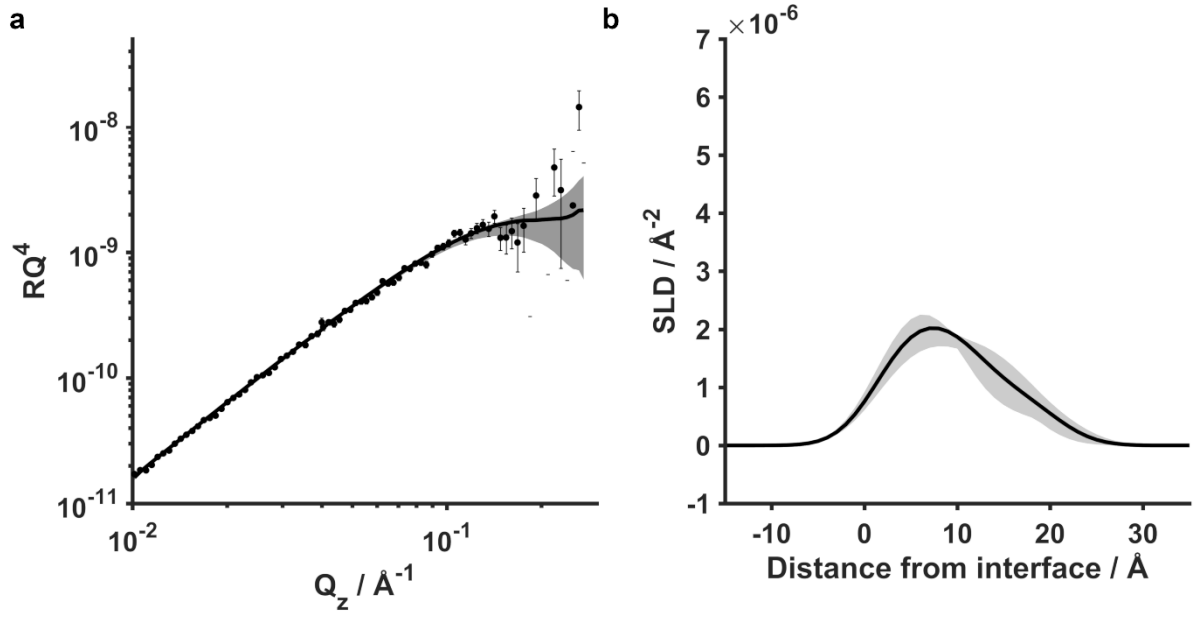

Figure 4.3. Full-Q NR data (points) and fit (solid line) plotted as RQ^4 (a) with corresponding SLD profile (b) collected 2 hours after dDMPC SMALPs were injected into an ACMW subphase with no monolayer present. Shaded regions represent the 95% confidence interval associated with the fit and model SLD profiles determined by Bayesian MCMC error estimation routines.

Table 4.4. Structural parameters obtained by fitting NR data at the air-water interface of dDMPC SMALPs injected into an ACMW subphase with no monolayer present after 2 hours incubation. Values marked * were held as a constant throughout the fitting procedure. Values in parentheses indicate the 95% confidence intervals estimated from Bayesian MCMC error estimation.

Layer	Parameter	After dDMPC SMALP injection
Air	SLD / $\times 10^{-6}$ Å^{-2}	0*
DMPC tails	SLD / $\times 10^{-6}$ Å^{-2}	2.25 (1.84, 2.81)
	Thickness / Å	11 (9, 12)
	Hydration / %	0*
	Roughness / Å	3.5*
DMPC headgroup	SLD / $\times 10^{-6}$ Å^{-2}	2.13*
	Thickness / Å	8 (5, 12)
	Hydration / %	33 (24, 53)
	Roughness / Å	3.5*
Subphase	SLD / $\times 10^{-6}$ Å^{-2}	0*
	Roughness / Å	3.5*

4.4.2 Kinetics of interactions between phospholipid nanodiscs and phospholipid Langmuir monolayers at the air-water interface

Once we had determined that both polymer and/ or lipid exchange was occurring between SMALP, RAFT-SMALP and SMILP nanodiscs and phospholipid monolayers, we next sought to determine the kinetics of the exchange process using time-resolved NR.[59] We initially looked to compare the changes in surface pressure to the surface excess of material at the interface, as calculated by low-Q time-resolved NR (Figure 4.4). These data indicate that in all cases there is a net gain of material at the monolayers upon nanodisc interaction, although as previously discussed, a large proportion of this is due to polymer incorporation, and not simply lipid exchange in the case of RAFT-SMALPs and SMALPs. However, we do observe discrepancies between the surface pressure and surface excess. Notably, RAFT-SMALPs lead to the smallest increase in surface pressure, but the largest increase in surface excess. One would expect a large gain in material at the surface, as defined by the surface excess, to lead to a similarly large change in surface pressure. As this is clearly not the case, and structural information on the monolayer structure indicate the presence of polymers after incubation with nanodiscs, these data further suggest

polymer incorporation causing differences between the molar quantity of material at the surface and the area per molecule compared to what would be expected from purely lipid gain.

By analyzing time-resolved NR data for hDMPC nanodiscs injected beneath a dDMPC monolayer, and *vice versa*, we were able to deconvolute the changes in surface excess in terms of lipid exchange from the nanodiscs to the monolayer to the bilayer (Figure 4.5). Due to the lack of availability of deuterated commercial polymers, the information contained within the low-Q reflected intensities of dDMPC nanodiscs injected beneath a dDMPC monolayer is not sufficient to allow for deconvolution of bidirectional lipid exchange and polymer association with the monolayers. These data indicate that the total amount of deposition at the monolayer from the nanodiscs was similar in all cases. However, the total decrease in surface excess of lipids originally in the monolayer is similar for both SMALPs and SMILPs. This is in contrast to RAFT-SMALPs where it appears material is primarily deposited at the interface.

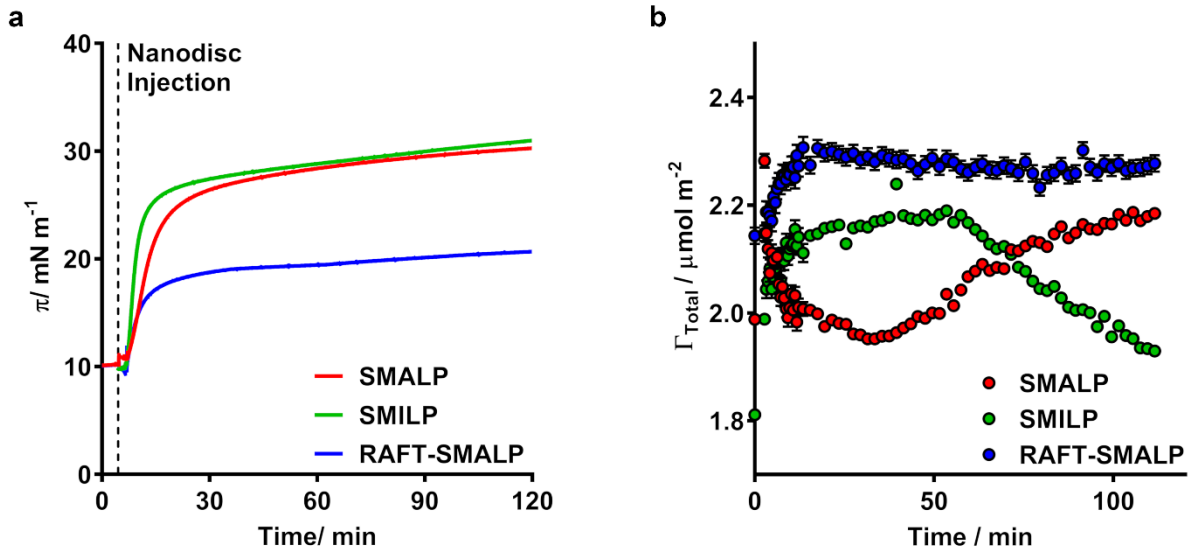

Figure 4.4. a. Surface pressure changes with respect to time of a DMPC Langmuir monolayer upon SMALP (red line), SMILP (green line) and RAFT-SMALP (blue line) introduction into the subphase. **b.** Total surface excess changes at the air-water interface with respect to time as measured using low-Q NR upon injection of SMALP (red points), SMILP (green) and RAFT-SMALP nanodiscs into the subphase.

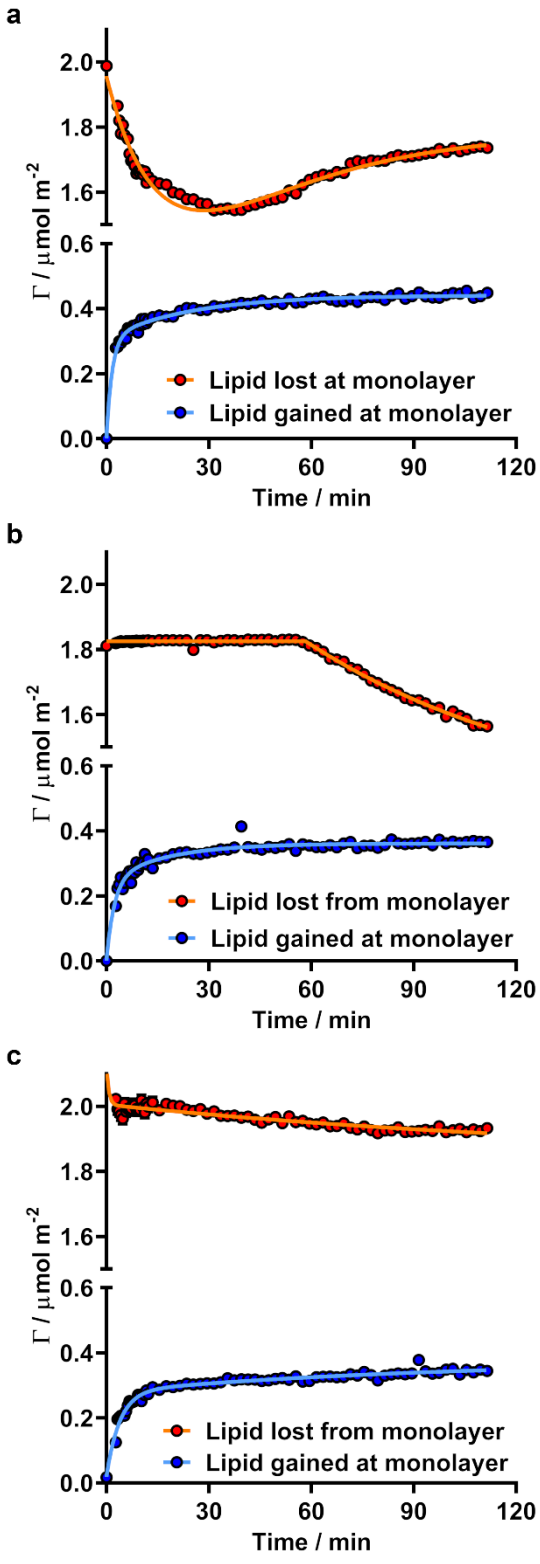

Figure 4.5. Kinetics of lipid exchange between SMALP **(a)**, SMILP **(b)** and RAFT-SMALP **(c)** nanodiscs and phospholipid Langmuir monolayers at the air-water interface measured by low-Q NR. The surface excess corresponding to phospholipids leaving the monolayer, Γ_M, (red) are plotted on the top Y axis and the surface excess corresponding to phospholipids arriving at the monolayer from the nanodiscs, Γ_N (blue points) are plotted on the lower Y axis. Fits of kinetic exponential equations to the experimental data are shown as solid lines.

Table 4.5. Lipid exchange parameters obtained for the extent and kinetics of lipid exchange occurring between phospholipid monolayers at the air-water interface and DMPC nanodiscs.

	Exchange with SMALPs	**Exchange with SMILPs**	**Exchange with RAFT-SMALPs**
Lipids from nanodiscs in monolayer / vol%	5.8 ± 1.1	4.3 ± 0.5	3.4 ± 0.4
Polymer in bilayer / vol%	8.3 ± 1.5	6.2 ± 0.7	5.0 ± 0.6
Total changes in surface excess			
$\Delta\Gamma_M$ **/ µmol m^{-2}**	-0.25 ± 0.01	-0.25 ± 0.01	-0.19 ± 0.02
$\Delta\Gamma_N$ **/ µmol m^{-2}**	0.45 ± 0.01	0.37 ± 0.01	0.33 ± 0.01
$\Delta\Gamma_{Total}$ **/ µmol m^{-2}**	0.20 ± 0.01	0.12± 0.01	0.14 ± 0.02
Kinetic parameters of lipid exchange from the monolayer to nanodiscs			
$k_{Loss,\ M\rightarrow N}$ **/ min^{-1}**	51.9 ± 1.8 ×10^{-3}	13.2 ± 2.0 ×10^{-3}	12.3 ± 5.7 ×10^{-3}
k_{Gain} **/ min^{-1}**	34.0 ± 1.4 ×10^{-3}	-	-
Kinetic parameters of lipid exchange from nanodiscs to the monolayer			
$k_{Fast,\ N\rightarrow M}$ **/ min^{-1}**	0.60 ± 0.04	0.44 ± 0.07	0.26 ± 0.02
$\Delta\Gamma^{eq}_{0,\ N,\ Fast}$ **/ %**	70.1 ± 1.4	67.9 ± 5.5	72.7 ± 5.4
$k_{Slow,\ N\rightarrow M}$ **/ min^{-1}**	0.04 ± 0.01	0.06 ± 0.01	10.3 ± 6.6 ×10^{-3}
$\Delta\Gamma^{eq}_{0,\ N,\ Slow}$ **/ %**	29.9 ± 1.4	32.1 ± 5,5	27.3 ± 5.4

First order kinetic equations were fit to these surface excess data to obtain apparent rate constants for the nanodisc-monolayer interactions (Table 4.5). In the case of exchange from the monolayer to the nanodiscs, SMILP and RAFT-SMALP interactions were modelled using single phase first order kinetics. The exchange of lipids from the monolayer to RAFT-SMALPs occurs at a similar rate to SMILPs, although to a lesser extent. Interestingly, the exchange of lipids from the monolayer to SMILPs shows an initial lag phase which is not observed in for the other systems tested. Exchange from the monolayer to SMALPs, however, show an interesting trend (Figure 4.5a). Initially there is a large, rapid decrease in the surface excess prior to a subsequent increase until a plateau is reached. This interaction was modelled using the sum of one dissociative first order rate equation and one associative first order rate equation, with two rate constants, denoted k_{Loss} and k_{Gain}, respectively (Table 4.5). This can be justified by the occurrence of both lipid exchange and polymer incorporation, both of which occur to

the greatest extent for SMALPs as determined by full-Q NR measurements. While speculative at this stage, we expect k_{Loss} to describe the rate of lipid exchange from the monolayer to the nanodiscs, and k_{Gain} to describe the rate of polymer incorporation into the monolayer. Confirmation of this assignment by this methodology would require deuterated versions of commercially available copolymers which are, at this time, unavailable.

Lipid (and polymer) exchange from the nanodiscs to the monolayer shows very similar trends in each case, whereby there is an initial rapid deposition of lipids and polymer at the monolayer, followed by a much slower increase. These interactions were modelled in all cases by a two-phase first order rate equation whereby the process is split into one fast and one slow phase, each with an individual rate constant, k_{Fast} and k_{Slow}, respectively, responsible for a fraction of the total increase in surface excess (Table 4.5). As we can see evidence of polymer presence in the monolayers for each nanodisc system, albeit to different extents, we suggest that the first rapid phase is the result of a re-equilibration of the polymers with the small quantity of additional lipids introduced into the system. This will result in a rapid deposition of both lipid and polymer from the nanodiscs in the monolayer. Once the system has reached a new thermodynamic equilibrium where polymer chains have re-partitioned amongst the available lipid within the system, the surface excess continues to increase as material is deposited within the monolayer. We propose that this process, described by k_{Slow}, is primarily a collisional lipid exchange between nanodiscs in solution and monolayers at the air-water interface. It is worth noting that due the timescale of the measurement feasible within allotted beamtime, k_{Slow} is poorly defined as there remains a high uncertainty towards the equilibrium value of the surface excess. As discussed above, this assignment of rate constants is speculative at this stage due to technical challenges relating to deconvoluting the kinetics of lipid exchange relative to polymer exchange.

4.4.3 Kinetics of nanodisc interactions with phospholipid bilayers at the Si-water interface

While the interactions of nanodiscs with a Langmuir monolayer at the air-water interface is highly informative, the thermodynamic stability of phospholipids within monolayers is substantially different to bilayers, as found at cell membranes. In the case of monolayers, the lipid tails protrude out of the aqueous subphase into the air, compared to the hydrophobic core of lipid tails in bilayers which is encapsulated by solvated, hydrophilic headgroups. Therefore there will be different thermodynamic driving forces for lipid and polymer partitioning into the bulk and interfacial phases, which will likely affect both the extent, directionality and rate of lipid/ polymer exchange. We have therefore investigated the interaction of nanodiscs with supported phospholipid bilayers at the silicon-water interface.

We measured these interactions using ATR-FTIR. Initially a dDMPC bilayer was deposited on a Si ATR crystal before injection of hDMPC nanodiscs, whereby spectra were periodically taken over 300 minutes during incubation with nanodiscs (Figure 4.6). Due to the increased mass of deuterium compared to hydrogen, the frequency of C-D bond vibrations is decreased relative to C-H bonds. In a similar strategy as we applied at the air-water interface, this allows direct observation of the relative decreases and increases in C-D_x and C-H_x, respectively from the lipid tails upon the introduction of nanodiscs into the superphase. Importantly, ATR-FTIR allows direct observation of lipid exchange, separate to polymer exchange due to the relatively low C-H_2 content of the polymers, and the presence of aromatic C=C bonds and carbonyl bonds in different chemical environments to the glycerol-ester present in the phospholipid head groups.

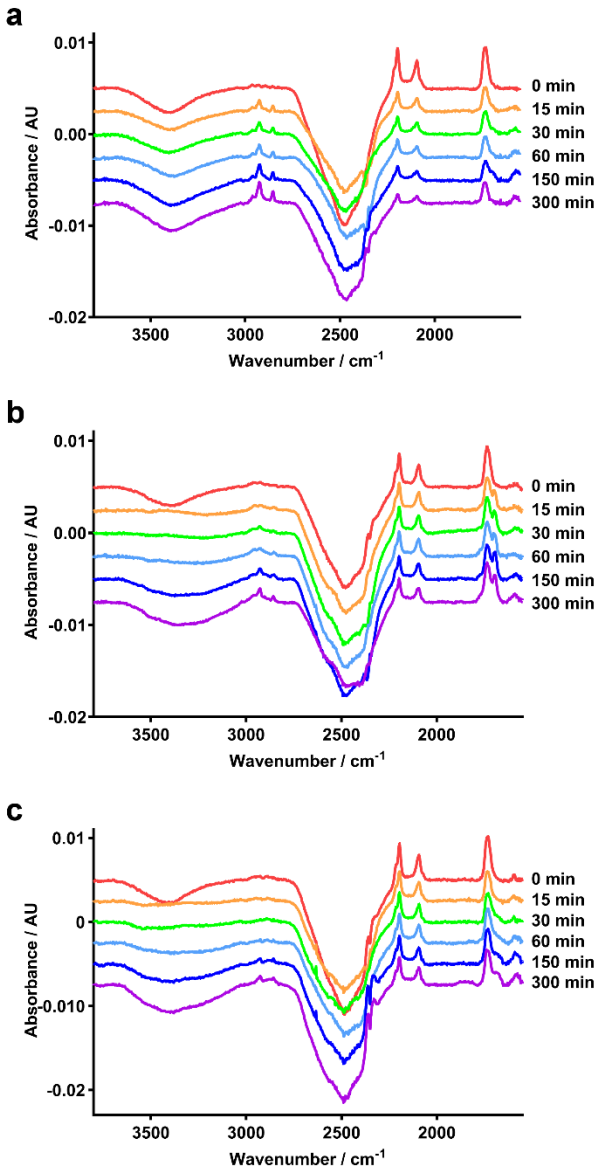

Figure 4.6. Representative ATR-FTIR spectra obtained during the incubation of (a) hDMPC SMALPs, (b) hDMPC SMILPs and (c) hDMPC RAFT-SMALPs with a dDMPC bilayer. A spectrum was collected during the injection of nanodiscs (0 min, red spectrum) and then at various time points during nanodisc incubation (orange through indigo spectra).

Overall, similar changes in the chemical composition of the interfacial bilayer are observed to structural changes at the air-water interface upon introduction of nanodiscs into the superphase. Upon incubation of the dDMPC bilayer with hDMPC SMALPs (Figure 4.7a, b, c) an increase in the intensity of absorbances arising from the symmetric and asymmetric C-H_2 and C-H_3 stretching vibrations is observed as hDMPC from the nanodiscs become incorporated at the interface (Figure 4.7a). A concurrent decrease in the intensity of absorbances arising from the symmetric and asymmetric C-D_2 and C-D_3 stretching vibrations is also observed as lipids are exchanged from the bilayer to the nanodiscs in bulk solution (Figure 4.7b). By inspecting the carbonyl and aromatic peaks (Figure 4.7c), we observed a decrease and then apparent plateau of the ester C=O stretch absorbance from the DMPC tails. Importantly, we also observe a gradual increase in the carboxylic acid C=O stretch absorbance and the aromatic C=C stretching absorbance, suggesting polymer is interacting with the bilayer. In comparison, spectra collected during the incubation of hDMPC SMILPs (Figure 4.7d, e, f) and RAFT-SMALPs (Figure 4.7h, i, j) show similar trends, although with smaller decreases in C-D_x and increases in C-H_x bonds. This suggests that the bilayer experiences a much decreased lipid exchange with SMILPs and RAFT-SMALPs compared to SMALPs. However, when inspecting the polymer-specific absorbances, we can observe a larger increase in the imide or carboxylic acid carbonyl bonds present within SMI and RAFT-SMA, respectively along with increases in the aromatic C=C bonds. This suggests that both SMI and RAFT-SMA have an increased propensity to interact with planar bilayers than SMA. Due to peak convolution, noise from imperfect water vapor subtraction and differing dipole moments between different bond vibrations, it is difficult for us to quantify the total amount of polymer incorporation into the bilayer.

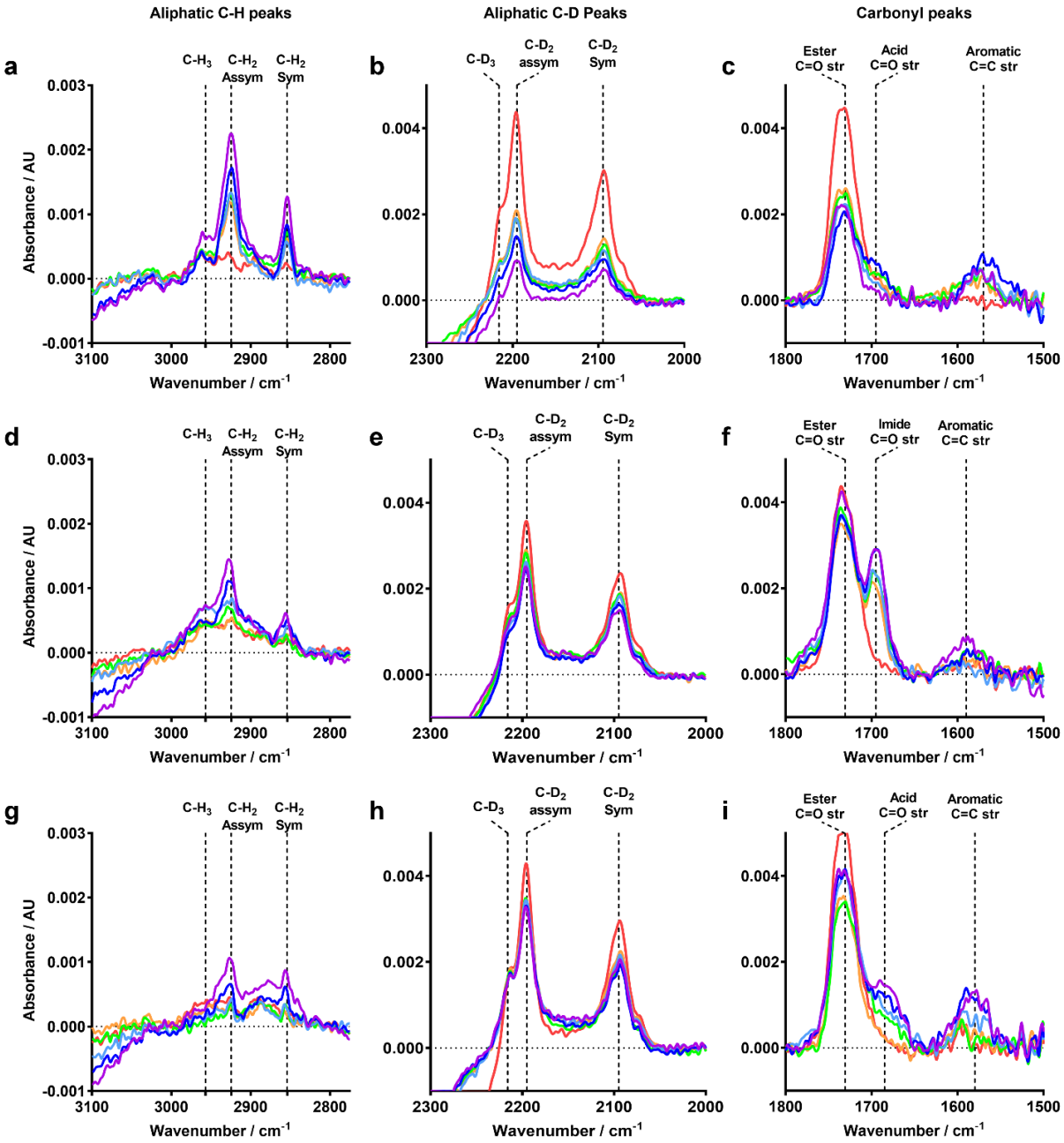

Figure 4.7. Excerpts of ATR-FTIR spetra measuring the interaction of hDMPC containing nanodiscs with dDMPC bilayers at the Si-water interface. Spectral regions showing aliphatic C-H_x peaks, aliphatic C-D_x peaks and carbonyl/ aromatic peaks are shown for incubations of hDMPC-containing SMALP (**a, b, c**), SMILP (**d, e, f**) and RAFT-SMALP (**g, h, i**) nanodiscs with dDMPC supported bilayers at the Si-water interface, respectively. Spectra are colored as described in Figure 4.6.

By integrating spectra collected at different time points during incubation with nanodiscs over the C-H_x stretch regions (2990 – 2810 cm^{-1}) and C-D_x stretch regions (2230 – 2050 cm^{-1}), we were able to obtain kinetic plots of lipid exchange from the bilayer to the nanodiscs and from the nanodiscs to the bilayer with minimal contribution from polymer incorporation (Figure 4.8). In contrast to exchange kinetics at the air-water interface, each system shows a similar two-phase removal of dDMPC from the bilayer. These data were analyzed using a two-phase first-order rate equation, similar to the analysis for lipid/polymer addition to monolayers at the air-water interface. This analysis yields two rate constants, $k_{Fast,\ B\rightarrow N}$ and $k_{Slow,\ B\rightarrow N}$, describing the fast and slow phases of lipid exchange from the bilayer to the nanodiscs, respectively (Table 4.6). The initial fast phase of lipid exchange from the bilayer to the nanodiscs is responsible for a similar proportion of the total removal of lipid from the bilayer for both SMALP and RAFT-SMALP systems, with approximately 75% of the total lipid removal occurring during this phase. SMILPs also show an initial rapid exchange of phospholipids from the bilayer to the nanodiscs, although this is responsible for less of the total lipid removal, at approximately 60%. Interestingly, the rate of this phase is significantly higher for the RAFT-SMALP system compared to SMALPs and SMILPs. The rate of the second, slower phase of lipid exchange from the bilayer to the nanodiscs show a different trend, whereby SMALPs exhibit a higher value for $k_{Slow,\ B\rightarrow N}$ than either SMILPs or RAFT-SMALPs. We propose a similar mechanism is responsible for these two-phase kinetics as was hypothesized for the air-water interface, where there is an initial rapid-repartitioning of the polymer amongst the additional lipid present in the system from the bilayer. Although in this case, polymer partitioning leads to solubilization and removal of lipids from the interfacial bilayer. Once the polymers have re-equilibrated amongst the available lipid, we suggest the second slow phase is a result of diffusion limited collisional lipid exchange. As discussed above, here $k_{Slow,\ B\rightarrow N}$ is poorly defined due to a high level of uncertainty in the equilibrium position of the C-D_x peak integrals.

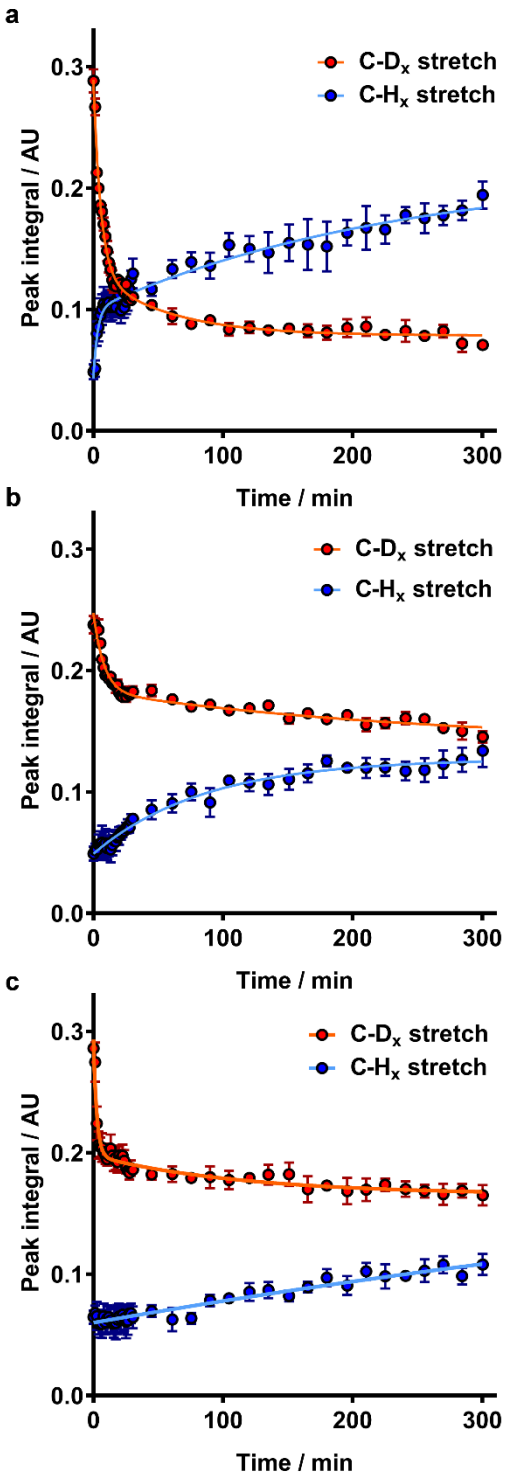

Figure 4.8. Kinetics of lipid exchange between hDMPC-containing SMALPs (a), SMILPs (b) and RAFT-SMALPs (c) and supported dDMPC bilayers at the Si-water interface. The integral of regions corresponding to C-D_x stretching vibrations are shown as red points and C-H_x stretching vibrations are shown as blue points. Points are the mean of three separate experiments with error bars representing ± 1 standard error. Kinetic fits to the experimental data are shown as solid lines.

Table 4.6. Lipid exchange parameters obtained for kinetics of lipid exchange occurring between dDMPC bilayers at the Si-water interface and hDMPC nanodiscs.

	Exchange with SMALPs	**Exchange with SMILPs**	**Exchange with RAFT-SMALPs**
Kinetic parameters of lipid exchange from the bilayer to nanodiscs			
$k_{Fast,\ B\rightarrow N}$ / **min^{-1}**	0.18 ± 0.02	0.12 ± 0.02	0.39 ± 0.06
$\Delta I^{eq}_{0,\ C-D_x,\ Fast}$ / **%**	75.37 ± 2.83	60.17 ± 8.60	74.81 ± 3.56
$k_{Slow,\ B\rightarrow N}$ / **min^{-1}**	0.018 ± 0.005	3.94 ± 3.08 ×10^{-3}	8.66 ± 5.29 ×10^{-3}
$\Delta I^{eq}_{0,\ C-D_x,\ Slow}$ / **%**	24.63 ± 2.83	39.83 ± 8.60	25.19 ± 3.56
Kinetic parameters of lipid exchange from nanodiscs to the bilayer			
$k_{Fast,\ N\rightarrow B}$ / **min^{-1}**	0.32 ± 0.11	11.69 ± 1.90 ×10^{-3}	1.08 ± 2.59 ×10^{-3}
$\Delta I^{eq}_{0,\ C-H_x,\ Fast}$ / **%**	32.96 ± 6.30	-	-
$k_{Slow,\ N\rightarrow B}$ / **min^{-1}**	4.30 ± 2.16 ×10^{-3}	-	-
$\Delta I^{eq}_{0,\ C-H_x,\ Fast}$ / **%**	67.04 ± 6.30	-	-

Analysis of C-H_x stretch peak integrals yields information describing lipid exchange from the nanodiscs to the bilayer. In the case of SMILPs and RAFT-SMALPs, the best fits to the experimental data were obtained by using a single-phase, first-order rate equation (Table 4.6). Here the rate of lipid exchange from the nanodiscs to the bilayer is over ten-fold higher for SMILPs than RAFT-SMALPs. SMALPs, however, show two phase kinetics, with a fast and slow phase, described by $k_{Fast,\ N\rightarrow B}$ and $k_{Slow,\ N\rightarrow B}$. $k_{Fast,\ N\rightarrow B}$ is significantly higher than the rate constants obtained for lipid exchange from either SMILPs or RAFT-SMALPs to the bilayer, but of a similar order of magnitude as $k_{Fast,\ B\rightarrow N}$, discussed above. In contrast, $k_{Slow,\ N\rightarrow B}$ has a value more akin to the rate of lipid deposition at the bilayer by both SMILPs and RAFT-SMALPs. In addition, the majority of lipid deposition at the bilayer by SMALPs occurs during the slow phase, in contrast to lipid removal discussed above. We therefore suggest that in all cases, lipid exchange from the nanodiscs to the bilayer is dominated by a slow, diffusion limited, collisional lipid exchange. However in the case of SMALPs, the initial repartitioning of the polymer amongst the available lipid in the bilayer also leads to a deposition of lipids which is not observed with either SMILPs or RAFT-SMALPs.

4.4.4 Structural changes to phospholipid bilayer structure upon interaction with phospholipid nanodiscs at the Si-water interface

From ATR-FTIR measurements, we were able to determine the kinetics of lipid exchange between phospholipid nanodiscs and supported phospholipid bilayers at the Si-water interface. However, we were also able to identify the presence chemical bonds arising from each of the polymers at the interface. ATR-FTIR does not give any structural information on nanodisc-bilayer interactions. We therefore used NR at the Si-water interface to determine the large-scale structure of DMPC bilayers which have been subject to incubation with nanodiscs. There are two main possibilities which could account for the observed spectral changes, which are not necessarily mutually exclusive. Firstly, a similar scenario to that observed at the air-water interface where no nanodisc adsorption can be identified, but polymers embed into the bilayer along with lipid exchange. The second possibility is that nanodiscs may adsorb to the surface of the bilayer, which would account for both the presence of C-H_x absorbances and polymer-specific absorbances in the ATR-FTIR spectra.

After characterization by NR of bare Si substrates in H_2O and D_2O contrasts, dDMPC bilayers were deposited on the substrates and measured in three contrasts (Figure 4.9a, 4.10a, 4.11a). Model SLD profiles, consisting of 5 layers corresponding to SiO_2, inner headgroups, two phospholipid tail layers, and outer headgroups, were fit to the experimental data (Figure 4.9a, b, 4.10a, b, 4.11a, b). These models were constrained such that the bilayers were symmetrical and represented a physically feasible bilayer (for more detail see section 4.3.2.10). In all cases, this model provided good fits and yielded structural parameters (Table 4.7, 4.8, 4.9) consistent with a high-coverage dDMPC bilayer, as determined by the low hydration of the hydrophobic tail regions, that is consistent with previous studies. [64,65,67]

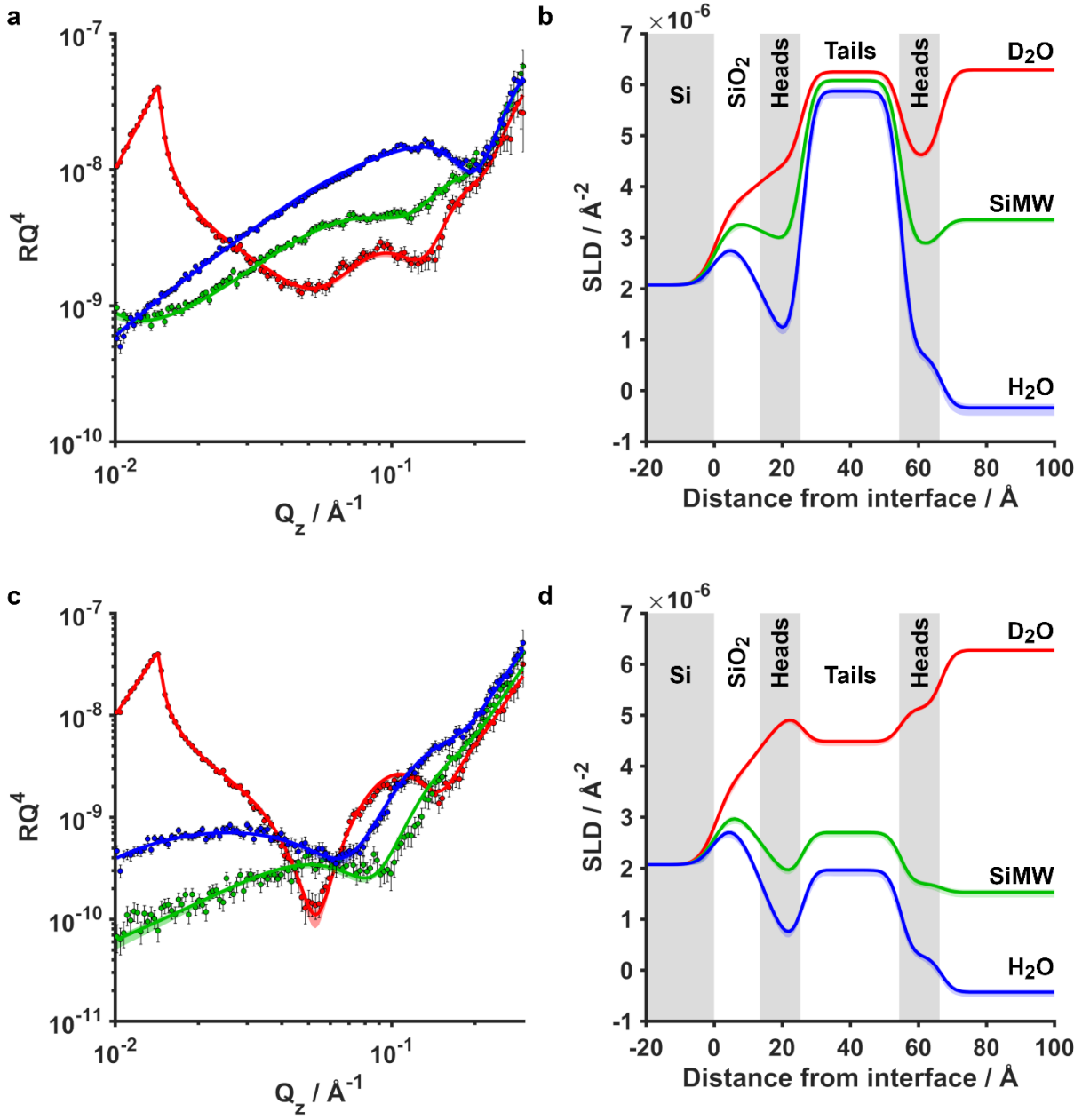

Figure 4.9. Neutron reflectometry data (points) with overlaid fits (solid lines) plotted as RQ^4 (a, c) and corresponding model SLD profiles (b, d) of a dDMPC supported bilayer deposited on a Si substrate before (a, b) and after (c, d) incubation with dDMPC SMALPs. Colored shaded regions represent the 95% confidence interval associated with the fit and model SLD profiles determined by Bayesian MCMC error estimation routines. Grey shaded regions denote layer boundaries in the model SLD profiles. In all cases, red, green and blue points/lines correspond to data collected in D_2O, SiMW and H_2O solution contrasts, respectively.

Table 4.7. Structural parameters obtained by fitting NR data of dDMPC bilayers at the Si-water interface before and after incubation with hDMPC SMALPs. Values marked * were held as a constant throughout the fitting procedure. Values in parentheses indicate the 95% confidence intervals estimated from Bayesian MCMC error estimation.

Layer	Parameter	dDMPC bilayer	dDMPC bilayer after hDMPC SMALP incubation
Si	SLD / $\times 10^{-6}$ Å^{-2}	2.07*	
	Roughness / Å	4 (3, 5)	
SiO_2	SLD / $\times 10^{-6}$ Å^{-2}	3.47*	
	Thickness / Å	13 (13, 14)	
	Hydration / %	8 (6, 10)	
	Roughness / Å	7 (6, 8)	
PC Headgroups	SLD / $\times 10^{-6}$ Å^{-2}	2.14*	
	Thickness / Å	11 (11, 12)	
	Hydration / %	58 (57, 59)	73 (72, 73)
	Roughness / Å	3 (2, 3)	
DM Tails	SLD / $\times 10^{-6}$ Å^{-2}	6.25 (6.22, 6.28)	3.41 (3.33, 3.47)
	Thickness / Å	15 (14, 15)	
	Hydration / %	6 (4, 7)	38 (37, 39)
	Roughness / Å	3 (2, 3)	
DM Tails	SLD / $\times 10^{-6}$ Å^{-2}	6.25 (6.22, 6.28)	3.41 (3.33, 3.47)
	Thickness / Å	15 (14, 15)	
	Hydration / %	6 (4, 7)	38 (37, 39)
	Roughness / Å	3 (2, 3)	
PC Headgroups	SLD / $\times 10^{-6}$ Å^{-2}	2.14*	
	Thickness / Å	11 (11, 12)	
	Hydration / %	58 (57, 59)	73 (72, 73)
	Roughness / Å	3 (2, 3)	
Bulk Solvent	SLD (D_2O)/ $\times 10^{-6}$ Å^{-2}	6.29 (6.28, 6.30)	6.27 (6.26, 6.28)
	SLD (SiMW)/ $\times 10^{-6}$ Å^{-2}	3.35 (3.32, 3.38)	1.53 (1.46, 1.59)
	SLD (H_2O)/ $\times 10^{-6}$ Å^{-2}	-0.34 (-0.43, -0.25)	-0.43 (-0.48, -0.38)

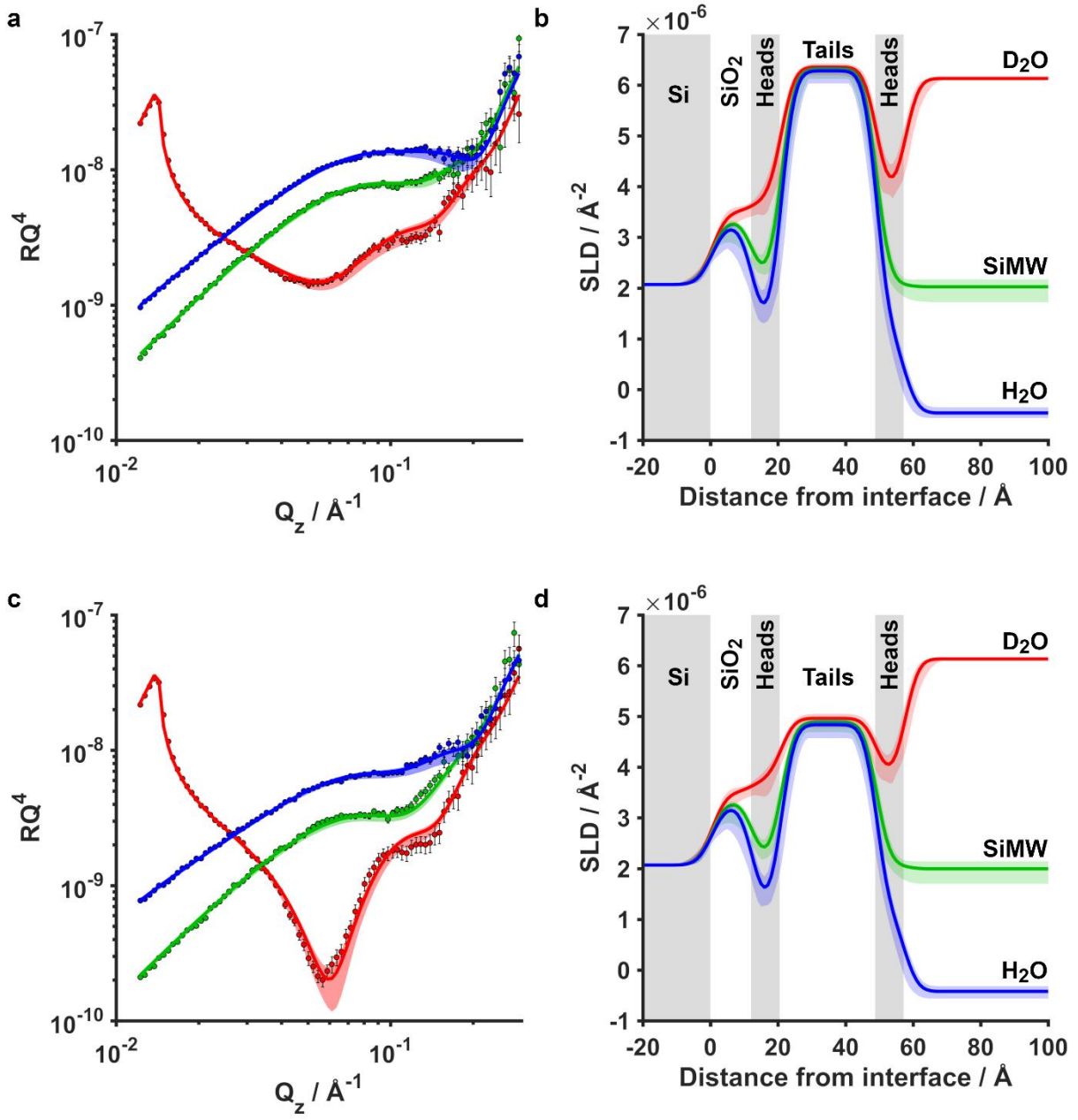

Figure 4.10. Neutron reflectometry data (points) with overlaid fits (solid lines) plotted as RQ^4 (a, c) and corresponding model SLD profiles (b, d) of a dDMPC supported bilayer deposited on a Si substrate before (a, b) and after (c, d) incubation with hDMPC SMILPs. Colored shaded regions represent the 95% confidence interval associated with the fit and model SLD profiles determined by Bayesian MCMC error estimation routines. Grey shaded regions denote layer boundaries in the model SLD profiles. In all cases, red, green and blue points/lines correspond to data collected in D_2O, SiMW and H_2O solution contrasts, respectively.

Table 4.8. Structural parameters obtained by fitting NR data of dDMPC bilayers at the Si-water interface before and after incubation with hDMPC SMILPs. Values marked * were held as a constant throughout the fitting procedure. Values in parentheses indicate the 95% confidence intervals estimated from Bayesian MCMC error estimation.

Layer	Parameter	dDMPC bilayer	dDMPC bilayer after hDMPC SMALP incubation
Si	SLD / $\times 10^{-6}$ Å^{-2}	2.07*	
	Roughness / Å	3 (3, 5)	
SiO_2	SLD / $\times 10^{-6}$ Å^{-2}	3.47*	
	Thickness / Å	12 (11, 13)	
	Hydration / %	4 (1, 9)	
	Roughness / Å	3 (3, 4)	
PC Headgroups	SLD / $\times 10^{-6}$ Å^{-2}	2.14*	
	Thickness / Å	8 (7, 9)	
	Hydration / %	40 (37, 42)	40 (38, 42)
	Roughness / Å	3 (2, 4)	
DM Tails	SLD / $\times 10^{-6}$ Å^{-2}	6.36 (6.27, 6.45)	4.94 (4.76, 5.12)
	Thickness / Å	14 (13, 15)	
	Hydration / %	1 (0, 3)	2 (0, 5)
	Roughness / Å	3 (2, 4)	
DM Tails	SLD / $\times 10^{-6}$ Å^{-2}	6.36 (6.27, 6.45)	4.94 (4.76, 5.12)
	Thickness / Å	14 (13, 15)	
	Hydration / %	1 (0, 3)	2 (0, 5)
	Roughness / Å	3 (2, 4)	
PC Headgroups	SLD / $\times 10^{-6}$ Å^{-2}	2.14*	
	Thickness / Å	8 (7, 9)	
	Hydration / %	40 (37, 42)	40 (38, 42)
	Roughness / Å	3 (2, 4)	
Bulk Solvent	SLD (D_2O)/ $\times 10^{-6}$ Å^{-2}	6.13 (6.12, 6.14)	6.13 (6.13, 6.14)
	SLD (SiMW)/ $\times 10^{-6}$ Å^{-2}	2.03 (1.85, 2.20)	2.00 (1.83, 2.17)
	SLD (H_2O)/ $\times 10^{-6}$ Å^{-2}	-0.46 (-0.53, -0.33)	-0.41 (-0.53, -0.30)

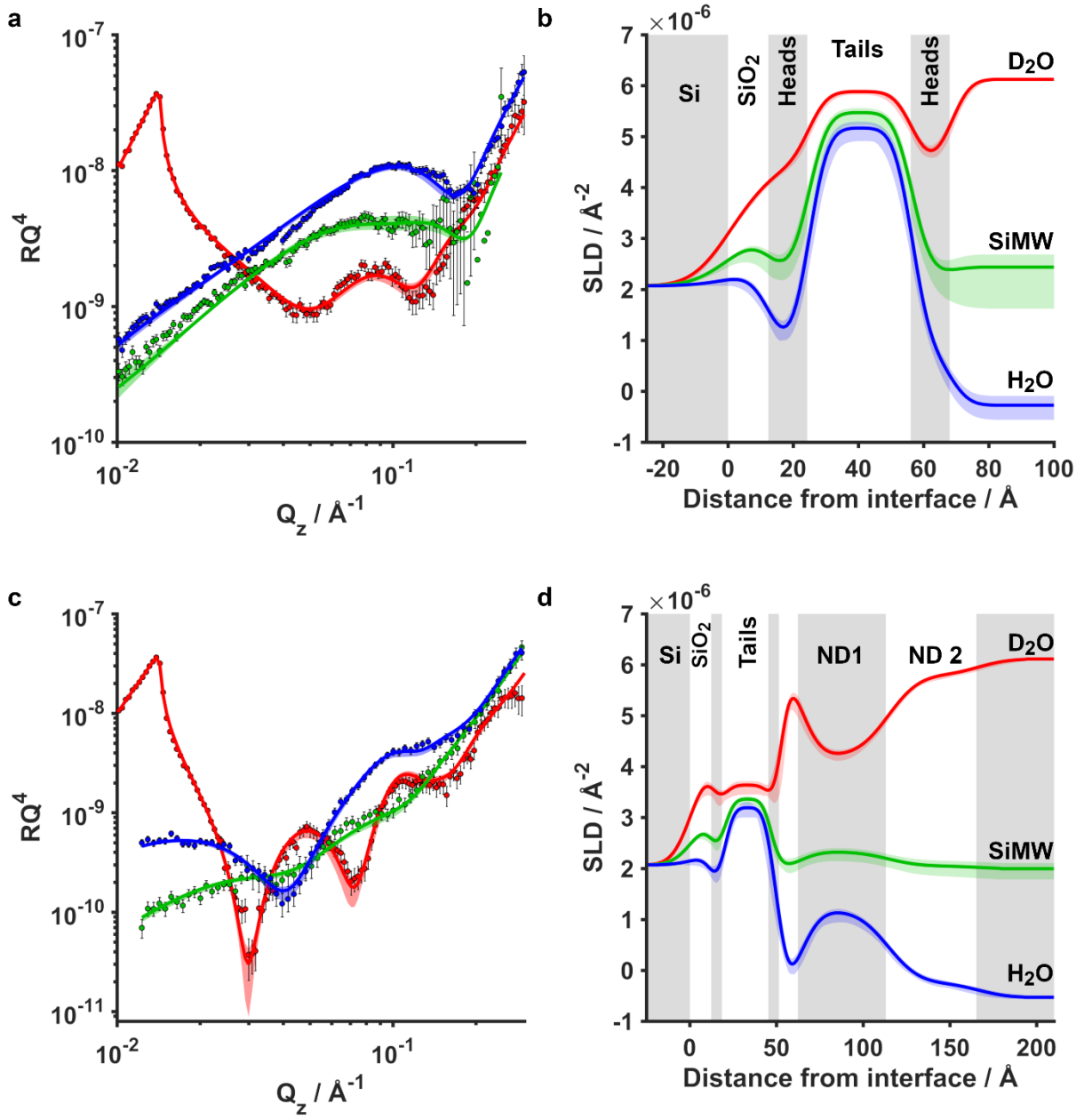

Figure 4.11. Neutron reflectometry data (points) with overlaid fits (solid lines) plotted as RQ^4 (a, c) and corresponding model SLD profiles (b, d) of a dDMPC supported bilayer deposited on a Si substrate before (a, b) and after (c, d) incubation with hDMPC RAFT-SMALPs. Colored shaded regions represent the 95% confidence interval associated with the fit and model SLD profiles determined by Bayesian MCMC error estimation routines. Grey shaded regions denote layer boundaries in the model SLD profiles. In all cases, red, green and blue points/lines correspond to data collected in D_2O, SiMW and H_2O solution contrasts, respectively.

Table 4.9. Structural parameters obtained by fitting NR data of dDMPC bilayers at the Si-water interface before and after incubation with hDMPC RAFT-SMALPs. Values marked * were held as a constant throughout the fitting procedure. Values in parentheses indicate the 95% confidence intervals estimated from Bayesian MCMC error estimation.

Layer	Parameter	dDMPC bilayer	dDMPC bilayer after hDMPC RAFT-SMALP incubation
Si	SLD / $\times 10^{-6}$ Å^{-2}	2.07*	
	Roughness / Å	9 (8, 10)	
SiO_2	SLD / $\times 10^{-6}$ Å^{-2}	3.47*	
	Thickness / Å	12 (11, 13)	
	Hydration / %	29 (26, 32)	
	Roughness / Å	5 (4, 6)	
PC Headgroups	SLD / $\times 10^{-6}$ Å^{-2}	2.14*	2.14*
	Thickness / Å	12 (11, 12)	6 (5, 7)
	Hydration / %	57 (56, 58)	7 (3, 9)
	Roughness / Å	4 (3, 5)	4 (2, 5)
DM Tails	SLD / $\times 10^{-6}$ Å^{-2}	5.85 (5.80, 5.91)	4.64 (4.60, 4.68)
	Thickness / Å	15 (15, 16)	13 (12, 14)
	Hydration / %	11 (9, 13)	6 (3, 10)
	Roughness / Å	4 (3, 5)	4 (2, 5)
DM Tails	SLD / $\times 10^{-6}$ Å^{-2}	5.85 (5.80, 5.91)	4.64 (4.60, 4.68)
	Thickness / Å	15 (15, 16)	13 (12, 14)
	Hydration / %	11 (9, 13)	6 (3, 10)
	Roughness / Å	4 (3, 5)	4 (2, 5)
PC Headgroups	SLD / $\times 10^{-6}$ Å^{-2}	2.14*	2.14*
	Thickness / Å	12 (11, 12)	6 (5, 7)
	Hydration / %	57 (56, 58)	7 (3, 9)
	Roughness / Å	4 (3, 5)	4 (2, 5)
Water gap	Thickness / Å	-	11 (10, 12)
	Roughness / Å	-	9 (7, 10)
Nanodiscs Layer 1	SLD / $\times 10^{-6}$ Å^{-2}	-	2.60 (2.50, 2.70)
	χ_{dDMPC}	-	0.60 (0.57, 0.62)
	Thickness / Å	-	51 (47, 54)
	Hydration / %	-	46 (43, 48)
	Roughness / Å	-	14 (10, 15)
Nanodiscs Layer 2	SLD / $\times 10^{-6}$ Å^{-2}	-	2.60 (2.50, 2.70)
	χ_{dDMPC}	-	0.60 (0.57, 0.62)
	Thickness / Å	-	52 (44, 60)
	Hydration / %	-	91 (88, 93)
	Roughness / Å	-	14 (10, 15)
Bulk Solvent	SLD (D_2O)/ $\times 10^{-6}$ Å^{-2}	6.12 (6.11, 6.13)	6.11 (6.10, 6.12)
	SLD (SiMW)/ $\times 10^{-6}$ Å^{-2}	2.45 (1.77, 2.71)	1.99 (1.87, 2.12)
	SLD (H_2O)/ $\times 10^{-6}$ Å^{-2}	-0.27 (-0.55, -0.07)	-0.53 (-0.56, -0.47)

hDMPC nanodiscs were then injected into bulk solution and incubated for 5 hours, after which the flow cells were flushed with buffer to remove excess, non-adsorbed polymer/ nanodiscs and the resultant structures analyzed by NR in three solution contrasts. In the case of dDMPC bilayers with hDMPC SMALPs, we were able to obtain satisfactory fits to the experimental data by using the same 5 layer model as described for dDMPC bilayers before nanodisc interaction (Figure 4.9c, d), indicating that SMALP nanodiscs do not adsorb to the interfacial bilayer. Structural parameters obtained from these fits (Table 4.7) indicate that incubation with hDMPC SMALPs leads to a net loss of material from the bilayer. Hydration of the DMPC tails region increases from approximately 6 to 38%. We also observe a decrease in SLD of the tails, from 6.45 to 3.41 $\times 10^{-6}$ Å^{-2}. If this change is solely down to the introduction of hDMPC, then we can estimate that 43% of the remaining lipid is hDMPC from the nanodiscs. While modelling subtle changes to the bilayer structure after the interaction with hDMPC SMALPs was able to produce a slightly improved fit, this introduces a high level of uncertainty in the model parameters. As evidenced by the ability of the presented model to adequately describe the experimental data, the disruption to the bilayer structure is likely minor and we therefore proceed with the simpler model. Similarly, small changes to the SLD of the lipid headgroup, modelling polymer incorporation, was also able to marginally improve the fit quality. However, the we were unable to describe the location of SMA within the bilayer to any certainty due to the similarity in SLD of SMA to the lipid headgroups.

NR data collected after the interaction of dDMPC bilayer with hDMPC SMILPs could also be fit using the same 5 layer model (Figure 4.10c, d). Parameters obtained through fitting of this model (Table 4.8) suggest that, within error, there is no addition or removal of phospholipids from the bilayer, as shown by only a very slight decrease in hydration of the lipid tails. We also observed a smaller decrease in SLD of the lipid tails from 6.36 to 4.94 $\times 10^{-6}$ Å^{-2}. Again, if this decrease in SLD is solely due to lipid exchange, we can estimate that 21% of the lipid in the resultant bilayer is hDMPC from SMILPs. As with the interaction of hDMPC SMALPs, modelling subtle changes to the bilayer structure was able to provide a marginal improvement to the fit. However, the same caveats apply that such a minor structural change introduces a high level of uncertainty into the model, and as such we opted for the simpler model.

In contrast to SMALPs and SMILPs, the NR data collected after the incubation of a dDMPC bilayer with hDMPC RAFT-SMALPs shows the appearance of strong Keissig fringes which are indicative of a much thicker interfacial layer (Figure 4.11c). Satisfactory fits to these data could not be obtained by using the 5 layer model as described above, nor by including a single extra layer modelling RAFT-SMA adsorption to the bilayer surface. We were, however, able to fit an 8-layer model to the experimental data with the additional layers corresponding to a thin, fully solvated water layer and two layers corresponding to adsorbed RAFT-SMALP nanodiscs (Figure 4.11d). Parameters obtained through fitting of this model (Table 4.9) indicate that there is a slight net addition of lipids to the bilayer, as indicated by the decrease in hydration of the tail layer from 11 to 6%. Additionally, a decrease in SLD of the phospholipid tail layer from 5.85 to 4.64 $\times 10^{-6}$ Å^{-2}, allowing us to estimate that 21% of the lipids in the bilayer are hDMPC from RAFT-SMALPs. Unlike the interactions of hDMPC SMALPs and SMILPs, retaining the bilayer structure before and after RAFT-SMALP interaction was unable to produce satisfactory fits to the experimental data. A thinning of all layers within the bilayer was observed, countering our earlier observation of a net lipid deposition. One would expect that packing more lipids in the bilayer would increase the observed thickness by reducing the tilt angle. A thinner membrane and decreased hydration could be indicative of RAFT-SMA embedding throughout the bilayer whilst also removing lipids. Therefore our estimate of the total amount of lipid incorporation in the bilayer is likely an overestimation.

The layers corresponding to adsorbed RAFT-SMALPs were modelled with an SLD calculated for the entire nanodisc, fitting for the mole fraction of dDMPC from the bilayer contained within the adsorbed nanodiscs (for more detail see section 4.3.2.10). This allows us to estimate that 60% of the lipid contained within the adsorbed nanodiscs are dDMPC. This suggests that adsorbed RAFT-SMALPs undergo lipid exchange with deuterated lipids present in the supported bilayer. The thicknesses of both layers are similar, and each thicker than that expected for a planar nanodisc-encapsulated bilayer adsorbed parallel to the original supported bilayer. The hydration of the outermost nanodisc layer is significantly higher than that of the inner nanodisc layer. When taking this in combination with the high

roughness associated with these layers, we propose that RAFT-SMALPs adsorb in multiple orientations to the supported lipid bilayer, whilst undergoing bidirectional lipid exchange.

4.5 DISCUSSION

By using a combination of NR and ATR-FTIR spectroscopy, we have been able to quantify lipid and polymer exchange between nanodiscs in bulk solution and phospholipid monolayers at the air-water interface or phospholipid bilayers at the Si-water interface. Due to the contribution of polymers embedding into the monolayer in the case of the air-water interface, and the limitation to relative changes in arbitrary peak integrals in the case of the Si-water interface, we are unable to directly compare kinetic parameters obtained from the interaction of nanodiscs with different interfacial membranes. We can, however, identify similarities and differences between the interactions and hypothesize as to underlying mechanisms.

When comparing the total changes in surface excess from lipid/polymer gained and lost at the monolayers, we can identify an interesting trend. While on initial inspection, SMALPS and SMILPs lead to a similar loss of material from the monolayer, as discussed above, SMALPs lead to a subsequent increase in the surface excess after the initial decrease. We suggest that this increase is due to polymer incorporation into the monolayers which is not accounted for in the surface excess calculations. Therefore the total loss of lipid from the bilayer to SMALPs is likely an underestimation. If this assumption is correct, then the trend emerges that SMALPs lead to both the highest amount of removal and deposition at the monolayer and RAFT-SMALPs the least. Previous studies investigating the thermodynamics of self-assembly of these nanodiscs show that the Gibbs energy of transition for the polymers associating with the lipids is most negative for RAFT-SMALPs and least negative for SMALPs.[39,43] By investigating lipid exchange between nanodiscs and bilayers at the Si-water interface determined by ATR-FTIR spectroscopy, the same trend emerges, whereby RAFT-SMALPs exchange the least lipids with bilayers at the Si-water interface and SMALPs exchange the most. Therefore we propose that the thermodynamic stability associated with each of the polymers dictates the propensity of each nanodisc to exchange material with planar lipid membranes.

When comparing the kinetics of lipid/polymer exchange at both the air-water and Si-water interfaces, two phase kinetics can be seen in both cases. This suggests that the interactions at both interfaces are mediated by a two-phase process. As described above, we propose that the initial, rapid phase is due to polymer re-partitioning amongst the additional lipid present in the system when taking into account the interfacial lipids, and the second phase is due to collisional lipid exchange between nanodiscs in bulk solution and the interfacial lipids. While, biphasic kinetics are seen at both interfaces, interestingly, the result of the fast polymer-equilibration phase at the air-water interface leads to a deposition of lipids and polymer from the nanodiscs at the membrane, while at the solid-liquid interface, this leads to a removal of lipid from the membrane.

In the case of equilibration with a monolayer at the air-water interface, lipid/ polymer deposition must occur through a disruption of the nanodisc structure. Once disassembled, the high stability of the monolayer will likely prohibit solubilization of the interfacial lipids, leading to the observed deposition of lipids and polymer. This is supported by the surface activity of SMALPs, indicating that once in contact with the air-water interface, the nanodiscs will disassemble leading to a mixed polymer/phospholipid monolayer at the air-water interface. Structural information obtained by NR of monolayers after incubation with nanodiscs also supports this hypothesis. While we have observed evidence of polymer incorporation into the tail region of the phospholipid monolayer in all cases, we remain insensitive to the association of polymers with the headgroups due to the similarity in SLD.

As described above, a bilayer at the Si-water interface presents a substantially different thermodynamic environment than monolayers at the air-water interface. The bilayers themselves are a very similar environment to the bilayer-containing phospholipid core of nanodiscs. Previous studies have shown that there is very little thermodynamic penalty from the perspective of the lipids in transitioning from a curved, vesicular bilayer to a planar nanodisc. [35,38,39,43] This penalty is likely to be decreased further as lipids move between planar bilayers. Therefore, the rapid equilibration of the polymers with the additional lipid present in the monolayer will likely lead to solubilization and removal of lipids from the interfacial bilayer without the thermodynamic barriers present at the air-water

interface. However, in all cases, polymer can be identified associated with the bilayer by both ATR-FTIR and NR measurements. This suggests that lipids in the bilayer still experience a thermodynamic penalty in transitioning from the interfacial bilayer to the nanodisc phases, leading to polymer incorporation in the bilayers.

In the case of SMALPs, two-phase kinetics are observed for both lipid deposition and removal from the membranes at each interface measured. If our hypothesis is correct of an initial rapid polymer re-equilibration, then this suggests that during this phase, lipid is deposited at the interfaces from the nanodiscs and transferred from the interface to nanodiscs as the nanodiscs disassemble and reassemble. At the air-water interface, more polymer was observed in the monolayer when compared to SMILPs and RAFT-SMALPs. Due to the preferred interaction of SMA with phospholipids over self-interaction, an overloading of the monolayer with SMA will likely lead to the observed removal of lipid from the monolayer accompanying the deposition of lipids at the monolayer from nanodisc disassembly. SMALP nanodiscs experience the least perturbation to the thermodynamic environment of the phospholipids upon solubilization as well as the weakest thermodynamic driving force for polymer to interact with lipids. At the Si-water interface, this will lead to an increased propensity for lipids to move bidirectionally between the nanodiscs and the bilayer due to the thermodynamic similarity of the two environments.

Exchange of polymers in addition to lipids is not unexpected. Recent studies have shown by fluorescently labelling SMA polymers, that in addition to the now-accepted lipid exchange between nanodiscs in solution,[49,50] there is also exchange of polymers between nanodiscs.[68] Furthermore, studies of nanodisc self-assembly have demonstrated that nanodiscs form via an initial adsorption of polymers to the bilayer surface, prior to embedding into the hydrophobic core and subsequent solubilization.[36,69] This is not dissimilar to what we observe here. Additionally, studies have also shown that polymers will partition between the available lipid in a system leading to changes in nanodisc structure which are dependent on the lipid:polymer ratio.[35,38,39,43] This suggests that here, by introducing nanodiscs to an additional source of lipids at the interface, we change the lipid:polymer ratio which will result in the

repartitioning of polymers amongst the available lipid, leading to simultaneous lipid and polymer exchange.

In stark contrast to the interactions of SMALPs and SMILPs with planar bilayers at the Si-water interface, RAFT-SMALPs adsorb to the membrane in addition to undergoing lipid and polymer exchange, as measured by NR. Kinetic data obtained by FTIR indicates that the majority of the lipid and polymer exchange occurs rapidly as a result of the aforementioned polymer equilibration. After this phase, we observe only a minor loss of lipid from the bilayer and a steady deposition of hydrogenated lipid as RAFT-SMALPs adsorb to the interfacial bilayer. If we assume a uniform discoidal structure of RAFT-SMALPs, then given triangular packing on the surface, the highest coverage achievable will be 90.7%. Previous studies on the structure of SMALPs have found that approximately 42 mol% solvent is found in the polymer rim, which itself occupies 35% of the volume of the nanodisc core (lipid tails + polymer). If we assume a similar structure for RAFT-SMALPs, given hexagonal packing, the highest theoretical coverage achievable with hexagonal packing gives an apparent 24% hydration. Through fitting of the model SLD profile to the experimental data, we observe 46% hydration of the inner nanodisc layer. In reality, the formal negative charge present on the polymer will lead to electrostatic repulsion between nanodiscs, to decrease the maximum surface coverage further. While the thickness of each nanodisc layer within the model is thicker than would formed by a nanodisc-encapsulated lipid bilayer adsorbed parallel to the interface, the total thickness we obtained for both RAFT-SMALP layers is of the order of 10 nm, in good agreement with nanodisc diameters reported in previous studies on SMALP structure. We, therefore, are therefore confident in our model describing nanodisc adsorption in multiple orientations and expect that we observe close to the maximum achievable coverage of a RAFT-SMALP film.

Previous studies investigating the interaction of RAFT-SMALPs with DOPC monolayers deposited on a hydrophobic surface at the Si-water interface saw little to no nanodisc adsorption [48]. The reasons as to why, in this case, clear increases in thickness were observed is unclear. Previously, RAFT-SMALPs were not purified prior to incubation with phospholipid monolayers. During SEC purification

of RAFT-SMALPs, we did observe a small peak with a higher retention volume which is likely to be non-associated polymer. If this small quantity of excess polymer was not removed, then the lipid:polymer ratio would have been altered which is likely to change the interaction with the surface. In addition, it is possible that DOPC monolayers are less amenable to adsorption than DMPC bilayers. Incomplete coverage of hydrophobic silicon could promote nanodisc disassembly at the Si-water interface, which would disrupt the adsorption of intact nanodiscs. Furthermore, the high gel to liquid transition temperature of DOPC relative to DMPC could affect the kinetics of the interaction such that adsorption is not favored. This clearly points to an area which would merit from further investigation if reliable and robust assembly of nanodisc films is to be achieved for functional and structural studies of nanodisc-solubilized MPs at interfaces.

4.6 CONCLUSIONS

Here, we have demonstrated that both lipid and polymer exchange occurs between polymer-stabilized phospholipid nanodiscs stabilized by three structurally related polymers and model phospholipid membranes at the air-water and Si-water interfaces. While the most lipid and polymer exchange occurs with SMALP nanodiscs, each nanodisc tested experiences lipid and polymer exchange with planar model membranes. It has been previously demonstrated that both phospholipid composition of nanodiscs and ionic strength of the solution can change the kinetics of lipid exchange between nanodiscs in solution. It remains to be seen as to whether changing these properties could influence lipid exchange between nanodiscs and planar phospholipid membranes. Nonetheless, our results present some exploitable differences between the lipid exchange properties of different nanodiscs. For example, for probing the influence of the local lipid environment on MP activity, polymer choice may be dictated by that which leads to the highest amount and rate of lipid exchange. In addition, for the first time, we have demonstrated the creation of nanodisc films adsorbed to planar bilayers at the Si-water interface. This demonstrates the potential of SMALP nanodiscs to be used for structural and functional characterization of solubilized MPs within a phospholipid environment by techniques such as X-ray and neutron reflectometry, surface plasmon resonance and quartz-crystal microbalance.

4.7 REFERENCES

(1) Fagerberg, L.; Jonasson, K.; von Heijne, G.; Uhlén, M.; Berglund, L. Prediction of the Human Membrane Proteome. *Proteomics* **2010**, *10* (6), 1141–1149. https://doi.org/10.1002/pmic.200900258.

(2) Uhlén, M.; Fagerberg, L.; Hallström, B. M.; Lindskog, C.; Oksvold, P.; Mardinoglu, A.; Sivertsson, Å.; Kampf, C.; Sjöstedt, E.; Asplund, A.; et al. Tissue-Based Map of the Human Proteome. *Science* **2015**, *347* (6220), 1260419. https://doi.org/10.1126/science.1260419.

(3) Overington, J. P.; Al-Lazikani, B.; Hopkins, A. L. How Many Drug Targets Are There? *Nat. Rev. Drug Discov.* **2006**, *5* (12), 993–996. https://doi.org/10.1038/nrd2199.

(4) Seddon, A. M.; Curnow, P.; Booth, P. J. Membrane Proteins, Lipids and Detergents: Not Just a Soap Opera. *Biochim. Biophys. Acta BBA - Biomembr.* **2004**, *1666* (1–2), 105–117. https://doi.org/10.1016/j.bbamem.2004.04.011.

(5) Arnold, T.; Linke, D. The Use of Detergents to Purify Membrane Proteins. *Curr. Protoc. Protein Sci.* **2008**, *Chapter 4*, Unit 4.8.1-4.8.30. https://doi.org/10.1002/0471140864.ps0408s53.

(6) Smith, S. M. Strategies for the Purification of Membrane Proteins. *Methods Mol. Biol. Clifton NJ* **2011**, *681*, 485–496. https://doi.org/10.1007/978-1-60761-913-0_29.

(7) Krishnamani, V.; Lanyi, J. K. Molecular Dynamics Simulation of the Unfolding of Individual Bacteriorhodopsin Helices in Sodium Dodecyl Sulfate Micelles. *Biochemistry* **2012**, *51* (6), 1061–1069. https://doi.org/10.1021/bi201770y.

(8) Frey, L.; Lakomek, N.-A.; Riek, R.; Bibow, S. Micelles, Bicelles, and Nanodiscs: Comparing the Impact of Membrane Mimetics on Membrane Protein Backbone Dynamics. *Angew. Chem. Int. Ed.* **2016**, *56* (1), 380–383. https://doi.org/10.1002/anie.201608246.

(9) Popot, J.-L. Amphipols, Nanodiscs, and Fluorinated Surfactants: Three Nonconventional Approaches to Studying Membrane Proteins in Aqueous Solutions. *Annu. Rev. Biochem.* **2010**, *79*, 737–775. https://doi.org/10.1146/annurev.biochem.052208.114057.

(10) Parmar, M. J.; Lousa, C. D. M.; Muench, S. P.; Goldman, A.; Postis, V. L. G. Artificial Membranes for Membrane Protein Purification, Functionality and Structure Studies. *Biochem. Soc. Trans.* **2016**, *44* (3), 877–882. https://doi.org/10.1042/BST20160054.

(11) Hardy, D.; Bill, R. M.; Jawhari, A.; Rothnie, A. J. Overcoming Bottlenecks in the Membrane Protein Structural Biology Pipeline. *Biochem. Soc. Trans.* **2016**, *44* (3), 838–844. https://doi.org/10.1042/BST20160049.

(12) Denisov, I. G.; Sligar, S. G. Nanodiscs in Membrane Biochemistry and Biophysics. *Chem. Rev.* **2017**, *117* (6), 4669–4713. https://doi.org/10.1021/acs.chemrev.6b00690.

(13) Bayburt, T. H.; Grinkova, Y. V.; Sligar, S. G. Self-Assembly of Discoidal Phospholipid Bilayer Nanoparticles with Membrane Scaffold Proteins. *Nano Lett.* **2002**, *2* (8), 853–856. https://doi.org/10.1021/nl025623k.

(14) Denisov, I. G.; Grinkova, Y. V.; Lazarides, A. A.; Sligar, S. G. Directed Self-Assembly of Monodisperse Phospholipid Bilayer Nanodiscs with Controlled Size. *J. Am. Chem. Soc.* **2004**, *126* (11), 3477–3487. https://doi.org/10.1021/ja0393574.

(15) Denisov, I. G.; Sligar, S. G. Nanodiscs for Structural and Functional Studies of Membrane Proteins. *Nat. Struct. Mol. Biol.* **2016**, *23* (6), 481–486. https://doi.org/10.1038/nsmb.3195.

(16) Bayburt, T. H.; Sligar, S. G. Membrane Protein Assembly into Nanodiscs. *FEBS Lett.* **2010**, *584* (9), 1721–1727. https://doi.org/10.1016/j.febslet.2009.10.024.

(17) Roh, S.-H.; Stam, N. J.; Hryc, C. F.; Couoh-Cardel, S.; Pintilie, G.; Chiu, W.; Wilkens, S. The 3.5-Å CryoEM Structure of Nanodisc-Reconstituted Yeast Vacuolar ATPase Vo Proton Channel. *Mol. Cell* **2018**, *69* (6), 993-1004.e3. https://doi.org/10.1016/j.molcel.2018.02.006.

(18) Skar-Gislinge, N.; Kynde, S. A. R.; Denisov, I. G.; Ye, X.; Lenov, I.; Sligar, S. G.; Arleth, L. Small-Angle Scattering Determination of the Shape and Localization of Human Cytochrome P450 Embedded in a Phospholipid Nanodisc Environment. *Acta Crystallogr. D Biol. Crystallogr.* **2015**, *71* (Pt 12), 2412–2421. https://doi.org/10.1107/S1399004715018702.

(19) Gao, Y.; Cao, E.; Julius, D.; Cheng, Y. TRPV1 Structures in Nanodiscs Reveal Mechanisms of Ligand and Lipid Action. *Nature* **2016**, *534* (7607), 347–351. https://doi.org/10.1038/nature17964.

(20) Pandit, A.; Shirzad-Wasei, N.; Wlodarczyk, L. M.; van Roon, H.; Boekema, E. J.; Dekker, J. P.; de Grip, W. J. Assembly of the Major Light-Harvesting Complex II in Lipid Nanodiscs. *Biophys. J.* **2011**, *101* (10), 2507–2515. https://doi.org/10.1016/j.bpj.2011.09.055.

(21) Frauenfeld, J.; Gumbart, J.; Sluis, E. O. van der; Funes, S.; Gartmann, M.; Beatrix, B.; Mielke, T.; Berninghausen, O.; Becker, T.; Schulten, K.; et al. Cryo-EM Structure of the Ribosome–SecYE Complex in the Membrane Environment. *Nat. Struct. Mol. Biol.* **2011**, *18* (5), 614–621. https://doi.org/10.1038/nsmb.2026.

(22) Kijac, A. Z.; Li, Y.; Sligar, S. G.; Rienstra, C. M. Magic-Angle Spinning Solid-State NMR Spectroscopy of Nanodisc-Embedded Human CYP3A4. *Biochemistry* **2007**, *46* (48), 13696–13703. https://doi.org/10.1021/bi701411g.

(23) Nikolaev, M.; Round, E.; Gushchin, I.; Polovinkin, V.; Balandin, T.; Kuzmichev, P.; Shevchenko, V.; Borshchevskiy, V.; Kuklin, A.; Round, A.; et al. Integral Membrane Proteins Can Be Crystallized Directly from Nanodiscs. *Cryst. Growth Des.* **2017**, *17* (3), 945–948. https://doi.org/10.1021/acs.cgd.6b01631.

(24) Knowles, T. J.; Finka, R.; Smith, C.; Lin, Y.-P.; Dafforn, T.; Overduin, M. Membrane Proteins Solubilized Intact in Lipid Containing Nanoparticles Bounded by Styrene Maleic Acid Copolymer. *J. Am. Chem. Soc.* **2009**, *131* (22), 7484–7485. https://doi.org/10.1021/ja810046q.

(25) Jamshad, M.; Grimard, V.; Idini, I.; Knowles, T. J.; Dowle, M. R.; Schofield, N.; Sridhar, P.; Lin, Y.; Finka, R.; Wheatley, M.; et al. Structural Analysis of a Nanoparticle Containing a Lipid Bilayer Used for Detergent-Free Extraction of Membrane Proteins. *Nano Res.* **2015**, *8* (3), 774–789. https://doi.org/10.1007/s12274-014-0560-6.

(26) Lee, S. C.; Knowles, T. J.; Postis, V. L. G.; Jamshad, M.; Parslow, R. A.; Lin, Y.-P.; Goldman, A.; Sridhar, P.; Overduin, M.; Muench, S. P.; et al. A Method for Detergent-Free Isolation of Membrane Proteins in Their Local Lipid Environment. *Nat. Protoc.* **2016**, *11* (7), 1149–1162. https://doi.org/10.1038/nprot.2016.070.

(27) Morrison, K. A.; Akram, A.; Mathews, A.; Khan, Z. A.; Patel, J. H.; Zhou, C.; Hardy, D. J.; Moore-Kelly, C.; Patel, R.; Odiba, V.; et al. Membrane Protein Extraction and Purification Using Styrene-Maleic Acid (SMA) Copolymer: Effect of Variations in Polymer Structure. *Biochem. J.* **2016**, *473* (23), 4349–4360. https://doi.org/10.1042/BCJ20160723.

(28) Jamshad, M.; Charlton, J.; Lin, Y.-P.; Routledge, S. J.; Bawa, Z.; Knowles, T. J.; Overduin, M.; Dekker, N.; Dafforn, T. R.; Bill, R. M.; et al. G-Protein Coupled Receptor Solubilization and Purification for Biophysical Analysis and Functional Studies, in the Total Absence of Detergent. *Biosci. Rep.* **2015**, *35* (2), e00188. https://doi.org/10.1042/BSR20140171.

(29) Swainsbury, D. J. K.; Scheidelaar, S.; van Grondelle, R.; Killian, J. A.; Jones, M. R. Bacterial Reaction Centers Purified with Styrene Maleic Acid Copolymer Retain Native Membrane Functional Properties and Display Enhanced Stability. *Angew. Chem. Int. Ed Engl.* **2014**, *53* (44), 11803–11807. https://doi.org/10.1002/anie.201406412.

(30) Laursen, T.; Borch, J.; Knudsen, C.; Bavishi, K.; Torta, F.; Martens, H. J.; Silvestro, D.; Hatzakis, N. S.; Wenk, M. R.; Dafforn, T. R.; et al. Characterization of a Dynamic Metabolon Producing the Defense Compound Dhurrin in Sorghum. *Science* **2016**, *354* (6314), 890–893. https://doi.org/10.1126/science.aag2347.

(31) Broecker, J.; Eger, B. T.; Ernst, O. P. Crystallogenesis of Membrane Proteins Mediated by Polymer-Bounded Lipid Nanodiscs. *Structure* **2017**, *25* (2), 384–392. https://doi.org/10.1016/j.str.2016.12.004.

(32) Bersch, B.; Dörr, J. M.; Hessel, A.; Killian, J. A.; Schanda, P. Proton-Detected Solid-State NMR Spectroscopy of a Zinc Diffusion Facilitator Protein in Native Nanodiscs. *Angew. Chem. Int. Ed Engl.* **2017**, *56* (9), 2508–2512. https://doi.org/10.1002/anie.201610441.

(33) Parmar, M.; Rawson, S.; Scarff, C. A.; Goldman, A.; Dafforn, T. R.; Muench, S. P.; Postis, V. L. G. Using a SMALP Platform to Determine a Sub-Nm Single Particle Cryo-EM Membrane

Protein Structure. *Biochim. Biophys. Acta BBA - Biomembr.* **2018**, *1860* (2), 378–383. https://doi.org/10.1016/j.bbamem.2017.10.005.

(34) Sun, C.; Benlekbir, S.; Venkatakrishnan, P.; Wang, Y.; Hong, S.; Hosler, J.; Tajkhorshid, E.; Rubinstein, J. L.; Gennis, R. B. Structure of the Alternative Complex III in a Supercomplex with Cytochrome Oxidase. *Nature* **2018**, *557* (7703), 123–126. https://doi.org/10.1038/s41586-018-0061-y.

(35) Vargas, C.; Arenas, R. C.; Frotscher, E.; Keller, S. Nanoparticle Self-Assembly in Mixtures of Phospholipids with Styrene/Maleic Acid Copolymers or Fluorinated Surfactants. *Nanoscale* **2015**, *7* (48), 20685–20696. https://doi.org/10.1039/c5nr06353a.

(36) Scheidelaar, S.; Koorengevel, M. C.; Pardo, J. D.; Meeldijk, J. D.; Breukink, E.; Killian, J. A. Molecular Model for the Solubilization of Membranes into Nanodisks by Styrene Maleic Acid Copolymers. *Biophys. J.* **2015**, *108* (2), 279–290. https://doi.org/10.1016/j.bpj.2014.11.3464.

(37) Scheidelaar, S.; Koorengevel, M. C.; van Walree, C. A.; Dominguez, J. J.; Dörr, J. M.; Killian, J. A. Effect of Polymer Composition and PH on Membrane Solubilization by Styrene-Maleic Acid Copolymers. *Biophys. J.* **2016**, *111* (9), 1974–1986. https://doi.org/10.1016/j.bpj.2016.09.025.

(38) Grethen, A.; Oluwole, A. O.; Danielczak, B.; Vargas, C.; Keller, S. Thermodynamics of Nanodisc Formation Mediated by Styrene/Maleic Acid (2:1) Copolymer. *Sci. Rep.* **2017**, *7* (1), 11517. https://doi.org/10.1038/s41598-017-11616-z.

(39) Hall, S. C. L.; Tognoloni, C.; Price, G. J.; Klumperman, B.; Edler, K. J.; Dafforn, T. R.; Arnold, T. Influence of Poly(Styrene-Co-Maleic Acid) Copolymer Structure on the Properties and Self-Assembly of SMALP Nanodiscs. *Biomacromolecules* **2018**, *19* (3), 761–772. https://doi.org/10.1021/acs.biomac.7b01539.

(40) Stroud, Z.; Hall, S. C. L.; Dafforn, T. R. Purification of Membrane Proteins Free from Conventional Detergents: SMA, New Polymers, New Opportunities and New Insights. *Methods* **2018**. https://doi.org/10.1016/j.ymeth.2018.03.011.

(41) Smith, A. A. A.; Autzen, H. E.; Laursen, T.; Wu, V.; Yen, M.; Hall, A.; Hansen, S. D.; Cheng, Y.; Xu, T. Controlling Styrene Maleic Acid Lipid Particles through RAFT. *Biomacromolecules* **2017**, *18* (11), 3706–2713. https://doi.org/10.1021/acs.biomac.7b01136.

(42) Craig, A. F.; Clark, E. E.; Sahu, I. D.; Zhang, R.; Frantz, N. D.; Al-Abdul-Wahid, M. S.; Dabney-Smith, C.; Konkolewicz, D.; Lorigan, G. A. Tuning the Size of Styrene-Maleic Acid Copolymer-Lipid Nanoparticles (SMALPs) Using RAFT Polymerization for Biophysical Studies. *Biochim. Biophys. Acta BBA - Biomembr.* **2016**, *1858* (11), 2931–2939. https://doi.org/10.1016/j.bbamem.2016.08.004.

(43) Hall, S. C. L.; Tognoloni, C.; Charlton, J.; Bragginton, É. C.; Rothnie, A. J.; Sridhar, P.; Wheatley, M.; Knowles, T. J.; Arnold, T.; Edler, K. J.; et al. An Acid-Compatible Co-Polymer for the Solubilization of Membranes and Proteins into Lipid Bilayer-Containing Nanoparticles. *Nanoscale* **2018**, *10* (22), 10609–10619. https://doi.org/10.1039/C8NR01322E.

(44) Patching, S. G. Surface Plasmon Resonance Spectroscopy for Characterisation of Membrane Protein–Ligand Interactions and Its Potential for Drug Discovery. *Biochim. Biophys. Acta BBA - Biomembr.* **2014**, *1838* (1, Part A), 43–55. https://doi.org/10.1016/j.bbamem.2013.04.028.

(45) Wadsäter, M.; Simonsen, J. B.; Lauridsen, T.; Tveten, E. G.; Naur, P.; Bjørnholm, T.; Wacklin, H.; Mortensen, K.; Arleth, L.; Feidenhans'l, R.; et al. Aligning Nanodiscs at the Air–Water Interface, a Neutron Reflectivity Study. *Langmuir* **2011**, *27* (24), 15065–15073. https://doi.org/10.1021/la203100n.

(46) Wadsäter, M.; Laursen, T.; Singha, A.; Hatzakis, N. S.; Stamou, D.; Barker, R.; Mortensen, K.; Feidenhans'l, R.; Møller, B. L.; Cárdenas, M. Monitoring Shifts in the Conformation Equilibrium of the Membrane Protein Cytochrome P450 Reductase (POR) in Nanodiscs. *J. Biol. Chem.* **2012**, *287* (41), 34596–34603. https://doi.org/10.1074/jbc.M112.400085.

(47) Bertram, N.; Laursen, T.; Barker, R.; Bavishi, K.; Møller, B. L.; Cárdenas, M. Nanodisc Films for Membrane Protein Studies by Neutron Reflection: Effect of the Protein Scaffold Choice. *Langmuir* **2015**, *31* (30), 8386–8391. https://doi.org/10.1021/acs.langmuir.5b00936.

(48) Hazell, G.; Arnold, T.; Barker, R. D.; Clifton, L. A.; Steinke, N.-J.; Tognoloni, C.; Edler, K. J. Evidence of Lipid Exchange in Styrene Maleic Acid Lipid Particle (SMALP) Nanodisc Systems. *Langmuir* **2016**, *32* (45), 11845–11853. https://doi.org/10.1021/acs.langmuir.6b02927.

(49) Cuevas Arenas, R.; Danielczak, B.; Martel, A.; Porcar, L.; Breyton, C.; Ebel, C.; Keller, S. Fast Collisional Lipid Transfer Among Polymer-Bounded Nanodiscs. *Sci. Rep.* **2017**, *7*, 45875. https://doi.org/10.1038/srep45875.

(50) Grethen, A.; Glueck, D.; Keller, S. Role of Coulombic Repulsion in Collisional Lipid Transfer Among SMA(2:1)-Bounded Nanodiscs. *J. Membr. Biol.* **2018**, *251* (3), 443–451. https://doi.org/10.1007/s00232-018-0024-0.

(51) Harrisson, S.; Wooley, K. L. Shell-Crosslinked Nanostructures from Amphiphilic AB and ABA Block Copolymers of Styrene-Alt-(Maleic Anhydride) and Styrene: Polymerization, Assembly and Stabilization in One Pot. *Chem. Commun.* **2005**, *26*, 3259–3261. https://doi.org/10.1039/b504313a.

(52) Campbell, R. A.; Wacklin, H. P.; Sutton, I.; Cubitt, R.; Fragneto, G. FIGARO: The New Horizontal Neutron Reflectometer at the ILL. *Eur. Phys. J. Plus* **2011**, *126* (11), 107. https://doi.org/10.1140/epjp/i2011-11107-8.

(53) Braun, L.; Uhlig, M.; von Klitzing, R.; Campbell, R. A. Polymers and Surfactants at Fluid Interfaces Studied with Specular Neutron Reflectometry. *Adv. Colloid Interface Sci.* **2017**, *247*, 130–148. https://doi.org/10.1016/j.cis.2017.07.005.

(54) *X-Ray and Neutron Reflectivity*; Daillant, J., Gibaud, A., Eds.; Beiglböck, W., Ehlers, J., Hepp, K., Weidenmüller, H. A., Beig, R., Domcke, W., Englert, B.-G., Frisch, U., Hänggi, P., Hasinger, G., et al., Series Eds.; Lecture Notes in Physics; Springer Berlin Heidelberg: Berlin, Heidelberg, 2009; Vol. 770. https://doi.org/10.1007/978-3-540-88588-7.

(55) Clifton, L. A.; Neylon, C.; Lakey, J. H. Examining Protein–Lipid Complexes Using Neutron Scattering. In *Lipid-Protein Interactions*; Kleinschmidt, J. H., Ed.; Humana Press: Totowa, NJ, 2013; Vol. 974, pp 119–150. https://doi.org/10.1007/978-1-62703-275-9_7.

(56) RasCAL https://sourceforge.net/projects/rscl/ (accessed May 16, 2019).

(57) Kučerka, N.; Kiselev, M. A.; Balgavý, P. Determination of Bilayer Thickness and Lipid Surface Area in Unilamellar Dimyristoylphosphatidylcholine Vesicles from Small-Angle Neutron Scattering Curves: A Comparison of Evaluation Methods. *Eur. Biophys. J.* **2004**, *33* (4), 328–334. https://doi.org/10.1007/s00249-003-0349-0.

(58) Campbell, R. A.; Saaka, Y.; Shao, Y.; Gerelli, Y.; Cubitt, R.; Nazaruk, E.; Matyszewska, D.; Lawrence, M. J. Structure of Surfactant and Phospholipid Monolayers at the Air/Water Interface Modeled from Neutron Reflectivity Data. *J. Colloid Interface Sci.* **2018**, *531*, 98–108. https://doi.org/10.1016/j.jcis.2018.07.022.

(59) Campbell, R. A. Recent Advances in Resolving Kinetic and Dynamic Processes at the Air/Water Interface Using Specular Neutron Reflectometry. *Curr. Opin. Colloid Interface Sci.* **2018**, *37*, 49–60. https://doi.org/10.1016/j.cocis.2018.06.002.

(60) Oelichmann, J. Surface and Depth-Profile Analysis Using FTIR Spectroscopy. *Fresenius Z. Für Anal. Chem.* **1989**, *333* (4–5), 353–359. https://doi.org/10.1007/BF00572327.

(61) Browning, K. L.; Lind, T. K.; Maric, S.; Malekkhaiat-Häffner, S.; Fredrikson, G. N.; Bengtsson, E.; Malmsten, M.; Cárdenas, M. Human Lipoproteins at Model Cell Membranes: Effect of Lipoprotein Class on Lipid Exchange. *Sci. Rep.* **2017**, *7* (1), 7478. https://doi.org/10.1038/s41598-017-07505-0.

(62) Miyoshi, T.; Kato, S. Detailed Analysis of the Surface Area and Elasticity in the Saturated 1,2-Diacylphosphatidylcholine/Cholesterol Binary Monolayer System. *Langmuir* **2015**, *31* (33), 9086–9096. https://doi.org/10.1021/acs.langmuir.5b01775.

(63) Baoukina, S.; Monticelli, L.; Risselada, H. J.; Marrink, S. J.; Tieleman, D. P. The Molecular Mechanism of Lipid Monolayer Collapse. *Proc. Natl. Acad. Sci.* **2008**, *105* (31), 10803–10808. https://doi.org/10.1073/pnas.0711563105.

(64) Tristram-Nagle, S.; Liu, Y.; Legleiter, J.; Nagle, J. F. Structure of Gel Phase DMPC Determined by X-Ray Diffraction. *Biophys. J.* **2002**, *83* (6), 3324–3335. https://doi.org/10.1016/S0006-3495(02)75333-2.

(65) Hollinshead, C. M.; Hanna, M.; Barlow, D. J.; De Biasi, V.; Bucknall, D. G.; Camilleri, P.; Hutt, A. J.; Lawrence, M. J.; Lu, J. R.; Su, T. J. Neutron Reflection from a Dimyristoylphosphatidylcholine Monolayer Adsorbed on a Hydrophobised Silicon Support. *Biochim. Biophys. Acta BBA - Biomembr.* **2001**, *1511* (1), 49–59. https://doi.org/10.1016/S0005-2736(00)00380-1.

(66) Bayerl, T. M.; Thomas, R. K.; Penfold, J.; Rennie, A.; Sackmann, E. Specular Reflection of Neutrons at Phospholipid Monolayers. Changes of Monolayer Structure and Headgroup Hydration at the Transition from the Expanded to the Condensed Phase State. *Biophys. J.* **1990**, *57* (5), 1095–1098. https://doi.org/10.1016/S0006-3495(90)82628-X.

(67) Hughes, A. V.; Roser, S. J.; Gerstenberg, M.; Goldar, A.; Stidder, B.; Feidenhans'l, R.; Bradshaw, J. Phase Behavior of DMPC Free Supported Bilayers Studied by Neutron Reflectivity. *Langmuir* **2002**, *18* (21), 8161–8171. https://doi.org/10.1021/la025765u.

(68) Schmidt, V.; Sturgis, J. N. Modifying Styrene-Maleic Acid Co-Polymer for Studying Lipid Nanodiscs. *Biochim. Biophys. Acta BBA - Biomembr.* **2018**, *1860* (3), 777–783. https://doi.org/10.1016/j.bbamem.2017.12.012.

(69) Xue, M.; Cheng, L.; Faustino, I.; Guo, W.; Marrink, S. J. Molecular Mechanism of Lipid Nanodisk Formation by Styrene-Maleic Acid Copolymers. *Biophys. J.* **2018**. https://doi.org/10.1016/j.bpj.2018.06.018.

CHAPTER 5

SMALPS PROVIDE A SOLUBLE MEMBRANE SURFACE FOR STRUCTURAL CHARACTERIZATION OF LIPID-BINDING PROTEIN YRAP UNDERGOING NANODISC-INDUCED FIBRILIZATION

Stephen C. L. Hall[†‡], Timothy J. Knowles[†], Najet Mahmoudi[‖], James Doutch[‖], Charles Moore-Kelly[†], Ian T. Cadby[†], Mark Jeeves[⊥], Luke A. Clifton[‖], Pooja Sridhar[†], Frank Wien[○], Ian R. Henderson[†], Karen J. Edler[§], Thomas Arnold[‡‖§Δ] and Tim R. Dafforn[†].

[†] School of Biosciences, University of Birmingham, Edgbaston, Birmingham, B15 2TT, U.K.

[‡] Diamond Light Source, Harwell Science and Innovation Campus, Didcot, OX11 ODE, U.K.

[‖] ISIS Neutron and Muon Source, Rutherford Appleton Laboratory, Didcot, OX11 0QX, U.K.

[§] Department of Chemistry, University of Bath, Claverton Down, Bath, BA2 7AY, U.K.

[○] Synchrotron Soleil, L'Orme des Merisiers, 91190 Saint-Aubin, France

[Δ] European Spallation Source ERIC, P.O Box 176, SE-221 00 Lund, Sweden

[⊥] School of Cancer Sciences, University of Birmingham, Edgbaston, Birmingam. B15 2TT, U.K.

Author contribution statement

SCLH conceived and designed the study, prepared the samples, performed the experiments, analyzed the data and prepared the manuscript. TJK provided the YraP construct used in the study, assisted in production of deuterated protein and optimization of YraP-SMALP self-assembly and edited the manuscript. NM and JD assisted in SANS data collection, set up the instrument, reduced data and performed SANS analysis. CMK assisted with SRCD data collection and processing. ITC, MJ and LAC assisted with SANS data collection. PS assisted with YraP purifications. FW assisted with SRCD data collection and processing and set up the instrument. IRH provided the YraP construct and assisted with assessing the biological significance of models obtained from SANS data. KJE and TA assisted with SANS data collection, analysis and edited the manuscript. TRD conceived the study, provided funding, advised on SRCD processing and edited the manuscript.

Signed:

Stephen Hall 

Tim Dafforn

5.1 ABSTRACT

Peripheral membrane proteins represent an important class of membrane proteins, responsible for a broad range of cellular functions, yet the specifics of protein-lipid interactions remain challenging to study. Here, we utilize SMALP nanodiscs as a soluble membrane surface to elucidate structural details of the interaction of YraP, a bacterial outer membrane lipoprotein of unknown function, with phospholipid bilayers. We show that YraP undergoes a large conformational change upon SMALP interaction, with a substantial increase in ß-sheet content. Furthermore, we show using small-angle neutron scattering that the YraP-SMALP complex self-assembles into long fibrillar structures which may be amyloid-like in nature. These data, for the first time, show the potential of SMALPs as a soluble membrane assembly platform for capturing peripheral membrane protein-lipid interactions for structural studies. Furthermore, the structural information obtained of the YraP-SMALP interaction provides clues as to its function.

5.2 INTRODUCTION

Peripheral membrane proteins (PMPs) represent a large proportion of membrane-associated proteins in both prokaryotes and eukaryotes. In contrast to integral membrane proteins, PMPs do not contain transmembrane regions which span the lipid bilayer, rather interact with a single leaflet of the bilayer. Membrane binding is frequently achieved by the use of an amphipathic α-helix where one exposed side of the helix contains a high proportion of hydrophobic residues encouraging bilayer interactions, in addition to polar residues which can provide specificities to individual lipid headgroups. Alternatively, many proteins have sequences which get targeted for acylation during maturation to the mature protein, functioning as a membrane tether. These PMPs have a diverse range of cellular functions including initiating signalling cascades upon recognition of specific phospholipid headgroups, transfer of lipids between subcellular compartments,[1] and providing membrane anchors for cytoskeletal scaffolds.[2]

Significant progress has been made in functional characterization of PMPs, specifically in the study of protein-lipid interactions. The use of planar lipid bilayers as model membranes using techniques such as surface plasmon resonance and quartz-crystal microbalances can allow for investigation of membrane binding affinities and specificities.[3,4] Recently, the use of fluorescently labelled phospholipid vesicles in a microarray format has been used for systems-level screening for the specificity of PMPs for individual lipids.[5] However, structural characterization of PMP-lipid interactions has remained challenging. While neutron reflectometry allows investigation of the structure perpendicular to the bilayer, individual interactions cannot be observed.[6] Typically, in order to observe individual protein lipid interactions, X-ray crystallography has been employed where proteins have been co-crystalized in complex with lipid molecules.[7] However, obtaining diffraction quality protein crystals is often a substantial bottleneck.[8,9] Recent advances in cryo-electron microscopy has allowed investigations of protein interactions with vesicular model membranes. However resolution is often limited by the inherent polydispersity in vesicular preparations.[10]

One strategy which has been employed to investigate peripheral membrane protein interactions with phospholipid membranes has been the use of phospholipid nanodiscs. Nanodiscs are a discoidal, nanoscale section of phospholipid bilayer which is encapsulated by a membrane scaffold protein (MSP) belt. Here, this category of nanodiscs will be referred to as MSP-nanodiscs. The MSP is a modified form of Apolipoprotein A-I, and stabilizes the hydrophobic core of the lipid bilayer in aqueous solution.[11] Membrane proteins can be contained within the lipid bilayer-containing core of the MSP-nanodisc. This provides substantial stabilization when compared to classical surfactant alternatives, whilst maintaining the solubilized protein within a native-like phospholipid environment. This technology has been applied for extensive structural and functional characterization of a broad range of membrane proteins. [12–19]

When applied to PMPs, MSP-nanodiscs provide an ideal platform for investigating lipid-protein interactions by providing a soluble membrane surface.[20] In contrast to the methods described above, purified, isolated PMPs interaction with MSP-nanodisc-encapsulated membranes can be probed in a system which is applicable to a range of techniques such as SPR,[21] Förster resonance energy transfer (FRET)[22] and nuclear magnetic resonance spectroscopy (NMR).[23,24]

Recent studies have used MSP-nanodiscs for the reconstitution of cytochrome P450 3A4 (CYP3A4).[25] Structural studies of the cytochrome-MSP-nanodisc complex using small-angle scattering (SAS) have revealed the orientation of the cytochrome within the bilayer of the MSP-nanodisc. By using a hybrid modelling approach of model-dependent and *ab initio* modelling, a model of CYP3A4 was obtained in good agreement with models obtained through molecular dynamic simulations, where the membrane-anchor helix was found to sit close to the rim of the MSP-nanodisc, with the globular domain protruding into solution over the edge of the MSP belt.

Despite the progress made in the study of PMPs using MSP-nanodiscs, due to the proteinaceous nature of the stabilizing belt, the MSP itself will contribute to data collected using spectroscopic techniques such as circular dichroism spectroscopy, infra-red spectroscopy and intrinsic fluorescence experiments. Furthermore, for insoluble PMPs, such as CYP3A4 discussed above, MSP-nanodiscs have not been shown as capable of extracting proteins direct from native membranes, but require initial

detergent-mediated solubilization prior to reconstitution into MSP-nanodiscs. To address these issues, amphipathic copolymers of styrene and maleic acid (SMA) have been utilized to solubilize phospholipids and membranes into SMA lipid particles (SMALPs).[26] Similarly to MSP-nanodiscs, SMALPs contain a discoidal section of planar lipid bilayer but unlike MSP-nanodiscs, protein is replaced by a belt of SMA copolymer.[27] While styrene moieties intercalate into the lipid tail regions, the hydrophilic acid groups allow hydrogen bonding with the surrounding solvent.[27] When applied to membrane proteins, SMA is capable of extracting membrane proteins directly from native cell membranes whilst maintaining the local lipid environment. Proteins encapsulated within SMALPs, have been shown to have enhanced stability when compared to surfactant micelles and native membranes.[28,29] Furthermore, SMALPs are amenable to a range of structural techniques with demonstrated applications to cryo-EM, SAS, NMR and X-ray crystallography.[27,30–33]

In this study, we have, for the first time, investigated the applicability of SMALPs to PMP-lipid interactions. To assess the suitability of SMALPs as a peptide-free soluble membrane assembly platform, we investigated the interactions between the bacterial lipoprotein, YraP, and SMALPs. YraP is a conserved, albeit nonessential protein found throughout proteobacteria. Previous studies have demonstrated that it is localized to the inner leaflet of the outer membrane by means of an N-terminal lipobox motif leading to N-terminal acylation and trafficking through the Lol (Location of lipoproteins) pathway.[34] *ΔyraP* strains show only the mild phenotype of increased SDS sensitivity of the outer membrane.[35] While the function of YraP remains unknown, it has been hypothesized to be involved in cell division from its localization to the septum during cell division, where YraP has been proposed to regulate AmiC mediated peptidoglycan cleavage along with NlpD.[34] Furthermore, as SDS sensitivity is suggestive of outer membrane defects, YraP has also been suggested to be involved in outer membrane protein (OMP) insertion pathways mediated by the periplasmic chaperones DegP and Skp.[35]

Despite the unknown function of YraP, it is now well structurally characterized. The solution structure of YraP has been solved by NMR spectroscopy (Figure 5.1).[36] While YraP contains a globular core, NMR solutions suggest an intrinsically disordered, flexible N-terminus consisting of the first 25

residues of the mature protein as well as a short, flexible C-terminus (Figure 5.1a). The globular core of YraP is composed of two BON (Bacterial OsmY and Nodulation) domains connected by a short linker, each containing a 2-helix bundle and a short ß-sheet containing three ß-strands of mixed parallel/antiparallel orientation (Figure 5.1b, c). As BON domains have been implicated in mediating lipid binding,[37] subsequent NMR measurements (unpublished data presented with permission from T.J. Knowles and I.R. Henderson, see Appendix D, Figure D.2) have indicated that residues in the first helix of the second BON domain are predominantly responsible for lipid binding. These residues include a hydrophobic tryptophan and several polar residues (Figure 5.1d). It is suspected that the hydrophobic tryptophan side chain will embed into the hydrophobic core of the membrane while the polar residues may provide headgroup specificity. Indeed, it appears from NMR chemical shift perturbations that YraP is only capable of binding phosphatidylglycerol (PG), phosphatidylcholine (PC) and cardiolipin (CL) headgroups. Only minor chemical shift perturbations were observed upon incubation of YraP with phosphatidylethanolamine (PE), suggesting YraP does not interact with PE lipid species. However, headgroup specificity was measured using short chain, dihexanoyl micellar lipids, therefore it remains unknown what structural changes YraP undergoes upon binding to a bulk membrane.

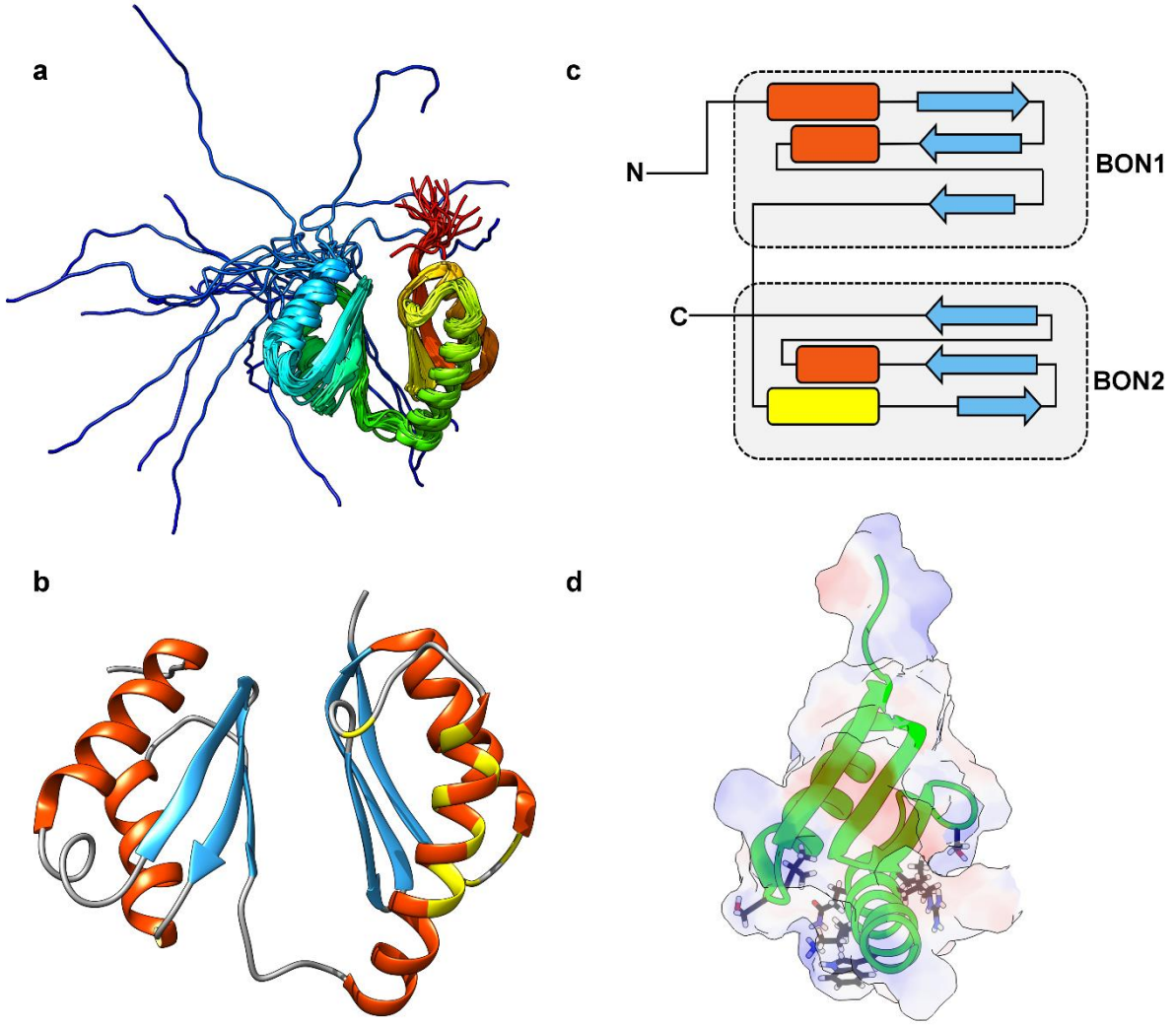

Figure 5.1. a. The solution structure of YraP as determined by NMR spectroscopy displayed as ribbon diagrams. The top 20 solutions are shown aligned with the minimum Cα RMSD. The ribbon is colored from blue (N-terminus) to red (C-terminus). **b**. An individual conformer showing the two BON domain structure of YraP. N and C terminal disordered regions are not shown for clarity. α helices are colored orange and ß-sheets are colored blue. The location of residues shown to interact with phospholipids are shown as yellow segments. **c**. Schematic showing the topology of YraP. Orange rectangles represent α-helices and blue arrows represent ß-sheets. Shaded regions depict the organization of secondary structural elements into individual BON domains. The yellow rectangle represents the amphipathic helix responsible for membrane binding. **d.** A close-up view of the BON2 domain containing the amphipathic helix responsible for membrane binding. The domain structure is shown as a green ribbon. Side-chains identified as important in phospholipid binding are shown as sticks. The semi-transparent surface is colored according to surface charge, where red regions represent areas of net positive charge, and blue regions represent areas of net negative charge.

Here, we seek to investigate what structural changes occur upon the interaction of YraP with a phospholipid bilayer in order to provide clues as to its function. By utilizing SMALPs as a soluble membrane surface, we capture the YraP-membrane interaction and show that YraP undergoes a large change in secondary structure composition upon SMALP interaction using synchrotron radiation circular dichroism (SRCD) spectroscopy. Following this, we investigate the large scale structural changes in YraP and SMALPs induced by their interaction using small-angle neutron scattering (SANS). We show that while both YraP and SMALPs have a structure as expected when in isolation, the interaction of YraP with SMALPs leads to the self-assembly of an elongated cylindrical structure. We hypothesize on the fibrillar, amyloid-like nature of this assembly and perform thioflavin T fluorescence experiments to support this hypothesis. These data not only demonstrate the potential of SMALPs for capturing PMP-membrane interaction, but also provide hints as to the function of YraP.

5.3 MATERIALS AND METHODS

5.3.1 Materials

Hydrogenated and tail-deuterated ($^2H_{54}$-)1,2-dimyristoyl-*sn*-glycero-3-phosphocholine (hDMPC and dDMPC, respectively) were purchased from Avanti Polar Lipids. Poly(styrene-*co*-maleic anhydride) was purchased from Cray Valley (UK) as SMA2000 resin. All other chemicals were purchased from Sigma-Aldrich at > 98% purity and used without further purification.

5.3.2 Methods

5.3.2.1 Expression and purification of YraP

The signal-sequence-free DNA sequence of *Escherichia coli* (*E. coli*) K12 YraP corresponding to residues 19 – 191, with a C19A mutation introduced to remove a potential acylation site, and a C-terminal 6×His tag attached via a GGLE linker was chemically synthesized (Genscript) and inserted into a pET-28b plasmid (Merck-Millipore) used to transform *E. coli* BL21(DE3) cells. Expression was performed by growing a 1% (v/v) inoculum of cells in 2x YT media (16 g/L peptone, 10 g/L yeast extract, 5 g/L NaCl, pH 7) at 37°C until an OD_{600} of 0.6 was reached. Expression was induced by the

addition of 1 mM isopropyl-β-D-1-thiogalactopyranoside (IPTG) and cultures grown for 16 hours at 18°C.

In order to produce deuterated YraP, cells were transformed and grown on lysogeny broth (LB)-agar. A single colony was selected and grown in LB for 6 hours at 37°C. In order to condition cells for growth in D_2O, a 1% v/v inoculum was then transferred to M9 minimal media containing 70% w/w D_2O and grown for 16 hours at 37°C. A 1% v/v inoculum of the D_2O-conditioned culture was grown in M9 minimal media containing 100% D_2O and grown at 37°C until an OD_{600} of 0.6 was reached. Expression was induced by the addition of 1 mM IPTG and cultures grown at 18°C for 24 hours.

Both hydrogenated and deuterated YraP were purified identically. Cells were pelleted by centrifugation at 6000 × *g* and resuspended in a minimal volume of 50 mM Tris, 500 mM NaCl, 20 mM imidazole, pH 8.0 supplemented with cOmplete EDTA-free protease inhibitor cocktail (Sigma). Resuspended cells were lysed by five passages through an Emulsiflex C3 cell disruptor (Avestin), then centrifuged at 75,000 × *g*, 4°C for 30 minutes in order to remove cell debris and intact cells. The clarified lysate was then passed over a 5 mL Ni-NTA HisTrap column (GE Healthcare Life Sciences) at room temperature and washed with ten column volumes of 50 mM Tris, 500 mM NaCl, 50 mM imidazole, pH 8.0 to remove non-specifically bound contaminants. YraP was eluted in the same buffer containing 250 mM imidazole. Fractions containing YraP, as determined by SDS-PAGE, were further purified using size exclusion chromatography (SEC) to remove contaminant proteins and aggregates by injection onto a Superdex 75 26/600 column (GE Healthcare Life Sciences) at 4°C, equilibrated in 50 mM Tris, 150 mM NaCl, pH 8.0. Fractions containing YraP, as determined by SDS-PAGE were pooled and concentrated to 10 mg/mL. The deuteration level of YraP was determined using MALDI-TOF mass spectrometry. The masses of hydrogenated and deuterated YraP were found as 19.251 kDa and 20.267 kDa respectively (Appendix D, Figure D.1). By taking into account exchangeable protons of the peptide backbone and ionizable functional groups, we were able to calculate a deuteration level of approximately 81%.

5.3.2.2 SMA copolymer hydrolysis

SMA2000 was hydrolyzed from poly(styrene-*co*-maleic anhydride) to soluble poly(styrene-*co*-maleic acid) as previously described.[38] Briefly, a 10% w/v suspension of SMA2000 in 1 M NaOH and heated under reflux for 2 hours, whereby the solution clarified. After cooling, SMA was precipitated by the dropwise addition of concentrated HCl until the pH < 5. Precipitated SMA was centrifuged at 10,000 × *g* and the pellet washed by resuspension in water. The washing procedure was repeated a further two times. After washing, the SMA pellet was dissolved in a minimal volume of 0.6 M NaOH and incubated at 37°C for 16 hours prior to repeating the precipitation and washing procedure. Finally, SMA was again dissolved in a minimal volume of 0.6 M NaOH, adjusted to pH 8.0 by the dropwise addition of concentrated HCl, lyophilized and used without further purification.

5.3.2.3 Self-assembly and purification of DMPC-SMALPs

DMPC SMALPs were made and purified essentially as previously described.[26,39] Briefly, 10 mg/mL DMPC in $CHCl_3$ was transferred to a glass vial and dried under a stream of nitrogen to create a lipid film on the inside of the glass vial. Vials were desiccated for at least 2 hours to remove residual solvent. Lipids were rehydrated at 30°C in 50 mM Tris, 500 mM NaCl, pH 8.0 to a concentration of 10 mg/mL. Small unilamellar vesicles (SUVs) were formed by sonication at 30°C for 30 minutes. 3% w/v SMA copolymer was prepared in the same buffer and mixed at a 1:1 v/v ratio with the SUV suspension. SMALP self-assembly was allowed to equilibrate at room temperature for 2 hours. After equilibration, SMALPs were concentrated in a 10,000 MWCO centrifugal concentrator tubes and purified by SEC using a HiLoad Superdex 200 16/600 column (GE Healthcare Life Sciences) equilibrated in 50 mM Tris, 500 mM NaCl, pH 8.0 attached to an Äkta purification system (GE Healthcare Life Sciences) monitoring UV absorbance at 254 nm. Fractions corresponding to SMALPs were pooled, flash frozen in liquid nitrogen and stored at -80°C.

5.3.2.4 Self-assembly and purification of the YraP-SMALP complex

In order to produce the YraP-SMALP complex, we employed the strategy of initially forming proteoliposomes prior to solubilization into SMALPs. 5 mg YraP was added to DMPC SUVs in 50 mM Tris, 500 mM NaCl, pH 8.0 at a YraP:DMPC molar ratio of 1:600 and incubated at 25°C for 1 hour. Resultant proteoliposomes were solubilized by the addition of SMA at a polymer:lipid molar ratio of 1.5. Self-assembly of SMALPs was allowed to equilibrate for 2 hours. In order to remove 'empty' SMALPs that are not interacting with YraP, the YraP SMALP mixture was passed over a 1 mL Ni-NTA HisTrap column (GE Healthcare). 'Empty' SMALPs were removed by washing the column with 10 column volumes of 50 mM Tris, 500 mM NaCl, pH 8.0. YraP-SMALPs were eluted from the column with 50 mM Tris, 500 mM NaCl, 50 mM ethylenediaminetetraacetic acid (EDTA) pH 8.0. Elution fractions were pooled and further purified by SEC using a HiLoad Superdex 200 16/600 column equilibrated in 50 mM Tris, 500 mM NaCl, pH 8.0. The purification was monitored by UV absorbance at 280 nm and 254 nm so as to be sensitive to the presence of YraP and SMA.

5.3.2.5 Far-UV synchrotron radiation circular dichroism (SRCD)

Far-UV SRCD was performed using the SRCD end-station of the DISCO beamline at Synchrotron Soleil.[40] Both YraP and YraP-SMALP were buffer exchanged into 50 mM Tris, 150 mM NaCl using PD-10 desalting columns (GE Healthcare) and concentrated to 10 and 4 mg/mL, respectively, using 10,000 MWCO centrifugal concentrator tubes (Amicon). Samples were loaded into discoidal CaF_2 cells with a 30 μm path length. Cells were mounted in a bespoke, temperature controlled stage within a nitrogen flushed chamber. SRCD spectra were collected using a monochromatic, 3 mm diameter beam. Spectra were measured from 261 to 170 nm with a resolution ($\Delta\lambda/\lambda$) of 1 nm, integration time of 1.2 s. Thermal denaturation experiments were performed between 25 and 95°C. Spectra were collected every 5°C after 120 s equilibration at the desired temperature. All spectra were recorded three times for each sample at each measured temperature and the spectra averaged. Spectra were calibrated to a 6.19 mg/mL solution of (1S)-(+)-10-camphorsulfonic acid (CSA) in water and the background spectra of buffer alone subtracted from the sample spectra.Thermal stability was monitored by plotting individual wavelengths

(222 nm and 193 nm) as a function of temperature. The temperature at the midpoint of the structural transition, T_m, was determined by fitting of these data to the Gibbs-Helmholtz equation.[41]

5.3.2.6 Small-angle neutron scattering (SANS)

Small-angle neutron scattering (SANS) was performed using the SANS2D instrument at the ISIS neutron and muon source. Detailed descriptions of the theoretical bases of SANS including instrumental details and applications to soft matter and biomolecules have been described in depth elsewhere.[42,43] Therefore, here we will only include a brief description of the technique. SANS measures the scattered neutron intensity, $I(Q)$, by randomly oriented particles in solution at small angles as a function of the scattering vector, Q, where

$$Q = \frac{4\pi \sin\theta}{\lambda}$$

Where 2θ represents the scattering angle between the incident and scattered beam and λ represents the wavelength of scattered neutrons. The measured scattered intensity as a function of Q, $I(Q)$, is dependent on scattering between particles in solution as described by the structure factor, $S(Q)$, scattering occurring within isolated particles in solution described by the form factor, $P(Q)$, the number of particles in solution, the volume of particles, V, and the difference in neutron scattering length density (SLD) contrast, Δρ:

$$I(Q) = S(Q)\sum_{i=1}^{n}[(\Delta\rho \cdot V)^2 P(Q)]$$

As the structure of independent particles is described by $P(Q)$, if we assume a non-interacting, randomly oriented distribution of homogenous particles in solution, the contribution of $S(Q)$ will be negligible and we can approximate the Q-dependence of SANS intensity to:

$$I(Q) = N(\Delta\rho V)^2 P(Q)$$

where N is the number density of particles in solution. The scattering length density (SLD) of a particle or component thereof is defined as

$$\rho = \frac{\sum_{i=1}^{n} b_c}{V_m}$$

where SLD, ρ, is given by the sum of the coherent scattering lengths, b_c, for each atomic nuclei, n, within a given molecular volume, V_m. Due to the large difference in coherent scattering length between hydrogen and deuterium (-3.74 × 10^{-5} Å and 6.67 × 10^{-5} Å, respectively), by differentially isotopically labelling components of macromolecular complexes and that of the bulk solvent, the scattering length density of individual components can be matched to each other and/ or that of the solvent. This means that the measured SANS intensity will not distinguish between matched components and/ or solvent as Δρ = 0. This makes SANS a powerful tool for structural studies of complex particles by allowing localization of the different components within a complex through variation in isotopic contrast.

In order to deconvolute structural details of both SMALPs and the YraP-SMALP complex, SMALPs were prepared with either hDMPC or dDMPC and YraP-SMALPs prepared with either hYraP or dYraP with either hDMPC SMALPs, or SMALPs with a mix of hDMPC and dDMPC such that the SLD of the lipids match that previously reported for the SMA polymer belt. As the polymer belt is hydrated in solution, the apparent SLD will increase as a function of % D_2O (Figure 5.2). Therefore, to account for the change in SLD, YraP-SMALPs were prepared with lipids that match SMA in H_2O and a separate sample prepared with lipids matching SMA in D_2O (i.e. a 0.09 and 0.57 molar ratio of hDMPC;dDMPC to match the SLD of SMA in H_2O and D_2O, respectively). Throughout this sample preparation we have made the assumption that there is no preference to hDMPC or dDMPC incorporation within SMALPs with or without associated YraP, and that lipids will be homogenously mixed between all SMALPs present.

All samples were extensively dialyzed against 50 mM Tris, 500 mM NaCl pH 8 in H_2O or the same buffer at pH 8.0 in D_2O. After sufficient dialysis, YraP was concentrated to 260 μM, DMPC SMALPs concentrated to 50 μM (polymer concentration) and the YraP-SMALP complex to 80 μM (protein concentration). In order to measure at intermediate solution contrasts, samples dialyzed into H_2O and D_2O were mixed in the correct volume fraction.

Samples were loaded into 12 mm diameter circular quartz cells with a 1 mm path length and mounted within the sample changer maintained at 25°C. SANS data were collected using TOF-SANS in event mode with source to sample distance of 4 m, an 8 mm beam aperture with a wavelength range covering 2 – 14 Å at a pulse frequency of 10 Hz. Two 96.5 cm^2 detectors positioned at 2.4 m and 4 m from the sample collected high and low angle data respectively with the high angle detector bank offset from the beam path and rotated to face the sample, covering an effective Q range of 0.005 – 1.2 $Å^{-1}$ where δQ/Q = 8%. Data were reduced using Mantid (v 3.10.1) [44] where data collected at each detector were normalized to the flux of the direct beam and transmissions collected from a monitor at the beam stop prior to radially averaging and stitching the scattering profile from the two detectors. Finally, subtraction of the background scattering profile collected of the final dialysis buffers was subtracted from the sample scattering profile to obtain the SANS profile of the particles in solution.

5.3.2.7 SANS data analysis

We have performed several analyses on our SANS data, each of which provides information on different structural properties of particles in solution. Initial transformations of the SANS data by means of the Guinier and Kratky plots provide information on the overall particle size and compactness. While this is useful for initial inspection of the data, and can be informative in downstream analysis, neither are informative on the precise structure of particles in solution. In order to gain finer structural insights, we took two approaches: indirect inverse Fourier transforms of data describing particles of homogenous SLD in real space, and model-dependent analysis where models describing homogeneous geometric slabs of different SLDs in real space are fit to the experimental data in reciprocal space. In the following section, we provide a description of these analyses and their application within this study.

Potential aggregation and low-Q structure factor contributions to the scattering pattern were initially inspected by means of Guinier plots, where:

$$\ln\big(I(Q)\big) = \ln\big(I(0)\big) - \frac{R_g^2}{3}Q^2$$

In order to gain information on the size of particles in solution, linear regression was performed to data plotted as ln(I(Q)) vs Q^2 over the region where $QR_g < 1.3$ in order to obtain the radii of gyration, R_g, and the extrapolated zero-angle intensity, I(0).[45]

The compactness of particles in solution was gauged by means of dimensionless Kratky plots. Here, data is normalized to the expected decay in scattering intensity for a gaussian coil, and scaled with respect the R_g and I(0) for that sample by plotting as $(QRg)^2 \times I(Q)/I(0)$ vs QR_g. A distinct peak within the Kratky plot indicates a globular, compact particle, whereas a non-zero plateau suggests a gaussian coil conformation.[45,46]

The full SANS patterns collected for YraP were further analyzed using CRYSON.[47] CRYSON calculates the theoretical scattering pattern for a spherically averaged macromolecule of known structure in solution and fits this to experimental data by iteratively modifying the hydration shell around the molecule, taking into account instrumental Q smearing, the scattering length densities of the particle and solvent and exchangeable protons/ deuterons between the scattering particles and the bulk solution. We used the ensemble structure of YraP derived from solution-NMR as the input to CRYSON.[36] A fraction of non-exchanged NH in the peptide backbone of 0.l was used throughout and in the case of dYraP, the perdeuteration level of YraP was set to 0.81 based on the mass of dYraP determined from mass spectrometry. Data were fitted between Q values of 0.01 and 0.5 $Å^{-1}$. All other input parameters were kept as default values.

The pair-distance distribution function, P(r), of both hYraP and dYraP was fit to the experimental scattering pattern using GNOM.[48] The P(r) describes the contrast-weighted, real space probable distance, r, distribution between scattering centers within a particle. An indirect Fourier transform of I(Q) over $0 < r < D_{max}$ is performed, where D_{max} is the maximum particle dimension. This distribution is then fit to the experimental scattering pattern in order to minimize χ^2.

Low resolution *ab initio* models were obtained using DAMMIF [49] to generate a spherical search volume of diameter D_{max} obtained from the P(r) function which is filled with 'dummy atoms' representing a scattering object. A simulated annealing procedure is then used to vary positions of atoms

representing both the particle and solution (constrained to encourage interconnectivity) tending towards decreased energy until the distribution matches that expected in from the P(r) calculations. DAMMIF was run 10 times using default parameters with no assumptions applied on particle symmetry. All ten models were then aligned, averaged with outliers identified and filtered using DAMAVER.[50] The final averaged, model was then used as an input to DAMMIN to refine the model using a slower, finer calculation.[51]

SANS data collected for DMPC SMALPs were analyzed by means of model-dependent analysis using the models available in the National Institute of Standards and Technology Small-Angle Neutron Scattering (NIST-SANS) Analysis Package [52] implemented within IGOR Pro (Wavemetrics). This analysis method describes a theoretical model based on interconnected geometric shapes with distinct SLDs and back-calculates a theoretical scattering pattern. This model is simultaneously and iteratively fit to multiple experimental scattering patterns. In fitting SANS patterns collected from DMPC SMALPs, we used a polydisperse core-shell cylinder model which has previously been employed determine structural parameters of DMPC SMALPs in solution.[27] This model is comprised of a core-shell cylinder with additional cylinders at either face of the central core cylinder, representing phospholipid tails (core), phospholipid head groups (face) and the SMA copolymer belt (shell). Polydispersity in the radius was modelled as a Schultz distribution in the central phospholipid core of the particle. The SLDs of the phospholipid tails and headgroups were held as constant based on literature values for DMPC molecular volumes (281.9 $Å^3$ and 779.0 $Å^3$ for DMPC headgroups and tails, respectively)[53] and their isotopic composition. Similarly the SLD of the SMA polymer belt and solvent penetration into the DMPC headgroups was held constant based on literature values [27] and solvent SLDs calculated and held constant in an analysis strategy consistent with previous studies.[27] Parameters describing the dimensions of the particle, radial polydispersity and solvent penetration into the polymer rim were linked across all data sets and fit to the experimental data.

A similar approach of model-dependent analysis was employed in order to decipher structural information on the YraP-SMALP complex using models available within SasView

(http://www.sasview.org/). Here, we used a model of a polydisperse core-shell elongated cylinder, with polydispersity of the cylinder radius modeled by a Schultz distribution. As with fitting DMPC SMALP data, SLDs of the solvent were calculated and held as constant during fitting. We made the assumption that the structure of SMALPs are essentially unchanged from that determined by the DMPC SMALP analysis. This assumption allows calculation of the SLDs of the entire SMALP in each contrast:

$$\rho_T = \sum \chi_V \, \rho_{app}$$

where the total SLD of the SMALP, ρ_T is defined by the sum of the products of volume fractions, χ_V, and apparent SLDs taking into account solvent penetration, ρ_{app}, for each component as determined for SMALPs in the absence of YraP (Figure 5.2). The SLDs of the SMALPs were calculated and held constant throughout fitting. The SLDs of YraP, were calculated using MULCh [54] and also held constant (Figure 5.2). The parameters describing the dimensions of the particle and polydispersity were linked between all data sets and fit to the experimental data.

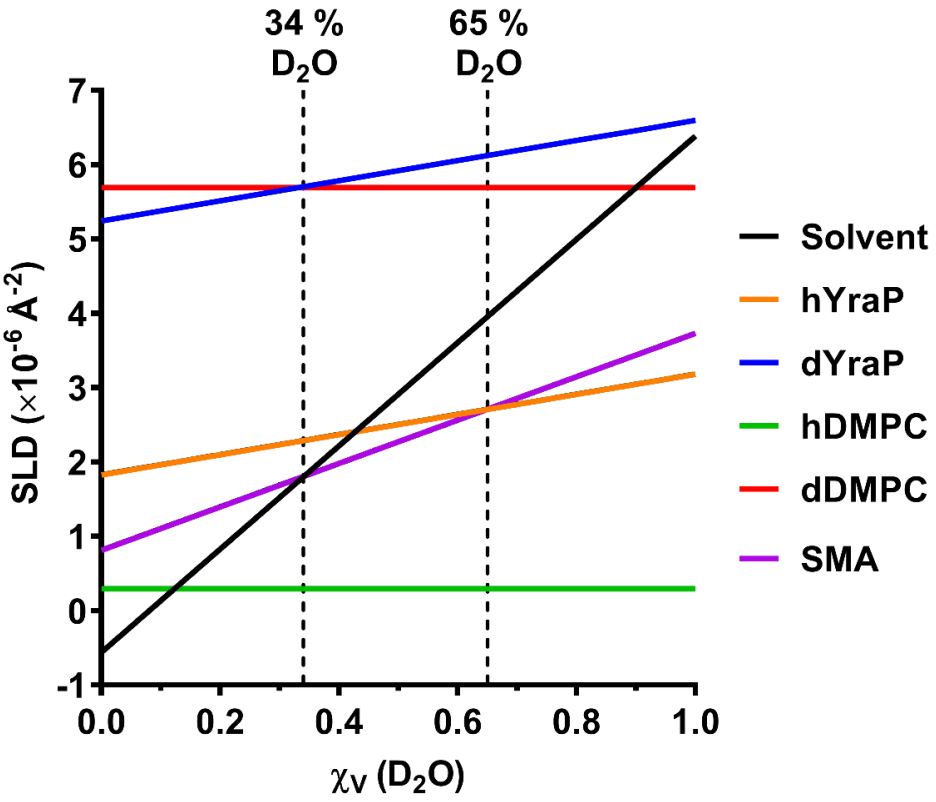

Figure 5.2. Changes in SLD of each component of the YraP-SMALP complex as a function of the volume fraction of D_2O. Match points measured are marked as dashed vertical lines.

5.3.2.8 Thioflavin T fluorescence

Thioflavin T (ThT) fluorescence experiments were performed using a PerkinElmer luminescence spectrometer (LS 50B) with an excitation wavelength of 440 nm and an emission wavelength of 482 nm with both emission and excitation slits set to 2 mm. Initially a 20 μM solution of ThT in 50 mM Tris, 150 mM NaCl in 10 mm path length glass cuvettes was measured for 1 minute with an integration time of 10 seconds to measure baseline fluorescence. Following this YraP, DMPC SMALPs or YraP-SMALPs were added in the same buffer to a concentration of 1 μM (polymer concentration in the case of DMPC SMALPs and YraP-SMALPs) and incubated for 10 minutes at 25℃ in dark tubes to allow for equilibration of ThT partitioning. Following this, the fluorescent intensity was measured for 1 minute with an integration time of 10 seconds. All experiments were repeated three times on independently prepared samples.

5.4 RESULTS

5.4.1 Purification of YraP and the YraP-SMALP complex

In order to investigate the lipid-protein interactions between SMALPs and YraP, we first required isolation of YraP. While YraP has been identified as a putative lipid binding protein, there are only two regions of interaction with membranes by means of a cysteine linked acylation site and an amphipathic helix. As the membrane recognition is mediated by the selectivity inferred by the amphipathic helix, we removed the cysteine acylation site by means of an alanine mutation, rendering YraP soluble. Overexpression of YraP and purification by means of immobilized metal affinity purification (IMAC, Figure 5.3a) and size exclusion chromatography (SEC, Figure 5.3b, c) yielded a high level of expression and purity. The mass of purified YraP was measured by MALDI-TOF mass spectrometry, where two peaks were identified with a mass of 19.07 and 19.25 kDa were observed, in good agreement with the expected mass of 19.5 kDa based on the peptide sequence (Appendix D, Figure D.1). While this suggests minor degradation is occurring, we were still able to obtain pure, non-aggregated samples which are of sufficient quality for further characterization.

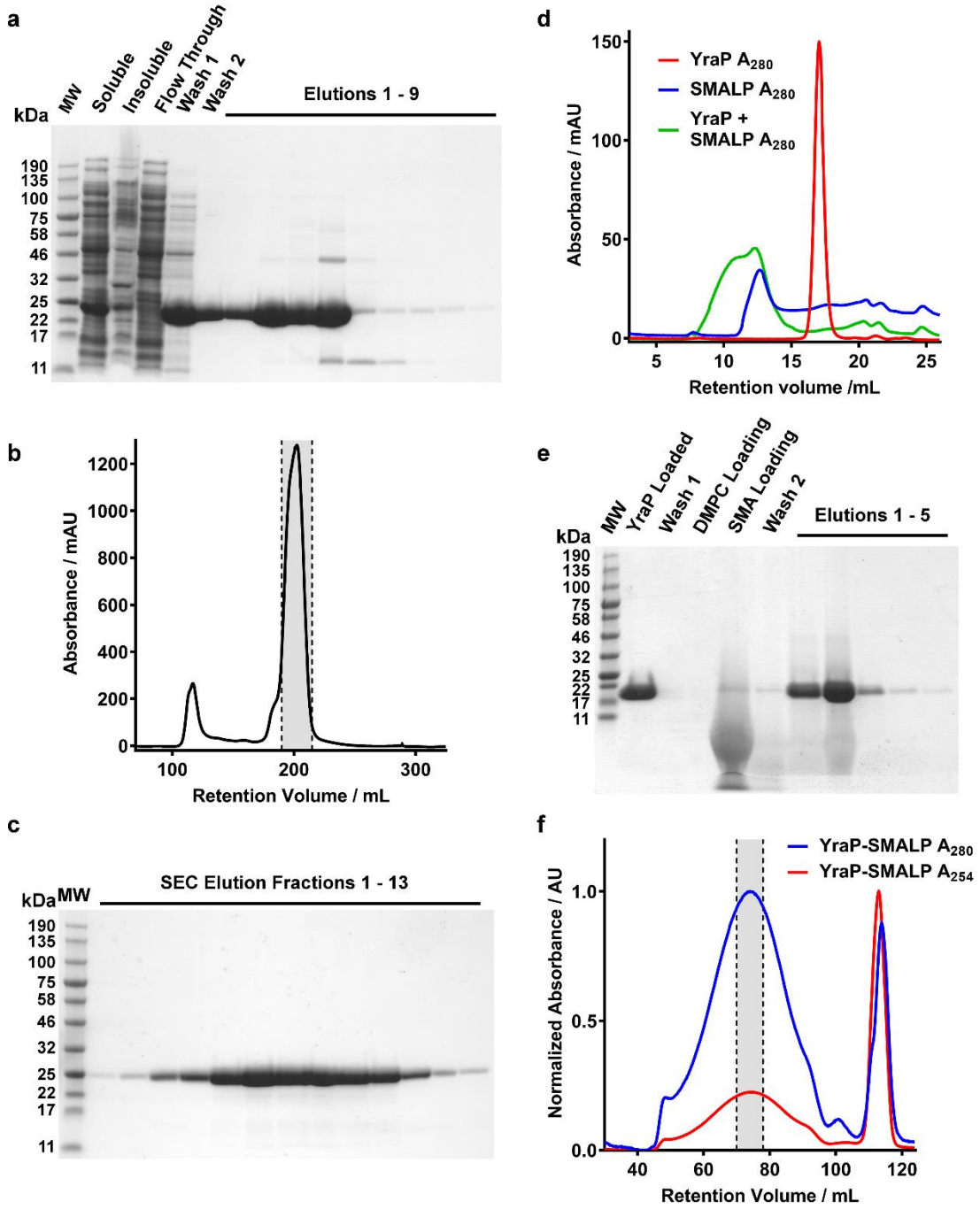

Figure 5.3. Purification of YraP and the YraP-SMALP complex. **a**. SDS-PAGE showing the Ni-NTA purification of YraP. **b**. Representative Superdex 75 SEC chromatogram of the post-IMAC purification of YraP. Trace represents the absorbance at 280 nm. Fractions collected are shown within the shaded region. **c**. SDS-PAGE of SEC elution fractions of YraP. **d**. Analytical Superdex 200 SEC chromatograms demonstrating the interaction of YraP with SMALPs. Traces represent the absorbance at 280 nm for YraP (red trace), DMPC SMALPs (blue trace) and YraP in the presence of DMPC SMALPs (green trace). **e**. SDS-PAGE showing the on-column self-assembly of YraP-SMALPs and subsequent purification from empty SMALPs. **f**. Representative Superdex 200 SEC- chromatogram of the purification of the YraP-SMALP post Ni-NTA purification. Traces represent the absorbance at 280 nm (blue trace) and absorbance at 254 nm (red trace). Fractions collected for further analysis are shown within the shaded region.

We next investigated the interaction of YraP with SMALPs. Previous NMR studies have shown that YraP is able to bind PG, PC and CL lipid headgroups (Appendix D, Figure D.2). As SMALPs containing DMPC are now well characterized in terms of their structure [27] and self-assembly [38], we chose this system as a model to investigate the membrane-interaction of YraP. YraP was incubated with small unilamellar vesicles (SUVs) of DMPC in a lipid:protein molar ratio of 600, prior to solubilization by the addition of SMA to a polymer:lipid ratio of 1.5. This ratio has been previously shown to lead to complete solubilization of phospholipids, yielding SMALPs of a small diameter.[38] This strategy should minimize the likelihood of more than one monomer of YraP interacting with the bilayer solubilized within an individual SMALP. The efficiency of this interaction was investigated by analytical SEC (Figure 5.3d). YraP alone shows a sharp peak eluting at volume of 17 mL, consistent with the sample being monomeric and non-aggregated. DMPC SMALPs show a trace similar to that previously reported,[38] where the SMALPs elute from the column at approximately 13 mL. After incubation of YraP with DMPC SUVs and subsequent solubilization by SMA, we observe no peak corresponding to monomeric YraP. Two further peaks are resolved at elution volumes of 13 and 10 mL. We assign the 10 mL peak to YraP-SMALPs, whereby the adsorption of YraP to the SMALPs leads to a larger size, and therefore a decreased retention volume. The peak at 13 mL overlaps with that observed for DMPC SMALPs in the absence of YraP, which we propose are 'empty' SMALPs present due to the excess of phospholipids added.

While this observation confirms that no monomeric YraP remains in solution, it is not sufficient to distinguish between a YraP-SMALP interaction and a soluble aggregation of YraP where no SMALPs are present. In order to distinguish between these two possibilities, we performed the same interaction but where YraP is specifically bound to a Ni-NTA column, and elution fractions at various stages of the self-assembly process analyzed by SDS-PAGE (Figure 5.3e). After extensively washing the column to remove any excess, unbound YraP, DMPC SUVs were loaded onto the column. After sufficient incubation, SMA was loaded to solubilize any vesicles associated with the column matrix via YraP. While a minor elution of YraP is observed at this stage, we can identify an intense, low M_W band which has been previously assigned to SMA.[38,39] After washing the column again to remove any excess SMA

and DMPC SMALPs, YraP was eluted using 50 mM EDTA. SDS-PAGE analysis of these fractions identifies a band at the same apparent M_W as YraP in addition to the broad, low M_W band corresponding to SMA. This further supports out earlier assignment of the low-retention volume SEC peak to YraP-SMALPs. While we still remain insensitive to the presence of phospholipids, the co-elution of YraP and SMA strongly suggests the assembly of a YraP-SMALP complex.

While the on-column method is indicative of YraP-SMALP complex, in order to produce larger quantities, we reverted to the batch self-assembly procedure as described above, and subsequently purified this complex by IMAC and SEC to remove any 'empty' SMALPs and aggregates which may form as a result of the purification. The SEC trace of this purification (Figure 5.3f) shows a broad peak identified by UV absorbance at both 280 nm and 254 nm, suggesting the presence of both YraP and SMA. The center of this peak is consistent with that observed above during the analytical SEC experiments. As a broad peak is indicative of polydispersity, only the central fraction of this peak was taken for further analysis to minimize this effect.

5.4.2 YraP undergoes secondary structural rearrangements upon SMALP interaction

In order to investigate any structural changes occurring in YraP as a result of SMALP interaction, we used far-UV circular dichroism spectroscopy. Due to the high UV absorbance of SMA, we used a synchrotron light as opposed to a standard UV lamp. This allows greater flux to illuminate the sample, with benefits of collimation and coherence which are unachievable using a home source, allowing high sample concentrations to be measured in small-pathlength cells. SRCD spectra obtained for YraP alone (Figure 5.4a) show a spectrum with characteristic minima at 222 and 208 nm indicating an α-helical component, a small minimum at 218 nm indicating a ß-sheet component, and a peak of lower than expected intensity at 192 nm for a folded mixed α/β structure suggests a significant disordered component. In contrast, different spectral trends were observed for YraP-SMALP (Figure 5.4b) where no characteristic minima (at 208 and 222 nm) were observed, in addition to a strong minimum at 219 nm. This suggests a decreased α-helical content and increased β-sheet component of YraP when

interacting with SMALPs. Furthermore, the maximum at 192 nm is of greater intensity than observed for YraP alone, suggesting a decreased irregular composition.

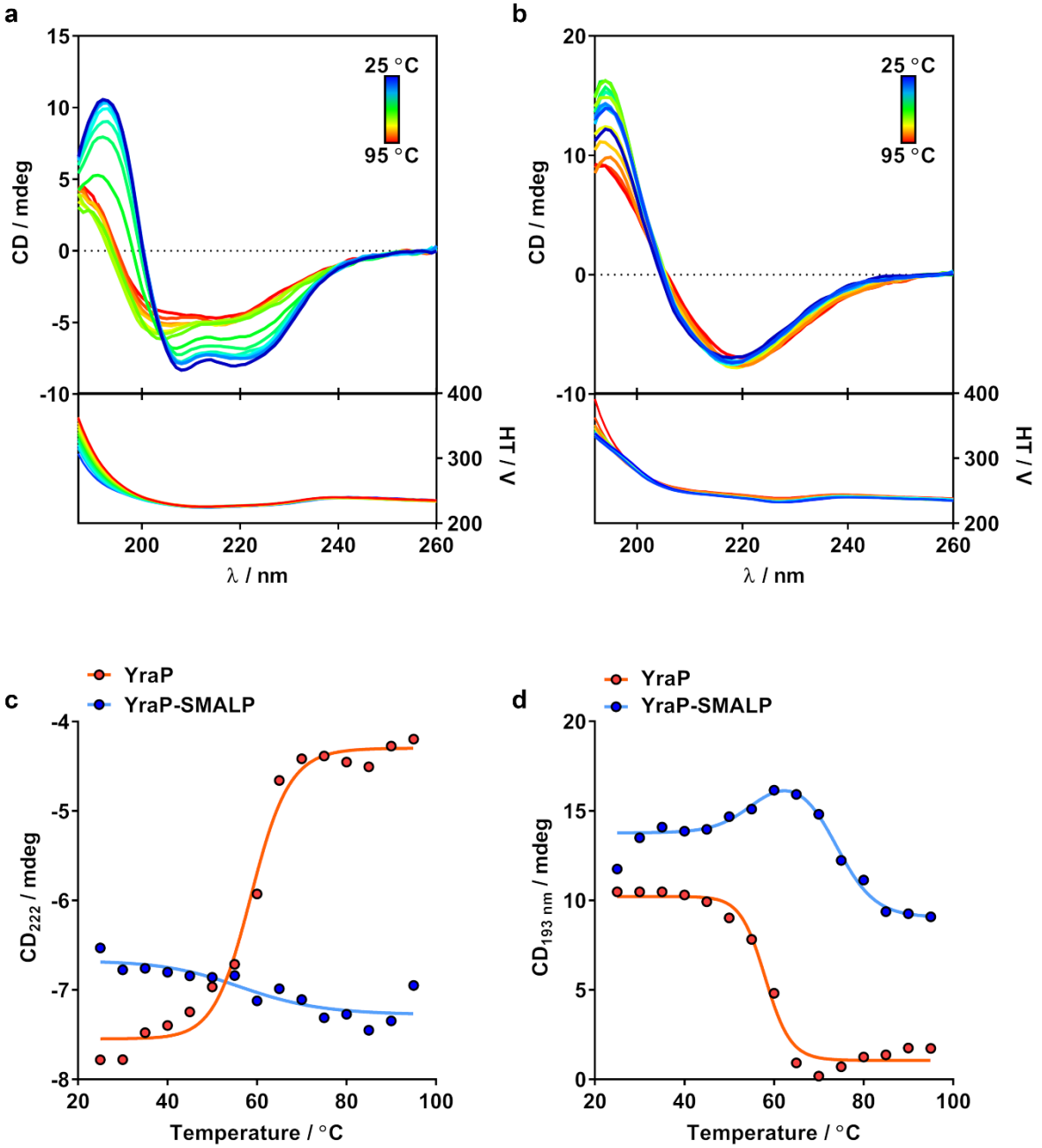

Figure 5.4. Synchrotron radiation far-UV circular dichroism (SRCD) spectra of **a**. YraP and **b**. YraP-SMALP. Spectra were collected between 25°C and 95°C in steps of 5°C displayed as a color gradient from blue to red. Spectra are shown in the top panels, and corresponding high tension voltages are shown beneath. **c**,**d**. SRCD thermal melts of YraP (Red) and YraP-SMALP (blue) tracked at 222 nm and 193 nm, respectively. Data are shown as points and denaturation curves fit to the data are shown as solid lines

The stability of YraP and the YraP-SMALP complex was assessed by means of thermal denaturation measured by SRCD (Figure 5.4c, d). Plotting the circular dichroism ellipticity at an individual wavelength as a function of temperature and subsequent fitting of these data to the Gibbs-Helmholtz equation allows identification of the melting temperature, T_m, associated with structural components with characteristic dichroic absorptions. Due to the convolution of the β-sheet minimum at 218 nm with the much stronger α-helical minima at 222 and 208 nm, it is not possible to monitor changes to these structural components as a function of temperature independently. Nonetheless, by monitoring the changes in ellipticity at 222 nm (Figure 5.4c), which contains both α-helical and β-sheet contributions, we were able to identify a large loss of α/β secondary structure in YraP with a T_m of 58.8 ± 0.9°C. In contrast, the YraP-SMALP complex shows a small increase in secondary structure. The temperature at which this broad transition occurs is similar to the T_m of YraP in the absence of SMALPs, with a transition temperature of 57.0 ± 7.0°C. When inspecting the full spectra (Figure 5.4b), no minima at 222 or 208 nm can be observed, suggesting that YraP experiences a small increase in β-sheet content at elevated temperature.

Additionally, the spectral changes at 193 nm were inspected as a function of temperature (Figure 5.4d). While both α-helices and β-sheets contribute to a positive signal at 193 nm, disordered regions will contribute a negative signal. YraP shows a decrease in CD. A similar trend is observed for YraP denaturation at 193 nm as for 222 nm, where a loss of secondary structure can be identified with a T_m of 58.1 ± 0.7°C. The YraP-SMALP complex, however, shows a markedly different behavior. Initially, an increase in secondary structure can be observed with a T_m of 55.6 ± 2.0°C, similarly to that observed at 222 nm. However, further increases in temperature show a loss of secondary structure and increase in loop content, leading to a decrease in signal with a T_m of 75.8 ± 0.9°C. This suggests a two-stage structural rearrangement which initially causes a small increase in β-sheet content before partial denaturation occurs at an elevated temperature compared to YraP in the absence of SMALPs. These data suggest that YraP undergoes a large-scale structural rearrangement upon interaction with SMALPs leading to increased thermostability.

5.4.3 The SANS solution model of YraP agrees with that obtained with solution NMR

Before structural investigations of the YraP-SMALP complex, it is necessary to independently characterize the solution structures of YraP and DMPC SMALPs. Due to the complexity of chemical composition within both DMPC SMALPs and YraP-SMALPs, we performed small-angle neutron scattering (SANS) to utilize selective deuteration and isotopic contrast to distinguish relative positions of components within the particles. Due to the similar chemical nature of phospholipids, SMA and YraP, techniques such as small-angle X-ray scattering (SAXS) and cryo-transmission electron microscopy would provide insufficient contrast to be able to deconvolute structural details of each component of the complex.

In order to investigate the effects of deuteration of YraP, which is widely acknowledged to result in aberrations to protein structure,[55,56] we first measured SANS profiles of hydrogenated and deuterated YraP (hYraP and dYraP) in D_2O and H_2O respectively (Figure 5.5a). By fitting the theoretical scattering pattern produced by the NMR ensemble structure to the experimental data, taking into account $^1H/^2H$ exchange and the solvation shell surrounding the molecules using CRYSON,[47] good agreement was seen to the experimental data in both cases (Figure 5.5a). This suggests that the structure of YraP is largely maintained, irrespective of isotopic effects. Guinier analysis of hYraP and dYraP allows determination of their respective radii of gyration, R_g (Figure 5.5b). In both cases, good fits can be obtained to the experimental data over which $QR_g < 1.3$ and the data are linear until very low-Q which is likely due to large error in counting statistics due to low neutron flux at these Q-values. This allows us to be confident that YraP is monodisperse in solution in both cases and free from any contaminating species or larger particles leading to a low-Q structure factor. Slight differences observed in the R_g values are likely due to changes in hydration and solvent interaction in H_2O and D_2O.

R_g and I(0) values obtained by Guinier analysis allows transformation of the data by means of the dimensionless Kratky plot (Figure 5.5c). These plots suggest that both hYraP and dYraP contain a folded domain, as indicated by the bell-shaped peak. However, as neither plot decays to zero, this also suggests

a disordered component. This is in good agreement with the solution NMR ensemble, whereby all models show an extended, disordered N-terminus. The peak in the Kratky plot is slightly shifted from that observed for dYraP, where QR_g = 1.9 to QR_g = 2.1 for hYraP. This suggests a somewhat more elongated structure for hYraP than dYraP. Furthermore, the greater subsequent rise in intensity for hYraP in D_2O suggests there is a larger disordered region than for dYraP in H_2O.

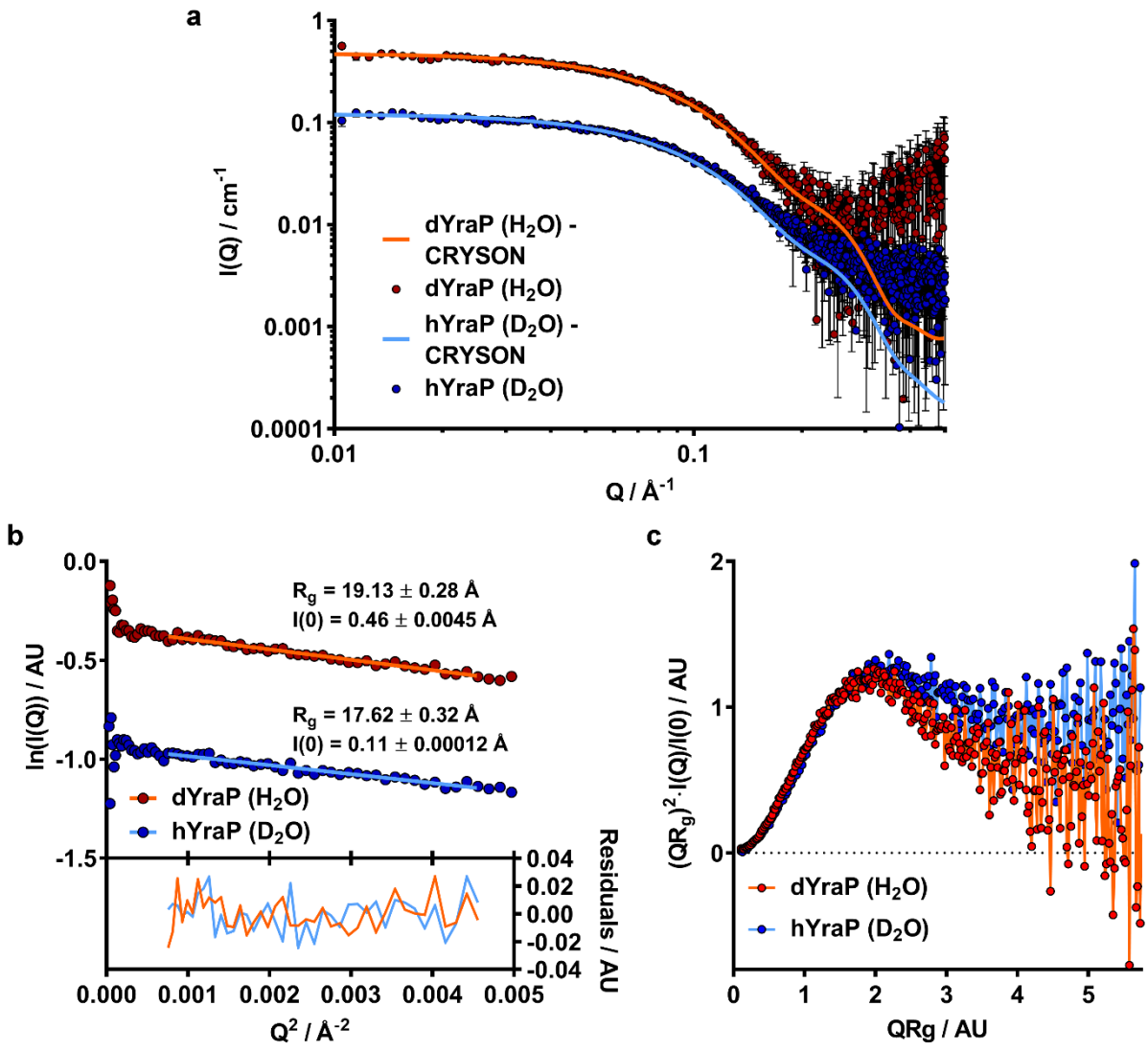

Figure 5.5. a. 1-D small-angle neutron scattering (SANS) patterns of hydrogenated YraP in D_2O (blue points) and deuterated YraP in H_2O. CRYSON was used to calculate the expected scattering pattern based on the solution-NMR ensemble of YraP taking into account the scattering length density of the protein, solvent and H/D exchange and fit to the experimental data (sold lines). **b**. Guinier plots (top panel) for hYraP in D_2O (blue points) and dYraP in H_2O (red points). Linear regression was used to fit the data in order to obtain the radius of gyration (R_g) and the extrapolated 0-angle intensity (I(0)). Fits are shown as solid lines in the top panel, and residuals shown in the bottom panel. **c**. Normalized Kratky plots for hYraP in D_2O (blue points) and dYraP in H_2O (red points).

To gauge with a higher degree of precision, the structural effects of isotopic labelling on YraP structure, the I(Q) vs Q data were transformed by means of an indirect Fourier transform to yield the pair-distance distribution function, P(r), using GNOM (Figure 5.6a, b). The peak in the P(r) function appears at 20 Å in both cases, in good agreement with the R_g values obtained by Guinier analysis. In both cases, the shape of the P(r) curves are indicative of a predominantly globular monomeric particle, although extensions towards D_{max} suggest a degree of anisotropy. Interestingly, a larger D_{max} is observed for dYraP in H_2O compared to hYraP in D_2O. This is in agreement with the R_g values determined by Guinier analysis which suggests a slightly larger radius of gyration for dYraP in H_2O. *Ab initio* dummy atom models calculated for hYraP in D_2O (Figure 5.6c) and dYraP in H_2O (Figure 5.6d) show that both forms of the protein maintain a similar overall structure, where the models obtained by solution NMR fit well within the envelopes modeled from SANS data. Interestingly, the disordered N-terminus is not resolved in either case, suggesting that a high degree of flexibility in solution leads to loss of orientational information upon radial averaging. However, *ab initio* model of dYraP in H_2O shows extra resolved density corresponding to the smaller flexible C-terminus. This suggests that the conformation of this region is stabilized in H_2O compared to D_2O, adopting a more rigid, less flexible conformation. These models support the observations from the Kratky plots, that hYraP in D_2O has a higher degree of flexibility than dYraP in H_2O. Aside from subtle structural changes in natively flexible regions, the core of YraP, including both BON domains, proposed to contain residues important for phospholipid interaction, is retained irrespective of isotopic effects.

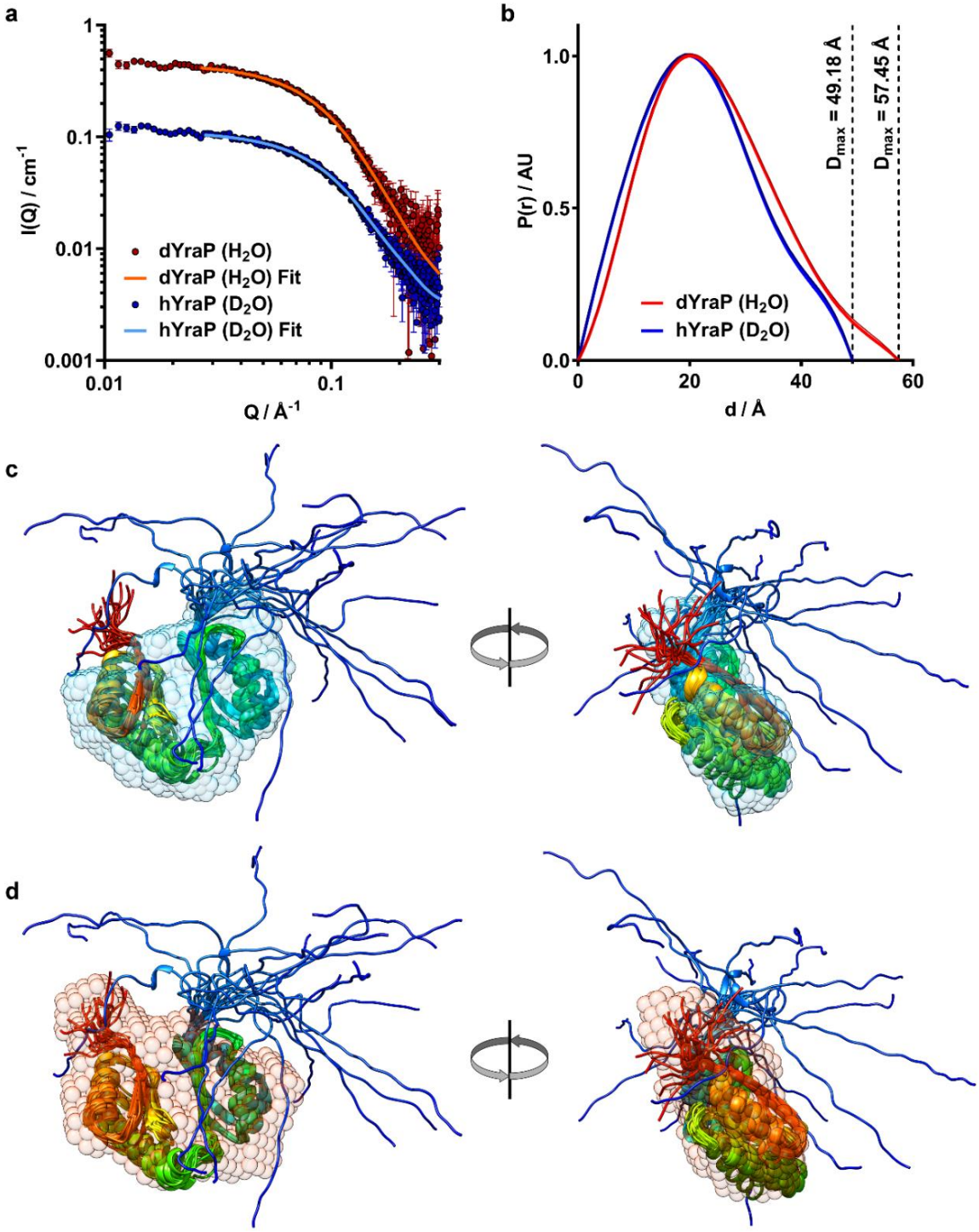

Figure 5.6. a. SANS data (points) with overlaid GNOM fits (solid lines) for dYraP in H_2O (red) and hYraP in D_2O (blue). **b.** Corresponding normalized pair distance distribution P(r) functions of data and fits shown in panel 'a' for dYraP in H_2O (red) and hYraP in D_2O (blue). The maximum dimension of the particle, D_{max}, is shown in each case as a dashed vertical line. **c**. *Ab initio* dummy atom model of hYraP in D_2O (blue spheres) with the solution-NMR ensemble model (ribbon diagram) aligned within the volume of the model. **d**. *Ab initio* dummy atom model of dYraP in H_2O (red spheres) with the solution-NMR ensemble model (ribbon diagram) aligned within the volume of the model.

5.4.4 SMALPs appear at a smaller diameter than previously determined

Following confirmation of YraP structural integrity in the absence of SMALPs, we next sought to determine structural parameters associated with DMPC SMALPs under the solution conditions for which the YraP-SMALP complex was assembled. Here, we measured SANS profiles of 4 separate contrasts: hDMPC SMALPs in D_2O and dDMPC SMALPs in D_2O, H_2O and 34% D_2O. Fits to Guinier plots for each contrast (Figure 5.7a) show good fits to the data where $QR_g < 1.3$, although a significant up-turn is observed for hDMPC SMALP and dDMPC SMALP in D_2O, suggesting degree of aggregation or larger particles contributing to a structure factor. Inspection of the R_g values obtained from these fits (Table 5.1) show that those hDMPC SMALPs and dDMPC SMALPs in D_2O appear larger, further indicating the presence of larger particles. However, the observed structure factor is not severe, allowing further analysis of the data, although we should make the reader aware that while the most pronounced effects of aggregation are at the low-Q structure factor, it can lead to more subtle changes throughout the entire Q-range. Dimensionless Kratky plots (Figure 5.7b) suggest that all samples are globular as expected with no substantial shifts in the peak maxima between samples, suggesting that the structure is consistent between isotopic solution contrasts. The exception is dDMPC SMALPs in 34% D_2O, where due to a poor signal:noise ratio, reliable conclusions cannot be drawn.

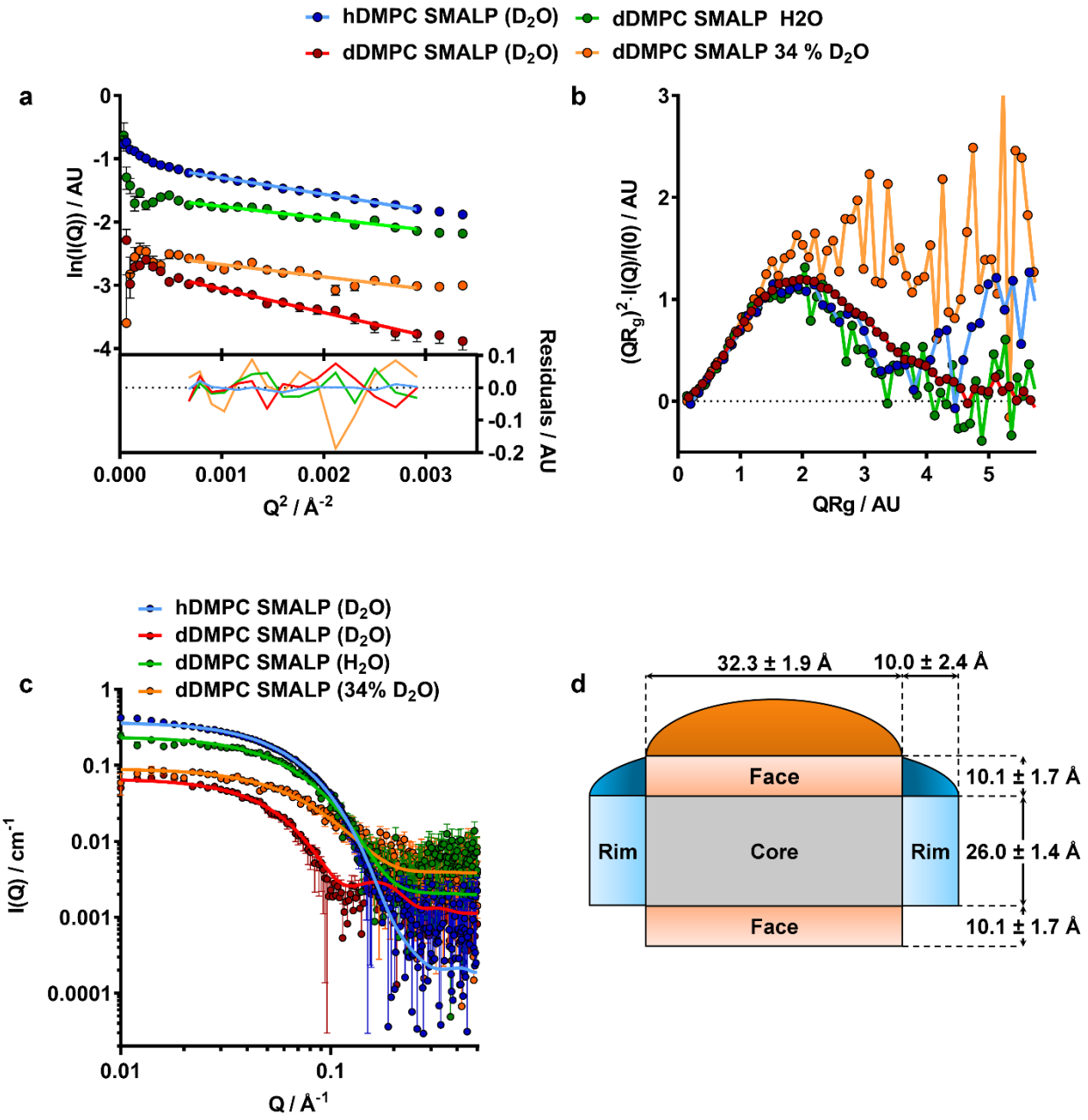

Figure 5.7. a. Guinier plots (top panel) for hDMPC SMALPs in D_2O (blue points), dDMPC SMALPs in H_2O (green points), dDMPC SMALPs in D_2O (red points) and dDMPC SMALPs in 34% D_2O (orange points). Linear regression was used to fit the data in order to obtain R_g and I(0). Fits are shown as solid lines in the top panel, and residuals shown in the bottom panel. **b**. Normalized Kratky plots of DMPC SMALPs. Points are colored as described in panel a. **c**. 1-D SANS patterns (points) with corresponding co-refined fits (solid lines) to a polydisperse core-shell cylinder model with a face layers on top and bottom. **d**. Schematic of a cutaway of the core-shell cylinder model used to fit SANS data with labelled dimensions obtained through the fitting procedure.

Table 5.1. Structural parameters describing the polydisperse core-shell cylinder model obtained though simultaneous fitting of SANS data of DMPC SMALPs across multiple contrasts. Parameters held as constant throughout the fitting procedure are marked with *.

Parameter	**hDMPC SMALP (D_2O)**	**dDMPC SMALP (D_2O)**	**dDMPC SMALP (34% D_2O)**	**dDMPC SMALP (H_2O)**
Guinier R_g / Å	28.07 ± 0.20	33.26 ± 0.77	24.46 ± 1.39	23.73 ± 0.90
Guinier I(0) / cm^{-1}	0.35 ± 0.0023	0.068 ± 0.0019	0.08 ± 0.0034	0.21 ± 0.0052
Volume fraction	0.0021 ± 0.0004	0.0031 ± 0.0003	0.0021 ± 0.0004	0.0016 ± 0.0003
Mean core radius / Å	16.14 ± 1.43			
Radial polydispersity	0.42 ± 0.03			
Core length / Å	26.00 ± 1.42			
Radial shell thickness / Å	10.03 ± 2.39			
Face shell thickness / Å	10.11 ± 1.67			
Core SLD / $\times 10^{-6}$ $Å^{-2}$	-0.37 *		6.84	
Radial shell SLD / $\times 10^{-6}$ $Å^{-2}$	1.89 *			
Face shell SLD / $\times 10^{-6}$ $Å^{-2}$	2.13 *			
Solvent SLD / $\times 10^{-6}$ $Å^{-2}$	6.34 *	1.79 *	-0.56 *	
Mol% solvent in rim	0.60 ± 0.11			
Mol% solvent in face	0.57 *			
Incoherent background / cm^{-1}	0.00016 ± 0.00008	0.0011 ± 0.00009	0.0038 ± 0.0002	0.0021 ± 0.0003

More precise information on the structure of DMPC SMALPs in solution can be obtained by model dependent analysis. Here, we fit the parameters of a model previously used to ascertain structural parameters of DMPC SMALPs,[27] describing a cylindrical core of phospholipids, split into slabs representing phospholipid head and tail regions with a shell surrounding the phospholipid tails representing the SMA belt. Polydispersity was modelled by a Schultz distribution of the radius of the central phospholipid core. Simultaneously fitting the parameters of this model to the SANS profiles measured for each solution contrast provided good fits to the experimental data (Figure 5.7c) allowing determination of parameters describing the structure of DMPC SMALPs (Figure 5.7d, Table 5.1). The parameters describing the thickness of the bilayer solubilized within the core of the SMALP show a thickness of the tail region of 26.00 ± 1.42 Å and a headgroup thickness of 10.11 ± 1.67 Å. This is consistent with previous structural studies of DMPC SMALPs by SANS [27] and with previous studies of

PC bilayer structure.[57] However, we observed a smaller radius of the phospholipid core than previously reported: 16.14 ± 1.43 Å compared to 38 ± 2 Å. In addition, we were only able to fit the experimental data when taking into account a large radial polydispersity of 0.42 ± 0.03. This shows that DMPC SMALPs formed under conditions of high ionic strength and with a high polymer:lipid ratio have a smaller diameter and increased polydispersity.

5.4.5 YraP-SMALP complex forms elongated fibrillar-like structures

With a characterization and understanding of the solution structure of YraP and DMPC SMALPs individually, we next sought to investigate the structure of the YraP-SMALP complex by isotopic contrast SANS. As mentioned above, by utilizing selective isotopic labelling, SANS allows identification of the contributions to the scattering pattern by individual components of the structure. Figure 5.2 shows how the scattering length density of the individual components of the YraP-SMALP complex varies as a function of D_2O volume fraction of the solvent. In order to simplify analysis of SANS profiles, we initially took the strategy of attempting to use SMALPs with a homogenous SLD across the nanodisc. By incubating either hYraP or dYraP with a mixture of hDMPC and dDMPC lipids to match the SLD of SMA (see materials and methods for a description) we could create a complex reduced to two effective SLDs across the particle. By measuring dYraP SMALPs with SMA-matched lipids in D_2O, the majority of the scattering contribution will be from the SMALPs allowing identification of the SMALP structure. Furthermore, measurement of hYraP SMALPs containing SMA-matched lipids in D_2O, should then allow us to determine the relative positions of SMALP and YraP in the complex.

SANS profiles from these simplified contrast models are shown in Figure 5.8. We were surprised to find that the Guinier region for this data (where $QR_g < 1.3$) occurs at an inaccessibly low Q for the instrument (given the detector position chosen for this experiment). This suggests that a substantially larger structure has formed than was observed for YraP or DMPC SMALPs in isolation. Similarly, due to the restricted Q-range, attempted P(r) inversions were deemed unreliable due to the absence of low-Q data describing the large real space distributions. Despite the absence of a low-Q Guinier region,

model-dependent analysis is still a viable analysis strategy. In order to determine the shape of the YraP-SMALP complex, a range of models were simultaneously fit to both experimental data sets (Figure 5.8). We have therefore considered a number of possible structural models to explain the measured data. Initially we attempted fitting the form factor of a core-shell sphere, modelling a globular aggregation of YraP-SMALPs, where the core is composed of YraP and the shell of DMPC-SMALPs, or *vice versa* (Model 1 and 2, respectively). These models did not provide a good fit to the experimental data. We also considered whether an YraP may be able to bind two SMALPs via each BON domain, or whether an individual SMALP may be able to bind two YraP molecules on either bilayer face. These scenarios were modelled using a stacked disc model with a central cylindrical SLD slab representing YraP is flanked on either face by cylindrical SLD slab representing SMALPs, or *vice versa* (Model 3 and 4, respectively). Again, neither of these models provided a good fit to the experimental data. The absence of a low-Q Guinier region suggests that at least one dimension of the complex is larger than the minimum Q value measurable with the instrumental setup. We therefore considered the possibility of the complex forming an alternating stack of YraP and SMALPs. This was also modelled by a stacked cylinder model with alternating SLD slabs corresponding to YraP and SMALPs (Model 5). While this model provided a better fit to the experimental data at low Q, strong interference fringes appear in the data for both contrasts due to the periodic structure of this model. By removing the periodicity and modelling an extended core-shell cylinder with a SMALP core and a YraP shell (Model 6), we were able to obtain good fits to both experimental contrasts.

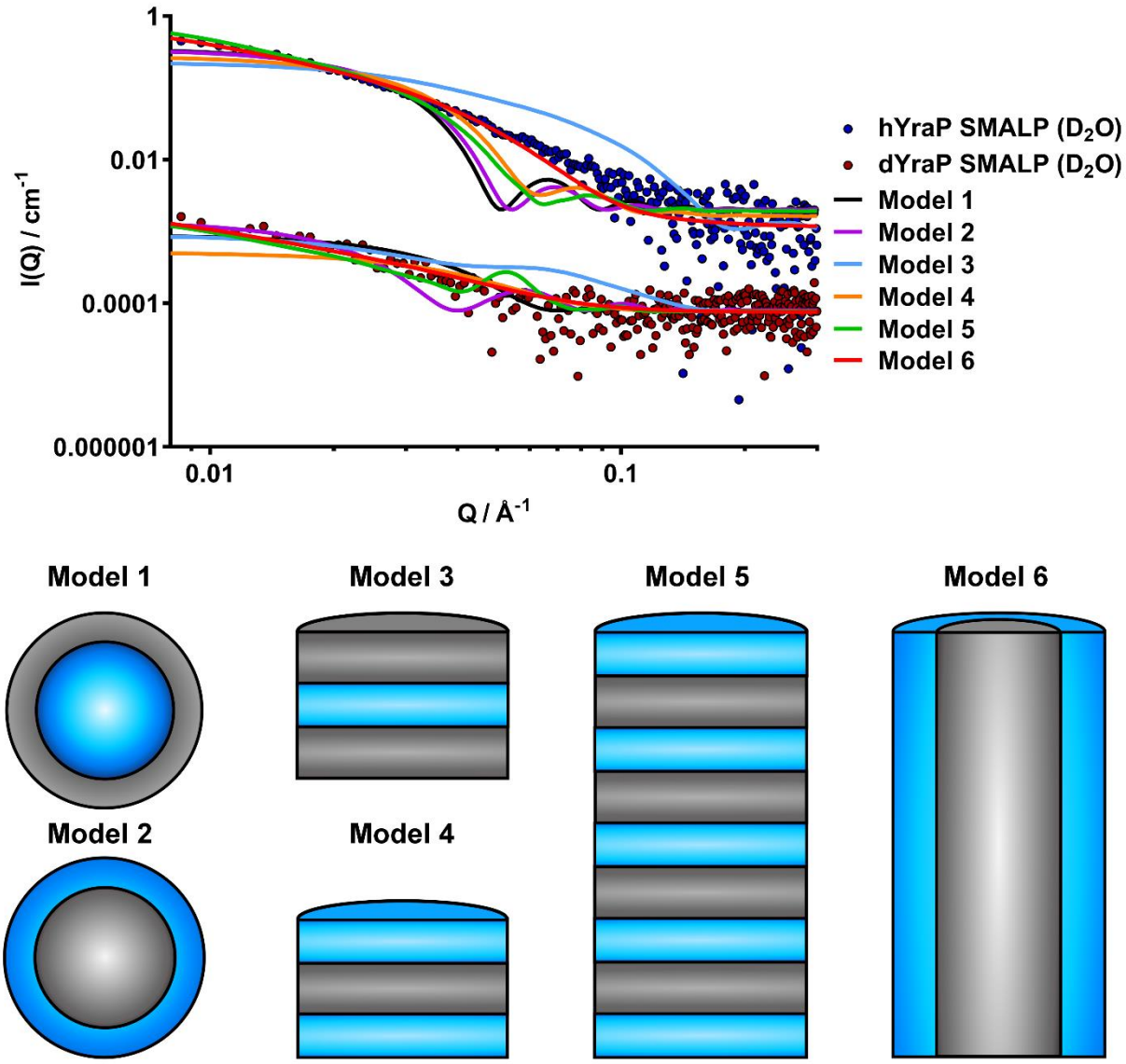

Figure 5.8. Model-dependent analysis of SANS data for hYraP SMALP (blue points) and dYraP SMALP (red points) where lipids have been contrast-matched to SMA in both cases. Error bars have been omitted and SANS data offset for clarity. Solid lines show the simultaneous best fit to the data for each model tested, where schematics below show a representation of the model used in each case, where grey shaded regions represent regions of SLD assigned to DMPC SMALPs and blue colored areas represent regions of SLD assigned to YraP. **Model 1** (black fit lines) is a core-shell sphere with a core of YraP and a shell of SMALPs. **Model 2** (purple fit lines) is a core-shell sphere with a core composed of SMALPs with YraP shell. **Model 3** (blue fit lines) is a stacked cylinder where YraP is the central region, bound by two SMALPs either side. **Model 4** (orange fit lines)is a stacked cylinder where one SMALP has bound YraP on each face of the cylinder. **Model 5** (green fit lines) is a repeated stacked cylinder model with alternating layers of YraP and SMALPs. **Model 6** (red fit lines) is an elongated core-shell cylinder model where the core is composed of SMALPs, and the shell of YraP.

We also measured dYraP SMALPs containing hDMPC, in D_2O, 34% D_2O and H_2O in order to maximize the contrast between individual components and provide finer structural information on the relative positions of YraP and SMALPs. Furthermore, YraP-SMALPs containing SMA-matched lipids measured in 65% D_2O, should in theory provide a homogenous SLD across the whole particle, allowing constraints describing the absolute dimensions to be defined. SANS profiles from these contrasts are shown in Figure 5.9. Based on the simplified model-dependent analysis, an elongated cylinder model provides the best fit to the experimental data. Simultaneous fitting of all contrasts was performed to define the model parameters. All contrasts could only be fit when assuming a core-shell structure of the cylinder, where the core is composed of SMALPs, and the shell composed of either hydrogenated or deuterated YraP. Since the low-Q region that defines the length of the cylinder was outside the measurable Q-range we have fixed this parameter at 10,000 Å, a value that corresponds to a Q well below the minimum measurable value. The parameters obtained through fitting this model are listed in Table 5.2; we are able to define a radius of the SMALP core of 19.35 ± 0.47 Å, where the YraP shell has a thickness of 10.01 ± 0.34 Å (Figure 5.9c). A radial polydispersity within the SMALP core region of 0.5 ± 0.03 was also observed. Alternative orientations of SMALPs and YraP, either as alternating protein-SMALP stacks, or as a core-shell cylinder with a protein core and a SMALP shell were unable to provide satisfactory fits to all contrasts measured.

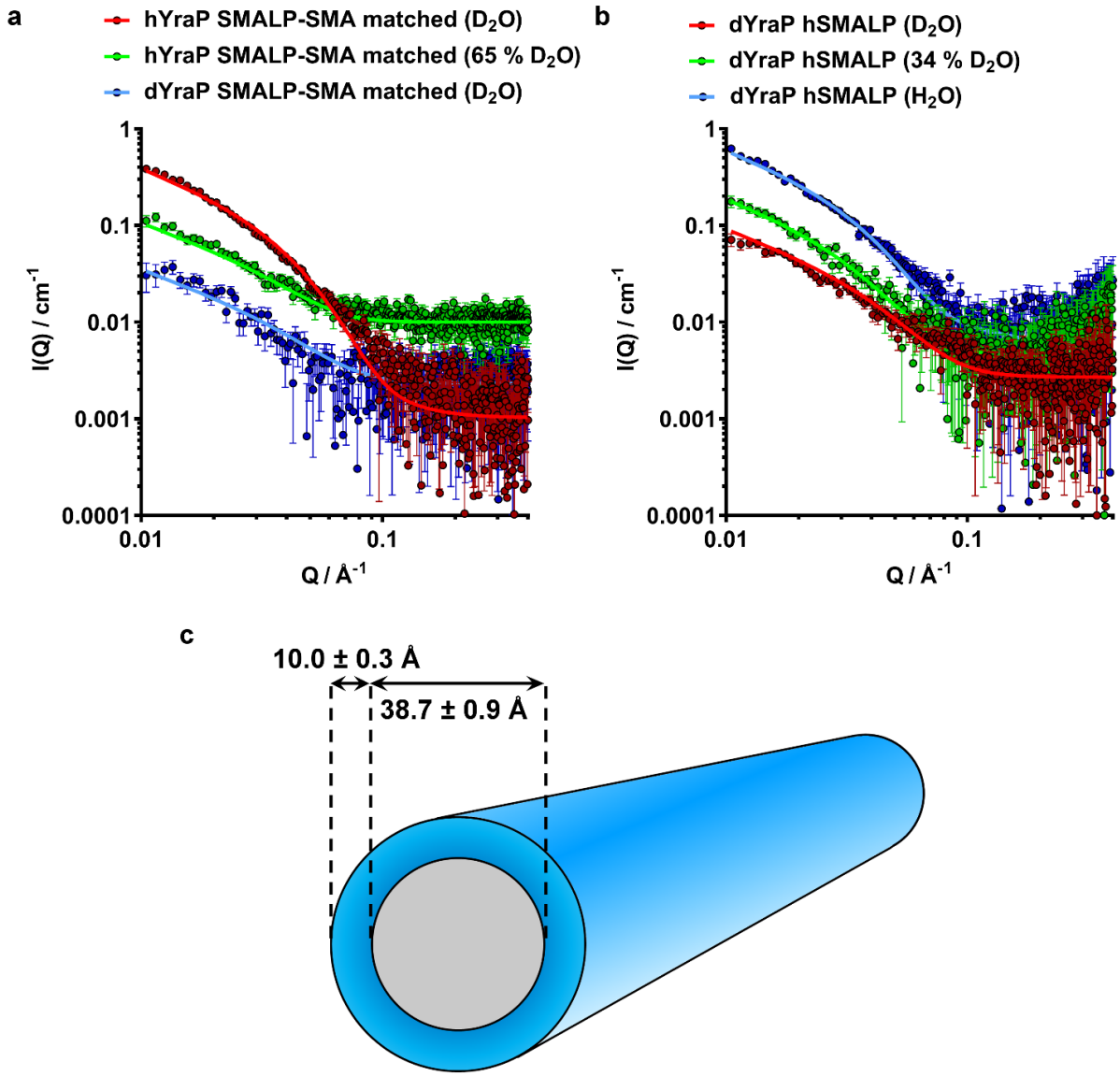

Figure 5.9. a. 1-D SANS patterns (points) of hYraP-SMALPs in D_2O (red) and 65% D_2O (green) and dYraP-SMALPs in D_2O (blue) each assembled with a mixture of hydrogenated and deuterated lipids such that the scattering length density of the lipid core of the SMALP matches that of the SMA polymer belt. **b**. 1-D SANS patterns (points) of dYraP-SMALPs in D_2O (red) 34% D_2O (green) H_2O (blue), assembled with fully hydrogenated DMPC. Solid lines in both a and b represent the co-refined fits of an elongated, polydisperse core-shell cylinder model to the experimental data. All scattering curves shown were simultaneously fit to this model. **c**. Schematic representation of the elongated core-shell cylinder model used to fit SANS data, where the central core has an SLD corresponding to that of SMALPs, and the outer shell has an SLD corresponding to that of YraP. The dimensions of the core and shell of the model obtained through the fitting procedure are labelled

Table 5.2. Structural parameters describing the elongated core-shell cylinder model obtained though simultaneous fitting of SANS data of YraP-SMALPs across multiple contrasts. Parameters held as constant throughout the fitting procedure are marked with *.

Protein contrast **DMPC contrast** **Solution contrast** **Parameter**	**hYraP SMA-matched** **D_2O**	**hYraP SMA-matched** **65% D_2O**	**dYraP SMA-matched** **D_2O**	**dYraP hDMPC** **D_2O**	**dYraP hDMPC** **34% D_2O**	**dYraP hDMPC** **H_2O**
Volume fraction / $\times10^{-4}$	5.48 ± 0.13	5.80 ± 0.29	1.29 ± 0.10	2.29 ± 0.04	4.32 ± 0.19	8.04 ± 0.73
Mean core radius / Å	19.35 ± 0.47					
Radial Polydispersity	0.50 ± 0.03					
Shell thickness / Å	10.01 ± 0.34					
Length / Å	10000 *					
SLD core / $\times10^{-6}$ Å^{-2}	3.73 *	2.71 *	3.73 *	2.18 *	0.91 *	0.26 *
SLD shell / $\times10^{-6}$ Å^{-2}	3.18 *	2.71 *	6.58 *	6.58 *	5.71 *	5.69 *
SLD solvent / $\times10^{-6}$ Å^{-2}	6.36*	3.94 *	6.36 *	6.36 *	1.79 *	-0.56 *
Incoherent background / cm^{-1}	0.0078 ± 0.0003	0.010 ± 0.0002	0.0023 ± 0.0001	0.0027 ± 0.0001	0.0055 ± 0.0004	0.0019 ± 0.0003

In order to provide further information regarding the likely structural properties of YraP when interacting with SMALPs, Thioflavin T (ThT) fluorescence experiments were performed. ThT is commonly used to detect the presence of amyloid or amyloid-like fibrils. In the absence of protein in solution, ThT self-quenches such that no fluorescent intensity can be measured. However, ThT is able to bind to fibrillar proteins via channels formed by the protein backbone parallel to the long axis of ß-sheet structures found within many forms of ß-sheet based protein fibers, whereby self-quenching is inhibited and ThT fluorescence can be measured. As we have shown an increase in ß-sheet content of YraP within the YraP-SMALP complex by CD, and SANS experiments show formation of a long cylindrical object, the YraP shell may be fibrillar in nature and lead to an increase in ThT fluorescence. As ThT has been shown to interact with hydrophobic pockets non-fibrillar proteins, we initially measured the change in ThT fluorescence upon incubation with either YraP or DMPC SMALPs (Figure

5.10). ThT in the presence of YraP alone lead to no significant increase in fluorescence, while ThT in the presence of DMPC SMALPs lead to a 2.37 ± 0.08 fold increase in fluorescent intensity. However, upon incubation with YraP-SMALPs, a 5.67 ± 0.26 fold increase in intensity was observed, suggesting that YraP undergoes a structural rearrangement upon SMALP interaction which is sufficient for ThT binding such that self-quenching is inhibited.

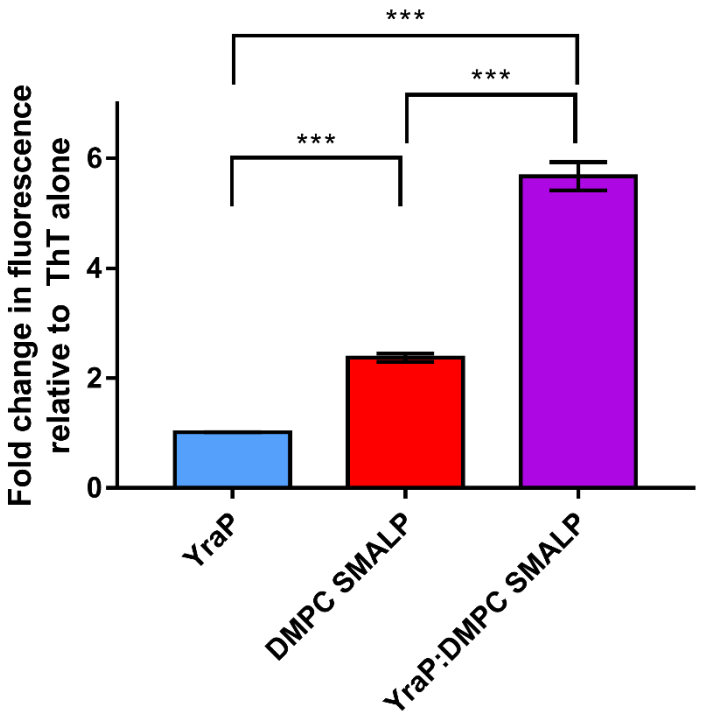

Figure 5.10. Increase in thioflavin T fluorescence in response to 5 µM YraP (blue), DMPC SMALPs (red) or YraP-SMALPs (purple). All data are n=3 with error bars representing ± standard error. Significance was assessed by means of a one-way ANOVA where *** represents $p < 0.0001$ indicating a statistically significant difference between means of each sample

5.5 DISCUSSION

We have shown that a clear structural rearrangement of YraP occurs upon interaction with DMPC SMALPs. SRCD experiments showed distinct spectral changes, suggesting decreased α-helical, and increased β-sheet content upon interaction of YraP with SMALPs. Through secondary structure deconvolution, we are able to estimate the extent of secondary structural changes. While an increase in ß-sheet structure is indeed predicted, along with a decrease in irregular loops, the α-helical content of YraP remains essentially unchanged. Previous studies have identified residues hypothesized for membrane interaction being located on one face of helix α3 within BON domain 2. If this mode of membrane binding is retained upon solubilization into SMALPs, it is likely that the amphipathic helix responsible for membrane binding remains present, maintaining YraP anchored to the bilayer face.

While a substantial increase of ß-sheet content is observed in YraP upon interaction with SMALPs, the ß-fold is also predicted to change from predominantly anti-parallel to incorporate parallel ß-sheets. Analysis of SANS data collected from the YraP-SMALP complex suggests an extended cylindrical structure, where a core of SMALPs is wrapped by a layer of protein. The thickness of the protein layer was found to be ~ 10 Å. When compared to the structure of YraP, both the NMR ensemble structure and the SANS solution structure for both isotopic labeling indicate the two BON domains in the core of the protein form an oblate spheroid structure with a polar diameter of ~ 20 Å and an equatorial diameter of ~ 50 Å. Furthermore, the experimentally determined R_g of YraP in the absence of SMALPs is 19.1 Å and 17.6 Å for dYraP and hYraP, respectively. This suggests that YraP does not maintain its solution structure upon interaction with SMALPs, as suggested by SRCD. The increased ß-sheet content, elongated nature of the particles in addition to the increased fluorescence of ThT in the presence of YraP SMALPs suggest that SMALPs may induce a fibrillar conformation of YraP.

Structural studies of other ß-sheet rich protein fibrils, such as the prototypical Amyloid ß proteins, Aß(1-40)[58] and Aß(1-42),[59,60] implicated in plaque formation in Alzheimer's disease, and α-synuclein,[61] responsible for Lewy body formation in Parkinson's disease have revealed common structural elements.[62] Notably, a so-called 'cross-beta' structure is overarchingly conserved. Here, stacks of

antiparallel ß-loop-ß motifs (ß-arch), are hydrogen bonded together forming two extended, twisted parallel ß-sheets (ß-arcade) which interact via hydrogen bonds of the side chains rather than the peptide backbone, as expected for standard ß-hairpin motifs. This is in good agreement with the proposed fibrilization of YraP, where a large parallel ß-sheet content is only predicted when in complex with SMALPs. Furthermore, the maximum distance between the two ß-strands within an individual ß-arch motif are 10 – 11 Å. As the thickness of the YraP shell in the elongated cylinder model which was fit to SANS data is ~ 10 Å, a ß-arch motif would be accommodated by the real space constraints of the model. In addition, the broadness of the SEC elution profile for the YraP-SMALP complex could be explained by the polydispersity of the self-assembled fibrillar structures which was also observed by SANS.

While the data presented here is suggestive of fibril formation by YraP when interacting with DMPC SMALPs, it is not indicative. Compared to the secondary structure of known amyloid fibrils, YraP is predicted to contain a large proportion of α-helices, more than would be expected if only the membrane binding helix is maintained. Similarly, while YraP-SMALPs lead to a larger increase in ThT fluorescence than either YraP or SMALPs alone, ThT is known to bind to non-fibrillar structures. It is clear from SRCD and SANS data that YraP undergoes a large conformational change upon interaction with SMALPs. Therefore, it is equally likely that the protein is not in an amyloid-like conformation within the core shell cylinder model. While SANS suggests an elongated structure is formed, the orientational averaging of particles in solution and the inherently high polydispersity of those particles means we are insensitive to the presence, or absence of specific folds or structural motifs. Notably, the extended N-terminus of YraP was not accounted for in the *ab initio* models presented above. This is due to the high level of flexibility and mobility, meaning a specific region of neutron scattering length density cannot be defined. SRCD predicts that much of the irregular loop content of YraP is still present when interacting with SMALPs. While we cannot comment on the residues involved in irregular structural elements with any certainty, it may be that the N-terminus remains essentially unchanged, and acts as a bridge between SMALP-bound YraP monomers leading to the observed elongated structures.

The assumption we have made up until this point is that the SMALP structure remains unperturbed by the inclusion of YraP. The core of the YraP-SMALP structure, assigned to SMALPs, has a diameter of ~ 39 Å. This is thinner than both the total diameter of the SMALP and the total bilayer thickness in the absence of YraP as determined by SANS. Due to the simplification of the model used to fit SANS data of the YraP-SMALP complex, we are unable to define an orientation of the SMALP within the cylinder core. Recent studies of amyloid formation in the presence of MSP-nanodiscs have shown that a monomeric helical conformation of α-synuclein binds to the membrane surface prior to fibril formation.[24] If the same mechanism is occurring here, then the observed thinning of the cylinder core compared to that expected for a SMALP could be a result of protein embedding into the phospholipid headgroups. However, the same could be said for an interaction of YraP with the SMA polymer belt. Due to the lack of orientational information on the particle core we were able to obtain by SANS, we cannot distinguish between a protein-polymer or a protein-lipid interaction. Recent studies have shown that amyloidosis can lead to widespread membrane defects including pore formation,[63] removal of phospholipids in a surfactant-like manner,[64] and polymerization on the membrane surface leading to lipid reorganization [65] where the composition, curvature and phase of the bilayer can modify amyloid binding and fibrilization kinetics.[66,67] If YraP does form amyloid-like fibers upon interaction with phospholipid membranes, the vesicular structure could be perturbed prior to solubilization by SMA, where the resultant core does not contain SMALPs with the structure as expected in the absence of YraP.

Despite the hypotheses presented here, we cannot comment on the propensity of YraP to form elongated, fibrous structures *in vivo*. Despite SMALPs providing a native-like membrane environment, it is not a realistic mimic of the gram negative outer membrane. While NMR data suggest that YraP can bind PG, PC and CL, PC is not found in bacterial membranes. Furthermore, coulombic effects from the highly negatively charged polymer belt may further lead to structural aberrations of YraP upon SMALP interaction which may not occur in the cell. Nonetheless, the ability of YraP to form elongated fibrillar structures when interacting with a SMALP may provide clues as to its function, which is currently unknown. YraP has been shown to localize to the inner leaflet of the outer membrane and after the initiation of cell division localizes to the division site at the septum. Further genetic evidence suggests

a role for YraP as an outer membrane regulator of cell division.[34] While YraP is conserved across proteobacteria, *yraP* deletion mutants are viable (indicating non-essentiality) but exhibit a phenotype of SDS sensitivity, which is indicative of outer membrane defects.[35] This suggests that YraP may be involved in stabilizing the outer membrane during cell division. While speculative at this stage, as YraP becomes localized to the site of cell division, it may be involved in sensing positive membrane curvature, where fibrilization could provide a mechanism by which extreme positive membrane curvatures (from the perspective of YraP at the periplasmic face of the dividing outer membrane, or the exterior of SUVs) experienced by dividing cells are stabilized. While gram-negative bacteria are known to secrete functional amyloid fibers to facilitate in biofilm formation,[68] and other inner membrane localized components of the divisome, FtsZ and FtsA, are well characterized in forming fibrous assemblies,[2] *in vivo* observation of YraP fibrilization at the cell division site would be required to confirm this hypothesis.

5.6 CONCLUSIONS

Here, we have demonstrated that SMALPs can be used to capture the lipid binding protein YraP interaction with membranes for structural studies. Whilst both YraP and SMALPs had an expected structure in isolation, we have shown that YraP undergoes a large scale conformational change when interacting with DMPC SMALPs. The secondary structural composition of YraP shows a marked increase in ß-content with a large proportion of ß-sheets being in a parallel arrangement. SANS has revealed that the YraP-SMALP complex forms an elongated core-shell cylinder structure, which we hypothesize is likely driven by YraP fibrilization into an amyloid-like structure. While *in vivo* confirmation of YraP fibrilization is required, these data provide important clues as to the potential function of YraP. Despite uncertainties in the precise nature of the structural reorganization of YraP upon membrane interaction, these results demonstrate the potential of SMALPs to provide a soluble membrane surface for structural investigations of peripheral membrane proteins and complexes through high-resolution techniques such as cryo-transmission electron microscopy, solid-state NMR spectroscopy as well as SAS techniques to provide information on large-scale lipid-protein organization.

5.7 REFERENCES

(1) Chiapparino, A.; Maeda, K.; Turei, D.; Saez-Rodriguez, J.; Gavin, A.-C. The Orchestra of Lipid-Transfer Proteins at the Crossroads between Metabolism and Signaling. *Prog. Lipid Res.* **2016**, *61*, 30–39. https://doi.org/10.1016/j.plipres.2015.10.004.

(2) Loose, M.; Mitchison, T. J. The Bacterial Cell Division Proteins FtsA and FtsZ Self-Organize into Dynamic Cytoskeletal Patterns. *Nat Cell Biol* **2014**, *16* (1), 38–46.

(3) Hodnik, V.; Anderluh, G. Surface Plasmon Resonance for Measuring Interactions of Proteins with Lipid Membranes. *Lipid-Protein Interact.* **2013**, 23–36. https://doi.org/10.1007/978-1-62703-275-9_2.

(4) Nielsen, S. B.; Otzen, D. E. Quartz Crystal Microbalances as Tools for Probing Protein-Membrane Interactions. *Methods Mol. Biol. Clifton NJ* **2013**, *974*, 1–21. https://doi.org/10.1007/978-1-62703-275-9_1.

(5) Saliba, A.-E.; Vonkova, I.; Deghou, S.; Ceschia, S.; Tischer, C.; Kugler, K. G.; Bork, P.; Ellenberg, J.; Gavin, A.-C. A Protocol for the Systematic and Quantitative Measurement of Protein-Lipid Interactions Using the Liposome-Microarray-Based Assay. *Nat. Protoc.* **2016**, *11* (6), 1021–1038. https://doi.org/10.1038/nprot.2016.059.

(6) Wadsäter, M.; Laursen, T.; Singha, A.; Hatzakis, N. S.; Stamou, D.; Barker, R.; Mortensen, K.; Feidenhans'l, R.; Møller, B. L.; Cárdenas, M. Monitoring Shifts in the Conformation Equilibrium of the Membrane Protein Cytochrome P450 Reductase (POR) in Nanodiscs. *J. Biol. Chem.* **2012**, *287* (41), 34596–34603. https://doi.org/10.1074/jbc.M112.400085.

(7) Marsh, D. Lipid-Binding Proteins: Structure of the Phospholipid Ligands. *Protein Sci. Publ. Protein Soc.* **2003**, *12* (9), 2109–2117. https://doi.org/10.1110/ps.0396803.

(8) Holcomb, J.; Spellmon, N.; Zhang, Y.; Doughan, M.; Li, C.; Yang, Z. Protein Crystallization: Eluding the Bottleneck of X-Ray Crystallography. *AIMS Biophys.* **2017**, *4* (4), 557–575. https://doi.org/10.3934/biophy.2017.4.557.

(9) Carpenter, E. P.; Beis, K.; Cameron, A. D.; Iwata, S. Overcoming the Challenges of Membrane Protein Crystallography. *Curr. Opin. Struct. Biol.* **2008**, *18* (5), 581–586. https://doi.org/10.1016/j.sbi.2008.07.001.

(10) Mio, K.; Sato, C. Lipid Environment of Membrane Proteins in Cryo-EM Based Structural Analysis. *Biophys. Rev.* **2017**, *10* (2), 307–316. https://doi.org/10.1007/s12551-017-0371-6.

(11) Bayburt, T. H.; Grinkova, Y. V.; Sligar, S. G. Self-Assembly of Discoidal Phospholipid Bilayer Nanoparticles with Membrane Scaffold Proteins. *Nano Lett.* **2002**, *2* (8), 853–856. https://doi.org/10.1021/nl025623k.

(12) Denisov, I. G.; Sligar, S. G. Nanodiscs for Structural and Functional Studies of Membrane Proteins. *Nat. Struct. Mol. Biol.* **2016**, *23* (6), 481–486. https://doi.org/10.1038/nsmb.3195.

(13) Bayburt, T. H.; Sligar, S. G. Membrane Protein Assembly into Nanodiscs. *FEBS Lett.* **2010**, *584* (9), 1721–1727. https://doi.org/10.1016/j.febslet.2009.10.024.

(14) Roh, S.-H.; Stam, N. J.; Hryc, C. F.; Couoh-Cardel, S.; Pintilie, G.; Chiu, W.; Wilkens, S. The 3.5-Å CryoEM Structure of Nanodisc-Reconstituted Yeast Vacuolar ATPase Vo Proton Channel. *Mol. Cell* **2018**, *69* (6), 993-1004.e3. https://doi.org/10.1016/j.molcel.2018.02.006.

(15) Gao, Y.; Cao, E.; Julius, D.; Cheng, Y. TRPV1 Structures in Nanodiscs Reveal Mechanisms of Ligand and Lipid Action. *Nature* **2016**, *534* (7607), 347–351. https://doi.org/10.1038/nature17964.

(16) Pandit, A.; Shirzad-Wasei, N.; Wlodarczyk, L. M.; van Roon, H.; Boekema, E. J.; Dekker, J. P.; de Grip, W. J. Assembly of the Major Light-Harvesting Complex II in Lipid Nanodiscs. *Biophys. J.* **2011**, *101* (10), 2507–2515. https://doi.org/10.1016/j.bpj.2011.09.055.

(17) Frauenfeld, J.; Gumbart, J.; Sluis, E. O. van der; Funes, S.; Gartmann, M.; Beatrix, B.; Mielke, T.; Berninghausen, O.; Becker, T.; Schulten, K.; et al. Cryo-EM Structure of the Ribosome–SecYE Complex in the Membrane Environment. *Nat. Struct. Mol. Biol.* **2011**, *18* (5), 614–621. https://doi.org/10.1038/nsmb.2026.

(18) Kijac, A. Z.; Li, Y.; Sligar, S. G.; Rienstra, C. M. Magic-Angle Spinning Solid-State NMR Spectroscopy of Nanodisc-Embedded Human CYP3A4. *Biochemistry* **2007**, *46* (48), 13696–13703. https://doi.org/10.1021/bi701411g.

(19) Nikolaev, M.; Round, E.; Gushchin, I.; Polovinkin, V.; Balandin, T.; Kuzmichev, P.; Shevchenko, V.; Borshchevskiy, V.; Kuklin, A.; Round, A.; et al. Integral Membrane Proteins Can Be Crystallized Directly from Nanodiscs. *Cryst. Growth Des.* **2017**, *17* (3), 945–948. https://doi.org/10.1021/acs.cgd.6b01631.

(20) McLean, M. A.; Gregory, M. C.; Sligar, S. G. Nanodiscs: A Controlled Bilayer Surface for the Study of Membrane Proteins. *Annu. Rev. Biophys.* **2018**, *47* (1), 107–124. https://doi.org/10.1146/annurev-biophys-070816-033620.

(21) Gillette, W. K.; Esposito, D.; Blanco, M. A.; Alexander, P.; Bindu, L.; Bittner, C.; Chertov, O.; Frank, P. H.; Grose, C.; Jones, J. E.; et al. Farnesylated and Methylated KRAS4b: High Yield Production of Protein Suitable for Biophysical Studies of Prenylated Protein-Lipid Interactions. *Sci. Rep.* **2015**, *5*, 15916. https://doi.org/10.1038/srep15916.

(22) Ye, X.; McLean, M. A.; Sligar, S. G. Conformational Equilibrium of Talin Is Regulated by Anionic Lipids. *Biochim. Biophys. Acta BBA - Biomembr.* **2016**, *1858* (8), 1833–1840. https://doi.org/10.1016/j.bbamem.2016.05.005.

(23) Mazhab-Jafari, M. T.; Marshall, C. B.; Smith, M. J.; Gasmi-Seabrook, G. M. C.; Stathopulos, P. B.; Inagaki, F.; Kay, L. E.; Neel, B. G.; Ikura, M. Oncogenic and RASopathy-Associated K-RAS Mutations Relieve Membrane-Dependent Occlusion of the Effector-Binding Site. *Proc. Natl. Acad. Sci.* **2015**, *112* (21), 6625–6630. https://doi.org/10.1073/pnas.1419895112.

(24) Viennet, T.; Wördehoff, M. M.; Uluca, B.; Poojari, C.; Shaykhalishahi, H.; Willbold, D.; Strodel, B.; Heise, H.; Buell, A. K.; Hoyer, W.; et al. Structural Insights from Lipid-Bilayer Nanodiscs Link α-Synuclein Membrane-Binding Modes to Amyloid Fibril Formation. *Commun. Biol.* **2018**, *1* (1), 44. https://doi.org/10.1038/s42003-018-0049-z.

(25) Skar-Gislinge, N.; Kynde, S. A. R.; Denisov, I. G.; Ye, X.; Lenov, I.; Sligar, S. G.; Arleth, L. Small-Angle Scattering Determination of the Shape and Localization of Human Cytochrome P450 Embedded in a Phospholipid Nanodisc Environment. *Acta Crystallogr. D Biol. Crystallogr.* **2015**, *71* (Pt 12), 2412–2421. https://doi.org/10.1107/S1399004715018702.

(26) Knowles, T. J.; Finka, R.; Smith, C.; Lin, Y.-P.; Dafforn, T.; Overduin, M. Membrane Proteins Solubilized Intact in Lipid Containing Nanoparticles Bounded by Styrene Maleic Acid Copolymer. *J. Am. Chem. Soc.* **2009**, *131* (22), 7484–7485. https://doi.org/10.1021/ja810046q.

(27) Jamshad, M.; Grimard, V.; Idini, I.; Knowles, T. J.; Dowle, M. R.; Schofield, N.; Sridhar, P.; Lin, Y.; Finka, R.; Wheatley, M.; et al. Structural Analysis of a Nanoparticle Containing a Lipid Bilayer Used for Detergent-Free Extraction of Membrane Proteins. *Nano Res.* **2015**, *8* (3), 774–789. https://doi.org/10.1007/s12274-014-0560-6.

(28) Morrison, K. A.; Akram, A.; Mathews, A.; Khan, Z. A.; Patel, J. H.; Zhou, C.; Hardy, D. J.; Moore-Kelly, C.; Patel, R.; Odiba, V.; et al. Membrane Protein Extraction and Purification Using Styrene-Maleic Acid (SMA) Copolymer: Effect of Variations in Polymer Structure. *Biochem. J.* **2016**, *473* (23), 4349–4360. https://doi.org/10.1042/BCJ20160723.

(29) Jamshad, M.; Charlton, J.; Lin, Y.-P.; Routledge, S. J.; Bawa, Z.; Knowles, T. J.; Overduin, M.; Dekker, N.; Dafforn, T. R.; Bill, R. M.; et al. G-Protein Coupled Receptor Solubilization and Purification for Biophysical Analysis and Functional Studies, in the Total Absence of Detergent. *Biosci. Rep.* **2015**, *35* (2), e00188. https://doi.org/10.1042/BSR20140171.

(30) Sun, C.; Benlekbir, S.; Venkatakrishnan, P.; Wang, Y.; Hong, S.; Hosler, J.; Tajkhorshid, E.; Rubinstein, J. L.; Gennis, R. B. Structure of the Alternative Complex III in a Supercomplex with Cytochrome Oxidase. *Nature* **2018**, *557* (7703), 123–126. https://doi.org/10.1038/s41586-018-0061-y.

(31) Parmar, M.; Rawson, S.; Scarff, C. A.; Goldman, A.; Dafforn, T. R.; Muench, S. P.; Postis, V. L. G. Using a SMALP Platform to Determine a Sub-Nm Single Particle Cryo-EM Membrane Protein Structure. *Biochim. Biophys. Acta BBA - Biomembr.* **2018**, *1860* (2), 378–383. https://doi.org/10.1016/j.bbamem.2017.10.005.

(32) Bersch, B.; Dörr, J. M.; Hessel, A.; Killian, J. A.; Schanda, P. Proton-Detected Solid-State NMR Spectroscopy of a Zinc Diffusion Facilitator Protein in Native Nanodiscs. *Angew. Chem. Int. Ed Engl.* **2017**, *56* (9), 2508–2512. https://doi.org/10.1002/anie.201610441.

(33) Broecker, J.; Eger, B. T.; Ernst, O. P. Crystallogenesis of Membrane Proteins Mediated by Polymer-Bounded Lipid Nanodiscs. *Structure* **2017**, *25* (2), 384–392. https://doi.org/10.1016/j.str.2016.12.004.

(34) Tsang, M.-J.; Yakhnina, A. A.; Bernhardt, T. G. NlpD Links Cell Wall Remodeling and Outer Membrane Invagination during Cytokinesis in Escherichia Coli. *PLOS Genet.* **2017**, *13* (7), e1006888. https://doi.org/10.1371/journal.pgen.1006888.

(35) Onufryk, C.; Crouch, M.-L.; Fang, F. C.; Gross, C. A. Characterization of Six Lipoproteins in the ΣE Regulon. *J. Bacteriol.* **2005**, *187* (13), 4552–4561. https://doi.org/10.1128/JB.187.13.4552-4561.2005.

(36) Maderbocus, R. A Study of Outer Membrane Biogenesis in E. Coli. PhD, University of Birmingham, 2014.

(37) Yeats, C.; Bateman, A. The BON Domain: A Putative Membrane-Binding Domain. *Trends Biochem. Sci.* **2003**, *28* (7), 352–355. https://doi.org/10.1016/S0968-0004(03)00115-4.

(38) Hall, S. C. L.; Tognoloni, C.; Price, G. J.; Klumperman, B.; Edler, K. J.; Dafforn, T. R.; Arnold, T. Influence of Poly(Styrene-Co-Maleic Acid) Copolymer Structure on the Properties and Self-Assembly of SMALP Nanodiscs. *Biomacromolecules* **2018**, *19* (3), 761–772. https://doi.org/10.1021/acs.biomac.7b01539.

(39) Lee, S. C.; Knowles, T. J.; Postis, V. L. G.; Jamshad, M.; Parslow, R. A.; Lin, Y.-P.; Goldman, A.; Sridhar, P.; Overduin, M.; Muench, S. P.; et al. A Method for Detergent-Free Isolation of Membrane Proteins in Their Local Lipid Environment. *Nat. Protoc.* **2016**, *11* (7), 1149–1162. https://doi.org/10.1038/nprot.2016.070.

(40) Giuliani, A.; Jamme, F.; Rouam, V.; Wien, F.; Giorgetta, J.-L.; Lagarde, B.; Chubar, O.; Bac, S.; Yao, I.; Rey, S.; et al. DISCO: A Low-Energy Multipurpose Beamline at Synchrotron SOLEIL. *J. Synchrotron Radiat.* **2009**, *16* (6), 835–841. https://doi.org/10.1107/S0909049509034049.

(41) Greenfield, N. J. Using Circular Dichroism Collected as a Function of Temperature to Determine the Thermodynamics of Protein Unfolding and Binding Interactions. *Nat. Protoc.* **2006**, *1* (6), 2527. https://doi.org/10.1038/nprot.2006.204.

(42) Svergun, D. I.; Koch, M. H. J. Small-Angle Scattering Studies of Biological Macromolecules in Solution. *Rep. Prog. Phys.* **2003**, *66* (10), 1735. https://doi.org/10.1088/0034-4885/66/10/R05.

(43) Gabel, F. Applications of SANS to Study Membrane Protein Systems. In *Biological Small Angle Scattering: Techniques, Strategies and Tips*; Advances in Experimental Medicine and Biology; Springer, Singapore, 2017; pp 201–214. https://doi.org/10.1007/978-981-10-6038-0_12.

(44) Arnold, O.; Bilheux, J. C.; Borreguero, J. M.; Buts, A.; Campbell, S. I.; Chapon, L.; Doucet, M.; Draper, N.; Ferraz Leal, R.; Gigg, M. A.; et al. Mantid—Data Analysis and Visualization Package for Neutron Scattering and μ SR Experiments. *Nucl. Instrum. Methods Phys. Res. Sect. Accel. Spectrometers Detect. Assoc. Equip.* **2014**, *764*, 156–166. https://doi.org/10.1016/j.nima.2014.07.029.

(45) Trewhella, J.; Duff, A. P.; Durand, D.; Gabel, F.; Guss, J. M.; Hendrickson, W. A.; Hura, G. L.; Jacques, D. A.; Kirby, N. M.; Kwan, A. H.; et al. 2017 Publication Guidelines for Structural Modelling of Small-Angle Scattering Data from Biomolecules in Solution: An Update. *Acta Crystallogr. Sect. Struct. Biol.* **2017**, *73* (9), 710–728. https://doi.org/10.1107/S2059798317011597.

(46) Kikhney, A. G.; Svergun, D. I. A Practical Guide to Small Angle X-Ray Scattering (SAXS) of Flexible and Intrinsically Disordered Proteins. *FEBS Lett.* **2015**, *589* (19, Part A), 2570–2577. https://doi.org/10.1016/j.febslet.2015.08.027.

(47) Svergun, D. I.; Richard, S.; Koch, M. H.; Sayers, Z.; Kuprin, S.; Zaccai, G. Protein Hydration in Solution: Experimental Observation by x-Ray and Neutron Scattering. *Proc. Natl. Acad. Sci. U. S. A.* **1998**, *95* (5), 2267–2272.

(48) Svergun, D. I. Determination of the Regularization Parameter in Indirect-Transform Methods Using Perceptual Criteria. *J. Appl. Crystallogr.* **1992**, *25* (4), 495–503. https://doi.org/10.1107/S0021889892001663.
(49) Franke, D.; Svergun, D. I. DAMMIF, a Program for Rapid Ab-Initio Shape Determination in Small-Angle Scattering. *J. Appl. Crystallogr.* **2009**, *42* (Pt 2), 342–346. https://doi.org/10.1107/S0021889809000338.
(50) Volkov, V. V.; Svergun, D. I. Uniqueness of Ab Initio Shape Determination in Small-Angle Scattering. *J. Appl. Crystallogr.* **2003**, *36* (3–1), 860–864. https://doi.org/10.1107/S0021889803000268.
(51) Svergun, D. I. Restoring Low Resolution Structure of Biological Macromolecules from Solution Scattering Using Simulated Annealing. *Biophys. J.* **1999**, *76* (6), 2879–2886. https://doi.org/10.1016/S0006-3495(99)77443-6.
(52) Kline, S. R. Reduction and Analysis of SANS and USANS Data Using IGOR Pro. *J. Appl. Crystallogr.* **2006**, *39* (6), 895–900. https://doi.org/10.1107/S0021889806035059.
(53) Kučerka, N.; Kiselev, M. A.; Balgavý, P. Determination of Bilayer Thickness and Lipid Surface Area in Unilamellar Dimyristoylphosphatidylcholine Vesicles from Small-Angle Neutron Scattering Curves: A Comparison of Evaluation Methods. *Eur. Biophys. J.* **2004**, *33* (4), 328–334. https://doi.org/10.1007/s00249-003-0349-0.
(54) Whitten, A. E.; Cai, S.; Trewhella, J. MULCh: Modules for the Analysis of Small-Angle Neutron Contrast Variation Data from Biomolecular Assemblies. *J. Appl. Crystallogr.* **2008**, *41* (1), 222–226. https://doi.org/10.1107/S0021889807055136.
(55) Cho, Y.; Sagle, L. B.; Iimura, S.; Zhang, Y.; Kherb, J.; Chilkoti, A.; Scholtz, J. M.; Cremer, P. S. Hydrogen Bonding of β-Turn Structure Is Stabilized in D2O. *J. Am. Chem. Soc.* **2009**, *131* (42), 15188–15193. https://doi.org/10.1021/ja9040785.
(56) Sheu, S.-Y.; Schlag, E. W.; Selzle, H. L.; Yang, D.-Y. Molecular Dynamics of Hydrogen Bonds in Protein−D2O: The Solvent Isotope Effect. *J. Phys. Chem. A* **2008**, *112* (5), 797–802. https://doi.org/10.1021/jp0771668.
(57) Nagle, J. F.; Tristram-Nagle, S. Structure of Lipid Bilayers. *Biochim. Biophys. Acta BBA - Rev. Biomembr.* **2000**, *1469* (3), 159–195. https://doi.org/10.1016/S0304-4157(00)00016-2.
(58) Bertini, I.; Gonnelli, L.; Luchinat, C.; Mao, J.; Nesi, A. A New Structural Model of Aβ40 Fibrils. *J. Am. Chem. Soc.* **2011**, *133* (40), 16013–16022. https://doi.org/10.1021/ja2035859.
(59) Xiao, Y.; Ma, B.; McElheny, D.; Parthasarathy, S.; Long, F.; Hoshi, M.; Nussinov, R.; Ishii, Y. Aβ(1–42) Fibril Structure Illuminates Self-Recognition and Replication of Amyloid in Alzheimer's Disease. *Nat. Struct. Mol. Biol.* **2015**, *22* (6), 499–505. https://doi.org/10.1038/nsmb.2991.
(60) Lührs, T.; Ritter, C.; Adrian, M.; Riek-Loher, D.; Bohrmann, B.; Döbeli, H.; Schubert, D.; Riek, R. 3D Structure of Alzheimer's Amyloid-Beta(1-42) Fibrils. *Proc. Natl. Acad. Sci. U. S. A.* **2005**, *102* (48), 17342–17347. https://doi.org/10.1073/pnas.0506723102.
(61) Guerrero-Ferreira, R.; Taylor, N. M.; Mona, D.; Ringler, P.; Lauer, M. E.; Riek, R.; Britschgi, M.; Stahlberg, H. Cryo-EM Structure of Alpha-Synuclein Fibrils. *eLife* **2018**, *7*. https://doi.org/10.7554/eLife.36402.
(62) Kajava, A. V.; Baxa, U.; Steven, A. C. Beta Arcades: Recurring Motifs in Naturally Occurring and Disease-Related Amyloid Fibrils. *FASEB J.* **2010**, *24* (5), 1311–1319. https://doi.org/10.1096/fj.09-145979.
(63) Kandel, N.; Zheng, T.; Huo, Q.; Tatulian, S. A. Membrane Binding and Pore Formation by a Cytotoxic Fragment of Amyloid β Peptide. *J. Phys. Chem. B* **2017**, *121* (45), 10293–10305. https://doi.org/10.1021/acs.jpcb.7b07002.
(64) Brender, J. R.; Salamekh, S.; Ramamoorthy, A. Membrane Disruption and Early Events in the Aggregation of the Diabetes Related Peptide IAPP from a Molecular Perspective. *Acc. Chem. Res.* **2012**, *45* (3), 454–462. https://doi.org/10.1021/ar200189b.
(65) Walsh, P.; Vanderlee, G.; Yau, J.; Campeau, J.; Sim, V. L.; Yip, C. M.; Sharpe, S. The Mechanism of Membrane Disruption by Cytotoxic Amyloid Oligomers Formed by Prion

Protein(106–126) Is Dependent on Bilayer Composition. *J. Biol. Chem.* **2014**, *289* (15), 10419–10430. https://doi.org/10.1074/jbc.M113.515866.

(66) Sugiura, Y.; Ikeda, K.; Nakano, M. High Membrane Curvature Enhances Binding, Conformational Changes, and Fibrillation of Amyloid-β on Lipid Bilayer Surfaces. *Langmuir* **2015**, *31* (42), 11549–11557. https://doi.org/10.1021/acs.langmuir.5b03332.

(67) Gibson Wood, W.; Eckert, G. P.; Igbavboa, U.; Müller, W. E. Amyloid Beta-Protein Interactions with Membranes and Cholesterol: Causes or Casualties of Alzheimer's Disease. *Biochim. Biophys. Acta BBA - Biomembr.* **2003**, *1610* (2), 281–290. https://doi.org/10.1016/S0005-2736(03)00025-7.

(68) Taglialegna, A.; Lasa, I.; Valle, J. Amyloid Structures as Biofilm Matrix Scaffolds. *J. Bacteriol.* **2016**, *198* (19), 2579–2588. https://doi.org/10.1128/JB.00122-16.

CHAPTER 6

SUMMARY AND FUTURE WORK

The requirement to solubilize and stabilize membrane proteins in aqueous solution is of great interest to both fundamental science and the pharmaceutical industry. Polymer-stabilized nanodiscs present a promising strategy, allowing the solubilization of membrane proteins directly from the cell membrane, whilst maintaining the presence of annular lipids and imparting a high level of stability.[1–3] Despite the increasing adoption of polymer-stabilized phospholipid nanodiscs for the study of membranes and membrane proteins, their application has outpaced our understanding of the fundamental physicochemical properties which influence nanodisc properties and self-assembly. Only by investigating the fundamental properties of nanodiscs, and nanodisc forming polymers can their application be fully utilized, whilst providing an understanding of limiting factors which could have substantial impact on results obtained using these systems. The data presented throughout this thesis has aimed to address this imbalance, whilst highlighting potential novel applications for polymer-stabilized phospholipid nanodiscs.

The most commonly utilized nanodisc-forming polymer to date has been poly(styrene-*co*-maleic acid) (SMA) containing a 2:1 ratio of styrene to maleic acid. The two commercially available varieties of SMA(2:1) are SMA2000 (Cray Valley) and Xiran SZ30010 (Polyscope), which differ in their chain length and molecular weight distribution. A thermodynamic model describing nanodisc self-assembly, first proposed by Vargas *et al.*, has been successfully applied to SMA(3:1)[4] and the Xiran SZ30010 SMA(2:1).[5] Chapter 2 provides the first thermodynamic description of nanodisc self-assembly by SMA2000. In an attempt to deconvolute the structural properties of polymers which influence nanodisc self-assembly, an SMA(2:1) polymer with a defined monomer sequence and controlled size distribution

was produced by reversible addition-fragmentation chain transfer (RAFT) polymerization. Comparison of the thermodynamics of nanodisc self-assembly mediated by SMA2000 and RAFT-SMA showed that in both cases nanodisc self-assembly is driven by the large negative Gibbs energy change associated with polymers during nanodisc formation. In comparison to previous studies, SMA2000 is the most thermodynamically efficient commercially available copolymer amongst those investigated to date. RAFT-SMA, however, displayed a substantially larger negative Gibbs free energy change indicating a more thermodynamically favourable process. However, this increased thermodynamic efficiency does not correlate with the efficiency of membrane protein extraction from biological membranes, where RAFT-SMA is less effective than SMA2000. This is potentially due to the presence of a poly(styrene) tail in RAFT-SMA. This is likely to protrude into the acyl chain core of the polymer-encapsulated bilayer, leading to interactions with hydrophobic, membrane-spanning regions of membrane proteins which could disrupt membrane protein solubilization. Combined with previous work,[6,2,7,8] these results suggest an interplay between various polymer structural properties which can influence nanodisc self-assembly. In order to fully understand the influence of polymer structure on nanodisc self-assembly, and the apparent disparity between thermodynamic efficiency and efficacy in the solubilization of biological membranes, further studies are required to systematically deconvolute the relative effects of polymer properties.

Furthermore, RAFT-SMA forms nanodiscs with an increased diameter compared to SMA2000. While speculative at this stage, this could be an exploitable property, enabling solubilization of large complexes which would not be accommodated within the bilayer encapsulated by SMA2000. However, in order to confirm the relevance of the apparent increase in diameter of RAFT-SMALPs, determination of the nanodisc structure formed by RAFT-SMA is required in order to determine whether the increased diameter is due to a larger lipid area within the disc or an increased thickness of the polymer belt.

Despite its numerous benefits, SMA is not without limitations. Most notably, SMA is incompatible with low pH or divalent cations, both of which render the polymer insoluble. While chemical modifications to the SMA polymer have been shown to alleviate this issue,[9–14] none are commercially

available and have not been shown to extract membrane proteins from native cell membranes. Chapter 3 investigates the use of a commercially available poly(styrene-*co*-maleimide) (SMI) copolymer in nanodisc self-assembly under acidic conditions. SMI is capable of solubilizing phospholipids into nanodiscs with increased thermodynamic efficiency compared to SMA whilst remaining soluble in the presence of low pH or divalent cations. Furthermore, SMI is functional in extraction of membrane proteins from *E. coli* membranes at low pH. However, SMI is less efficient than SMA2000 when solubilizations are performed at neutral pH. This identifies a similar trend to that observed in Chapter 2, whereby an improved thermodynamic efficiency does not necessarily correlate with improved efficiency in the solubilization of biological membranes.

Interestingly, nanodiscs formed by SMI (SMILPs) show a decreased diameter compared to SMALPs, where SMILP diameter can be controlled, to an extent, by variation of the polymer:lipid ratio during solubilization. From the data presented in Chapter 3, it is unclear in what manner SMI is stabilizing membrane proteins in solution. If the diameter of SMILPs remains constant upon the incorporation of membrane proteins, then only proteins with small transmembrane regions would be accommodated. As SDS-PAGE showed no selectivity towards molecular weight, it may be the case that SMI is functioning more as an amphipol when in the presence of protein. To determine between a nanodisc *vs* amphipol mode of action, various strategies could be applied. For example, lipid profiling of purified SMILP-solubilized proteins using mass spectrometry or thin layer chromatography would allow detection of lipid species which have been co-extracted with the membrane protein of interest, suggesting a nanodisc model. Furthermore, structural studies using small-angle neutron scattering (SANS) or cryo-electron microscopy would allow for identification of density corresponding to lipid and/or polymer in addition to encapsulated protein, which would definitively confirm the mode of action of SMI.

To date, polymer-stabilized nanodiscs have been considered to represent a static snapshot of the cell membrane environment. However, in attempting to align SMALP nanodiscs at lipid interfaces, lipids were observed to rapidly exchange between nanodiscs in solution and interfacial lipids without adsorption.[15] While lipid exchange between SMALPs in solution has been investigated in more

detail,[16,17] the initial observation raises important questions. Notably, what physicochemical properties of SMALPs lead to lipid exchange instead of adsorption and do nanodiscs formed using different polymers interact differently with interfacial membranes?

Chapter 4 addresses these questions by investigating the interactions between nanodiscs formed of the polymers characterized in Chapters 2 and 3 and interfacial phospholipid membranes. We were able to determine that all nanodiscs investigated exchange phospholipids with the interfacial lipids. However, we also obtained evidence of polymers embedding into the interfaces in addition lipid exchange. These data challenge the viewpoint of SMALP nanodiscs representing a kinetically trapped snapshot of the cell membrane environment. Polymer presence within interfacial membranes suggests that the nanodiscs disassemble and re-assemble in a dynamic equilibrium, partitioning amongst the available lipid within a system. Therefore, it remains to be seen as to what extent SMALP-solubilized proteins retain their native lipid environment. While it is possible that specifically bound lipids will not exchange between nanodiscs, this is purely speculative at this stage. In this regard, the slower exchange kinetics observed with RAFT-SMA could be utilized to minimize the lipid exchange and allowing analysis of the native-like lipid environment. Conversely, polymers which exhibit increased lipid exchange, such as SMA2000, could be utilized to change the lipid environment of SMALP-solubilized protein in order to investigate the influence of lipid composition of protein structure and function.

The most surprising observation was that of RAFT-SMALPs, which adsorb to supported phospholipid bilayers at the Si-water interface. While lipid exchange between the adsorbed nanodiscs and the supported bilayer was also observed, these data present the possibility of utilizing RAFT-SMALPs for structural studies of nanodisc-encapsulated membrane proteins at interfaces. While this has been achieved using MSP-nanodiscs, it remains to be seen whether protein incorporation within RAFT-SMALPs will interfere with their interfacial adsorption. Furthermore, these results have potential pharmaceutical relevance. As RAFT-SMALPs adsorb to supported phospholipid bilayers, this could be utilized for interaction studies in drug screening measurements, using surface-sensitive techniques.

As a final aspect, Chapter 5 demonstrates the first application of SMALP nanodiscs used as a soluble membrane surface, allowing investigation of protein-lipid interactions. The bacterial lipoprotein YraP was used as a test case. While YraP is well structurally characterized in the absence of membranes, and preliminary evidence supports the capability of YraP to bind specific phospholipid headgroups, its function remains unknown. Unexpectedly, a combination of synchrotron radiation circular dichroism spectroscopy (SRCD) and SANS revealed that YraP undergoes large-scale structural rearrangements upon membrane interaction. Best fits to SANS data were obtained using a an elongated cylinder model. Changes to the secondary structure of YraP from SRCD indicated a gain in ß-sheet content. This led to the hypothesis that YraP forms amyloid-like fibrils upon interaction with a membrane, which may play roles in bacterial cell division. While our *in vitro* data supports this hypothesis, the precise mode of interaction of YraP with membranes could not be determined. In order to provide a more detailed structural model, ultra-small-angle neutron scattering (USANS) would be required in order to measure at small enough Q values to observe the largest dimension of the particles. However, obtaining precise structural models could still be hampered by the difficulty in obtaining an accurate form factor describing the YraP-SMALP complex and components thereof. Therefore, direct imaging methods such as cryo-electron microscopy would be required to determine the precise interaction between YraP and SMALP nanodiscs whilst also providing more detail on the tertiary and quaternary structural changes occurring.

Regardless of the precision of any structural models obtained *in vitro*, the relevance of YraP fibrilization to its *in vivo* function remains unknown. The observation, or lack thereof, of YraP fibers in living cells will provide important evidence as to the biological relevance of the *in vitro* models obtained in this study. Furthermore, it remains unknown what membrane properties, aside from phospholipid composition, can modulate the YraP-membrane interaction. X-ray and neutron scattering, combined with calorimetric measurements would be able to identify binding affinities of YraP for various model membranes whilst being able to observe any YraP-induced perturbations to the membrane structure or bilayer integrity.

In summary, results presented in this study provide answers to some important questions regarding the application of polymer stabilized nanodiscs for membrane and membrane protein research, whilst opening up further avenues of research which could benefit from polymer-stabilized phospholipid nanodiscs.

6.1 REFERENCES

(1) Knowles, T. J.; Finka, R.; Smith, C.; Lin, Y.-P.; Dafforn, T.; Overduin, M. Membrane Proteins Solubilized Intact in Lipid Containing Nanoparticles Bounded by Styrene Maleic Acid Copolymer. *J. Am. Chem. Soc.* **2009**, *131* (22), 7484–7485.

(2) Morrison, K. A.; Akram, A.; Mathews, A.; Khan, Z. A.; Patel, J. H.; Zhou, C.; Hardy, D. J.; Moore-Kelly, C.; Patel, R.; Odiba, V.; et al. Membrane Protein Extraction and Purification Using Styrene-Maleic Acid (SMA) Copolymer: Effect of Variations in Polymer Structure. *Biochem. J.* **2016**, *473* (23), 4349–4360.

(3) Lee, S. C.; Knowles, T. J.; Postis, V. L. G.; Jamshad, M.; Parslow, R. A.; Lin, Y.-P.; Goldman, A.; Sridhar, P.; Overduin, M.; Muench, S. P.; et al. A Method for Detergent-Free Isolation of Membrane Proteins in Their Local Lipid Environment. *Nat. Protoc.* **2016**, *11* (7), 1149–1162.

(4) Vargas, C.; Arenas, R. C.; Frotscher, E.; Keller, S. Nanoparticle Self-Assembly in Mixtures of Phospholipids with Styrene/Maleic Acid Copolymers or Fluorinated Surfactants. *Nanoscale* **2015**, *7* (48), 20685–20696.

(5) Grethen, A.; Oluwole, A. O.; Danielczak, B.; Vargas, C.; Keller, S. Thermodynamics of Nanodisc Formation Mediated by Styrene/Maleic Acid (2:1) Copolymer. *Sci. Rep.* **2017**, *7* (1), 11517.

(6) Scheidelaar, S.; Koorengevel, M. C.; Pardo, J. D.; Meeldijk, J. D.; Breukink, E.; Killian, J. A. Molecular Model for the Solubilization of Membranes into Nanodisks by Styrene Maleic Acid Copolymers. *Biophys. J.* **2015**, *108* (2), 279–290.

(7) Dominguez Pardo, J. J.; Dörr, J. M.; Renne, M. F.; Ould-Braham, T.; Koorengevel, M. C.; van Steenbergen, M. .; Killian, J. A. Thermotropic Properties of Phosphatidylcholine Nanodiscs Bounded by Styrene-Maleic Acid Copolymers. *Chem. Phys. Lipids* **2017**, *208*, 58–64.

(8) Domínguez Pardo, J. J.; Koorengevel, M. C.; Uwugiaren, N.; Weijers, J.; Kopf, A. H.; Jahn, H.; van Walree, C. A.; van Steenbergen, M. J.; Killian, J. A. Membrane Solubilization by Styrene-Maleic Acid Copolymers: Delineating the Role of Polymer Length. *Biophys. J.* **2018**, *115* (1), 129–138.

(9) Ravula, T.; Ramadugu, S. K.; Di Mauro, G.; Ramamoorthy, A. Bioinspired, Size-Tunable Self-Assembly of Polymer-Lipid Bilayer Nanodiscs. *Angew. Chem. Int. Ed Engl.* **2017**, *56* (38), 11466–11470.

(10) Ramadugu, V. S. K.; Mauro, G. M. D.; Ravula, T.; Ramamoorthy, A. Polymer Nanodiscs and Macro-Nanodiscs of a Varying Lipid Composition. *Chem. Commun.* **2017**, *53* (78), 10824–10826.

(11) Ravula, T.; Hardin, N. Z.; Ramadugu, S. K.; Ramamoorthy, A. PH Tunable and Divalent Metal Ion Tolerant Polymer Lipid Nanodiscs. *Langmuir* **2017**, *33* (40), 10655–10662.

(12) Yasuhara, K.; Arakida, J.; Ravula, T.; Ramadugu, S. K.; Sahoo, B.; Kikuchi, J.; Ramamoorthy, A. Spontaneous Lipid Nanodisc Fomation by Amphiphilic Polymethacrylate Copolymers. *J. Am. Chem. Soc.* **2017**, *139* (51), 18657–18663.

(13) Oluwole, A. O.; Klingler, J.; Danielczak, B.; Babalola, J. O.; Vargas, C.; Pabst, G.; Keller, S. Formation of Lipid-Bilayer Nanodiscs by Diisobutylene/Maleic Acid (DIBMA) Copolymer. *Langmuir* **2017**, *33* (50), 14378–14388.

(14) Ravula Thirupathi; Hardin Nathaniel Z.; Ramadugu Sudheer Kumar; Cox Sarah J.; Ramamoorthy Ayyalusamy. Formation of PH-Resistant Monodispersed Polymer–Lipid Nanodiscs. *Angew. Chem. Int. Ed.* **2018**, *57* (5), 1342–1345.
(15) Hazell, G.; Arnold, T.; Barker, R. D.; Clifton, L. A.; Steinke, N.-J.; Tognoloni, C.; Edler, K. J. Evidence of Lipid Exchange in Styrene Maleic Acid Lipid Particle (SMALP) Nanodisc Systems. *Langmuir* **2016**, *32* (45), 11845–11853.
(16) Cuevas Arenas, R.; Danielczak, B.; Martel, A.; Porcar, L.; Breyton, C.; Ebel, C.; Keller, S. Fast Collisional Lipid Transfer Among Polymer-Bounded Nanodiscs. *Sci. Rep.* **2017**, *7*, 45875.
(17) Grethen, A.; Glueck, D.; Keller, S. Role of Coulombic Repulsion in Collisional Lipid Transfer Among SMA(2:1)-Bounded Nanodiscs. *J. Membr. Biol.* **2018**, *251* (3), 443–451.

APPENDIX A

SUPPLEMENTARY INFORMATION FOR CHAPTER 2: INFLUENCE OF POLY(STYRENE-*CO*-MALEIC ACID) COPOLYMER STRUCTURE ON THE PROPERTIES AND SELF-ASSEMBLY OF SMALP NANODISCS

A.1 SUPPLEMENTARY METHODS

A.1.1 Polymer Hydrolysis

Both coSMAnh and altSMAnh were hydrolyzed from the anhydride forms to the acid forms using a previously published procedure [1]. In brief, a 10 % (w/v) solution of SMAnh in 1 M sodium hydroxide was prepared by stirring overnight and then heating under reflux for 2 h. After cooling, the copolymer was precipitated with conc. HCl and washed three times with water. The product was re-dissolved in 0.6 M NaOH and the precipitation and washing procedure repeated before dissolving in a minimal volume of 0.6 M NaOH and adjusting to pH 8.0. The final product was freeze dried. Stock solutions were prepared from the dry powder and the concentrations determined by constructing a calibration curve of UV-absorbance at 254 nm for polymer solutions of known concentration (Figure S3).

A.1.2 Dynamic light scattering data analysis

DLS data were analyzed after taking into account the viscosity and refractive index of all buffer constituents. A non-negatively constrained least squared function was fit to the measured autocorrelation function. This gives an intensity weighted particle size distribution (PSD), assuming spherical particles, which is converted to a volume weighted PSD using Mie scattering theory [2,3]. A volume weighted PSD takes into account the increased scattering of light by larger particles to give a more realistic

representation of the particles present. Cumulant analysis was also performed to obtain the Z-average diameter and polydispersity index (PDI) [4]. It is worth noting that in DLS, the PDI is defined as the square of the ratio of the peak value to the width of the Gaussian distribution obtained from cumulant analysis.

A.1.3 SEC-MALS data analysis

To analyze the MALS data, we have assumed that the majority of the scattering volume in SMALPs is occupied by DMPC. This assumption allows us to use the literature value of the refractive index increment, *dn/dc*, of 0.16 [5] and thereby calculate the mass of the particles. This is the only way that the mass can be extracted from this data since the refractive index increment of SMA is unknown. We do, however, have a good estimate for the number of lipids per nanodisc (from SANS data [6]) and can compare this to the total volume of a nanodisc (also from SANS). This estimation suggests that lipids do indeed occupy 77 % of the total volume of the nanodiscs and so the basis of our assumption is valid. As a result, the masses quoted are an estimation and equivalent to particles comprised purely of DMPC. Hydrodynamic radius was also calculated by analyzing the experimentally measured autocorrelation function by cumulant analysis to give a Z-average R_h. Molar Mass was calculated using ASTRA software (Wyatt Technologies, Suffolk, UK) by combining Rayleigh-Gans-Debye scattering theory into the Zimm equation [7,8]:

$$\frac{K^*c}{R(\theta,c)} = \frac{1}{M_w P(\theta)} + 2A_2c$$

The Zimm equation describes the relationship between the concentration of solute, *c*, the second virial coefficient in the virial expansion for osmotic pressure, A_2 (describing the Brownian motion of solute particles), the excess Rayleigh ratio of the solution, *R(θ,c),* the molar mass of the solute, M_w, the angular dependence of scattered light, *P(θ)* and the constant K^*. K^* describes the refractive index increment, dn/dc, for a given wavelength of incident light, λ_0, where:

$$K^* = \frac{4\pi^2(\frac{dn}{dc})^2 {n_0}^2}{N_a {\lambda_0}^4}$$

A global fit to the Zimm equation is applied across all measured angles to yield the molar mass of the solute. In contrast to DLS measurements, in static light scattering experiments, PDI is defined as the ratio of M_w/M_n determined using the MALS measurement.

A.1.4 Isolation of *E. coli* BL21 (DE3) membranes

E.coli BL21 (DE3) cultures were inoculated from a single colony on an LB-agar plate and grown in 15 mL LB at 37 °C for 16 hours. A 1 % (v/v) inoculum was used to inoculate 1 L LB. This culture was grown at 37 °C until stationary phase was reached, monitored by measuring absorbance at 600 nm. Cells were isolated by centrifugation at 7000 × *g* for 10 minutes at 4 °C. Pelleted cells were washed in PBS and resuspended in 3.5 mL lysis buffer (50 mM Tris, 5 % (w/v) glycerol, 2 mM EDTA pH 7.5 containing 1 Pearce EDTA-free protease inhibitor tablet per 50 mL) per gram of cells at 4 °C. Cells were lysed by 5 passes through an Emmulsiflex C3 cell disruptor at 4 °C. Cell debris was removed by centrifugation at 11000 × *g* for 30 minutes at 4 °C. Supernatant was removed and membranes isolated by centrifugation at 100000 × *g* for 60 minutes at 4 °C. Supernatant was removed and membranes weighed.

A.2 SUPPLEMENTARY DATA

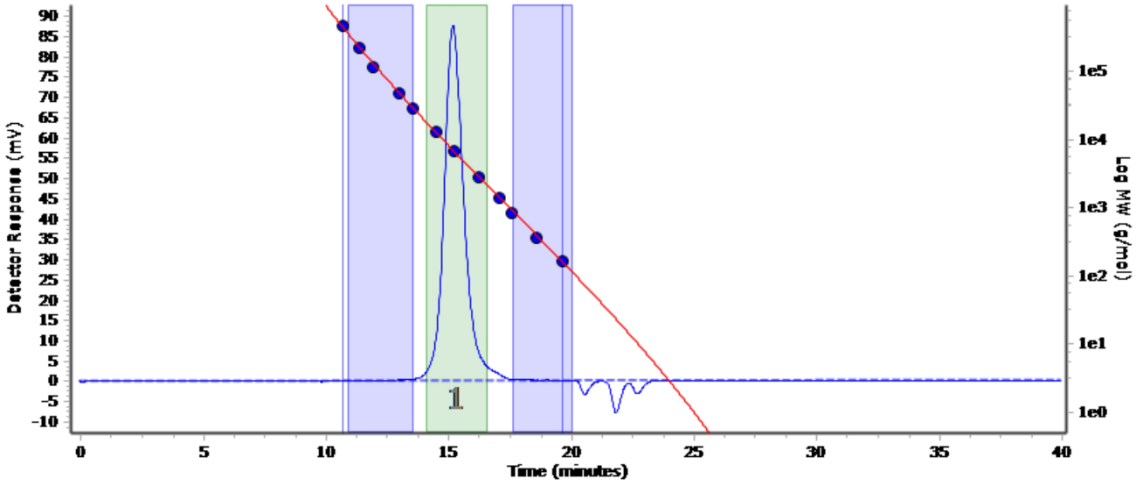

Figure A.1 A SEC chromatogram showing the retention time of RAFT-synthesized altSMAnh compared to polystyrene standards (red line, blue points). The altSMAnh has a number average molecular weight, M_n, of 6.0 kDa, a mass averaged molecular weight, M_w, of 6.8 kDa and a polydispersity index, PDI, of 1.13. SEC was carried out on an Agilent Technologies 1260 Infinity using THF at a flow rate of 1 cm^3 min^{-1} at 35 °C with refractive index detection and calibration with polystyrene standards.

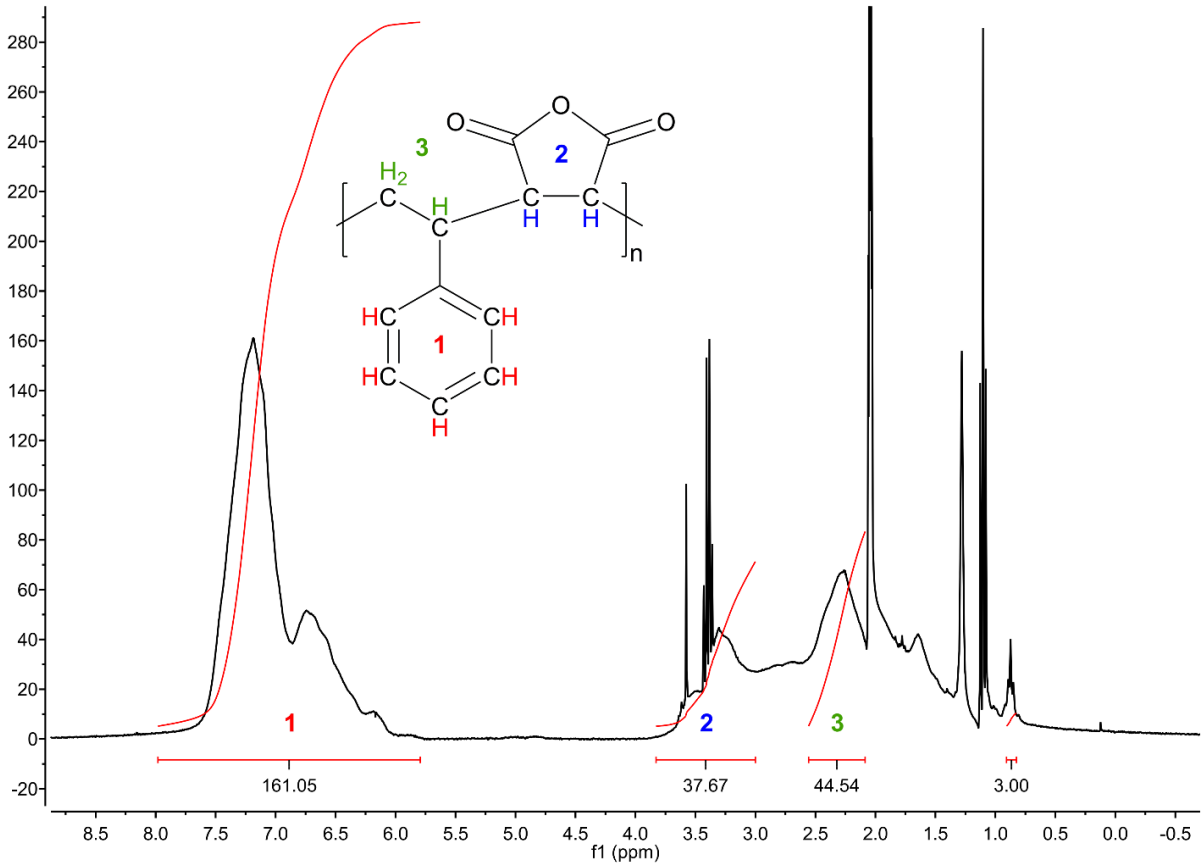

Figure A.2. The ^{1}H-NMR spectrum displays three prominent peaks associated with the polymer. The peak at 2.05 ppm is due to acetone. Peaks appearing downfield of 5.5 ppm have been assigned to protons bound to aromatic carbons, designated region 1. Peaks appearing between 0 – 4 ppm appear due to protons present in aliphatic regions. Protons present on the maleic anhydride moiety have been assigned to region 2, while the aliphatic protons of styrene have been assigned to region 3. Sharp peaks upfield of the d-acetone solvent peak are due to a combination of unreacted monomeric styrene and maleic anhydride and the DDMAT RAFT termination. The ratio of styrene:maleic anhydride can be estimated by taking the ratio of integrals for one aromatic proton on styrene to one aliphatic proton on maleic anhydride. This yields a ratio of 1.7:1, which is close to the predicted 2:1 ratio given that the spectrum will underestimate the amount of maleic anhydride.

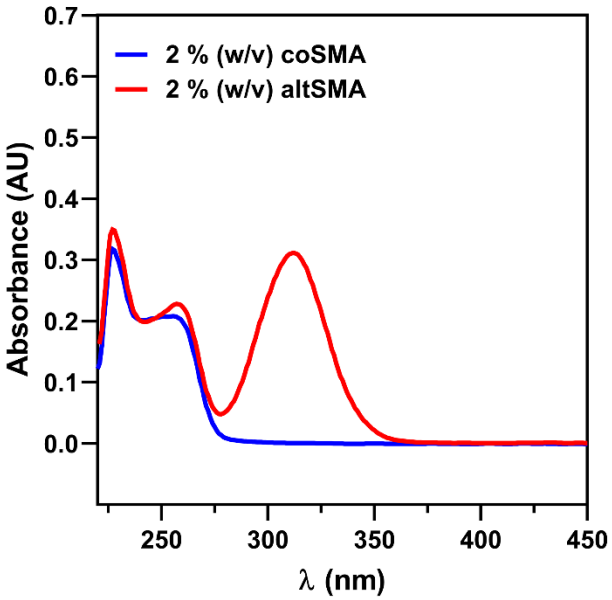

Figure A.3. UV-Vis spectra of 2 % (w/v) coSMA and altSMA recorded against a background collected on 50 mM NaH_2PO_4 pH 8, 0.2 M NaCl. The spectra of both polymers show a peak at 254 nm, due to the presence of styrene [9] which was used to determine the concentration of polymer and nanodiscs present compared to the A_{254} value of polymer solutions of known concentrations. The additional peak at 312 nm for altSMA is due to the $\pi \rightarrow \pi^*$ electronic transition of the C═S double bond present in the trithiocarbonate RAFT end group [10]

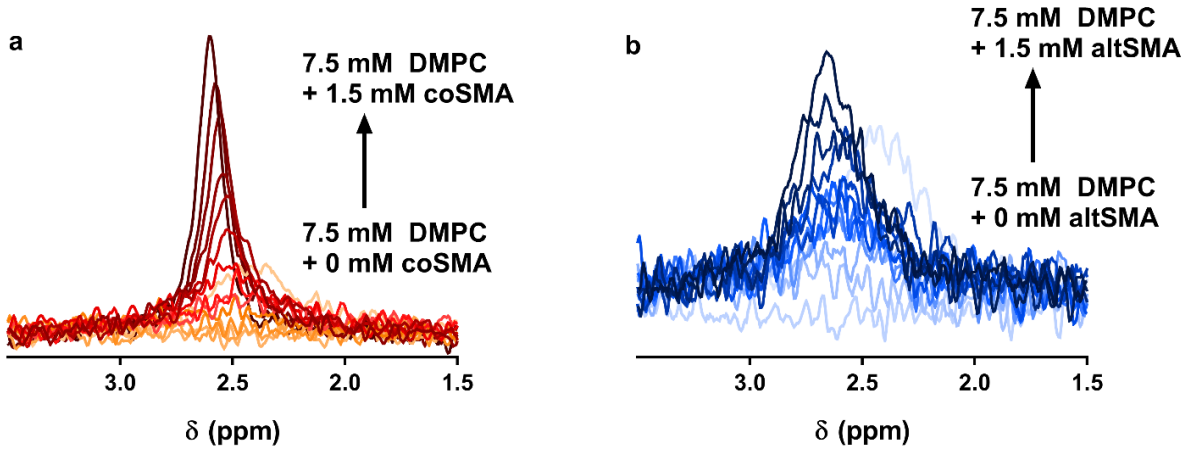

Figure A.4. Representative ^{31}P NMR spectra showing the increase in peak area and slight chemical shift induced in response to increasing coSMA (a) and altSMA (b) concentrations added to 7.5 mM DMPC small unilamellar vesicle (SUV) suspensions.

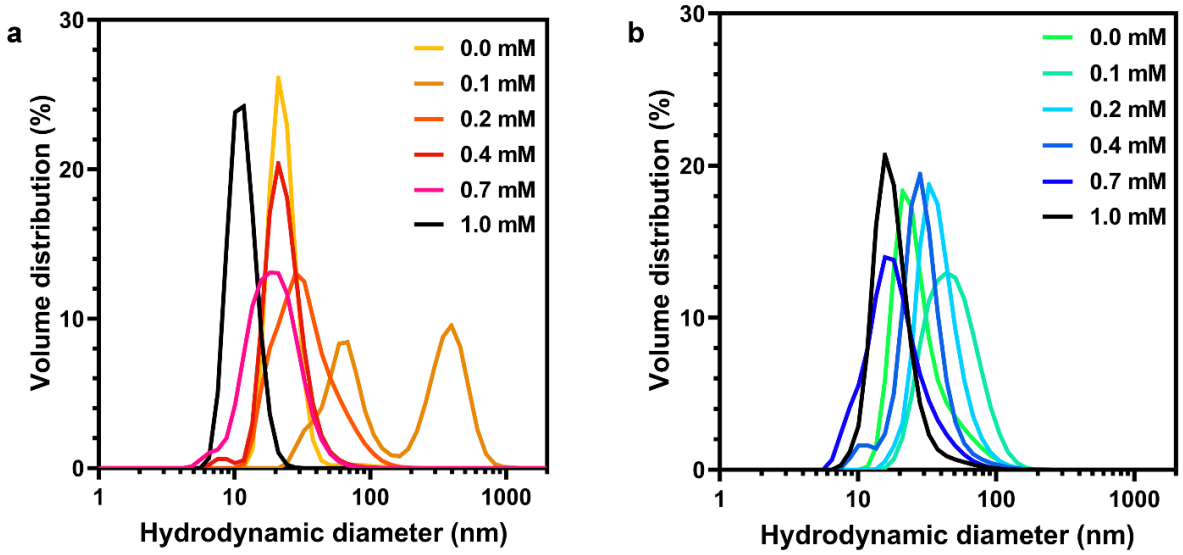

Figure A.5. Volume weighted PSD data for coSMA (a) and altSMA (b) concentrations below c_s^{SOL}. Lines represent the mean PSD of three separate experiments, each measured in triplicate. Error bars are not shown for clarity. In both cases, addition of 0.1 mM coSMA (a) or altSMA (b) induces aggregation of the lipids to larger particles. This effect is most noticeable for coSMA, where a highly polydisperse distribution of particles is observed. In both cases, as c_s^{SOL} is approached, lipid aggregates become solubilized as the PSD starts to shift towards smaller diameters. At c_s^{SOL}, a sharp peak is observed for both polymers (black line), representing the completion of solubilization

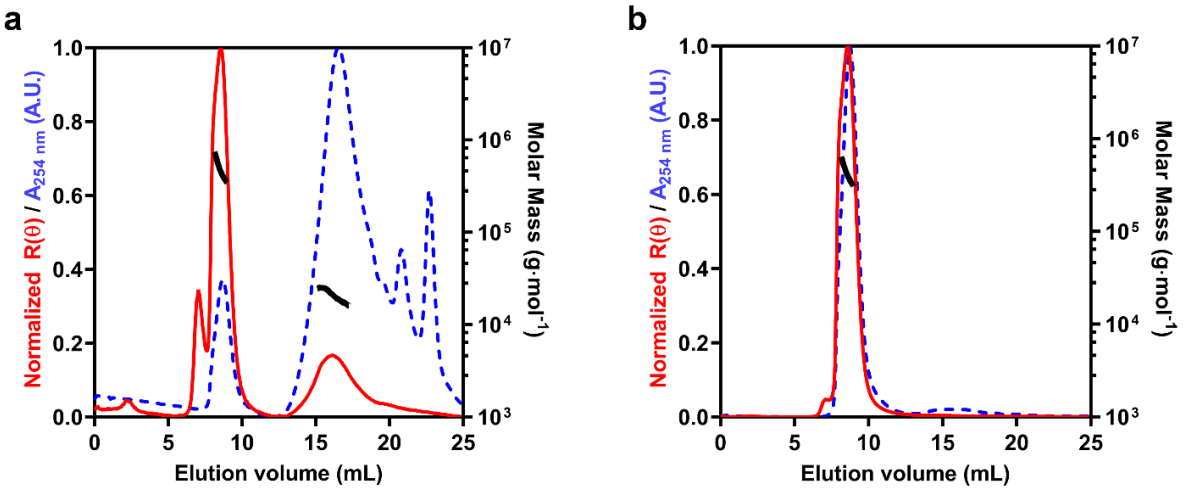

Figure A.6. Normalized Rayleigh ratio (R(θ), red trance), normalized UV absorbance at 254 nm ($A_{254\ nm}$, blue dashed trace) with overlaid molar mass calculations (black trace) for 1.5 % (w/v) coSMA (a), and 1.5 % (w/v) altSMA (b) in the absence of lipid. coSMA forms a large aggregate in the absence of lipid. This peak is detected by light scattering but also contains substantial UV absorbance, unlike the aggregate peak seen with coSMALPs. This suggests coSMA forms larger structures in solution which are re-structured into nanodiscs upon interaction with phospholipids. In addition, a peak eluting at a larger volume is also observed which also persists after SMALP self-assembly. This supports our peak assignments in Figure 4. The peak which we have assigned to coSMALPs is not present (at ~ 12 mL elution volume) and the peak eluting at 17 mL is still present, in agreement that this peak is due to bundled, extended polymer chains. Interestingly, in the absence of lipids, altSMA also forms a large polymer aggregate which elutes at the same volume as the self-assembled altSMALPs. We suggest this is a spherical, micellar-like particle, based on the R_g/R_h ratio, which re-structures to form a nanodisc upon interaction with phospholipids.

Table A.1. Parameters determined from analysis of SEC-MALS data of coSMA and altSMA in the absence of phospholipids shown in Figure 2.6

`	**coSMA**		**altSMA**
Peak elution volume (mL)	8.5 mL	16.5 mL	8.5 mL
Hydrodynamic diameter (nm)	18.64 ± 0.49	3.68 ± 0.44	17.72 ± 0.10
R_g **(nm)**	14.00 ± 0.90	Insufficient scattering intensity	5.60 ± 0.41
R_g/R_h	1.50 ± 0.07	Insufficient scattering intensity	0.63 ± 0.07
M_w **(kDa)**	460.70 ± 1.35	20.52 ± 2.51	409.40 ± 0.21
M_n **(kDa)**	441.30 ± 1.40	20.07 ± 2.52	393.40 ± 0.20
$Đ$	1.04 ± 0.01	1.02 ± 0.01	1.04 ± 0.01

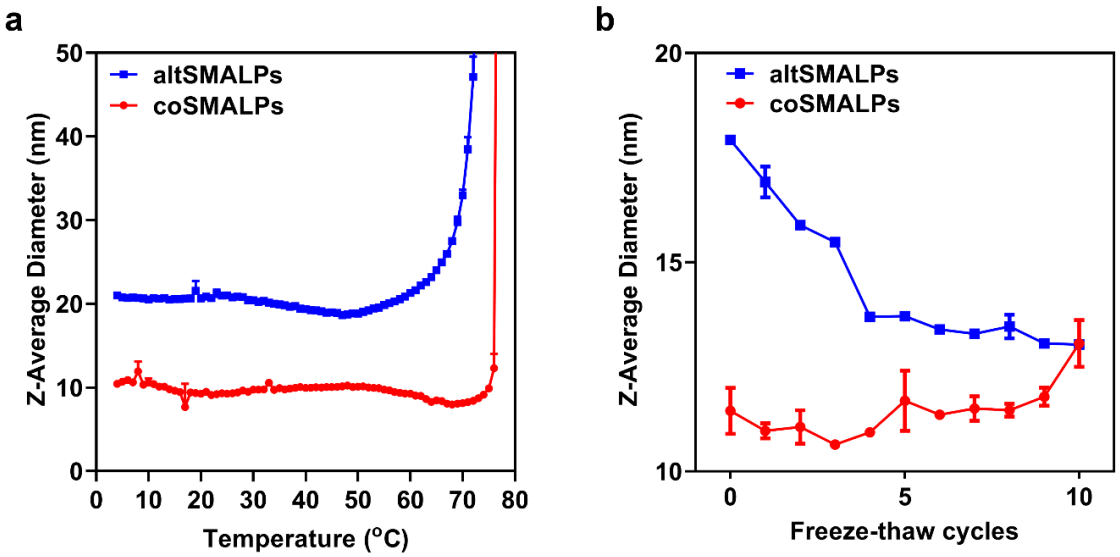

Figure A.7. DLS data showing the effect of exposing DMPC SMALPs to elevated temperature (a) and multiple freeze-thaw cycles (b) on the Z-average diameter. These data are shown in Figure 2.5 and plotted here as absolute Z-average diameters, with each point representing the mean of three separate experiments with error bars representing ± 1 standard error.

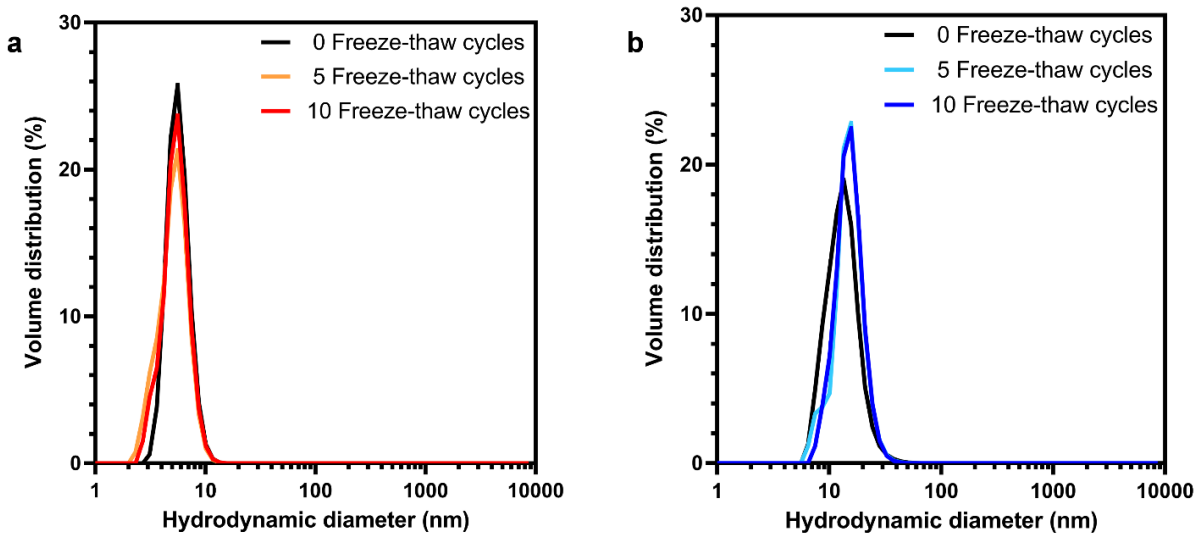

Figure A.8. Volume weighted PSD data for coSMALP (a) and altSMALP (b) DMPC nanodiscs subjected to repeated freeze-thaw cycles. Lines represent the mean PSD of three separate experiments, each measured in triplicate. Error bars are not shown for clarity. These data demonstrate that neither DMPC coSMALPs or altSMALPs aggregate or precipitate upon repeated freeze-thaw cycles.

A.3 SUPPLEMENTARY REFERENCES

(1) Lee, S. C.; Knowles, T. J.; Postis, V. L. G.; Jamshad, M.; Parslow, R. A.; Lin, Y.-P.; Goldman, A.; Sridhar, P.; Overduin, M.; Muench, S. P.; et al. A Method for Detergent-Free Isolation of Membrane Proteins in Their Local Lipid Environment. *Nat. Protoc.* **2016**, *11* (7), 1149–1162.

(2) Mie, G. Beiträge Zur Optik Trüber Medien, Speziell Kolloidaler Metallösungen. *Ann. Phys.* **1908**, *330* (3), 377–445.

(3) Hassan, P. A.; Rana, S.; Verma, G. Making Sense of Brownian Motion: Colloid Characterization by Dynamic Light Scattering. *Langmuir* **2015**, *31* (1), 3–12.

(4) Koppel, D. E. Analysis of Macromolecular Polydispersity in Intensity Correlation Spectroscopy: The Method of Cumulants. *J. Chem. Phys.* **1972**, *57* (11), 4814.

(5) Theisen, A.; Johann, C.; Deacon, M. P.; Harding, S. E. *Refractive Increment Data-Book for Polymer and Biomolecular Scientists*; Nottingham University Press: Nottingham, UK, 2000.

(6) Jamshad, M.; Grimard, V.; Idini, I.; Knowles, T. J.; Dowle, M. R.; Schofield, N.; Sridhar, P.; Lin, Y.; Finka, R.; Wheatley, M.; et al. Structural Analysis of a Nanoparticle Containing a Lipid Bilayer Used for Detergent-Free Extraction of Membrane Proteins. *Nano Res.* **2015**, *8* (3), 774–789.

(7) Zimm, B. H. The Scattering of Light and the Radial Distribution Function of High Polymer Solutions. *J. Chem. Phys.* **1948**, *16* (12), 1093.

(8) Wyatt, P. J. Light Scattering and the Absolute Characterization of Macromolecules. *Anal. Chim. Acta* **1993**, *272* (1), 1–40.

(9) Talrose, V.; Yermakov, A. N.; Usov, A. A.; Goncharova, A. A.; Leskin, A. N.; Messineva, N. A.; Trusova, N. V.; Efimkina, M. V. UV/Visible Spectra. In *NIST Chemistry WebBook*; Linstrom, P. J., Mallard, W. G., Eds.; NIST Standard Reference Database; National Institute of Standards and Technology: Gaithersburg MD, 20899.

(10) McKenzie, T. G.; Fu, Q.; Wong, E. H. H.; Dunstan, D. E.; Qiao, G. G. Visible Light Mediated Controlled Radical Polymerization in the Absence of Exogenous Radical Sources or Catalysts. *Macromolecules* **2015**, *48* (12), 3864–3872.

APPENDIX B

SUPPLEMENTARY INFORMATION FOR CHAPTER 3: AN ACID COMPATIBLE COPOLYMER FOR THE SOLUBILIZATION OF MEMBRANES AND PROTEIN INTO LIPID BILAYER-CONTAINING NANOPARTICLES

B.1 SUPPLEMENTARY METHODS

B.1.1 Negative stain transmission electron microscopy (TEM)

400 mesh carbon coated Cu grids were glow discharged twice for 15 seconds with a 15 second pause between charges. SMILP solutions were diluted to 0.1 mg/mL DMPC, 0.03 % w/v SMI in 50 mM NaOAc, 200 mM NaCl, pH 5 and centrifuged at 16,000 × *g* for 10 minutes to remove particulate contaminants. 5 µL of diluted SMILP solutions were added to the glow discharged grids and allowed to adsorb for 1 minute. The grids were washed three timed with ultra-pure water and stained twice successively for 1 minute with 1 % w/v phosphotungstic acid. Excess liquid was removed from the grids at each stage by blotting with filter paper.

Samples were imaged on a Tecnai T20 twin-lens transmission electron microscope (FEI, Cambridgeshire, UK) operating at an accelerating voltage of 200 kV. Images were recorded at a magnification of × 62,000 at -1.5 µm under focus. Images were recorded on an Eagle 4k × 4k CCD camera (FEI, Cambridgeshire, UK).

Subsequent image analyses were carried out in ImageJ (FIJI). A total of 1038 particles were analyzed from micrographs where staining was of high quality to allow for reliable particle picking.

B.1.2 Small angle X-ray scattering (SAXS)

SMILP samples were prepared as described above, at a final solution concentration of 1.5 wt% SMI, with 3, 5 or 7 mg/ml DMPC in a pH 5 acetate buffer containing 0.2 M NaCl. Samples were not gel filtered prior to measurement. SMILP solutions, a solution of the SMI polymer alone at 1.5 % (w/v) in the same buffer and the buffer were placed in a 96-well plate at 25 °C, and loaded into the Arinax BioSAXS robot sample changer on the SAXS beamline B21 at Diamond Light Source. Solutions were measured using the standard beamline configuration, at 12.4 keV, in a 1mm diameter quartz capillary, that was automatically washed, dried, and flushed with buffer before each measurement. Measurements were taken as 60 frames of 1 second using a Pilatus 2K detector. The buffer solution was measured before and after each sample solution in the same capillary, and background scattering was subtracted from the data. Data was measured over a Q range of 0.008 to 0.4 $Å^{-1}$, calibrated using silver behenate and reduced using the data reduction pipeline in DAWN[1].

B.1.3 Fitting of SAXS data

The data were fitted in the NIST SANS Analysis package (reference: Kline, S. R., Reduction and Analysis of SANS and USANS Data using Igor Pro. J Appl. Cryst. 2006, 39 (6), 895.) within Igor Pro (Wavemetrics) to a summed model consisting of one component to account for scattering from the SMILPs, and one from free polymer in solution. The solutions were not gel filtered prior to measurement but subsequent gel filtration measurements indicated the presence of free polymer. Therefore, scattering from the polymer in solution, which had been measured separately under the same buffer, salt and polymer concentrations (0.2 M NaCl, 50 mM acetate buffer, 1.5 % (w/v) polymer) was added to the scattering from the SMILPs. The dimensions of the polymer aggregates in polymer-only solutions in the same buffer were initially fitted to an ellipse model[2]. The values obtained for the radii of the polymer-only aggregates were then initially held during fitting of the scattering from the SMILP solutions. The scale factor (proportional to the relative concentration of these polymer-only objects) was allowed to vary. The SMILP component of the scattering was fitted to the polydisperse core-shell bicelle model[3] previously used for fitting scattering data from SMALPs[4]. This model, shown in Figure B.3, contains a central cylindrical lipid bilayer region (core) modeled as an inner cylinder region composed of the lipid

tails, with a layer at each end corresponding to the hydrated lipid headgroups. The hydrated polymer encircling the lipid bilayer is modelled as a concentric cylindrical layer (belt), extending the full height of the tail region of the bilayer but not covering the headgroup layers. As final refinement of the fitting, parameters for scale and bicelle model were held and parameters of the ellipsoid allowed to vary. The size of the polymer aggregates decreased compared to those of the free polymer alone in solution, which is expected: due to the loss of some of the polymer into the nanodiscs. The amount of free polymer in solution therefore decreased, decreasing the size of the structures.

During fitting as many parameters as possible were pre-calculated and held, to reduce the number of free parameters in the model. The scattering length density of the SMI polymer, the lipid tails, lipid headgroups and the solvent were all calculated and held during fitting (see Table B.1) while the lipid tail thickness and headgroup thickness were set to values previously determined for DMPC bilayers[5]. The background was set using the observed experimental background at high Q. The fitted parameters were therefore the scale factor for the ellipsoid model corresponding to the free polymer, and for the bicelle model, the scale factor, the core radius, the polydispersity in the core radius, the belt thickness and belt region scattering length density were fitted. Errors in fitted quantities were determined by observing the effect of variation of the fitted parameters and correspond to the amount of variation possible before the quality of the fit became worse, determined by an increase in the minimized chi-squared parameter. From the fitting of the belt region scattering length density it is possible to calculate the hydration of the belt as a linear combination of the scattering length density of both polymer and solvent. The hydration of the polymer belt is found to be ~56%.

B.1.4 Purification of SMALP-solubilized and SMILP-solubilized *E. coli* ZipA

Expression and purification of ZipA protein using SMA 2000 polymer was carried out as described previously[6]. Briefly, ZipA was overexpressed in BL21 E.coli, membranes harvested and solubilized at 30 mg/ml wet weight with 2.5% (w/v) SMA 2000 in buffer A (20mM Tris, 150mM NaCl, pH 8.0). Solubilized protein was harvested by ultracentrifugation (100,000g, 20 min, 4°C), and mixed with Ni-NTA resin (100 µl bed volume per ml solubilized protein) overnight at 4°C. Resin was washed 5 times

with 10 bed volumes of buffer A supplemented with 20mM imidazole, then twice with 10 bed volumes of buffer A supplemented with 40mM imidazole. ZipA was eluted in 6 fractions of 0.5 bed volume using buffer A supplemented with 200mM imidazole. Solubilization and purification using SMI 2000 was the same except that all buffers were at pH 6.5 and the concentration of NaCl was increased to 300mM. Elution fractions were analyzed by SDS-PAGE as described above.

B.1.5 HEK 293T cell culture and transfection

HEK 293T cells were routinely cultured in Dulbecco's modified Eagles medium (DMEM) containing L-glutamine (2 mM), D-glucose (4500 mg/l) and sodium pyruvate (1 mM) supplemented with 10 % (v/v) fetal calf serum (FCS) in humidified 5 % (v/v) CO_2 in air at 37 °C. For radioligand binding assays, cells were seeded at a density of ~5 x 10^5 cells/100 mm dish and transfected after 48 h. Transfection was essentially as described previously[7]. Briefly, cells were transfected with either human $A_{2A}R$ or human $V_{1a}R$ cDNA in pcDNA3.1(+) using a mixture of 5 µg DNA, 60 µl polyethyleneimine (10 mM) and 1 ml 5 % glucose solution, which was incubated for 30 min at room temperature before addition to an appropriate final volume of full media. GPCR-expressing HEK 293T cells were used 48 h post-transfection.

B.1.6 Radioligand binding assays

Binding assays with $A_{2A}R$ used [^{3}H]ZM241385 (1 nM) as tracer and for the $V_{1a}R$ [^{3}H]AVP (1 nM) was used as tracer. Non-specific binding was defined in a parallel incubation containing a saturating concentration (1 µM) of unlabeled ZM241385 or AVP, respectively. Radioligand alone (for determining total binding), or radioligand plus unlabeled competing ligand (for determining non-specific binding), was added to the culture medium of HEK 293T cells transiently expressing either $A_{2A}R$ or $V_{1a}R$ 48 h post-transfection and incubated at 37 °C . After incubation for 30 min for $A_{2A}R$-expressing membranes or 90 min for $V_{1a}R$-expressing membranes to establish equilibrium, the medium was removed and cells washed three times with ice-cold PBS. Receptors were SMI-solubilized by addition of 1 ml of 20 mM HEPES, 1 mM EGTA, 1 mM magnesium acetate pH 7.4 with 5 % (w/v) SMI, 5 units/ml of benzonase

supplemented by the Roche cOmplete (EDTA-free) protease inhibitor cocktail and incubated for 1 h at 37 °C before centrifugation at 100,000 x g for 1 h. The extracted A_{2A}R-SMILP and V_{1a}R-SMILP were present in the supernatant. Bound ligand in samples of supernatant was quantified by liquid scintillation counting using a PerkinElmer Tri-Carb 2810 TR liquid scintillation analyzer with HiSafe3 (Perkin Elmer, Wokingham) as cocktail. Specific binding to the SMI-solubilized receptors was calculated by subtracting non-specific binding from total binding.

B.2 SUPPLEMENTARY DATA

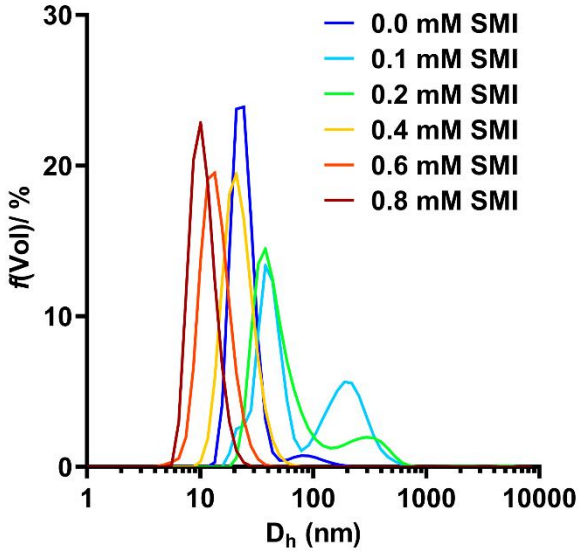

Figure B.1. Volume weighted particle size distribution data measured using DLS at SMI concentrations below the polymer concentration required to initiate solubilization of 7.5 mM DMPC, c_S^{SAT}, the saturation boundary. Before the addition of SMI, DMPC is present as small unilamellar vesicles. Upon addition of low concentrations of SMI below c_S^{SAT} (0.1 mM SMI), SMI induces aggregation of DMPC. As c_S^{SAT} is surpassed, the distribution shifts towards smaller diameters. As c_S^{SOL} is approached, a sharp peak of a smaller hydrodynamic diameter (D_h) appears as the proportion of DMPC present as SMILPs increases.

Table B.1. Fitting parameters used to fit SAXS data of SMILPs to a model of a poly-core bicelle. To account for free polymer in solution, this model was merged with that for an ellipsoid. Parameters marked with * were fixed throughout the fitting procedure.

Model	[DMPC] / mg/mL	7	5	3
	Molar Ratio SMI:DMPC	0.54	0.75	1.26
Poly-core bicelle	Scale	$(2.9 \pm 0.5) \times 10^{-12}$	$(2.5 \pm 0.5) \times 10^{-12}$	$(5.0 \pm 0.5) \times 10^{-12}$
	Core Radius/ Å	12 ± 2	10 ± 2	7 ± 2
	Polydispersity Index	0.18 ± 0.02	0.18 ± 0.02	0.18 ± 0.02
	Core Length/ Å	27.56 *		
	SMI belt Thickness/ Å	16 ± 2	18 ± 2	17 ± 2
	Headgroup Thickness/ Å	8.00 *		
	Scattering Length Density (SLD) Core/ $\times 10^{-6}$ Å^{-2}	8.00 *		
	SLD Headgroup/ $\times 10^{-6}$ Å^{-2}	12.70 *		
	SLD SMI Belt/ $\times 10^{-6}$ Å^{-2}	10 ± 1		
	SLD Solvent/ $\times 10^{-6}$ Å^{-2}	9.46 *		
	Incoherent Background/ cm^{-1}	7.00×10^{-13} *	2.00×10^{-13} *	4.00×10^{-13} *
Ellipsoid	Scale	$(7.2 \pm 0.5) \times 10^{-13}$	$(6.0 \pm 0.5) \times 10^{-13}$	$(2.1 \pm 0.5) \times 10^{-12}$
	Radius (a) rotation axis/ Å	10 ± 2	10 ± 2	5 ± 2
	Radius (b) axis/ Å	11 ± 2	11 ± 2	13 ± 2
	SLD Free SMI/ $\times 10^{-6}$ Å^{-2}	10.90 *		
	SLD Solvent/ $\times 10^{-6}$ Å^{-2}	9.46 *		
	Incoherent Background/ cm^{-1}	0.00 *		

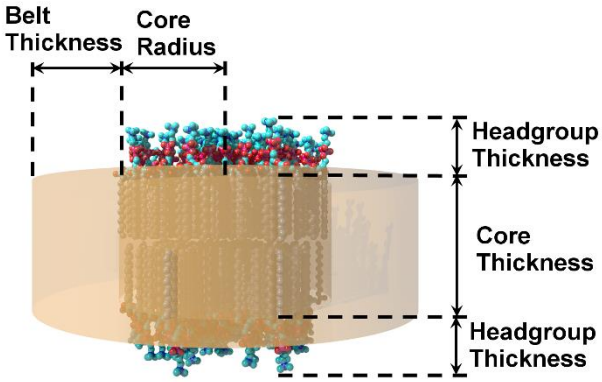

Figure B.2. A rendered representation of the poly-core bicelle model used to fit SAXS data with the labelled dimensions corresponding to parameters in Table B.1.

Table B.2. Parameters obtained through analysis of SEC-MALS chromatograms of SMI and SMILPs formed at three different SMI:DMPC ratios shown in Figure 3.3e.

DMPC concentration /mg ml^{-1}	**0**	**3**	**5**	**7**
Molar ratio [SMI]:[DMPC]	**N/A**	**1.26**	**0.75**	**0.54**
M_W / kDa	34.2 ± 0.8	91.4 ± 0.7	117.6 ± 0.3	139.8 ± 0.3
M_n / kDa	33.5 ± 0.8	90.0 ± 0.7	115.9 ± 0.3	138.2 ± 0.3
PDI	1.02 ± 0.03	1.02 ± 0.01	1.02 ± 0.01	1.01 ± 0.01
Hydrodynamic Diameter / nm	5.10 ± 0.31	7.24 ± 0.25	8.04 ± 0.23	8.64 ± 0.21

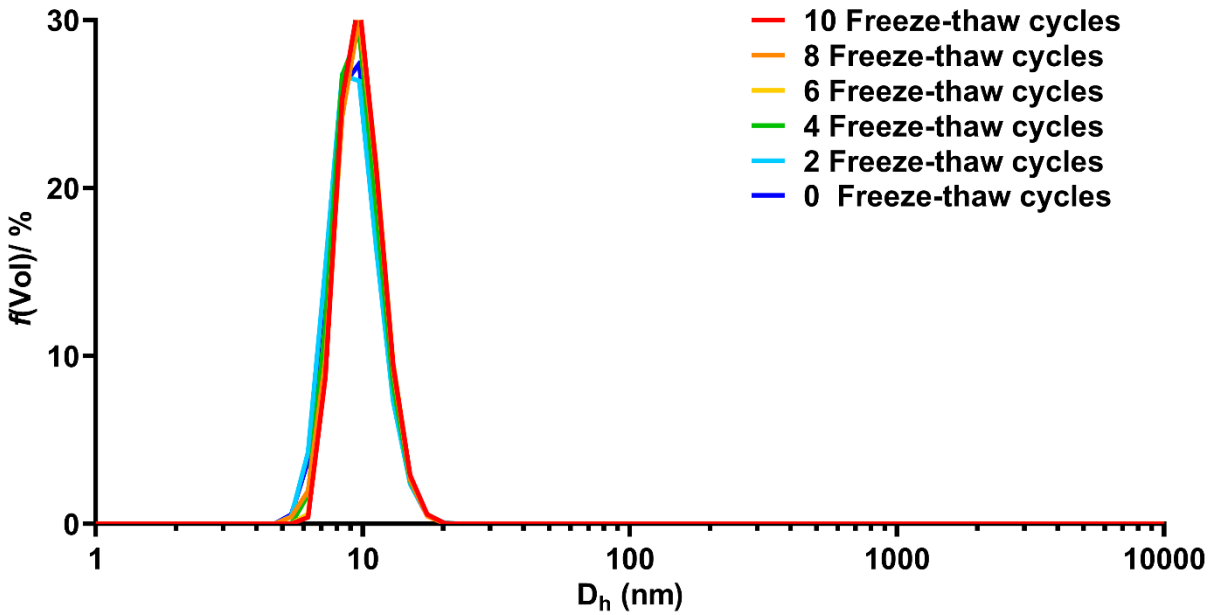

Figure B.3. DLS particle size distribution data for SMILP nanodiscs subjected to successive freeze-thaw cycles. After 10 freeze-thaw cycles, only a small shift of the distribution was observed. No large aggregates were observed, suggesting that SMILPs remain intact through multiple freeze-thaw cycles.

B.3 SUPPLEMENTARY REFERENCES

(1) Basham, M.; Filik, J.; Wharmby, M. T.; Chang, P. C. Y.; El Kassaby, B.; Gerring, M.; Aishima, J.; Levik, K.; Pulford, B. C. A.; Sikharulidze, I.; et al. Data Analysis WorkbeNch (DAWN). *J. Synchrotron Radiat.* **2015**, *22* (3), 853–858.

(2) Feigin, L.; Svergun, D. *Structure Analysis by Small-Angle X-Ray and Neutron Scattering*; Taylor, G. W., Ed.; Springer, **1987**.

(3) Singh, D. Small Angle Scattering Studies of Self Assembly in Lipid Mixtures, The Johns Hopkins University: Baltimore, Maryland, **2008**.

(4) Jamshad, M.; Grimard, V.; Idini, I.; Knowles, T. J.; Dowle, M. R.; Schofield, N.; Sridhar, P.; Lin, Y.; Finka, R.; Wheatley, M.; et al. Structural Analysis of a Nanoparticle Containing a Lipid Bilayer Used for Detergent-Free Extraction of Membrane Proteins. *Nano Res.* **2015**, *8* (3), 774–789.

(5) Kučerka, N.; Kiselev, M. A.; Balgavý, P. Determination of Bilayer Thickness and Lipid Surface Area in Unilamellar Dimyristoylphosphatidylcholine Vesicles from Small-Angle Neutron Scattering Curves: A Comparison of Evaluation Methods. *Eur. Biophys. J.* **2004**, *33* (4), 328–334.

(6) Morrison, K. A.; Akram, A.; Mathews, A.; Khan, Z. A.; Patel, J. H.; Zhou, C.; Hardy, D. J.; Moore-Kelly, C.; Patel, R.; Odiba, V.; et al. Membrane Protein Extraction and Purification Using Styrene-Maleic Acid (SMA) Copolymer: Effect of Variations in Polymer Structure. *Biochem. J.* **2016**, *473* (23), 4349–4360.

(7) Jamshad, M.; Charlton, J.; Lin, Y.-P.; Routledge, S. J.; Bawa, Z.; Knowles, T. J.; Overduin, M.; Dekker, N.; Dafforn, T. R.; Bill, R. M.; et al. G-Protein Coupled Receptor Solubilization and Purification for Biophysical Analysis and Functional Studies, in the Total Absence of Detergent. *Biosci. Rep.* **2015**, *35* (2), e00188.

APPENDIX C

SUPPLEMENTARY INFORMATION FOR CHAPTER 4: A STRUCTURAL AND KINETIC INVESTIGATION OF THE INTERACTIONS OF POLYMER-STABILIZED PHOSPHOLIPID NANODISCS WITH INTERFACIAL PHOSPHOLIPID MEMBRANES

C.1 SUPPLEMENTARY DATA

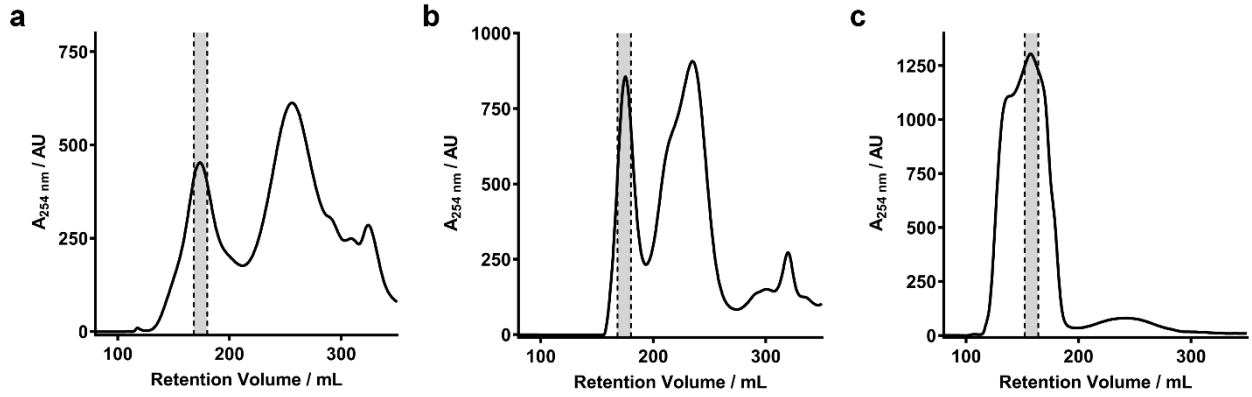

Figure C.1. Representative SEC chromatograms of (a) DMPC SMALP, (b) DMPC SMILP and (c) DMPC RAFT-SMALP purifications. Fractions taken are shown as shaded regions bound by dashed vertical lines.

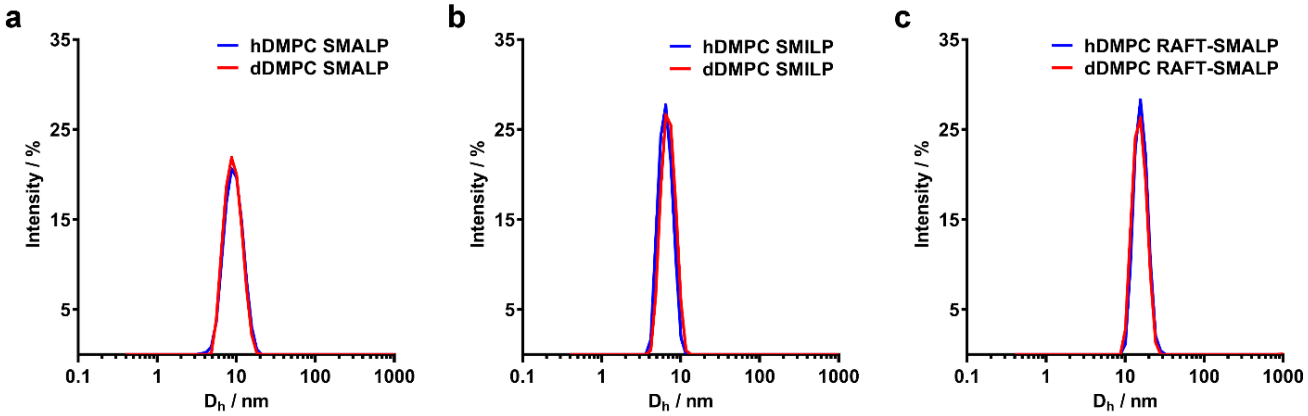

Figure C.2. DLS particle size distributions by scattering intensity percentage for (a) SMALPs, (b) SMILPs and (c) RAFT SMALPs containing either fully hydrogenated DMPC (hDMPC - blue lines) or tail-deuterated DMPC (dDMPC - red lines). In each case, incorporation of tail deuterated DMPC into to the nanodisc structure does not cause any observed change in hydrodynamic diameter. This suggests that our assumption throughout this study of the structural equivalence of hDMPC and dDMPC-containing nanodiscs is valid.

APPENDIX D

SUPPLEMENTARY INFORMATION FOR CHAPTER 5: SMALP NANODISCS PROVIDE A SOLUBLE MEMBRANE SURFACE FOR STRUCTURAL CHARACTERIZATION OF LIPID-BINDING PROTEIN YRAP UNDERGOING NANODISC-INDUCED FIBRILIZATION

D.1 SUPPLEMENTARY DATA

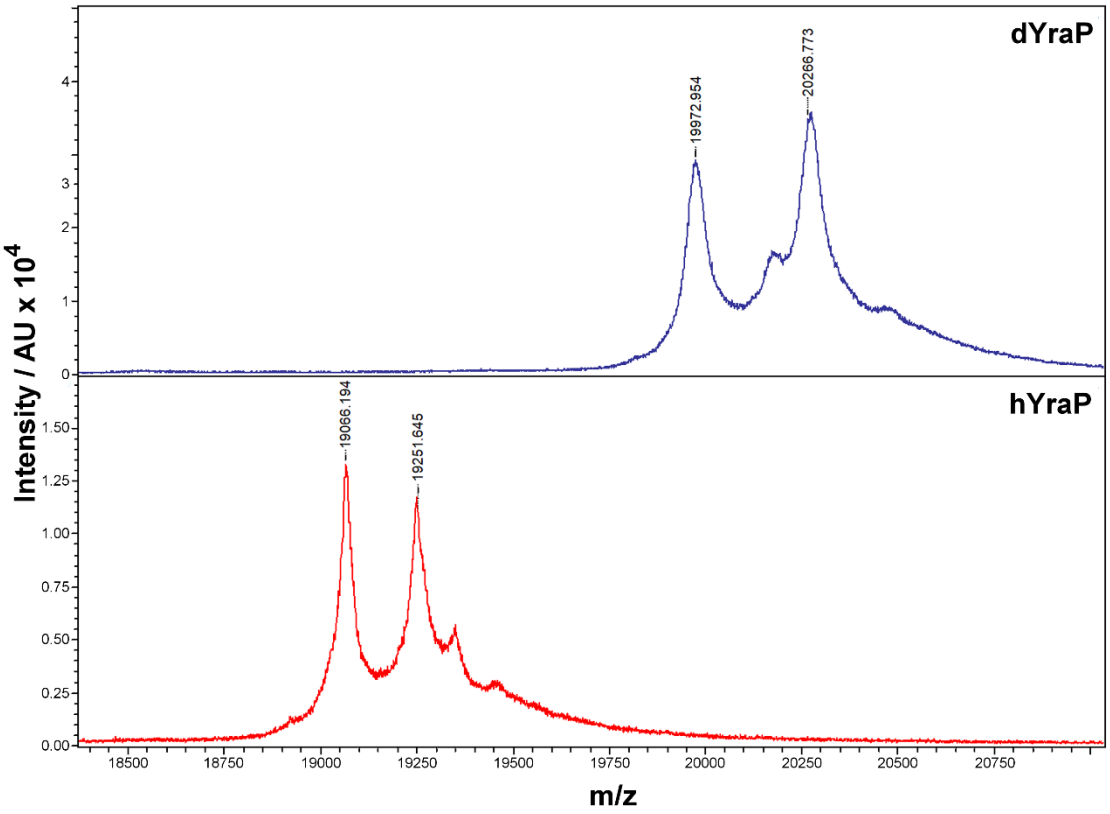

Figure D.1. MALDI-TOF mass spectrometry results displaying the mass of hydrogenated YraP (hYraP, red, bottom) and deuterated YraP (dYraP, blue, top)

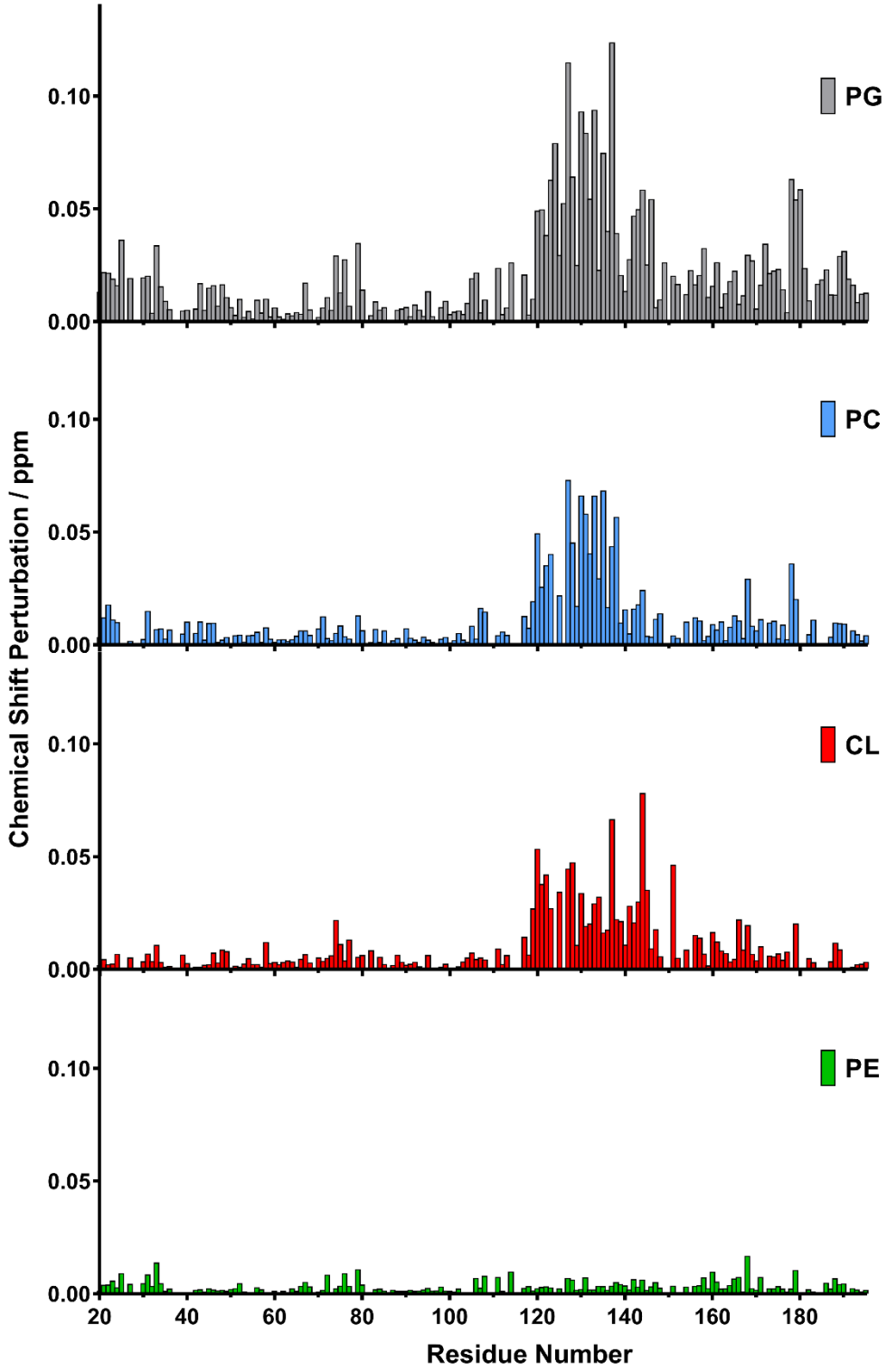

Figure D.2. Heteronuclear single quantum coherence (HSQC) spectroscopy-derived chemical shift perturbations experienced by backbone ^{15}N nuclei in YraP upon incubation with 20 mM phosphatidylglycerol (PG, grey bars), phosphatidylcholine (PC, blue bars), cardiolipin (CL, red bars) and phosphatidylethanolamine (PE, green bars). Residues which are involved in binding lipid headgroups experience a modification to their local chemical environment, leading to an observed perturbation to the chemical shift of the backbone ^{15}N nucleus in each residue.